IRON AND MANGANESE IN THE OCEAN

Atmospheric Input by Dust and Coastal Ocean Time Series

Thesis by

Jeffrey Mendez

In Partial Fulfillment of the Requirements for the

degree of

Doctor of Philosophy

CALIFORNIA INSTITUTE OF TECHNOLOGY

Pasadena, California

2008

(Defended February 20, 2008)

ACKNOWLEDGEMENTS

Many thoughts go through your head in the process of working on a graduate degree. Long hours alone in a lab or over a keyboard force one to question the reasons to continue with this process. The answers to these questions are not definite for anyone, but the day-to-day conclusions we come to while we contemplate them are important, and the people who surround us impact how we do that. I would like to thank those people who surrounded me during my graduate career.

First, I would like to acknowledge Captain Willy McCarthy and his many crew mates who always made me feel safe while at sea, and reminded me that you don't need a fancy degree to do a great job, be clever, and demonstrate ingenuity on a daily basis. I would like to thank Anita Leinweber and Cecile Guieu who reminded me that science is in fact fun, and showed me that while there are many stressful points along our path, we need to remember that our professional life is a choice and ultimately should be a happy one. I would like to thank the post-docs that have come to our research group, for giving me hope that there is an end to grad school, and all the other grad students who began school with me, who have taught me more about myself. Finally, I would like to give great thanks to Jess, my advisor. Jess always had confidence in me while I wandered around with my research. He continued to support me when I was ready to give up, and not only encouraged me to press on but somehow inspired me to further develop my work.

Lastly I must thank my family. My mom and dad gave me everything in life, and allowed me to get to this point. I truly believe that watching my mom go to college and work hard showed me that hard work does pay off, and my dad always pushed me to be better. I need to thank my wife for everything in my life. Gina has been my best friend for the last twelve years and given me the confidence to pursue all of my dreams. Lastly, I would like to write a message to my son. Thomas, you are only seventeen months old, but you have been the inspiration for me to finish this long journey. Your smiling face and wonderful

personality have made me very happy and content. You gave me the inspiration to finally finish this thesis and I must thank you. I hope one day you can feel the warmth in your heart that you have given me.

ABSTRACT

Trace metals such as iron (Fe) and manganese (Mn) are essential micronutrients in the biogeochemistry of the ocean (Turner and Hunter, 2001), and dry deposition is a substantial source of both Fe and Mn to the surface ocean (Duce and Tindale, 1991; Guieu *et al.*, 1994). Kinetic and thermodynamic values for the release of metals from dust are needed for computer models which incorporate dust as part of their ocean system. Here we investigate the thermodynamic and kinetics parameters involved in the dissolution of metals from dust in seawater. We added dust from the Sahara and the Western United States to seawater in a variety of ways to investigate the dissolution patterns of Fe and Mn.

Results show different apparent thermodynamic constants for manganese (Mn) and iron (Fe). The final Mn concentrations are proportional to the added dust concentration and light intensity, and independent of initial dissolution rate. Fe concentrations in fresh seawater reach a maximum concentration of less than 2 nM. However, depletion of organic ligands lead to the precipitation of Fe oxide from solution, and the addition of siderophores enhanced both the total Fe capacity of the seawater and the rate of Fe dissolution from dust. The first order rate constant for the dissolution of dust differed by dust source and was dependent on oxalate concentration and intensity of natural UV light. We conclude that final Mn concentrations are limited by available Mn on the dust surface, while Fe concentrations are limited by the ligand concentrations in the seawater, which ultimately are determined by the biological community.

Because the coastal ocean plays a significant role in global biogeochemical cycles, (Smith and Hollibaugh, 1993; Tsunogai and Noriki, 1991), we conducted a coastal ocean time series to investigate the basic modes and cycles which characterize the ocean. We found that Mn is highly dependent on seasonal rain events, with surface water concentrations observed as high as 30 nM after rain events. Fe within the coastal ocean is highly variable and can be used as a tool to track water mass movements and mixing patterns.

TABLE OF CONTENTS

LIST OF FIGURES AND TABLES

Introduction

IRON AND MANGANESE IN THE OCEAN

Iron (Fe) and manganese (Mn) are essential micronutrients required for enzymatic pathways such as: respiration, nitrogen and carbon fixation, and electron transfer in photosynthetic marine biology (Turner and Hunter, 2001). The availability of these trace metals can be critical to the biological productivity of the ocean. Therefore, a complete understanding of the mechanisms which control the trace metal cycles, and their sources & sinks is important to the overall knowledge of biological cycles in the ocean.

Mn is specifically important for photosynthetic and radical scavenging enzymes (Horsburgh et al., 2002; Kernen et al., 2002). Thermodynamically, Mn in fully oxygenated waters at natural pH is Mn(IV) and precipitates out of the water in the form MnO_2. However, dissolved Mn ocean profiles reveal that the surface waters contain high levels of soluble Mn(II). A portion of this soluble Mn is from direct atmospheric deposition (Guieu et al., 1994; Siefert et al., 1998), and while slow oxidation to the +3 or +4 forms allow Mn to stay dissolved on the order of days, Mn should oxidize over time and precipitate from the surface ocean (Stumm and Morgan, 1996). Oxidation does occur, but the build up of oxidized Mn is prevented by organic material (Sunda et al., 1983). Light in the surface ocean can promote an electron transfer between organics, such as humic material, and Mn, resulting in the photoreduction of Mn to the +2 oxidation state. This results in a large concentration of soluble Mn in the surface water, available for biological use.

Fe is the fourth most abundant element in the Earth's crust (Wedepohl, 1995). However in oxic pH 8 seawater the stable oxidation state, Fe (III), is relatively insoluble limiting the concentration to 0.1 nM (Morel and Hering, 1993). Any inorganic iron above this concentration will either form an Fe oxide solid or quickly adsorb onto nearby surfaces

(Rose and Waite, 2002). Despite this limit, dissolved oceanic Fe concentrations range from 0.1 – 2 nM (or higher in the coastal ocean). A major source of Fe to the ocean is dust (Duce and Tindale, 1991). While these aerosols are aloft in the atmosphere, photochemical reactions with a variety of oxidants can convert a significant fraction of the total Fe into soluble Fe(II) (Siefert et al., 1996). Therefore, Fe(II) additions to the surface water from aerosol deposition can elevate the total dissolved Fe concentration (Bruland et al., 1994; Erel et al., 1993; Johansen et al., 2000); however, like Mn(II), these too will quickly oxidize. Therefore, Fe must have a non-inorganic method for maintaining dissolved Fe in the seawater. Organic ligands appear to be responsible for this elevation of Fe concentrations. (Barbeau et al., 2001; Buck et al., 2007; Rue and Bruland, 1995; van den Berg, 1995). It is believed that marine bacteria produce these organic ligands, known as siderophores, under Fe depleted conditions in order to secure ample Fe resources from the ocean water (Davis and Byers, 1971; Haygood et al., 1993). During times of Fe depletion organisms which produce these ligands and have multiple pathways for Fe uptake will not become limited in their growth and cell production.

In high nutrient low chlorophyll (HNLC) waters Fe can be the limiting or co-limiting nutrient (Maldonado et al., 1999; Martin et al., 1989; Mills et al., 2004). Early bottle incubations studies in the Gulf of Alaska confirmed that Fe limitation does control ocean productivity within HNLC regions (Boyd et al., 2007; Martin and Fitzwater, 1988). Later studies found some HNLC regions to be permanently Fe limited over time such as the Southern Ocean (Boyd et al., 2000) and Equatorial Pacific (Martin et al., 1994), and others to be seasonally limited such as the Gulf of Alaska and the Northern California Coast (Johnson et al., 2001). Because Fe limitation can control biological production in large regions of the world's ocean, Fe may be a limiting factor in the flux of inorganic carbon, in the form of carbon dioxide (CO_2), from the atmosphere to the ocean. This flux of carbon can have an influence on the total atmospheric CO_2 and therefore global temperatures possibly effecting glacial to interglacial changes. The process of atmospheric Fe input to

the ocean controlling the global carbon budget and temperature is known as the Iron Hypothesis (Martin, 1990). Several mesoscale Fe addition experiments including IronEx I and II (equatorial Pacific) and SOIREE and SOFeX (Southern Ocean), have been conducted to investigate the Iron Hypothesis. Each experiment found increased phytoplankton growth, especially diatoms, followed by an increased grazer population (Boyd et al., 2007). The later experiments found that surface ocean carbon dioxide levels decreased during the course of the fertilization. However no mesoscale experiment to date has found an increase in organic carbon flux to the deep ocean or the permanent burial of carbon (Boyd et al., 2007).

Each of these Fe addition experiments were conducted in conditions far from nature. In Martin's Iron Hypothesis, dust is blown onto a HNLC ocean releasing Fe and promoting biological productivity. However, in the mesoscale experiments $FeCl_3$ is releases in pulses spaced several days apart. In a natural setting there would be dissolution of Fe from the dust, in the form of Fe(II) and Fe(III) occurring over time scales of seconds and days. Fe (III) may be complexed to organic molecules which would promote solubility, and other trace material associated with dust may also be key to a natural large scale Fe addition. In addition, for a global carbon dioxide effect, dust deposition must occur on a more continuous basis rather than the short pulses used in the experiments.

For comparison there are several natural Fe addition experiments which occur in the oceans today. Saharan dust is regularly blown off the coast of Africa and onto the North Atlantic ocean. There are periodic Chinese wind storms which blow Gobi desert dust onto the Pacific ocean, and Santa Ana winds located in Southern California can blow mineral and anthropogenic dust hundred of kilometers out to sea. (Powell et al., 1995) found Fe concentration in excess of 10 nM in the North Atlantic Ocean beneath the Sahara dust plume. These high levels of Fe have been linked to blooms of the nitrogen fixer, trichodesmium, forcing phosphate, rather that nitrate to be the limiting nutrient (Karl et al., 2002). The bio-productivity effects of Chinese dust over North Pacific have been observed

by several research cruises. In one experiment, autonomous floats were released in the North Pacific to observe chlorophyll and particulate organic matter. Two coincident dust events from China revealed that chlorophyll increased over a seven day period following the dust event, and particulate organic matter was transport below the thermocline approximately two weeks following each event. These results suggest that the biological response to a natural fertilization event is different from our synthetic Fe additions.

The overall importance of Fe to the ocean and potential importance to the global temperature has be verified by both these mesoscale fertilization experiments, and many laboratory studies. This has lead to the incorporation of Fe into computer models (Aumont et al., 2003; Moore et al., 2006) to more accurately describe overall ocean biogeochemical cycles. However, data comparisons to these models can be difficult due to the lack of complete temporal and spatial coverage of the world's ocean. An alternative to the global ocean model, is a regional ocean model, such as the coastal region, which can be used as a proxy for the global ocean (Smith and Hollibaugh, 1993; Tsunogai and Noriki, 1991). The Santa Ana winds and Southern California Bight region can provide a natural Fe addition experiment along the coast.

In the present work we studied Fe addition by dust within the Southern California Bight in order to clarify several aspects of the Iron Hypothesis. We have organized our work into three sections: developing and refining an accurate Fe measurement technique, a series of dust addition experiments, and participation is a coastal ocean time series.

In order to study Fe in the ocean we need to be able to accurately measure Fe. To that end, we adapted and modified an inductively coupled plasma mass-spectrometer (ICP-MS) technique (Wu and Boyle, 1998). In this method, we concentrate the trace amount of Fe by precipitating it along with magnesium hydroxides; therefore, we can also measure any other element which adsorbs onto these magnesium hydroxide particles. In addition to Fe we measured Mn, due to its importance in ocean productivity. The first chapter will describe

the mechanics of this technique, the theoretical reasons for each step, and finally the statistical information on our accuracy and precision for both Fe and Mn measurements in seawater.

Martin's Iron Hypothesis requires Fe to be released by wind blown dust into seawater. Therefore we need to understand the thermodynamics, kinetics, and mechanisms behind Fe dissolution from dust. We have conducted several laboratory experiments to study the mechanism in which trace metals, such as Fe and Mn, enter the ocean through dust input. We ran three dust dissolution experiments which we outline and discuss in chapters 2 and 3. The first experiment sought to study the differences in trace metal input by dust origin and dust concentration. Based on the results from the first experiment, our next dust experiment focused on the seawater organic background matrix, specifically concentrating on known small Fe binding molecules and aerobactin, a natural Fe binding ligand known as a siderophore. Our third experiment focused on the effects of light on dust dissolution for Fe and Mn in the presence of aerobactin.

Finally, we wanted to investigate whether a pulsed dust input into a coastal ocean region could have productivity effects. We chose to study the Santa Ana winds effect on the Southern California Bight. In collaboration with UCLA we participated in a biweekly time series in the Santa Monica Bay to examine the temporal cycles of Fe and Mn in the coastal ocean, described in chapter 4. This type of time series is needed to capture the events that may lead to changes in the biological production, but more importantly it is required to first understand the basic modes and cycles which characterize the ocean. After these background states have been observed and analyzed, the changes in biological production due to events like Santa Ana winds can be placed into their proper context.

BIBLIOGRAPHY

Aumont, O., Maier-Reimer, E., Blain, S. and Monfray, P., 2003. An ecosystem model of the global ocean including Fe, Si, P colimitations. Global Biogeochemical Cycles, 17(2).

Barbeau, K., Rue, E.L., Bruland, K.W. and Butler, A., 2001. Photochemical cycling of iron in the surface ocean mediated by microbial iron(III)-binding ligands. Nature, 413: 409-413.

Boyd, P.W. et al., 2007. Mesoscale iron enrichment experiments 1993-2005: Synthesis and future directions. Science, 315(5812): 612-617.

Boyd, P.W. et al., 2000. A mesoscale phytoplankton bloom in the polar Southern Ocean stimulated by iron fertilization. Nature, 407: 695-702.

Bruland, K.W., Orians, K.J. and Cowen, J.P., 1994. Reactive Trace-Metals in the Stratified Central North Pacific. Geochimica Et Cosmochimica Acta, 58(15): 3171-3182.

Buck, K.N., Lohan, M.C., Berger, C.J.M. and Bruland, K.W., 2007. Dissolved iron speciation in two distinct river plumes and an estuary: Implications for riverine iron supply. Limnology and Oceanography, 52(2): 843-855.

Davis, W.B. and Byers, B.R., 1971. Active Transport of Iron in Bacillus-Megaterium - Role of Secondary Hydroxamic Acids. Journal of Bacteriology, 107(2): 491-&.

Duce, R.A. and Tindale, N.W., 1991. Atmospheric transport of iron and its deposition in the ocean. Limnology and Oceanography, 36(8): 1715-1726.

Erel, Y., Pehkonen, S.O. and Hoffmann, M.R., 1993. Redox Chemistry of Iron in Fog and Stratus Clouds. Journal of Geophysical Research-Atmospheres, 98(D10): 18423-18434.

Guieu, C., Duce, R. and Arimoto, R., 1994. Dissolved Input of Manganese to the Ocean - Aerosol Source. Journal of Geophysical Research-Atmospheres, 99(D9): 18789-18800.

Haygood, M.G., Holt, P.D. and Butler, A., 1993. Aerobactin Production by a Planktonic Marine Vibrio Sp. Limnology and Oceanography, 38(5): 1091-1097.

Horsburgh, M.J., Wharton, S.J., Karavolos, M. and Foster, S.J., 2002. Manganese: elemental defense for a life with oxygen. Trends in Microbiology, 10(11): 496-501.

Johansen, A.M., Siefert, R.L. and Hoffmann, M.R., 2000. Chemical composition of aerosols collected over the tropical North Atlantic Ocean. Journal of Geophysical Research-Atmospheres, 105(D12): 15277-15312.

Johnson, K.S. et al., 2001. The annual cycel of iron and the biological response in central California coastal waters. Geophysical Research Letters, 28(7): 1247-1250.

Karl, D. et al., 2002. Dinitrogen fixation in the world's oceans. Biogeochemistry, 57(1): 47-98.

Kernen, N., Kidd, M.J., Penner-Hahn, J.E. and Pakrasi, H.B., 2002. A light-dependent mechanism for massive accumulation of manganese in the photosynthetic bacterium Synechocytis sp. PCC 6803. Biochemistry, 41(50): 15085-15092.

Maldonado, M.T., Boyd, P.W., Harrison, P.J. and Price, N.M., 1999. Co-limitation of phytoplankton growth by light and Fe during winter in the NE subarctic Pacific Ocean. Deep-Sea Research Part Ii-Topical Studies in Oceanography, 46(11-12): 2475-2485.

Martin, J.H., 1990. Glacial-interglacial CO_2 change: The Iron Hyphothesis. Paleoceanography, 5(1): 1-13.

Martin, J.H. et al., 1994. Testing the iron hypothesis in ecosystems of the equatorial Pacific Ocean. Nature, 371: 123-129.

Martin, J.H. and Fitzwater, S.E., 1988. Iron deficiency limits phytoplankton growth in the north-east Pacific subarctic. Nature, 331: 341-343.

Martin, J.H., Gordon, R.M., Fitzwater, S. and Broenkow, W.W., 1989. VERTEX: phytoplankton/iron studies in the Gulf of Alaska. Deep-Sea Research, 36(5): 649-680.

Mills, M.M., Ridame, C., Davey, M., La Roche, J. and Geider, R.J., 2004. Iron and phosphorus co-limit nitrogen fixation in the eastern tropical North Atlantic. Nature, 429(6989): 292-294.

Moore, J.K., Doney, S.C., Lindsay, K., Mahowald, N. and Michaels, A.F., 2006. Nitrogen fixation amplifies the ocean biogeochemical response to decadal timescale variations in mineral dust deposition. Tellus Series B-Chemical and Physical Meteorology, 58(5): 560-572.

Morel, F.M.M. and Hering, J.G., 1993. Principles and Applications of Aquatic Chemistry. John Wiley & Sons, Inc., New york, 588 pp.

Powell, R.T., King, D.W. and Landing, W.M., 1995. Iron Distribution in surface waters of the south Atlantic. Marine Chemistry, 50(1-4): 13-20.

Rose, A.L. and Waite, T.D., 2002. Kinetic model for Fe(II) oxidation in seawater in the absence and presence of natural organic matter. Environmental Science & Technology, 36(3): 433-444.

Rue, E.L. and Bruland, K.W., 1995. Complexation of Iron(III) by Natural Organic-Ligands in the Central North Pacific as Determined by a New Competitive Ligand Equilibration Adsorptive Cathodic Stripping Voltammetric Method. Marine Chemistry, 50(1-4): 117-138.

Siefert, R.L., Johansen, A.M., Hoffmann, M.R. and Pehkonen, S.O., 1998. Measurements of trace metal (Fe, Cu, Mn, Cr) oxidation states in fog and stratus clouds. Journal of the Air & Waste Management Association, 48(2): 128-143.

Siefert, R.L., Webb, S.M. and Hoffmann, M.R., 1996. Determination of photochemically available iron in ambient aerosols. Journal of Geophysical Research-Atmospheres, 101(D9): 14441-14449.

Smith, S.V. and Hollibaugh, J.T., 1993. Coastal Metabolism and the Oceanic Organic-Carbon Balance. Reviews of Geophysics, 31(1): 75-89.

Stumm, W. and Morgan, J.J., 1996. Aquatic Chemistry. Wiley-Interscience, New York, 1022 pp.

Sunda, W.G., Huntsman, S.A. and Harvey, G.R., 1983. Photoreduction of manganese oxides in seawater and its geochemical and biological implications. Nature, 301: 234-236.

Tsunogai, S. and Noriki, S., 1991. Particulate Fluxes of Carbonate and Organic-Carbon in the Ocean - Is the Marine Biological-Activity Working as a Sink of the Atmospheric Carbon. Tellus Series B-Chemical and Physical Meteorology, 43(2): 256-266.

Turner, D.R. and Hunter, K.A. (Editors), 2001. The biogeochemistry of iron in seawater. IUPAC series on analytical and physical chemistry of environmental systems ; v. 7. J. Wiley, New York.

van den Berg, C.M.G., 1995. Evidence for Organic Complexation of Iron in Seawater. Marine Chemistry, 50(1-4): 139-157.

Wedepohl, K.H., 1995. The Composition of the Continental-Crust. Geochimica Et Cosmochimica Acta, 59(7): 1217-1232.

Wu, J. and Boyle, E.A., 1998. Determination of iron in seawater by high-resolution isotope dilution inductively coupled plasma mass spectrometry after $Mg(OH)_2$ coprecipitation. Analytica Chimica Acta, 367: 183-191.

C h a p t e r 1

RESEARCH METHODS

Collection and Analysis of Seawater

Jeffrey Mendez[a], Jess Adkins[b]

a Department of Environmental Science and Engineering, California Institute of Technology
b Department of Geological and Planetary Sciences, California Institute of Technology

1. Time Series Sample Collection

All time series field work was conducted aboard the R/V *Seaworld* UCLA at the Santa Monica Bay Observatory Oceanographic Mooring site. The mooring is anchored at 33° 55.9' N, 118° 42.9' W; the mooring drifts about this point depending on the prevailing surface currents, as shown in figure 1. Seawater was collected using Teflon-coated external spring niskin bottles using Teflon coated messengers (General Oceanics Inc. model 1010X-5L) attached to ¼ inch polyester line. Niskin bottles were rinsed with surface seawater (15 - 40 m) before each day's use and milli-Q (mQ) water after each day of sampling (18.2 MΩ, 2 x 500 mL), and stored wet.

Water was pumped from each niskin bottle through a 0.2 μm cartridge filter (Sartobran cellulose acetate P 150, 0.45 μm prefilter) with a peristaltic pump using C-Flex tubing (acid leached in 10% v/v reagent HCl) into a hepafiltered work space. The filter and tubing were rinsed with at least one liter of seawater before sampling to remove any residual acid and condition the walls to reduce sample iron adsorption (Buck *et al.*, 2007). Samples were collected in 60 or 125 mL low density polyethylene (LDPE) bottles, rinsing each bottle 3 times with the seawater sample before collection. Final samples were acidified with hydrochloric acid (12 M, SeaStar® HCl) at an acid to seawater ratio of 1:1000, ultimately

reaching a pH of 2.0 - 2.3. All sampling and laboratory materials were acid leached using standard trace metal clean techniques.

2. Dust Dissolution Procedures

2.1 Seawater Collection

Four different types of seawater were used in the dust dissolution experiments. Open ocean seawater at two general depths was collected at 30°N 140°W in November 2004 aboard the R/V *Melville* during the Sampling and Analysis of Iron (SAFe) intercomparison cruise (Johnson *et al.*, 2007). Surface seawater was collected with the University of California Santa Cruz (UCSC) trace metal clean surface "sipper" sampler (Bruland Lab), and sub-surface seawater was collected with the University of Hawaii's 30 L GO-Flo niskin bottles at a depth range of 24-26 m (Measures Lab). There was a 76 m mixed layer during sub-surface sampling; therefore, all relevant chemical and physical properties of the sub-surface water used in these experiments should be identical in the 24-26 m depth range. Sub-surface water was in-line filtered at sea through a 0.2 μm cartridge filter and stored in an acid leached 4 L polycarbonate (PC) bottle unacidified and in the dark. Surface water was in-line filtered at sea through a 0.4 μm cartridge filter and stored in a 25 L high-density polyethylene (HDPE) carboy, also unacidified in the dark.

Seawater from two separate coastal locations was collected and treated in two different ways. The first coastal seawater was collected at 10 m depth while at the Santa Monica Bay Observatory Oceanographic Mooring (33° 55.9' N, 118° 42.9' W) aboard the R/V *Seaworld* UCLA in December 2005. Sub-surface sample water was collected using Teflon coated external spring niskin bottles with Teflon coated messengers (General Oceanics Inc. 1010X-5L) on ¼ inch polyester line. Water was pumped from the niskin bottle through a 0.2 μm cartridge filter (Sartobran cellulose acetate P 150) with a peristaltic pump using C-Flex tubing into a hepa-filtered work space. All sampling and laboratory materials were acid leached using trace metal clean techniques. The second coastal seawater was collected

and UV irradiated at UCSC (Bruland Lab) as described in (Donat and Bruland, 1988), but using Biobeads SM-2 and Amberlite XAD-16 resins in lieu of their Sumichelate Q10R resin. Both coastal seawater samples were stored frozen in one or two liter Teflon PFA bottles.

2.2 Dust Collection

Two sources of dust were tested in our dissolution experiments. The Saharan dust was a composite of 12 surface soils that were collected under clean conditions from the Hoggar region (Algeria) (Guieu *et al.*, 2002). The U.S. dust is a composite of 3 superficial deposits collected in natural dust traps in the Nevada desert (South-West of Las Vegas) (courtesy Marith Reheis, USGS). Both Saharan and U.S. dust were hand sieved through successive clean polyethylene meshes of 100 and 20 μm pore diameter. The smallest fraction (<20 μm) was collected and stored in a clean glass bottle. The U.S. sample was then autoclaved to destroy any possible bacteria spores, and both samples were stored in a dark cabinet.

2.3 Elemental Dust Analysis

Dust was acid digested inside a Milestone 1200 Mega microwave oven with 1 mL of HF and 3 mL HNO_3 (Suprapur®, Merck). Aluminum (Al), iron (Fe), and manganese (Mn) were determined using calibration curves by Inductively Coupled Plasma-Atomic Emission Spectroscopy (ICP-AES Ultra traces, Jobin Yvon). Blanks (reagent alone) were below the detection limit. The ratio of measured to recommended concentrations in the BCSS certified reference material ((n=3), National Research Council of Canada; range of weights: 10.7-16.08 mg) was 1.1 ± 0.1. Grain-size distributions in volume were established for the two dust samples dispersed in ultrapure water with a Mastersizer (Malvern Instruments, UK).

2.4 Dissolution Experiment 1, Dust Variation

Experiment 1 was designed to compare the dissolution effect of different dust types and concentrations over time. Samples were prepared by adding open ocean surface seawater to five 1 L clear Teflon bottles using an acid leached graduated cylinder. Within a 1 L

polyethylene bottle, approximately 10 mg of Saharan dust was added to 1 L of identical seawater. This solution was quickly shaken and proportioned via pipette or graduated cylinder to each of the sample bottles in order to reach the different dust concentrations (0.01, 0.05, 0.5, 1.0, 5.0 mg/L). The sample bottles (including a control bottle which received no dust) were then sealed with parafilm and immersed in a 13°C water bath (temperature of nitracline in the Santa Monica Bay), under a 50% light screen (to mimic the reduced light in the euphotic zone), on the roof of the laboratory. This sequence was repeated for the U.S. dust. The seawater was allowed to mature under the diurnal cycle for 35 days. Samples were removed from this bath on days 1, 2, 4, 7, 14, and 35 at 1:00 PM for about 2 hours to take sub-samples.

Sub-samples were taken to measure the progression of metal dissolution. Once removed from the roof, the bottles' exteriors were cleaned by thoroughly rinsing with mQ water in a hepafiltered flow bench. The parafilm was removed, and the bottles were individually opened for sub-sampling. The filter apparatus was rinsed by pouring 10 mL of the sample seawater through a 0.2 μm filter (Whatman 25 mm polycarbonate membrane). The sub-sample was then taken by pouring another 10 mL of sample through the filter and collecting it in a small high density polyethylene bottle. This sub-sample was immediately split into two and acidified with concentrated hydrochloric acid (12 M, SeaStar® HCl, 10 μL). Following each sample, the filter was exchanged and the filter apparatus was rinsed with diluted nitric acid (~25 mL, SeaStar® HNO_3), followed by clean mQ water (~150 mL).

2.5 Dissolution Experiment 2, Seawater Matrix

The first experiment was designed to compare dust dissolution in different seawater matrices, focusing on the effects of model and natural Fe binding ligands. Open ocean surface seawater, Santa Monica Bay coastal seawater, UV irradiated coastal seawater, and UV irradiated seawater with added organic molecules were used in this experiment. Seven separate "seawaters" were prepared.

1. Santa Monica Bay coastal water, “Coastal Water”
2. Open ocean surface seawater, “Open Ocean Water”
3. UV irradiated coastal seawater (Bruland Lab UVSW), “UV Water”
4. UV irradiated coastal seawater with the addition of citric acid (57 nM, Sigma-Aldrich Cat #25,127-5), “Citrate Water”
5. UV irradiated coastal seawater with the addition of oxalic acid dihydrate (69.5 nM, Sigma-Aldrich Cat # 24,753-7), “Oxalate Water”
6. UV irradiated coastal seawater with the addition of a combination of citric acid and oxalic acid dihydrate (57 nM & 69.5 nM, respectively), “Citrate & Oxalate Water”
7. UV irradiated coastal seawater with the addition of aerobactin (EMC Microcollections) at a concentration of 50.1 nM, “Aerobactin Water”

An initial sub-sample was taken from each bottle to dissolved measure metal concentrations (Mn, Fe) and Fe speciation, including Fe-binding organic ligand concentrations and binding constant. Each sub-sample was taken by directly filtering the sample seawater into a sub-sample bottle, (0.2 μm pore size, 25 mm polycarbonate Whatman). Following each filtration, the filter was exchanged and the filter apparatus rinsed with ~150 mL water (18 MΩ) and 5 mL of the next sample. All metal concentration sub-samples were acidified with hydrochloric acid (12 M, SeaStar® HCl), and all Fe speciation sub-samples were sealed and frozen.

After sub-sampling (t=0), the initial seven seawater samples were each split into two 1 L Teflon bottles, for a total of fourteen bottles. One bottle from each water type was sealed as a control, while the other bottle was saved for the dust addition. A mixture of 8.45 mg of dust and 52 mL of seawater was quickly shaken and then proportioned via pipette to each of the seven dust addition sample bottles in order to establish a dust concentration of 1.2 mg/L. This concentration is representative of typical dust deposition over ocean water (Duce and Tindale, 1991). Immediately following the addition of the dust, a sub-sample

(t=30 min to 2 hr 40 min) was taken from each bottle to measure the dissolved metal concentrations (Mn, Fe) and Fe speciation.

The sample bottles (including the control bottles) were sealed with parafilm, placed in clear zipper bags, and immersed in a 13°C water bath on the roof of the laboratory under a 50% light screen. The seawater samples were allowed to mature under the diurnal cycle for 28 days. Samples were removed from this bath on days 0.25, 0.5, 1, 2, 4, 7, 14, and 28 for ~2 hours to take sub-samples.

2.6 Dissolution Experiment 3, Light Exposure

Experiment 3 was designed to compare the dust dissolution effects of light on seawater, with and without amendments of the siderophore aerobactin, in order to elucidate the mechanism of siderophore-promoted dissolution. Two bottles of open ocean sub-surface seawater (SAFe; see Seawater Collection) were used in this experiment. One bottle was left unaltered, "Seawater"; while aerobactin was added to the second, "Aerobactin Water."

The Aerobactin Water was prepared by dissolving 1.088 mg of solid aerobactin in 1 mL of seawater. 111 μL of this solution was transferred to the seawater bottle via pipette to establish an aerobactin concentration of 51.1 nM. All work with solid aerobactin was conducted in an Ar filled glove bag in order to reduce any thermal oxidation and decomposition. Sub-samples of Seawater and Aerobactin Water were then taken to measure initial metal concentrations (Mn, Fe) and dissolved Fe speciation. The filter apparatus was rinsed by pouring 5 mL of the sample seawater through a 0.2 μm filter (Whatman 47 mm polycarbonate membrane). The rinse water was then used to rinse each container. The sub-sample was then taken by pouring another 5 mL of sample seawater through the filter collecting it in a small high density polyethylene bottle. This was repeated for a duplicate sample, followed by a sub-sample for Fe speciation analysis which required approximately 350 mL. The metal sub-samples were acidified with hydrochloric acid (12M, SeaStar® HCl, 10 μL) while the Fe speciation sub-sample was sealed and

frozen. Following each sample, the filter and the filter apparatus were rinsed with clean mQ water.

A portion of both seawater types was poured into two different types of Teflon bottles. One bottle was translucent Teflon (the "Light" bottle) and the other was an identical bottle wrapped in black electrical tape to prevent light exposure (the "Dark" bottle). These four new samples became the "no dust" controls. A concentrated solution of dust in seawater (0.87 g_{dust}/L) was added via pipette to the remaining Aerobactin Water and Seawater samples to reach a dust concentration of 1.1 mg/L. Immediately following this addition, a sub-sample was taken to measure initial Fe speciation. The samples were again partitioned into "Light" and "Dark" bottles, resulting in 8 total samples bottles: Seawater: light-no dust, dark-no dust, light-dust, dark-dust ; and Aerobactin: light-no dust, dark-no dust, light-dust, dark-dust.

The Light bottles were sealed with parafilm and placed in a clear zipper bag, while the Dark bottles were sealed and placed in three brown bags to further reduce light exposure. All samples were immersed in a 13°C water bath on the roof of the laboratory under a 50% light screen. The samples were allowed to mature under the diurnal cycle for 18 days. Samples were removed from this bath on days 0.5, 1, 1.5, 2, 2.5, 3, 6, 9, and 18 for ~ 2 hours to take sub-samples.

3. Isotope Dilution

The iron (Fe) concentration was determined through isotope dilution (Wu and Boyle, 1998) on an inductively coupled plasma mass spectrometer (ICP-MS, Finnigan Element 1). In isotope dilution, an enriched isotope of the analyte is added to the sample (referred to as a spike). This spike sets the ratio of the common to the enriched isotope. Once set, only the isotope ratios of the natural sample, the spike, and the resulting (or mixed) sample (which is measured on the ICP-MS), as well as the quantities of sample and spike used need to be known in order to calculate the original elemental concentration. Because the

isotopes will react in the same manner during a chemical reaction, numerous nonquantitative laboratory steps can be used to enrich or purify the sample without fear of changing the sample's set isotope ratio. Any changes will occur equally to both isotopes, preserving the initial ratio set by the spike. The analyte concentration is calculated with the isotope dilution (eq. 1), where C is the concentration, R is the isotope ratio, V is volume, % is the percentage of isotope, and the subscripts sa, sp, and m represent sample, spike, and mixed respectively.

$$C_{sa} = \frac{\left(R_{sp} - R_m\right) V_{sp} \%_{sp}}{\left(R_m - R_{sa}\right) V_{sa} \%_{sa}} C_{sp} \qquad \text{(eq. 1)}$$

3.1 Limitations

In equation 1, the calculated concentration of the analyte is dependent on the natural isotope ratio, the spike isotope ratio, the concentration of the spike, and the volumes of sample and spike added to the mixture. Any errors from these quantities' true values will result in errors in the final calculated concentration.

A mixed ratio which is similar to the natural or the spike ratio will result in large errors. Focusing on equation 1, when R_m approaches either R_{sa} or R_{sp}, the values of $(R_m - R_{sa})$ or $(R_{sp} - R_m)$ approach zero and the error associated with R_m propagated through equation 1 grows asymptotically, leading to low precision in the final calculated analyte concentration. R_m at the geometric mean of the spike and the sample's isotope ratio will center the ratio between these asymptotes and minimize this error as seen in figure 2.

A drawback of isotope dilution is that to reach the geometric mean of these two ratios, the concentration of the analyte must already be known. To get around this predicament we conduct our analysis with high purity spikes which have isotope ratios many orders of magnitude different from our natural samples. In figure 2, the right hand asymptote is set by the sample's ratio, while the left hand asymptote is set by the spike's ratio. By using a

high purity spike, we can shift the left hand asymptote in figure 2 further to the left, creating an error curve with a low error region which spans many orders of magnitude. In this situation, even if the resulting mixed isotope ratio is greatly different from the geometric mean, there should be a broad enough region in the error curve where the propagated error is acceptably low. Using high purity spikes allows us to add the same quantity of spike to every sample, even if they have different concentrations, and they will all most likely fall within this acceptable R_m region. For all of our measurements it was assumed that the isotope ratio ($^{56}Fe/^{57}Fe$) of the sample was equal to the known crustal value of 43.3006 (natural iron isotope variation is -4‰ to +1‰ $\delta^{56}Fe/^{54}Fe$ (Johnson and Beard, 2005); therefore, we believe that although our assumption is not completely accurate, the natural variation from this value is small.) Our spike is 93.547% ^{57}Fe with a ratio of 0.0673 (determined by Oak Ridge National Laboratories). These ratios (along with the spike concentration) lead to an measurable Fe concentrations range of 23.7 nM to 0.04 nM, which is well within oceanic values. Acceptable concentrations have been defined as those which have propagated errors less than 1.5% of the Fe concentration.

3.2 Fe Spike

The concentration of the spike solution was chosen so the range of measurable sample concentrations (23.7 nM – 0.04 nM) reasonably matched the range of oceanic values, and to maximize the accuracy despite uncertainty in the spike ratio. If the spike is contaminated with natural iron, inaccuracies in the calculated sample concentration will occur from the change in overall spike concentration and the spike ratio. This inaccuracy will depend on the amount of contamination, and vary with the quantity of spike used. We can minimize these errors by making the spike solution an ideal concentration. To determine the ideal spike concentration, we created a model which simulated changes in the spike ratio and concentration due to contamination from natural atmospheric Fe. For the ideal spike model described below, we measure the spike quantity in a relative manner by

keeping track of the ratio of the spike volume to sample volume, the volume ratio (V_{sp}/V_{sa} in eq. 1).

The ideal spike model tested the effects of atmospheric Fe contamination in the spike on the accuracy of the calculated sample Fe concentration. Within the model, we combined hypothetical spikes of varying C_{sp}, V_{sp}, and R_{sp}, (R_{sp} varied about the Oak Ridge value) with hypothetical samples of varying V_{sa}, and fixed C_{sa} and R_{sa} (C_{sa}=0.1 nM, R_{sa} = crustal values 43.3006). We calculated the R_m of each hypothetical mixture using equation 2:

$$R_m = \frac{C_{sa}\,{}^{56}Fe_{sa}V_{sa} + C_{sp}\,{}^{56}Fe_{sp}V_{sp}}{C_{sa}\,{}^{57}Fe_{sa}V_{sa} + C_{sp}\,{}^{57}Fe_{sp}V_{sp}} \quad , \qquad \text{(eq. 2)}$$

where $^{56}Fe_{sa}$ is the percentage of ^{56}Fe in the hypothetical sample, $^{56}Fe_{sp}$ the percentage of ^{56}Fe in the spike, $^{57}Fe_{sa}$ is the percentage of ^{57}Fe in the sample, $^{57}Fe_{sp}$ the percentage of ^{57}Fe in the spike. Using these R_m values as if they were measured on the mass spectrometer, we calculated the sample concentrations (eq. 1) as using the Oak Ridge value for R_{sp} (rather than the variable R_{sp}). This calculated concentration was different than the hypothetical concentration. We compared the calculated sample concentrations to the hypothetical concentration, and plotted the accuracy as percent change in concentrations versus the relative spike volume, V_{sp}/V_{sa} (Fig. 3).

In figure 3 we see that at low volume ratios (10^{-2} to 10^{-3}) differences in the R_{sp} of ±3.6% result in inaccuracies in the calculated sample concentration of less than 0.5%. These relatively low inaccuracies stay low at small volume ratios; however, as the volume ratio increases with larger spike volumes, the inaccuracy in the calculated sample concentration grows asymptotically. In order to make sure that we can accurately measure our sample's concentration even with a slight error in our spike ratio, we must choose a volume ratio for our method which lies to the left of these asymptotes. These curves are specific to the spike concentration chosen for the model, and the asymptotes will shift to higher or lower

volume ratios depending on the chosen spike concentration. By reducing the spike concentration, the asymptotes are shifted towards higher V_{sp}/V_{sa} ratios, making larger volume ratios usable; however, lower spike concentrations require more spike to reach the geometric mean of the isotope ratios and, thus, a larger V_{sp}/V_{sa}. These curves are also dependent on the sample's concentration, where lower sample concentrations shift the asymptotes to smaller V_{sp}/V_{sa} and larger concentrations shift them to higher V_{sp}/V_{sa}. In order to determine the best concentration for a spike in combination with the best volume ratio, we used a combination of the propagated error plot from figure 2 and data obtained from the volume ratio model demonstrated in figure 3.

Figure 4 is data from the ideal spike model (right hand y-axis) superimposed onto figure 2 (left hand y-axis). We began by calculating the R_m of the hypothetical mixtures from the ideal spike model, where C_{sa} = 0.1 nM, C_{sp} = 5 nM, and V_{sp}/V_{sa} vary (the correct isotope ratios: R_{sa}, R_{sp}, were used in each case). These R_m values were plotted against V_{sp}/V_{sa} on top of figure 2. We then repeated the process for hypothetical samples within our concentration range. This gave us a series of curved lines, representing our sample concentration range, which span the R_m space between R_{sa} and R_{sp} (Fig. 4).

By adjusting the spike's concentration, we shift these curves in order to make all the sample concentration curves fit within the R_m range, which resulted in a low propagated error at a volume ratio less than the asymptotes in figure 2. We determined that a V_{sp}/V_{sa} of 0.1 and a spike concentration of 5 nM would result in propagated errors less than 1.5% for all sample concentrations of interest. We diluted the ^{57}Fe spike such that its working concentration was 5.22 nM Fe.

The iron spike was made from solid ferric oxide (Fe_2O_3) synthesized at the Oak Ridge National Laboratory to have a ^{57}Fe isotopic abundance of 93.547% and $^{56}Fe/^{57}Fe$ ratio of 0.0673. This solid (0.926 mg) was added to a solution of nitric acid (10% v/v SeaStar® HNO_3, 100 mL) and hydrochloric acid (12M, SeaStar® HCl, 18.4 g) to form a solution of

10% HNO_3 and 10% HCl, and heated it overnight. This resulted in our primary iron spike (1° ^{57}Fe spike). A secondary spike (2° ^{57}Fe) was created by adding 266.62 mg of the 1° ^{57}Fe spike to 125.709 g of nitric acid (2% v/v SeaStar® HNO_3) by pipette. The secondary spike is 0.214 μM Fe and can be used for samples within the 100 nM – 1 μM range. The tertiary spike (3° ^{57}Fe spike) was made by adding 10.088 g of the 2° ^{57}Fe spike to 414.2 g of nitric acid (2% v/v SeaStar® HNO_3) by pipette. The tertiary spike is 5.22 nM Fe and is the working spike used for all the seawater samples.

4. Laboratory Procedures

4.1 The MagIC Method

All sample preparations are conducted within a Class 100 laminar flow bench using standard trace metal clean techniques. Seawater samples are processed through a modified Isotope Dilution MagIC (Magnesium Induced Co-precipitation) method (Wu and Boyle, 1997; Wu and Boyle, 1998), concentrating the metals by a factor of 20 while removing a majority of the ions in the sample. In a 1.7 mL polypropylene centrifuge tube (Globe Scientific Inc. Cat #111712 and 111672C) 100 μL of an iron spike (3° ^{57}Fe) and 1 mL of the sample were combined. A small amount of ammonium hydroxide (18-60 μL, 18.1 M SeaStar®) was added to the sample, increasing the pH and precipitating a small percentage (approximately 2-5%) of the magnesium (Mg) in the form of magnesium oxy-hydroxides, $MgO_x(OH)_y$. All surface reactive species (including Fe and Mn) adsorb (or co-precipitate) to the magnesium solids. The amount of ammonium hydroxide needed to precipitate the Mg was determined by trial and error on each type of sample during method development (approximate volumes of base are listed in appendix II). Differences in the volume of base required for precipitation result from varying amounts of acidification of the samples or strength of base, which changes with age of solution. Ammonium hydroxide is labile; therefore, we preserved it's concentration and strength by double bagging the bottle and storing it in a low evaporation environment, only opening it to remove daily supplies (which lose their strength over the course of about 12 hours). After ammonia addition, the

samples were allowed to develop MgOx(OH)y solids for 3 minutes. They were centrifuged for two minutes at 8000 rpm, separating the precipitate. The supernatant was poured out, the precipitate was re-centrifuged, and the remaining liquid was shaken out. Ideal precipitates should be gel-like, a translucent whitish color, and about 1 mm in diameter. Increasing the volume of base and the time of development will allow the magnesium to form more crystalline precipitates. Crystalline precipitates can be lost during the pouring steps, as they are easily mixed into the liquid, gel-like or amorphous precipitates stick to the walls of the vial and are more easily retained. Following these isolation steps, the precipitate was dissolved in nitric acid (5% v/v, 50 mL, SeaStar®).

4.2 Manganese Analysis

Manganese (Mn) cannot be directly determined through this isotope dilution process because it is monoisotopic. Mn concentrations were measured using both an internal ^{57}Fe isotope spike and an external standard calibration line between ^{55}Mn and the ^{57}Fe spike. The internal ^{57}Fe spike set the initial elemental ratio between Fe and Mn and reduced the effects of sensitivity fluctuations during analysis. The external standardization provided a calibration for reactivity differences between Fe and Mn during the chemical processing and analysis. The ^{57}Fe spike added to samples for the iron measurement was used for the Mn measurement as well. The external Mn standards (ranging from 0.6 nM to 4.9 nM Mn) were prepared by adding increasing additions of a $MnNO_3$ solution (24.5 nM Mn; 25, 50, 100, 250 μL) to 1 mL of low manganese seawater. The 3° ^{57}Fe spike equivalent to the samples was added to these standards and taken through the modified MagIC procedure described above.

4.3 Blanks and Standards

Metal contamination associated with chemical handling was determined by processing 50 μL of "blank" seawater through MagIC. "Blank" seawater has been determined to have 0.65 nM Mn and 0.07 nM Fe. Using 20 times less sample allowed us to precipitate

MgOx(OH)y from the sample without taking a large quantity of analyte with it. It was then assumed that all analyte found in the sample was added as a contaminate during the sample preparation steps. The MagIC procedures for these blanks are similar to the samples described above, although the addition of 200 μL of base was necessary because the smaller quantity of initial Mg was more difficult to precipitate. In the MagIC method for samples, magnesium oxy-hydroxides are only allowed to develop for 3 minutes, resulting in a 5% precipitation of the Mg. We attempt to precipitate all the Mg in our blanks by adding 5-6 times more base and allowing the precipitate to develop for over 30 minutes. As described above, this made the blank precipitate more crystalline, and thus greater care is required to preserve the sample during the separation process.

Mass fractionation in the sample uptake and delivery system of the mass spectrometer was corrected by running spiked gravimetric standards (SGS), which have a known isotopic ratio near the value of our spiked samples. SGS are measured using the same mass spectrometer method, and the measured (mass fractionated) SGS isotope ratio is corrected back to the known isotope ratio. That correction factor can then be used on all samples run during that analysis. SGS samples are prepared by adding 25 μL of a concentrated SGS solution to 1 mL of the "blank" seawater and then taking the mixture through the MagIC chemistry. This results in a SGS sample with the same solution matrix as our samples.

5. Sample Analysis

5.1 Matrix Matching

It is important to run all standards and blanks in a solution with a matrix similar to the samples; this process is called matrix matching. In our method we attempt to match the high magnesium matrix resulting from the MagIC method by adding our standard solutions to seawater with relatively low initial analyte (0.65 nM Mn and 0.07 nM Fe) and treating them in the same manner as a sample. This process yields standards in an equally high

magnesium matrix as well as allowing us to use the same blank subtraction and mass fractionation analysis on every sample and standard.

5.2 Analysis Mechanics

All samples, standards, and chemical blanks were analyzed in an identical manner on a Finnigan Element I magnetic sector inductively coupled plasma mass spectrometer (ICP-MS). Analysis of Fe and Mn was conducted in medium resolution to separate the natural isotopes from argon molecules (^{55}Mn and ^{40}Ar^{15}N, ^{56}Fe and ^{40}Ar^{16}O, ^{57}Fe, and ^{40}Ar^{16}O^{1}H). The Finnigan Element 1 is a single detector mass spectrometer with an Ar plasma ionization source. In a single detector mass spectrometer, isotopes are measured one at a time, jumping from isotope to isotope starting at the low masses and moving towards the higher masses (called a scan), and then repeating in order to gain precision in the measurement. As the spectrometer is isotope jumping, the ionization plasma can fluctuate in intensity, producing an uneven stream of ionized analyte. It is therefore important to minimize the time spent on each isotope in order to minimize the effect of the plasma fluctuation in between isotopes during the same scan. Mn and Fe were analyzed by scanning the center 10% of each isotope peak for 0.6 seconds and repeating 32 times. Each scan yielded a measurement of counts (atoms hitting the detector) for each isotope. We divided the counts of 55Mn and ^{56}Fe by the counts of ^{57}Fe for each scan and averaged the ratios from every scan, giving us an average R_m and standard error, σ, that we can use in equation 1 and equation 3 (see below).

Machine background noise (instrumental blank) was measured by analyzing dilute HNO_3 (5% v/v SeaStar® HNO_3) through the same analysis method. This noise was then subtracted from the samples' and standards' intensities before we evaluate the ratio of natural to spike isotope. Machine blank is less than 300 counts per second (cps) at the beginning of each days' analysis and decreases with time as Fe and Mn wash out of the system and the walls of the instrument are coated with Mg. Blank intensity is typically

0.2% of the Mn and Fe signal. After blank subtraction, the measured SGS ratios are divided by their true ratio (description of SGS analysis given below) to yield a correction factor. Standard and sample ratios were then divided by the SGS correction factor (changes varied by 28.5 ± 14.6 ‰/Δamu per run) to yield final ratios.

5.3 Calculations

Each sample's Fe concentration is determined by using the isotope dilution equation (eq. 1). As described above, R_m is the average measured ratio from the mass spectrometer after an instrumental blank subjection and SGS correction. Each sample's Fe concentration is then calculated using equation 1. Every sample run is subject to a chemical handling blank subjection. The blank samples (described above) are calculated as if they were regular samples (Vsa = 1.0 mL, not 50 μL), and all blanks are averaged (0.1 nM Fe and 0.06 nM Mn, n=3-4). The average value is subtracted from all samples and relative standards to yield a final Fe concentration.

The Mn concentration is calculated using the elemental ratio of Mn to ^{57}Fe, using equation 3 to give a preliminary concentration.

$$Mn_{sa} = \left(\frac{^{55}Mn}{^{57}Fe}\right)_m \bullet \left(V_{sp}\,{}^{57}Fe_{sp}C_{sp} + V_{sa}\,{}^{57}Fe_{sa}C_{sa}\right) \qquad \text{(eq. 3)}$$

These preliminary Mn concentrations are then corrected for elemental differences in efficiency during co-precipitation and uptake into the mass spectrometer, using the Mn standards described above. The preliminary concentrations of these standards are plotted against the Mn concentrations predicted given the known concentration of the $MnNO_3$ standard and volumes of each addition. The slope of this line represents the difference in the efficiency between iron and manganese, and each sample's concentration is divided by the slope of the standard calibration line to correct for this difference. This accounted for a 10-20% decrease in Mn concentration depending on the day of processing and analysis.

Blanks are also corrected in this manner, and are then subtracted from sample's concentration to yield the final Mn concentration measurement.

5.4 Sample Blanks and Standards

Contamination which occurred during sample handling was corrected by blanks run with each set of samples. Chemical blanks (prepared as described in section 4.3) had an average Fe concentration of 0.09 nM ± 0.11 nM (2σ) and Mn concentration of 0.06 nM ± 0.02 nM (2σ). The contamination of Fe and Mn in our blanks over time are plotted in figure 5. In general, Mn blank concentrations were very consistent, while the Fe blank concentration were more variable. Fe blanks were higher and more variable in our early work, and became more consistent with time.

A laboratory internal standard was run during sample analysis in order to determine day-to-day consistency and monitor any possible drift within any particular analysis. The low Fe and Mn "blank" seawater was used as the first consistency standard and had an Fe concentration of 0.05 nM ± 0.03 nM and Mn concentration of 0.66 nM ± 0.06 nM, later replacement standards (consistency standard 2 and 3) had concentrations of 1.36 ± 0.07 nM Fe, 5.36 ± 0.41 nM Mn; and 0.24 ± 0.06 nM Fe, 1.54 ± 0.13 nM Mn. The consistency standards over time are plotted in figure 6. The set of consistency standards with increasing Fe concentrations ([Fe] = 2.25 – 5 nM) was a mixture of the blank seawater with 25 μL of an Fe standard. Each day a small amount (1.5 – 2 mL) of the Fe standard was poured into a Teflon beaker. This "daily supply" was the source of the 25 μL Fe addition. This was designed to give us a consistency standard with more Fe than our blank seawater; however, because the volume of the "daily supply" was small and because it was not fully replaced, but simply added to each day, evaporation within the laminar flow bench increased the concentration over time. We therefore switched to a seawater standard with a set Fe concentration. Consistency standards 2 and 3 were surface seawater samples without any alterations. Our consistency can be measured by the first low Fe / Mn "blank"

seawater for low Fe concentrations and by consistency standards 2 and 3 for seawater samples with Fe concentrations above 1 nM.

A SGS solution was measured before and after each set of samples to determine mass fractionation and its drift over the coarse of each run. The ^{56}Fe / ^{57}Fe ratio of the SGS solution was determined by alternating measurements of the SGS and a solution with a known Fe isotope ratio (IRMM-014.0006). The ^{56}Fe / ^{57}Fe ratio of our SGS was 1.570 ± 0.014 with a variability of 25.9 ± 13.7 ‰/Δamu per day, with no overall drift in the ratio over time. The measured SGS ratios over time are plotted in figure 7.

FIGURES

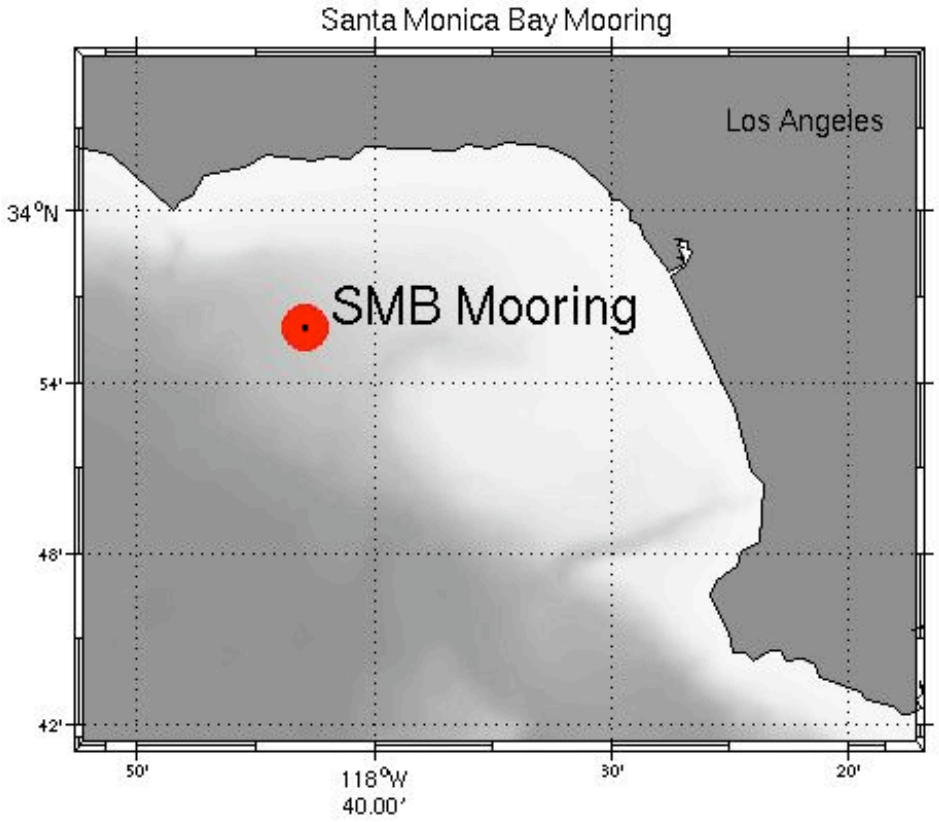

Figure 1: The Santa Monica Bay Observatory Oceanographic Mooring site is anchored at 33° 55.9' N, 118°42.9' W. Due to surface and sub-surface currents, the mooring rotates on its chain about this point. Time series samples were collected as close to this mooring site as possible.

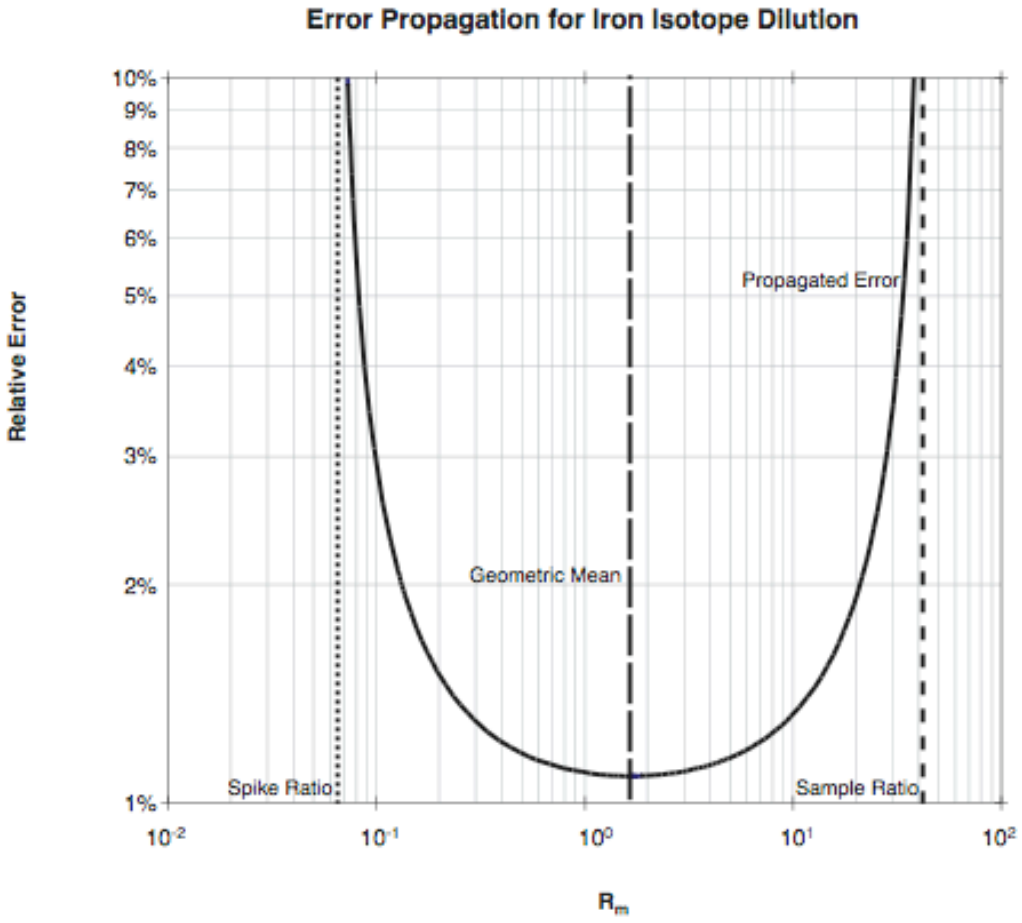

Figure 2: Error in sample concentration resulting from propagating the error in R_m through the isotope dilution equation. Using a σ of 1% for all R_m. Errors will rapidly increase as R_m approaches R_{sa} or R_{sp}.

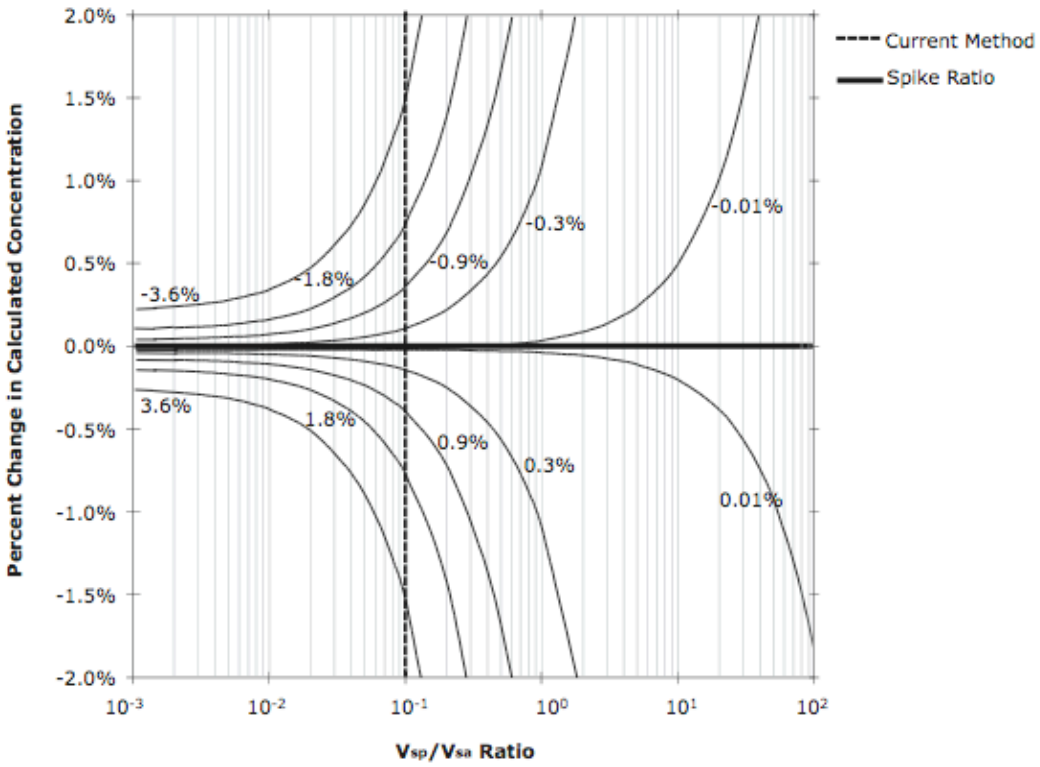

Figure 3: Contour plot of errors resulting from the incorrect spike ratios in the isotope dilution equation. This example uses C_{sp} = 5.22 nM, C_{sa} = 0.1 nM, and R_{sa} = 43.3006. The heavy black line represents the correct spike ratio, the light black lines are spike ratios which deviate from the correct ratio by the labeled amount, and the dotted black line is the V_{sp} / V_{sa} ratio used in our method (1000 µL sample : 100 µL spike).

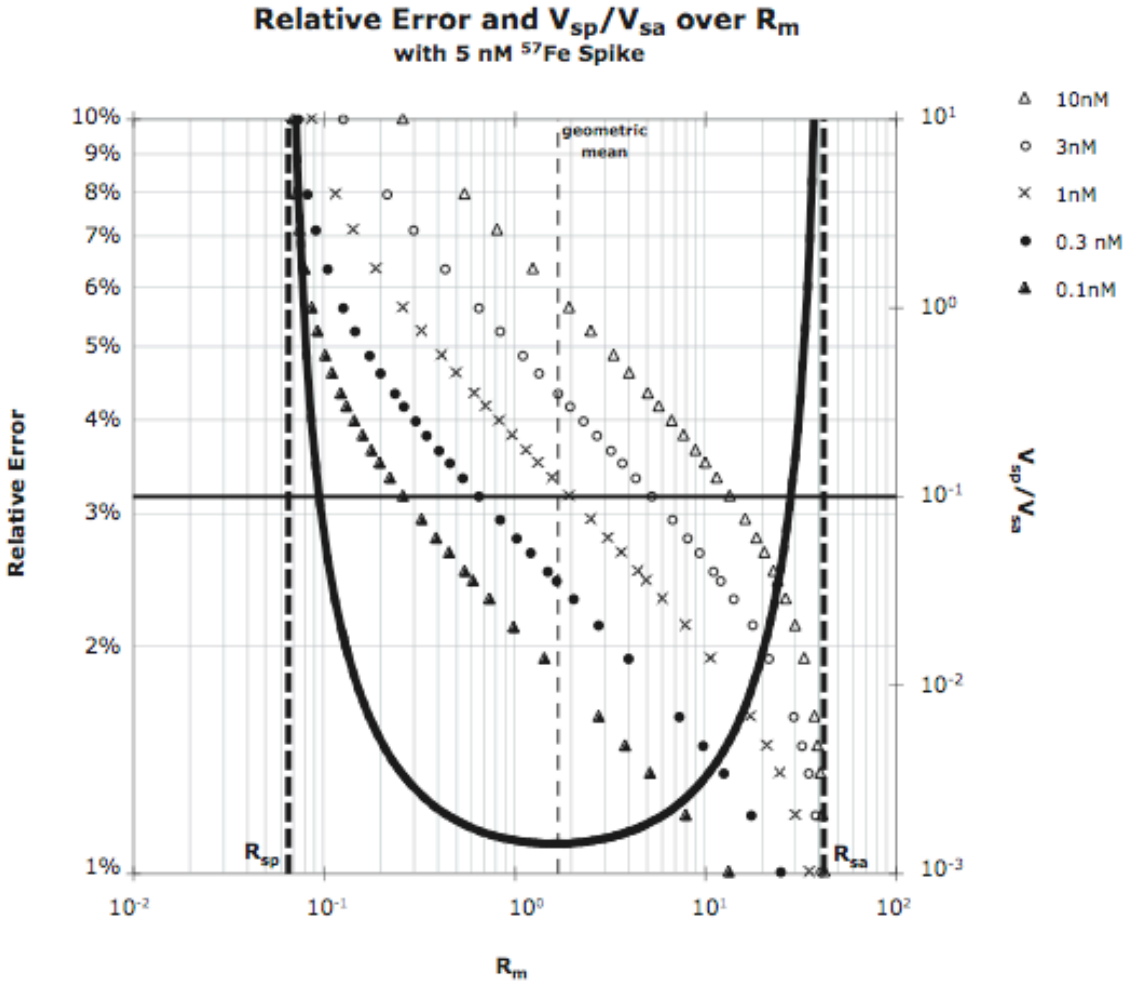

Figure 4: Calculated R_m associated with V_{sp}/V_{sa} ratios for a 5 nM ^{57}Fe spike with sample concentrations of 10 nM - 0.1 nM, plotted on the error propagation graph from figure 2. By constructing this plot we were able to determine the most appropriate spike concentration based on both error associated with non-ideal R_m and V_{sp}/V_{sa} ratios. The propagated error associated with a V_{sp}/V_{sa} ratio of 0.1 for 10, 3, 1, 0.3, and 0.1 nM samples was 1.45, 1.15, 1.08, 1.13, and 1.36% respectively.

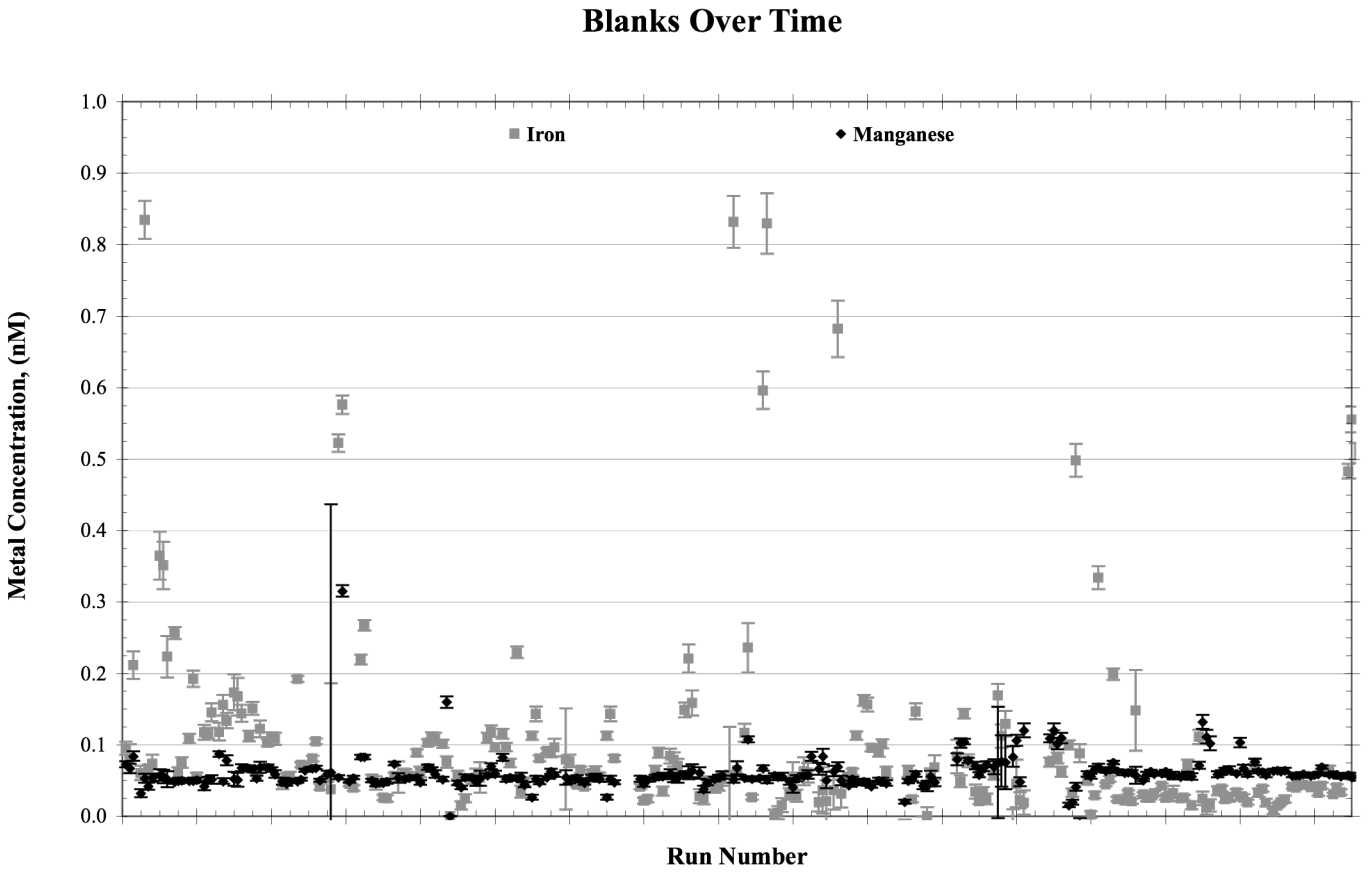

Figure 5: Contamination levels in blank samples over time. Iron (gray squares) were variable, ranging from 0.01 – 0.8 nM, while manganese (blank diamonds) were consistently about 0.06 nM. Error bars are 2 σ of the standard error of the measured ratio processed through the isotope dilution equation (eq. 1).

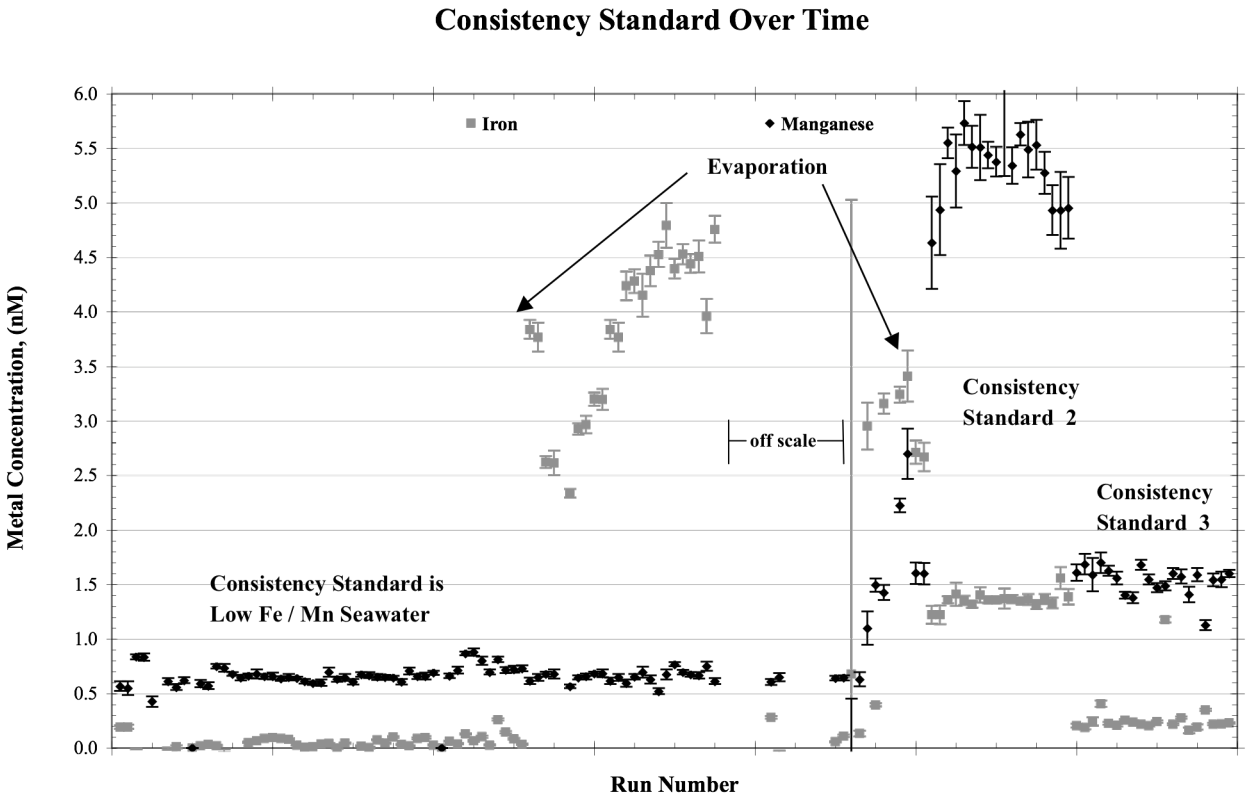

Figure 6: Consistency levels in the laboratory internal standards over time. Iron (gray squares) concentration in the original standard was 0.05 nM, while manganese (blank diamonds) were 0.66 nM. A 25 μL addition of an Fe standard was added to each standard to increase the concentration; however, we found evaporation to become a source of variation as can be seen in the increasing Fe concentrations. Later replacement standards had concentrations of 1.36 ± 0.07 nM Fe, 5.36 ± 0.41 nM Mn; and 0.24 ± 0.06 nM Fe, 1.54 ± 0.13 nM Mn. Error bars are 2 σ of the standard error of the measured ratio processed through the isotope dilution equation (eq. 1).

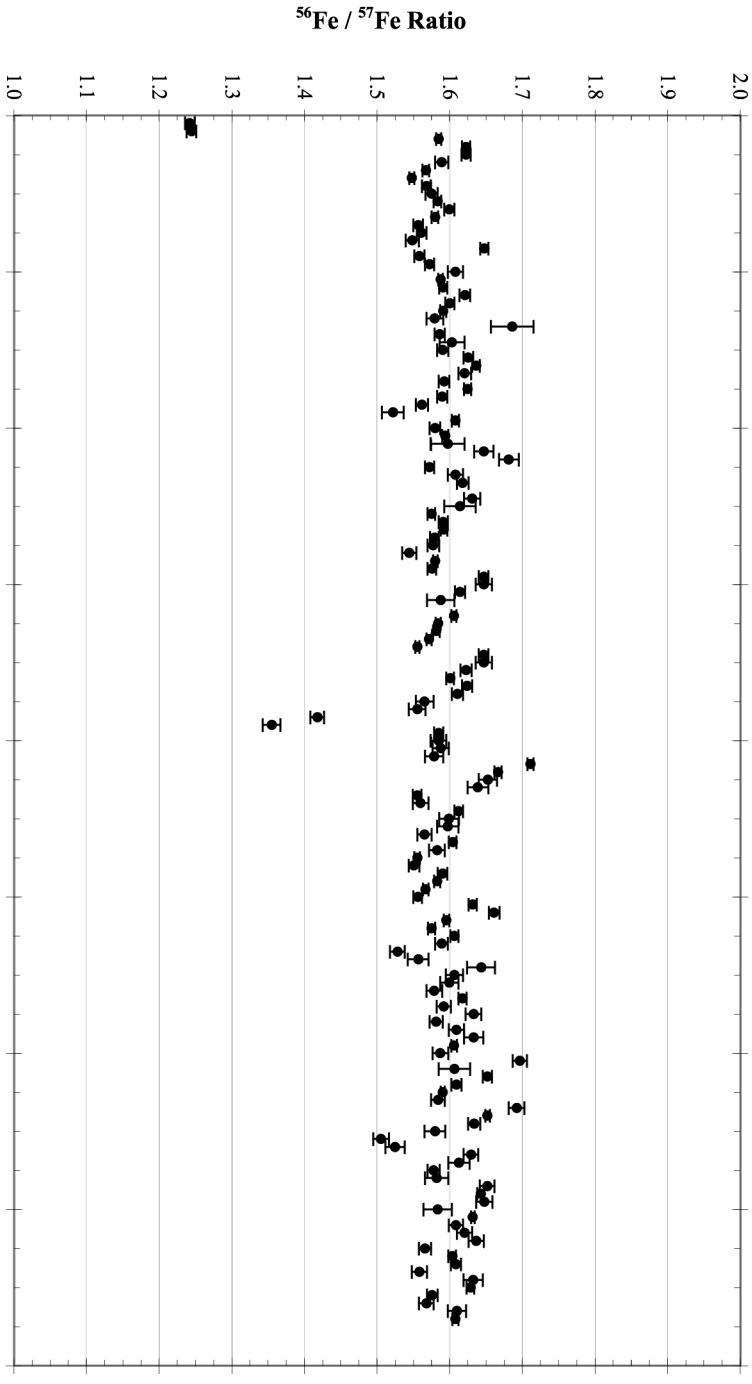

Figure 7: The measured SGS ratios over time. The measured ^{56}Fe / ^{57}Fe ratio of our SGS was 1.570 ± 0.014. SGS variability was 25.9 ± 13.7 ‰/Δamu per day and 26.0 ± 29.9 ‰/Δamu for all SGS samples.

APPENDIX I

Step by step process of sample preparation

This process can be done over the course of a few days, but once a step is started it must be completed. The end of each step is a natural stopping place, and the process can be picked up at a later date with no detrimental effects to the samples. It is advisable to multitask during step 2 in order to speed up the process, but the times required for precipitate development must not be exceeded. Do not move onto step 3 more than 24 hours before analysis.

Step 0. Set-up

1. Remove all needed centrifuge tubes and caps from 0.1% acid (HCl) container.
2. With blue cap tool, screw caps on tubes with 0.1% HCl filling the tubes
3. Rinse the outside of the tubes thoroughly with mQ water
4. Dry the caps with clean lint-free cloth
5. Label all caps with profile date or experiment name as well as sample identity

Step 1. Fill Tubes

1. With 1000 μL fixed pipette, clean new pipette tip
    a. If original sample volume is scare, use 500 μL pipette to reduce waste during rinses
2. Open one tube and empty the acid out, close tube
3. Add 1000 μL of sample to tube and screw cap on
4. Invert and thoroughly mix sample in tube
5. Open tube and pour sample out, close tube
6. Add 1000 μL of sample to tube and screw cap on
7. Invert and thoroughly mix sample in tube
8. Open and vigorously shake out contents (less than 3 μL should remain), close tube
9. Add 1 mL of sample and screw cap closed
10. Label side of tube identical to cap
11. Expel pipette tip
12. Repeat Step 1.2 – 1.11 for every sample
13. Fill “daily supplies” with new supply, if needed
    a. consistency standard
    b. low Fe and Mn seawater
    c. Mn standard

   d. SGS primary
   e. ^{57}Fe 3° spike
14. With 1000 μL fixed pipette, clean new pipette tip (may use for steps 1.15 – 1.17)
15. For consistency standards repeat steps 1.2 – 1.10 with consistency standard seawater
16. For all SGS (specific gravimetric standard), repeat steps 1.2 – 1.10 with low Fe and Mn seawater
17. With 25 μL fixed pipette, clean new pipette tip
18. For all SGS, add 25 mL of SGS standard (2°)
19. Expel tip
20. For all Mn standards, repeat steps 1.2 – 1.10 with low Fe and Mn seawater
21. With 25 μL fixed pipette, clean new pipette tip
   a. For Mn 1 standard, add 25 μL (1 addition) of 3° Mn standard
   b. For Mn 2 standard, add 50 μL (2 additions) of 3° Mn standard
   c. For Mn 3 standard, add 100 μL (4 additions) of 3° Mn standard
   d. For Mn 4 standard, add 250 μL (10 additions) of 3° Mn standard
22. For all chemical blanks, repeat steps 1.2 – 1.5 with low Fe and Mn seawater
23. With 50 μL fixed pipette, clean new pipette tip
24. For all blanks, add 50 μL of low Fe and Mn seawater
25. Label all blank samples
26. With 100 μL fixed pipette, clean new pipette tip
27. Add 100 μL of 3° ^{57}Fe spike to samples, consistency standards, Mn standards, and blanks, close tubes
   a. DO NOT add spike to the SGS tubes !!
28. Vigorously shake all tubes to thoroughly mix sample and spike

Step 2. Precipitation

1. With 200 μL adjustable pipette, clean new pipette tip up to 200 μL
2. Fill daily supply of NH_4OH with fresh NH_4OH from SeaStar® bottle
3. Add 200 μL of NH_4OH to blanks, close tubes
4. Shake, and let sit for at ≥30 minutes
5. Add 32 μL of NH_4OH to samples, close tubes
6. Quickly mix base with samples and let sit for 2-3 minutes
7. Centrifuge for 2 minutes at 8000 rpm
   a. Pay close attention to balancing the centrifuge
8. Remove all tubes from centrifuge, inverting them and setting them on flow bench counter
   a. Liquid should separate from solid

9. Open tube and gently pour out liquid without disturbing solid, close tube

   a. Ideal solid will be a small translucent clear-to-whitish smear extending from the tip of the centrifuge tube upward no more that 3 mm. Too much solid will be difficult to dissolve later and can alter the eventual mass spectrometer analysis. Minimize the solid by reducing the NH4OH used and time before centrifugation.

10. Again, centrifuge for 2 minutes at 8000 rpm
11. Remove from centrifuge, and with one or two powerful motions force the liquid to the top of the tube and into the cap
    a. If the solid moves with the liquid down the side of the tube or completely into the cap, re-centrifuge
12. Open the tube and shake the liquid out of the cap, close tube
13. Repeat steps 2.5 – 2.12 for every sample and standard
    a. The quantity of NH_4OH added to standards will vary with the strength of the primary NH_4OH, and acidity of final standard; a list of typical additions can be found in appendix II
14. Centrifuge the blanks, repeat steps 2.7 – 2.12
    a. Use more caution and less powerful motions
    b. The solids appearing at the bottom of the blank tubes will be fine white crystals and will be more concentrated towards the tip of the tube, this solid is less sticky and can be removed from the tube with the liquid if caution is not taken

Step 3. Dissolution

1. No more than 24 hours before analysis add 50 μL of 5% HNO_3 to every tube
2. Shake vigorously to dissolve solid
3. If solid remains, the pellet was too big and must be redone
4. Centrifuge for 10 – 30 seconds at 8000 rpm to push all liquid to bottom of tube
5. With blue tool remove the cap of tube and place in analysis tray, remove cap from tool
6. Spot one is indicated by a black dot on the tray
7. Repeat for every tube

Step 4. Ready for analysis

1. Measure isotope ratio on ICP-MS

APPENDIX II

Typical quantities of NH_4OH added to samples, standards, and chemical blanks for precipitation step of MagIC method

Samples

1:1000 conc. HCl acidified samples: 32 mL
1:500 conc. HCl acidified samples: 42 mL

Consistency Standards

Unacidified: 28 mL
Acidified: Follows Sample

SGS

25 mL addition: 18 mL

Blanks

50 mL Unacidified seawater with spike: 200 mL
1000 mL Unacidified Seawater without spike: 15 mL

Mn Standards

Mn (25 mL addition): 25 mL
Mn (50 mL addition): 35 mL
Mn (100 mL addition): 55 mL
Mn (250 mL addition): 100 mL

APPENDIX III

Method for Fe and Mn Analysis on Element I - Saved As FeMR.met

	Low + Med + High
Runs/Passes (Meas.):	0*0 + 32*1 + 0*0
Runs/Passes (Eval.):	0*0 + 32*1 + 0*0

Time per Pass	[min:sec:ms]	[h:min:sec]
Low	00:00:000	00:00:00
Med.	00:02:102	00:01:08
High	00:00:000	00:00:00
Total Time	00:01:08	

Locked	Isotope	Accurate Mass	Mass Offset	Mass Window	Mass Range	Magnet Mass	Settling Time	Sample Time	Samples per Peak	Search Window	Integration Window	Detection Mode
No	^{55}Mn	54.9375	changes	10 %	54.937-54.938	54.938	0.300	0.1000	60	50	60	Counting
No	^{56}Fe	55.9344	changes	10 %	55.933-55.935	54.938	0.001	0.1000	60	50	60	Counting
No	^{57}Fe	56.9349	changes	10 %	56.934-56.936	54.938	0.001	0.1000	60	50	60	Counting

BIBLIOGRAPHY

Buck, K.N., Lohan, M.C., Berger, C.J.M. and Bruland, K.W., 2007. Dissolved iron speciation in two distinct river plumes and an estuary: Implications for riverine iron supply. Limnology and Oceanography, 52(2): 843-855.

Donat, J.R. and Bruland, K.W., 1988. Direct Determination of Dissolved Cobalt and Nickel in Seawater by Differential Pulse Cathodic Stripping Voltammetry Preceded by Adsorptive Collection of Cyclohexane-1,2-Dione Dioxime Complexes. Analytical Chemistry, 60(3): 240-244.

Duce, R.A. and Tindale, N.W., 1991. Atmospheric transport of iron and its deposition in the ocean. Limnology and Oceanography, 36(8): 1715-1726.

Guieu, C., Loye-Pilot, M.D., Ridame, C. and Thomas, C., 2002. Chemical characterization of the Saharan dust end-member: Some biogeochemical implications for the western Mediterranean Sea. Journal of Geophysical Research-Atmospheres, 107(D15).

Johnson, C.M. and Beard, B.L., 2005. Biogeochemical cycling of iron isotopes. Science, 309(5737): 1025-1027.

Johnson, K.S. *et al.*, 2007. Developing Standards for Dissolved Iron in Seawater. EOS, 88(11): 131-132.

Wu, J. and Boyle, E.A., 1997. Low Blank Preconcentration Technique for the Determination of Lead, Copper, and Cadmium in Small-Volume Seawater Samples by Isotope Dilution ICPMS. Analytical Chemistry, 69: 2464-2470.

Wu, J. and Boyle, E.A., 1998. Determination of iron in seawater by high-resolution isotope dilution inductively coupled plasma mass spectrometry after $Mg(OH)_2$ coprecipitation. Analytica Chimica Acta, 367: 183-191.

C h a p t e r 2

ATMOSPHERIC INPUT OF MANGANESE AND IRON TO THE OCEAN:

Seawater dissolution experiments with Saharan and North American dusts

Jeffrey Mendez[a], Cecile Guieu[b1], Jess Adkins[b]

[a] Department of Environmental Science and Engineering, California Institute of Technology
[b] Department of Geological and Planetary Sciences, California Institute of Technology

Abstract

Dissolution of wind blown dust is a major source of iron, manganese, and other trace nutrients in the ocean. Kinetic and thermodynamic values for the release of metals from dust are needed for computer models which incorporate dust as part of their ocean system. Here we investigate both the thermodynamic and kinetics parameters involved in the dissolution of metals from dust in seawater. We added dust from the Sahara and the Western United States in five different concentrations (0.01 - 5.0 mg/L), representative of those concentrations found in seawater after dust events, to open ocean Pacific seawater. Sub-sampling of the reaction vessels took place on days 1, 2, 4, 7, 14, and 35 for the kinetic study.

Results show different apparent thermodynamic constants for manganese (Mn) and iron (Fe). The final Mn concentrations are proportional to the added dust concentration. Fe concentrations reach a maximum of less than 2 nM, independent of the quantity and type of dust added. The Fe dissolution kinetics are faster than our sampling resolution. The first order rate constant for the dissolution of Mn from the Western US and Sahara dusts were $0.94 \pm 0.04 \ \frac{nmol\ \mathrm{Mn}}{day \cdot mg\ \mathrm{Dust}}$ and $0.22 \pm 0.01 \frac{nmol\ \mathrm{Mn}}{day \cdot mg\ \mathrm{Dust}}$, respectively. We conclude

[1] Now at: Université Pierre et Marie Curie-Paris, CNRS, Laboratoire d'Océanographie de Villefranche (LOV), 06238 Villefranche-sur-mer, France, France, guieu@obs-vlfr.fr

that Mn concentrations are limited by available Mn on the dust surface, while Fe concentrations are limited by the ligand concentrations in the seawater, which ultimately are determined by the biological community.

1. Introduction

1.1 Dust as a Metal Source

Windblown dust is an important source of many trace metals to the open ocean. Metals such as aluminum (Al) (Measures *et al.*, 1986) and lead (Pb) (Nozaki *et al.*, 1980) have a typical atmospheric deposition profile with high concentrations in the surface due to contact with the atmosphere and a sharp decrease with depth. Manganese (Mn) (Klinkhammer and Bender, 1980) and iron (Fe) (Martin and Fitzwater, 1988) have more complicated profiles and are nutrients for phytoplankton in the ocean. Although there are many sources of Mn and Fe to the ocean, wind blown dust is the largest source to the open ocean (Duce and Tindale, 1991; Guieu et al., 1994). The degree to which eolian Fe and Mn dissolve and are accessible to the phytoplankton community is the focus of this study.

1.2 Iron

Although Fe is the fourth most abundant element in the Earth's crust, dissolved Fe concentrations in open-ocean seawater are extremely low. Dissolved Fe in the +3 oxidation state, the redox species believed to dominate in oxygenated seawater, has very low solubility with respect to Fe(III) oxyhydroxide solids (Morel and Herring, 1993). Above this solubility limit Fe is kept in the dissolved form with organic ligands (Barbeau *et al.*, 2001; Buck, 2007; Küpper *et al.*, 2006; Rue and Bruland, 1995; van den Berg, 1995). These ligands, produced by bacteria and phytoplankton, keep Fe in solution and available for biological uptake (Barbeau, 2006; Haygood *et al.*, 1993; Kraemer *et al.*, 2005).

Bottle incubations and mesoscale Fe addition experiments have shown Fe to be important to ocean productivity, and in many locations, the limiting or co-limiting nutrient. Computer models have incorporated Fe (Aumont *et al.*, 2003; Moore *et al.*, 2006) to more accurately

describe ocean biogeochemical cycles. Dust is the major source of Fe to the open ocean that cannot be reached by river deposits. Unfortunately, the amount and mechanism of Fe release from dust is not well understood. Recent models have used a wide range of Fe solubilities, ranging from 1-10% of the total Fe in the dust. In addition, there have been variations in the estimates of total dust deposition itself, based on measurements (Duce and Tindale, 1991; Gao *et al.*, 2003), modeling results (Tegen and Fung, 1994), and the speciation of the iron within the deposited dust (Hand *et al.*, 2004). To more accurately represent Fe within these models, more needs to be known about the exact nature of Fe dissolution from dust.

1.3 Manganese

Manganese is an important micronutrient for marine organisms via its use in photosynthetic and radical scavenging enzymes (Horsburgh *et al.*, 2002; Kernen *et al.*, 2002). Thermodynamically, an oxygenated ocean at a pH of 8 should lead to the insoluble Mn(IV) species in the form MnO_2. Dissolved Mn ocean profiles reveal that the surface waters contain high levels of soluble Mn(II). A portion of the soluble Mn is from direct atmospheric deposition, which contains Mn in the +2 oxidation state (Guieu et al., 1994; Siefert et al., 1998). Slow oxidation to the +3 or +4 state allows Mn to stay dissolved on the order of days. However, Mn still should oxidize over time and precipitate out of the surface ocean (Stumm and Morgan, 1996). This oxidation is prevented by photoreduction of Mn to the soluble +2 state in the presence of organic material (Sunda *et al.*, 1983), resulting in a large concentration of Mn in the surface water available for biological use.

1.4 Dust Experiments

Past dust dissolution experiments in seawater (Bonnet and Guieu, 2004; Buck *et al.*, 2006) have sought to address the question of how dust affects the Fe concentration of the surface ocean. Bonnet and Guieu, (2004) allowed ocean water to sit with different concentrations of Saharan dust for 24 hours and 7 days. Their experiment provided information on the thermodynamics of Fe dissolution revealing that 0.55 to 2.2% of the soil's Fe made its way

into the dissolved form. This result is on the low end of previous assumptions. Experiments conducted by Buck et. al., 2006 describe a different type of solubility, in which aerosols collected by air filtration were briefly exposed to seawater. This type of experiment measures the instantaneous dissolution or the leachable Fe component from the aerosols. Buck et. al., 2006 found that 6 ± 5 % of the Fe was leached from the aerosol particles in seawater. Yet there are still many questions about the mechanism and extent of dust dissolution, and the Fe solubility from this dust. Is instantaneous dissolution relevant to an element which is insoluble and highly reactive with OH^- and O_2, or is it in fact more relevant to measure the instantaneous dissolution because Fe may be precipitated quickly? In addition, what is the behavior of different types of mineral dusts and different dust concentrations in seawater? Our experiment has attempted to address these last two questions by conducting various bottle experiments using two different dust samples over a wide range of dust concentrations, and taking sub-samples over time to measure the dissolution progress and the initial rate constants.

2. Method

2.1 Collection and Experimental Set-up

Seawater was collected at 30°N 140°W in November 2004, aboard the RV Melville using the UC Santa Cruz trace metal surface sampler. This seawater was inline filtered at 0.2 μm (Pall #12941) into an acid leached 25 L polyethylene carboy and later stored in the dark.

Saharan dust is a composite of 12 surface soils that were collected under clean conditions from the Hoggar region (Algeria). U.S. dust is a composite of 3 superficial deposits collected in natural dust traps in the Nevada desert (South-West of Las Vegas). Both Saharan and U.S. dust have been hand sieved through successive clean polyethylene meshes of 100 and 20 μm pore diameter. The smallest fraction (<20 μm) was collected and stored in a clean glass bottle. The U.S. sample was then autoclaved to destroy any possible bacteria spores, and both samples were stored in a dark cabinet.

Samples were prepared by adding seawater to five 1 L clear Teflon bottles using an acid leached graduated cylinder. In a 1 L polyethylene bottle, 10 mg of Saharan dust was added to 1 L of seawater. This solution was quickly shaken and proportioned via pipette or graduated cylinder to each of the sample bottles in order to reach the different dust concentrations (0.01, 0.05, 0.5, 1.0, 5.0 mg/L). The sample bottles (including a control bottle which received no dust) were then sealed with parafilm and immersed in a 13°C water bath (temperature of nitracline), under a 50% light screen (to mimic the reduced light in the euphotic zone), on the roof of the laboratory. This sequence was repeated for the U.S. dust. The seawater was allowed to mature under the diurnal cycle for 35 days. Samples were removed from this bath on days 1, 2, 4, 7, 14, and 35 at 1:00 PM. Sub-sampling lasted for ~2 hours, and then the reservoir was returned to the water bath on the roof.

Sub-samples were taken to measure the progression of metal dissolution. Once removed from the roof, the bottles' exteriors were cleaned by thoroughly rinsing with mQ water in a class 100 laminar flow bench. The parafilm was removed, and the bottles were individually opened for sub-sampling. The filter apparatus was rinsed by pouring 10 mL of the sample through a 25 mm Whatman 0.2 μm polycarbonate membrane filter (Cat #110606). The sub-sample was then taken by pouring another 10 mL of sample through the filter and collecting it in a small high density polyethylene bottle. This sub-sample was immediately split into two and acidified with 10 mL of concentrated (12 M) SeaStar® hydrochloric acid (HCl). Following each sample, the filter was exchanged and the filter apparatus was rinsed with dilute nitric acid (~25 mL SeaStar® 5% (by volume) HNO_3), followed by clean milli-Q water (~150 mL).

2.2 Laboratory Procedures

All sample preparations were conducted within a Class 100 laminar flow bench using trace metal clean techniques. Seawater samples were processed using a modified Isotope

Dilution MagIC (**Mag**nesium **I**nduced **C**o-precipitation) method (Wu and Boyle, 1997; Wu and Boyle, 1998), amplifying the reactive metal concentrations by a factor of 20.

Because it is monoisotopic, Mn was measured using a modified isotope dilution method. Mn concentrations were measured using both an internal ^{57}Fe isotope spike and an external standard calibration line between ^{55}Mn and the ^{57}Fe spike. The internal ^{57}Fe spike set the initial elemental ratio between Fe and Mn and reduced the effects of sensitivity fluctuations during analysis. The external standardization provided a calibration for differences between Fe and Mn during the chemical processing and analysis. These external Mn standards (ranging from 0.5 nM to 10 nM) were prepared by adding small volumes of a $MnNO_3$ solution to 1 mL of low manganese seawater. An ^{57}Fe spike equivalent to the total dissolved Mn concentration in the samples was added to the Mn standards and taken through the modified MagIC procedure.

The metal blank associated with chemical handling was determined by processing 50 μL of "blank" seawater (which has been determined to have 0.65 nM Mn and 0.07 nM Fe) through MagIC, similar to Wu and Boyle's blank analysis. Spiking and precipitation of the blanks are similar to the samples, except it was necessary to add 4-5 times the volume of ammonium hydroxide because the smaller quantity of initial Mg was more difficult to precipitate.

Mass fractionation in the sample uptake and delivery system was corrected by running spiked gravimetric standards (SGSs), which have a known isotopic ratio near the value of our spiked samples. SGS are measured using the same mass spectrometer method, and the measured, mass fractionated, SGS isotope ratio is corrected back to the known isotope ratio. That correction factor can then be used on all samples run during that analysis. SGS were prepared by adding 25 μL of a concentrated SGS solution to 1 mL of the "blank" seawater and then taking the mixture through the MagIC chemistry. This results in a SGS sample with the same solution matrix as our samples and a total Fe concentration of 22 nM.

2.3 Sample Analysis

All samples, standards, and chemical blanks were analyzed in an identical manner on a Finnigan Element I magnetic sector Inductively Coupled Plasma Mass Spectrometer (ICP-MS). Analysis of Fe and Mn was conducted in medium resolution to separate the natural isotopes from argon interferences (^{55}Mn and ^{40}Ar^{15}N, ^{56}Fe and ^{40}Ar^{16}O, ^{57}Fe and ^{40}Ar^{16}O^{1}H). The machine blank was measured by analyzing dilute HNO_3 through the same analysis method and subtracting it from the samples before evaluating the ratio. This number was regularly less than 2% of the Mn and Fe signals.

The measured ratios of each SGS were adjusted to the known "true" ratio using a linear fractionation law. Sample ratios were then multiplied by the SGS correction factor (changes varied by 28.5 ± 14.6 ‰/Δamu per run) to yield final ratios of the spike sample. Each sample's [Fe] was determined by using the isotope dilution equation:

$$C_{sa} = \frac{\left(R_{sp} - R_m\right)}{\left(R_m - R_{sa}\right)} \frac{V_{sp}}{V_{sa}} \frac{\%^{57}Fe_{sp}}{\%^{57}Fe_{sa}} C_{sp} \quad , \qquad \text{(eq. 1)}$$

where C is the concentration, R is the isotope ratio, V is volume, and the subscripts sa, sp, and m represent sample, spike, and measured, respectively. The unspiked sample isotope ratio is assumed to be the natural iron isotope ratio (^{56}Fe/^{57}Fe = 43.3006). Uncertainties in the calculated sample concentration were determined from the standard error of the mean of R_m. This number was estimated from multiple scans of the isotope ratio (n= 17 to 40) and matches the external reproducibility of replicates from the same water. Preliminary sample concentrations of Mn were calculated using the elemental ratio of:

$$\left(\frac{^{55}Mn}{^{57}Fe}\right)_m = \frac{Mn}{\left(^{57}Fe_{sp} + ^{57}Fe_{sa}\right)} \quad . \qquad \text{(eq. 2)}$$

These concentrations were divided by the slope of the standard calibration line to correct for efficiency differences between Mn and Fe in the chemical and ICP-MS process. This accounted for a 10-20% decrease depending on the day of processing and analysis.

Dust was acid digested inside a Milestone 1200 Mega microwave oven with 1 mL of HF (concentrated Suprapur®, Merck, 40% in volume, in polypropylene container) and 3 mL HNO_3 (concentrated Suprapur®, Merck, 65% v/v). Aluminum (Al), Fe, and Mn were determined using calibration curves by Inductively Coupled Plasma-Atomic Emission Spectroscopy (ICP-AES 'Ultra traces', Jobin Yvon). Blanks (reagent alone) were below the detection limit. The ratio of measured-to-recommended concentrations in the BCSS certified reference material ((n=3), National Research Council of Canada; range of weights: 10.7-16.08 mg) was Fe = 1.06 ± 0.05, Al = 0.99 ± 0.05, Mn = 1.05 ± 0.04. Grain-size distributions in volume were established for the two dust samples dispersed in ultrapure water with a Mastersizer (Malvern Instruments, UK).

3. Results

3.1 Seawater sub-samples

Figure 1 shows dissolved (a) Mn and (b) Fe concentration versus time after dust addition. In general, dissolved Fe concentrations increase to about 0.5 nM by the first sub-sample and slowly increase to 1-1.5 nM over the course of the experiment. Dissolved Mn increases in proportion to dust concentration, with dust from the United States releasing Mn faster than dust from the Sahara.

3.2 Dust

Elemental analysis of the dusts used in our experiment show Mn, Fe, and Al concentrations similar to crustal abundances (Table 1). The grain size distributions measured in percentage of total volume per grain size are plotted in figure 2. The Saharan dust volume is shifted to smaller grain sizes compared to the U.S. dust. These distributions are in good agreement with the size spectrum obtained on Saharan end-member transported dust whose median

size was ~8 μm (this is the average size distribution of the particulate phase of six Saharan rains collected in Corsica and selected among a 12 year series to be as representative as possible of pure Saharan end-member, see details in (Guieu *et al.*, 2002,) indicating that the <20 μm fraction of the Saharan and U.S. soils are a suitable representation of an aeolian component that can be transported over short and medium range distance (like it is the case in the Mediterranean Sea) and possibly long distance.

3.3 Data Quality

Replicate analyses in the dissolution experiment are generally consistent, but Fe duplicates are less consistent than Mn duplicates due to their higher susceptibility to contamination. The laboratory seawater consistency standards processed and analyzed along with the sub-samples had measured Fe concentrations of 0.042 ± 0.030 nM, n=11, which is in agreement with all other previous analysis of this standard, [Fe] 0.05 ± 0.03 nM, n=28. Because the precision in these standards is high (measured within 30 pM of each other), we believe that variability between duplicates is a function of sample collection rather than chemical processing or analysis. Accuracy was checked by repeated measurement of three archived samples originally collected and measured by Sophie Bonnet (collection and measurement methods can be found in (Bonnet and Guieu, 2004)). The concentration of these samples (Fe concentrations of 1.37 nM, 0.83 nM, 0.89 nM) were found to be within ±0.03 nM of the previous measurements. Measurements of Mn in the consistency standard are 0.65 ± 0.03 nM, n=11 during this dissolution experiment, which is in agreement with all previous measurements (0.66 ± 0.06 nM, n=28).

Sub-samples collected on day 2 were subject to an unknown source of contamination leading to 40% of all samples taken on that day being over 25 nM for Fe and 30 nM for Mn, many of which were an unrealistic 100 - 5000 nM. All data from day 2 have been discarded. Other sub-samples not represented in the graphs are off scale and believed to be contaminated (control=1, U.S. dust = 1, Saharan dust = 2).

4. Discussion

4.1 Manganese

4.1.1 Mn Kinetics

All raw Mn data is shown in figure 1a. The dissolution rate of Mn (and Fe) is defined by the total increase in metal concentration over time. In order to highlight the different dissolution rates of the dusts, we plot the 5 mg/L data, which has the largest increase in dissolved Mn, in figure 3. The U.S. dust releases Mn into solution faster than the Saharan dust. After this initial increase, the dissolution slows and the [Mn] approaches a plateau after 14-21 days. To measure the initial rate of Mn dissolution, a best straight line fit over the initial linear portion of the curve was performed. The rapid dissolution in the 1 and 5 mg/L U.S. dust samples was a limit in defining this line to only the first two points (days 0-1). The Mn increase is slower in the U.S. samples containing less dust and all the Saharan samples, and we are able to incorporate days 0-4 in the line fits.

We plot the initial slopes versus their corresponding dust concentration in figure 4. The linear trend in the data indicates a first order reaction with dust; therefore, we can write a simple kinetic reaction, equation 3,

$$\frac{d\,\mathrm{Mn}}{dt} = k[Dust] \quad . \qquad \text{(eq. 3)}$$

Error associated with each point in this graph is the error associated with uncertainty in the slope calculation. The 1 and 5 mg/L U.S. dust samples have the largest error because only two points could be used. Manganese in the 0.01 mg/L experiment did not increase and is not included in this calculation. (Using the rate below, the 0.01 mg/L experiment would not see an increase in [Mn] of more than 0.08 nM (U.S. dust) and 0.015 nM (Saharan dust) over the first week, which is within the scatter of the duplicate measurements of both the control and the 0.01 mg/L experiment. Therefore, the low dust experiment does not constrain the initial rate.) The U.S. dust dissolution rate constant is 0.94 ± 0.04

$\frac{nmol\ \text{Mn}}{day \cdot mg\ \text{Dust}}$, and the Saharan dust dissolution rate constant is 0.22 ± $0.01 \frac{nmol\ \text{Mn}}{day \cdot mg\ \text{Dust}}$.

4.1.2 Mn Thermodynamics

The Mn concentration versus time figures also show that dissolved Mn equilibrates between the dust and seawater after about two weeks. Each experimental treatment reaches a constant Mn concentration that is directly proportional to the dust concentration. The exception, 0.01 mg dust/L, had a final Mn concentration smaller than both the control and t=0 samples and was too similar to the control and t=0 samples throughout the experiment to distinguish any changes. It has not been considered in the following discussion. We also calculated the percentage of Mn dissolved from the dust using equation 4, where Mn_{dis} (defined as Mn passing through a 0.2 μm filter) is the dissolved plus colloidal Mn in solution, $[Mn]_{dust}$ is the Mn concentration in the dust (880 ppm for Saharan and 750 ppm for United States dust, taken from table 1), and [Dust] is the dust concentration,

$$\%Mn_{dis} = \frac{[Mn_{dis}]}{([Mn_{dust}][Dust])} \quad . \qquad \text{(eq. 4)}$$

The seawater dissolved 12-14% of the total Mn from the Saharan dust, while the U.S. dust was slightly more soluble (17-20%, Fig. 5). These results, shown in figure 5, are lower but still comparable to previous studies which report Mn dissolution from a variety of dust particles in seawater from 25 – 30% (Chester et al., 1993; Guieu et al., 1994; Statham and Chester, 1988). Our results, in conjunction with previous work, lead to our determination that the final Mn concentration derived from dust dissolution is proportional to the dust concentration, but can be modeled using several different dissolution mechanisms.

4.1.3 Possible Mechanisms

We propose that Mn dissolution follows one of the following mechanisms. If we assume that all the manganese is adsorbed to the surface of the dust particles, then an adsorption –

desorption mechanism, where accessible Mn atoms can exchange with seawater cations, fits the data (Stumm and Morgan, 1996). In this simplification, all Mn within the dust is accessible. Although this is not absolutely correct, it will only differ from the true nature of the dust particles by a percentage of the total Mn. We have chosen to proceed with this simplification rather than apply an estimate of the percentage of Mn on the surface in order to stay as close to the unaltered natural dust as possible. In this reaction (eq. 5), using magnesium (Mg^{2+}) as an example, Mn acts as a tracer for cation exchange and is at a significantly lower concentration than Mg. Because of this large difference we assume that the magnesium concentration is unchanged during the adsorption process, and we are able to rewrite the equilibrium expression (eq. 6) to incorporate the magnesium terms in the chemical constant (eq. 7).

$$Mn(II) - dust + Mg^{2+} \rightleftarrows Mn^{2+} + Mg - dust \qquad \text{(eq. 5)}$$

$$K^* = \frac{Mn^{2+}}{Mn - Dust}\frac{Mg - Dust}{Mg^{2+}} \qquad \text{(eq. 6)}$$

$$K = \frac{Mn^{2+}}{Mn - Dust} \qquad \text{(eq. 7)}$$

Figure 6 represents the total dissolved Mn against the total Mn bound to the dust (assuming that all Mn within the dust is accessible). The slope of the data in this figure is the apparent equilibrium constant, K, described by equation 7. The apparent constant is 0.21 ± 0.01 (nM Mn_{dis})/(nM Mn_{dust}) for the United States dust, and 0.16 ± 0.01 (nM Mn_{dis})/(nM Mn_{dust}) for the Saharan dust. In addition, the y-intercept of the experimental data is 0.93 ± 0.29 nM Mn for the United States dust, and 0.74 ± 0.29 nM for Saharan dust. As an additional test of the adsorption mechanism, these intercepts agree with our measured initial Mn_{dis} of 0.77 ± 0.10 nM Mn.

This type of reaction is driven by accessible surface sites on the dust which would allow for desorption of the Mn as well as adsorption in the reverse reaction. (Baker and Jickells, 2006) have shown that the surface area to volume ratio of mineral aerosol can be directly

proportional to the total leachable Fe from those aerosols. If Mn dissolution is solely driven by accessible Mn, then the dust with the greater surface area per mass should have the larger percent dissolution. We calculated the percentage of the total number of particles and the surface area per grain size for our dusts by using the percentage volume data from figure 2, assuming a density of 2.7 g/cm^3 and assuming spherical grains. The results of this calculation are presented in figure 7. From this calculation, the integrated surface area to volume ratio of the Saharan and US dusts are 0.93 μm^{-1} and 0.42 μm^{-1}, respectively. While these calculations are based on a greatly simplified dust particle shape and density, we believe that they can add substantive information to this mechanism. If the cation exchange reaction is surface area driven, then the Saharan dust would have a larger percent dissolution due to its larger surface area; however, the opposite is observed. Therefore we believe that the dissolution is driven by a mineral specific solubility rather than cation exchange, and that the total surface area of the dust particles is either not relevant to Mn dissolution or cannot be represented accurately through our simplified model.

The dissolution of a manganese mineral of the form Mn_xO_y, (where x = 1-2 and y = 1-3) could account for the observed data. Depending on the oxidation state of the Mn within the dust, we can describe the system in several different ways. The most common oxidation state found in terrestrial soils is Mn(II), which is highly soluble in water. If the dust contained Mn(II) minerals, the seawater would have dissolved all accessible Mn, leaving only Mn found deep within the matrix of the particles. In this scenario, the manganese minerals would have completely dissolved into the seawater in direct proportion to the amount of dust added. Although this is our observation, it is possible that part of the Mn within these dusts is of a higher oxidation state. Another explanation, which does not restrict the Mn to a 2+ oxidation state, can also account for the direct relationship between dust concentration and dissolved Mn. Mn(III) and Mn(IV) are insoluble in water and require reduction to the Mn(II) form in order to dissolve. This can be achieved by photoreduction of the oxidized Mn with organic material (Sunda *et al.*, 1983). Sunda *et al.*, (1983) demonstrated photochemical manganese oxide dissolution in seawater within Pyrex

bottles. The FEP Teflon bottles used in this experiment are 10-50% less transparent than Pyrex bottles in the visible wavelengths. However, they are more transparent in the UV, and photoreduction of manganese oxides is likely to occur. Once in solution, this later scenario is similar to the Mn^{2+} mechanism, and simply requires organic material to be present in order to keep the Mn^{2+} in the reduced and soluble form. The oxidation, or reoxidation in the cases of Mn(III) and Mn(IV), is prevented by the continued photoreduction of oxidized species back to Mn(II) and the very slow kinetics of oxidation (Stumm and Morgan, 1996). In this mechanism, the measured K_{eq} in figure 6 can be translated to an apparent solubility product.

The above mechanisms, reductive dissolution with Mn(II) mineral solubility or cation exchange, cannot be distinguished from each other given the data at hand. In addition, we could also be observing a combination of these reactions. If there was dissolution of Mn from a soluble mineral, Mn^{2+} could interact with surface adsorption sites following the adsorption – desorption process. These reactions, if they occurred on the same timescale, could each account for the observation of a chemical equilibrium and proportionality to total dust concentration.

An additional complication to the system is the presence of the Teflon wall. Although FEP will reduce metal adsorption, as compared to other plastics or glass, it will not completely eliminate the adsorption of Fe and Mn. This adsorption will remove Fe and Mn from the dissolved phase, and thus reduce our concentrations at each sub-sample. This process will reduce the calculated rates of dissolution of both Fe and Mn. In addition, the final concentrations will be reduced, and thus the apparent equilibrium constant measured will be a minimum estimate of the actual seawater constant.

4.2 Iron

4.2.1 Fe Kinetics

Dissolved Fe concentrations increase rapidly from an initial concentration of 0.165 ± 0.035 nM to ~ 0.6 nM (Fig. 1b). The rate of Fe dissolution was much faster than the rate of Mn dissolution and was also faster than our rate of sub-sampling. This is consistent with the reports of rapid kinetics for Fe complexation reactions (half-times of milliseconds to hours, (Rose and Waite, 2003)). In addition, ^{55}Fe uptake onto particulate and colloidal matter shows iron dissolution and adsorption occurring within seconds of dust addition (unpublished data, Guieu and Mendez). Because of our comparably slow sub-sampling, we cannot determine the initial dissolution rate for Fe. But given the initial increase of about 0.4 nM Fe between the time zero and the first sub-sampling (at 24 hours), we can determine that the initial dissolution rate is faster than 0.4 nM Fe/day (0.32 nmol Fe/day). Dissolved Fe remains mostly constant for the first week of the experiment, with only small increases up until day 7, where we see a second increase in Fe concentration between days 7 and 14 with little increase thereafter.

4.2.2 Fe Thermodynamics

The final Fe concentrations in these experiments are not dependent on dust concentration, and both Saharan and U.S. dusts yielded similar results. Indeed, nine of the ten samples (excluding the control) had a final iron concentration of 1.5 – 2.0 nM, the exception being the 5 mg/L U.S. dust experiment which fell within these values on day 14 and then increased to ~ 4 nM at the final sub-sampling day. Because of this consistency, we believe that Fe dissolution is a function of the seawater's individual dissolution capacity.

The dissolved Fe concentration in seawater is strongly affected by the thermodynamics of Fe solubility. The maximum solubility of amorphous iron hydroxides is 0.1 nM at the natural pH range of seawater (Morel and Hering, 1993). This limited dissolved iron concentration was reached before our experiment began; thus, there must be another mechanism for the observed increase in Fe solubility. It has long been believed that

seawater's Fe capacity is governed by the natural ligand complexing capacity within the water; we therefore propose that Fe dissolution is a function of the ligand concentration and the biological community, which are related to the source of the seawater.

This Fe dissolution mechanism is fundamentally different than the Mn dissolution mechanisms proposed above. Mn dissolution appears to follow a mechanism that is proportional to the source of Mn, while Fe does not. This difference in dissolution is driven by the large difference in solubility. While Mn(II) is highly soluble and seawater can dissolve as much Mn as is accessible from natural dust sources, Fe is very insoluble, and no matter how much dust is added, only a small total quantity of Fe may dissolve. Therefore, a large majority of the dissolved Fe must be associated with ligands in the seawater. The concentration of that ligand complexing capacity will dictate the solubility of Fe. We will refer to this possible Fe dissolution as the dust concentration independent mechanism.

4.2.3 Possible Mechanisms

The percentage of Fe dissolved from the dust is inversely proportional to both the concentration of dust and thus the mass of Fe within the dust. Using equation 8, we calculated the final percentage of Fe dissolved from the dust, (Fig. 8),

$$\%Fe_{dis} = \frac{[Fe_{dis}]}{([Fe_{dust}][Dust])} \quad , \qquad \text{(eq. 8)}$$

where $[Fe]_{dust}$ is 5.0% for Saharan and 3.8% for United States dust, taken from table 1. By holding $[Fe_{dis}]$ constant and only changing the dust concentration, we can model the proposed dust concentration independent model. The contours in figure 8 reflect Fe dissolution, which is independent of dust concentration. This dust concentration independent mechanism gives each line a slope of negative one (in log space) and is more sensitive to $[Fe_{dis}]$ changes at lower concentrations (due to the log-log scale). If dissolution is linearly proportional to dust concentration, the slope is zero, as demonstrated in the Mn

data in figure 5. Any slope between negative one and zero indicates a partial dependence on dust concentration.

The Saharan dust results (Fig. 8B) are consistent with the hypothesis that Fe dissolution is independent of dust concentration. The data have a slope of negative one and match the model at 1.5 nM (shown with a solid line). Also plotted on figure 8B is data from day 7 of Bonnet and Guieu, (2004) (the final day of their experiment) that used the same Saharan dust. Data from Bonnet and Guieu, (2004) are similar to our model; however, their data have a slope of -0.79 (± 3.7%) and therefore are partially dependent on dust concentration. The U.S. dust experiment (Fig. 8A) indicates that at the high dust concentrations there may be more Fe dissolution, similar to high dust concentration results in Bonnet and Guieu, (2004). However, the slope of the U.S. data is more consistent with the concentration independent mechanism suggested by the Saharan data (this study). Why should the same Saharan dust yield data reflecting different dissolution behavior? We believe that while the nature of the dust is important in controlling the mechanism of dissolution in seawater, the seawater itself is more important to the total dissolution. Therefore we must investigate the difference in the seawater used in these two experiments to understand the different behavior.

Total ligand measurements made aboard ship on seawater collected at the same depth and at nearly the same time of the water used for this experiment were:

$[L_1]$=1.67 ± 0.03 nM $\log K_1 = 12$,

$[L_2]$=3.2 ± 0.1 nM $\log K_2 = 11$. (Buck, K.N. pers. comm.)

Adjusting for the relative strength of the L_2 ligand, the total Fe binding capacity of this water is 4.56 ± 0.10 nM. This indicates that the stoichiometry of the L_1 and L_2 ligands together to $[Fe]_{dis}$ is 3:1. The ligand measurements in this study give us an upper limit for ligand concentration and, therefore, Fe binding capacity. Our seawater was stored in the dark, but was not frozen between collection and the beginning of the experiment; therefore,

ligand concentrations most likely experienced thermochemical and photochemical decay. The ligand concentrations and their Fe binding capacity can only be used as a maximum. Despite this potential complication, the L_1 and L_2 concentrations measured at sea are close to the Fe concentration we measured in our experiments. This indicates that the ligand concentrations in the seawater are the primary controlling factors for Fe solubility, not the dust concentration. Bonnet and Guieu, (2004) examined the dissolution of anthropogenic particles showing extremely large dissolution of Fe, up to 13 nM. It is possible that this increase in solubility is due to an increase in labile iron associated with the anthropogenic particles as suggested by Bonnet and Guieu, (2004). This hypothesis is dependent upon on the availability of the iron atoms within the aerosol that would most likely be high in anthropogenic aerosols, which are typically composed of fine particles (Kiehl and Rodhe, 1995). A different yet complimentary hypothesis which can explain the increase in solubility is that the large organic component associated with typical anthropogenic aerosols (Heintzenberg, 1989) may act as weak Fe ligands. Under this hypothesis, the ligands which hold Fe in solution would simply come with the aerosol rather than being present in the seawater beforehand. A terrigenous particle, such as our Saharan and United States dusts, that did not undergo long range transport does not have as large an organic component as urban aerosol (Jacobson *et al.*, 2000), and thus a larger percentage of the ligands must originate from the biological community within the seawater.

Comparing the organic ligands between our seawater and the seawater used in Bonnet and Guieu, (2004) may elucidate reasons behind the difference between our results. Experimental conditions differed between the studies. Our study was held at 13°C under 50% of ambient light, whereas Bonnet and Guieu, (2004) conducted their experiments at 20°C under completely dark conditions. Bonnet and Guieu, (2004) may have found even higher dissolution if their experiment had been conducted with natural light due to photo-reduction of Fe to the soluble Fe^{2+} (Zhu *et al.*, 1993). The initial Fe concentration in our experiment's seawater was 0.165 ± 0.003 nM, which leads us to believe the measured

ligand concentrations are relatively small compared to those found in the Mediterranean. Ligand concentrations from the oligotrophic North Pacific have been measured at approximately 2 nM (Rue and Bruland, 1995), similar to the measured ligands in our study. However, in Bonnet and Guieu, (2004) the seawater had an initial Fe concentration of 0.38 nM, which may be due to a larger initial natural ligand concentration. Although the ligands were not measured in their experiment, ligand concentrations as high as 12 nM have been measured in the surface Western Mediterranean (van den Berg, 1995). These possible ligand concentrations could have increased the capacity of Fe in the water used in Bonnet and Guieu, (2004). This allowed more Fe to ultimately stay dissolved at the higher dust concentrations but does not explain the reason why the data indicate a partial dust concentration dependence.

5. Conclusions

Mn dissolution is dependent upon the dust concentration. This differs greatly from Fe dissolution due to the dramatic difference in Mn solubility compared to Fe. The exact mechanism for Mn dissolution from the dust particles cannot be determined from these experiments, but we are able to hypothesize that there is dissolution of Mn(II)-rich minerals which are held in the Mn (II) oxidation state through photo-reduction. Because of this, the type and quantity of dust is important and will affect both the kinetics and thermodynamics of Mn dissolution. We see that Saharan dust and U.S. dust react differently, and we believe this is due to the different mineral state of the Mn.

Fe dissolution is dependent on the water's ligand complexing capacity rather than the type or quantity of dust deposited on the surface. Dissolved inorganic Fe is saturated at 0.1 nM in natural seawater. Because of these thermodynamics, an increase in dust deposition will not increase Fe in the ocean, unless initial Fe inputs fertilize the ocean in such a way that the biologically community within the region is accustomed to dust deposition events and can produce ligands which will hold Fe in the dissolved form. Ultimately, the role of Fe

binding ligands toward atmospheric Fe dissolution is one of the important controls among the various processes controlling iron cycle in the surface waters.

TABLE

U.S. Dust	Saharan dust	Saharan end-member, Guieu *et al.*, 2002	Upper Crust, Wedepohl, 1995
Mn = 750 ppm	Mn = 880 ppm	-	Mn = 527 ppm
Fe = 3.81 %	Fe = 5.0%	Fe = 4.45 ± 0.49 %	Fe = 3.1 %
Al = 7.58 %	Al = 7.1 %	Al = 7.09 ± 0.49 %	Al = 7.7 %

Table 1: Elemental analysis of the dust samples used in the dissolution experiment. Measurements are total metal mass concentrations.

FIGURES

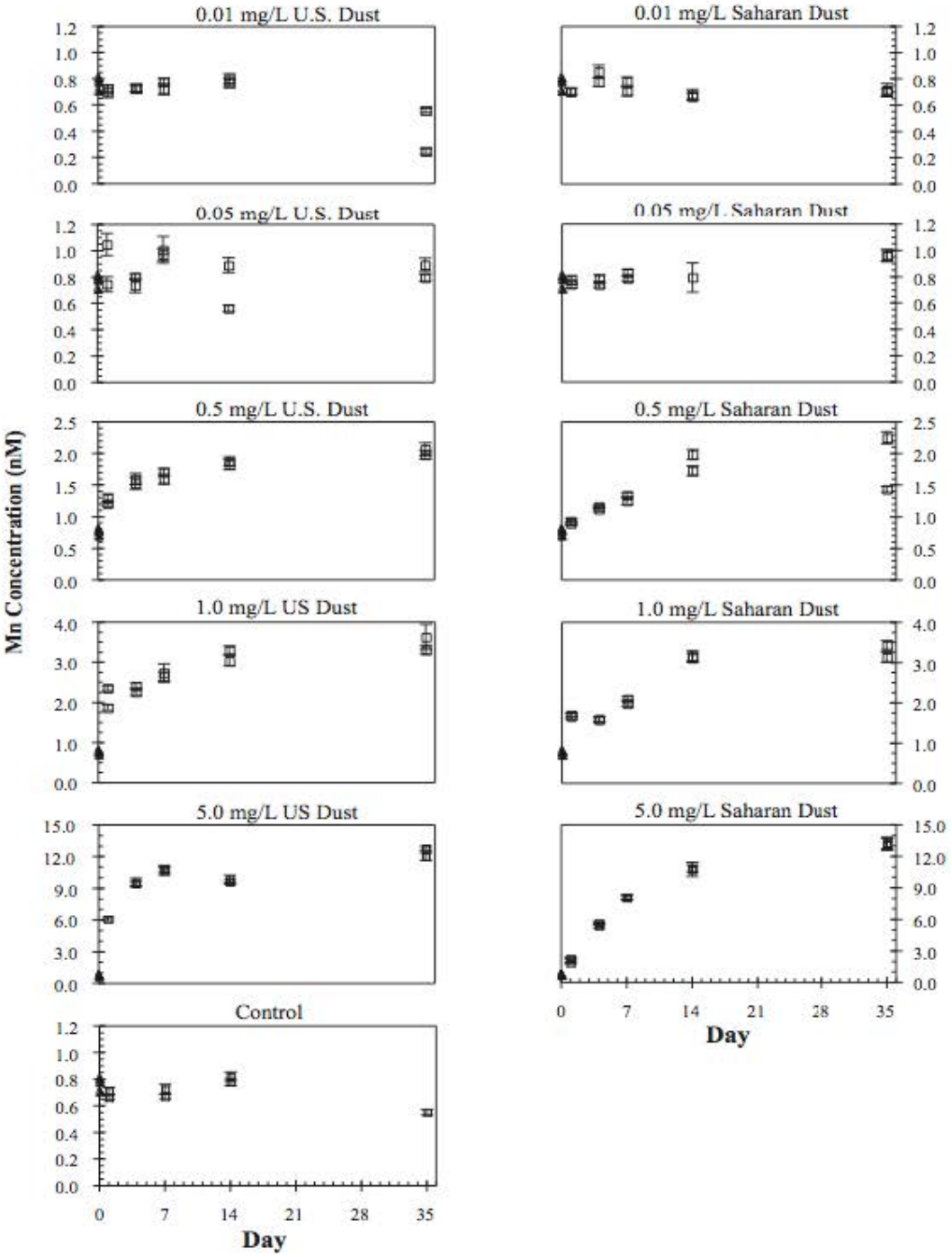
0.01 mg/L U.S. Dust
0.01 mg/L Saharan Dust
0.05 mg/L U.S. Dust
0.05 mg/L Saharan Dust
0.5 mg/L U.S. Dust
0.5 mg/L Saharan Dust
1.0 mg/L US Dust
1.0 mg/L Saharan Dust
5.0 mg/L US Dust
5.0 mg/L Saharan Dust
Control
Mn Concentration (nM)
Day

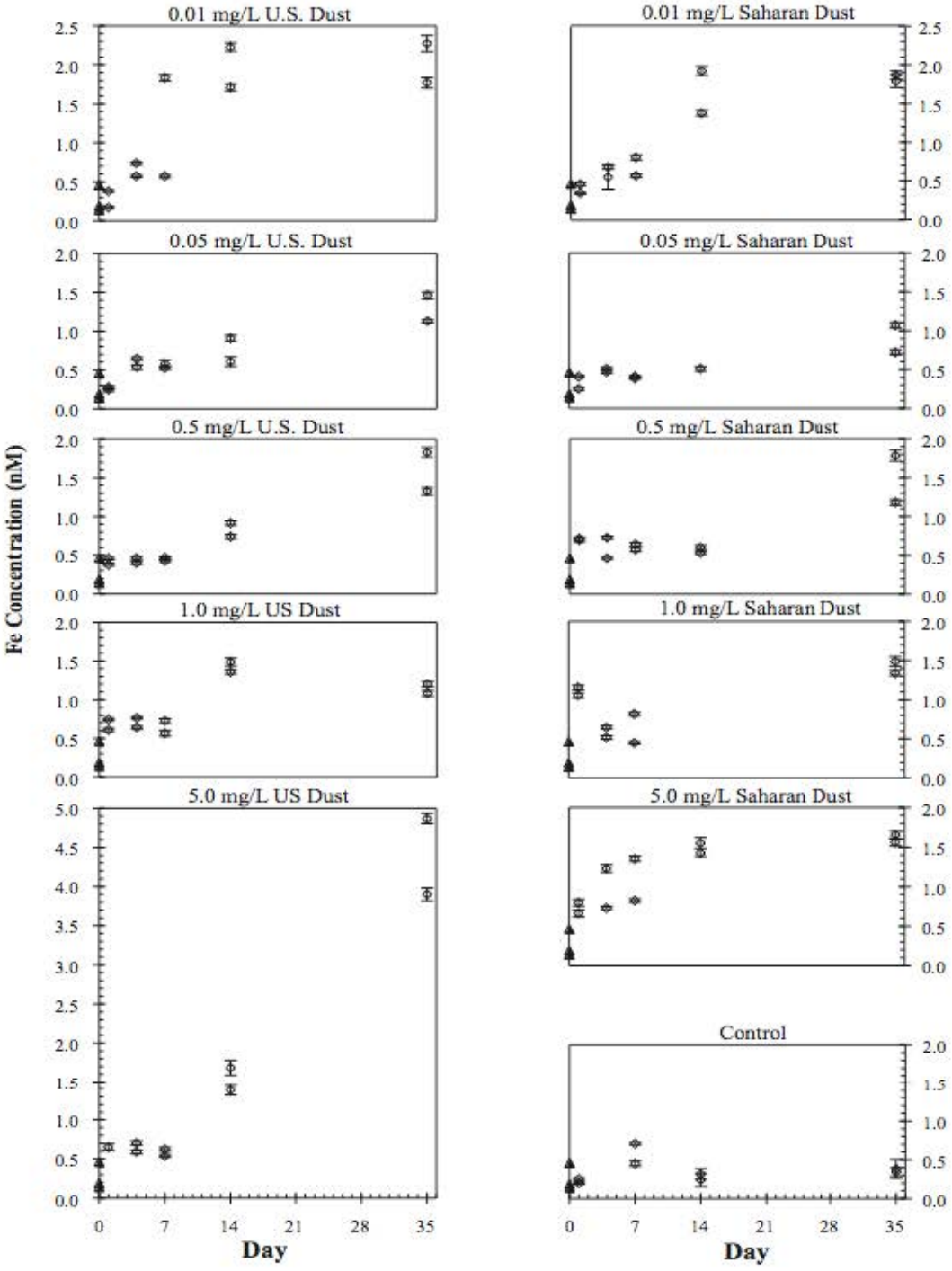

Figure 1: The concentration of (a) Mn versus time and (b) Fe versus time. Sub-samples (open squares, Mn; open diamonds, Fe) and the time zero samples (solid triangles) are plotted with 2 σ error bars.

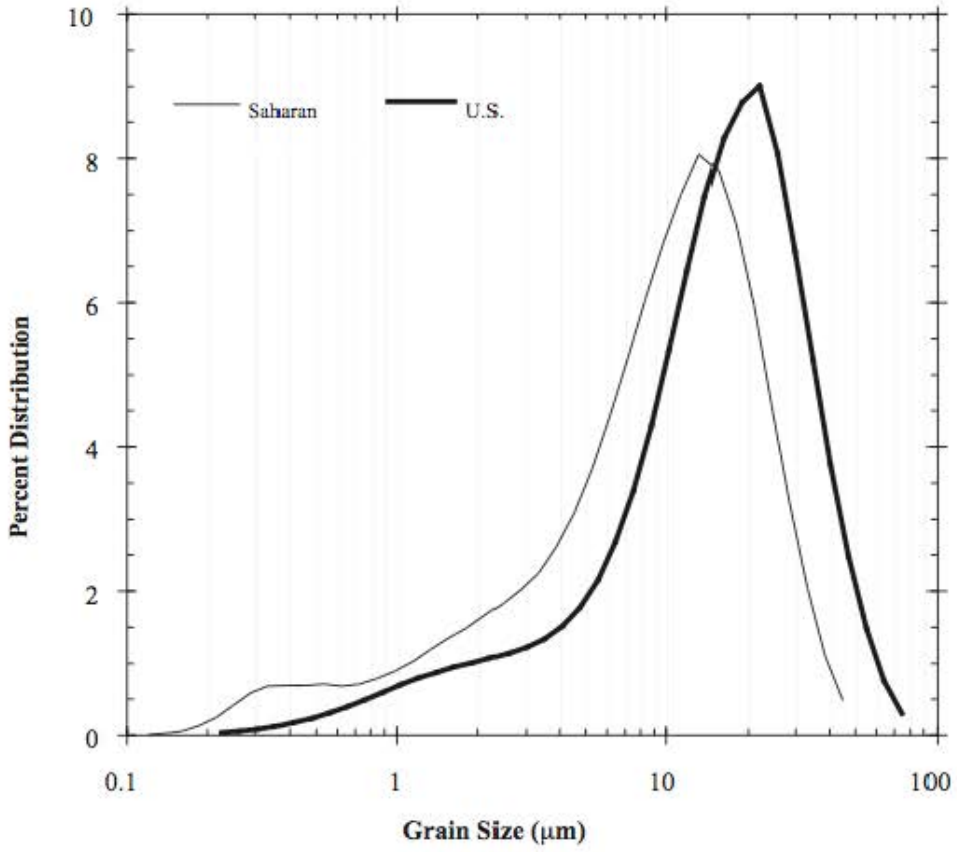

Figure 2: Size distribution of dust particles, in percentage of total volume. Saharan dust (thin line) has a group of particles below 0.6 μm, while this group is absent in the U.S. dust (heavy line).

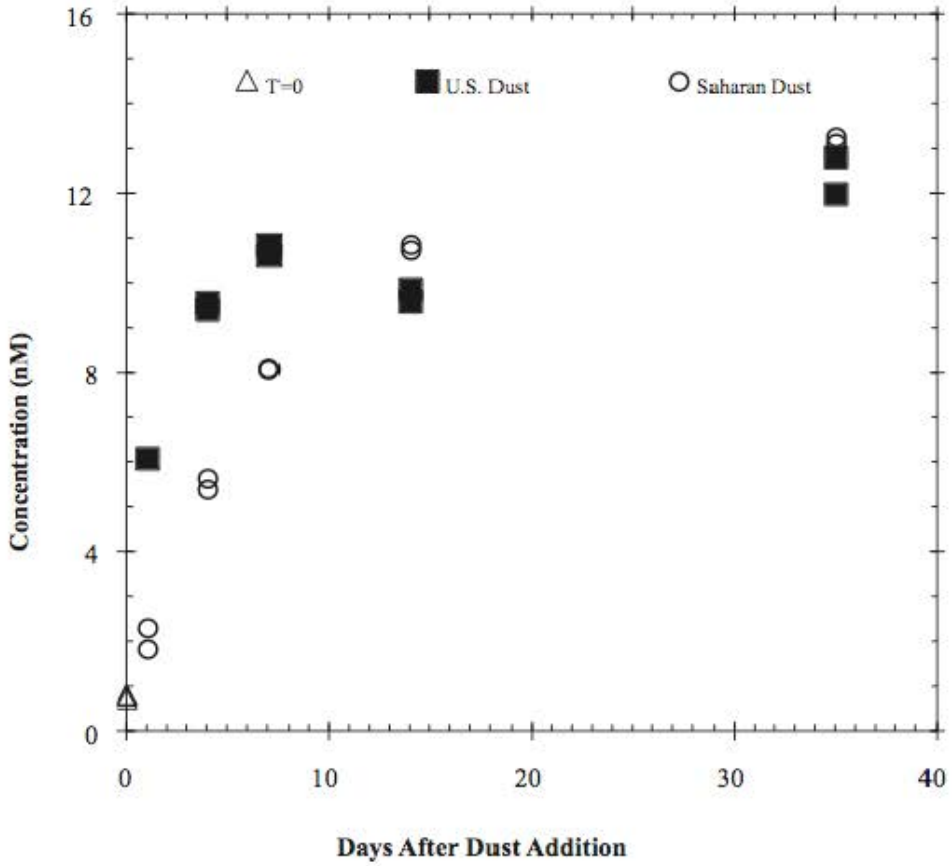

Figure 3: A comparison of Mn concentrations over time for the 5.0 mg/L of U.S. and Saharan dust samples. Mn concentrations before dust addition are represented by the open triangle, Saharan dust samples are represented by the closed square, and the U.S. dust is represented by the open circle. Error bars are 2 σ of the standard error.

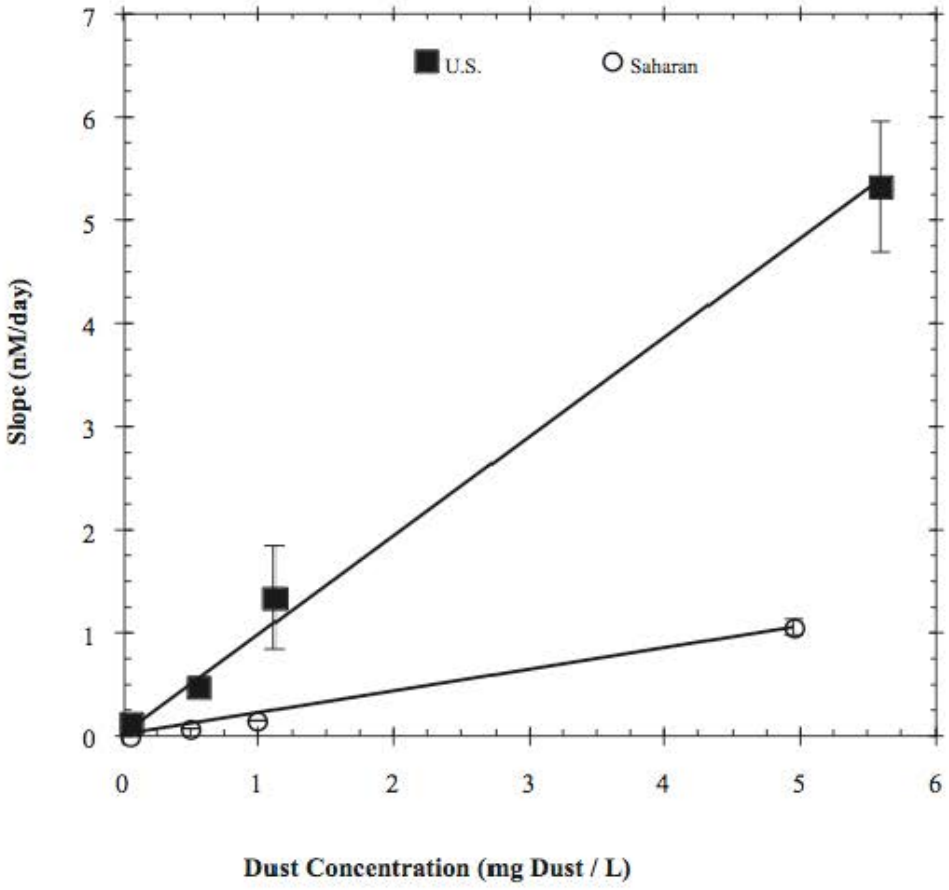

Figure 4: Plot of the slope of the initial increase in Mn concentration versus dust concentration. U.S. dust (closed squares) has a linear increase in slope with dust concentration which is an order of magnitude larger that the Saharan dust (open circles). Error bars are 2 σ of the standard error of the calculated slope.

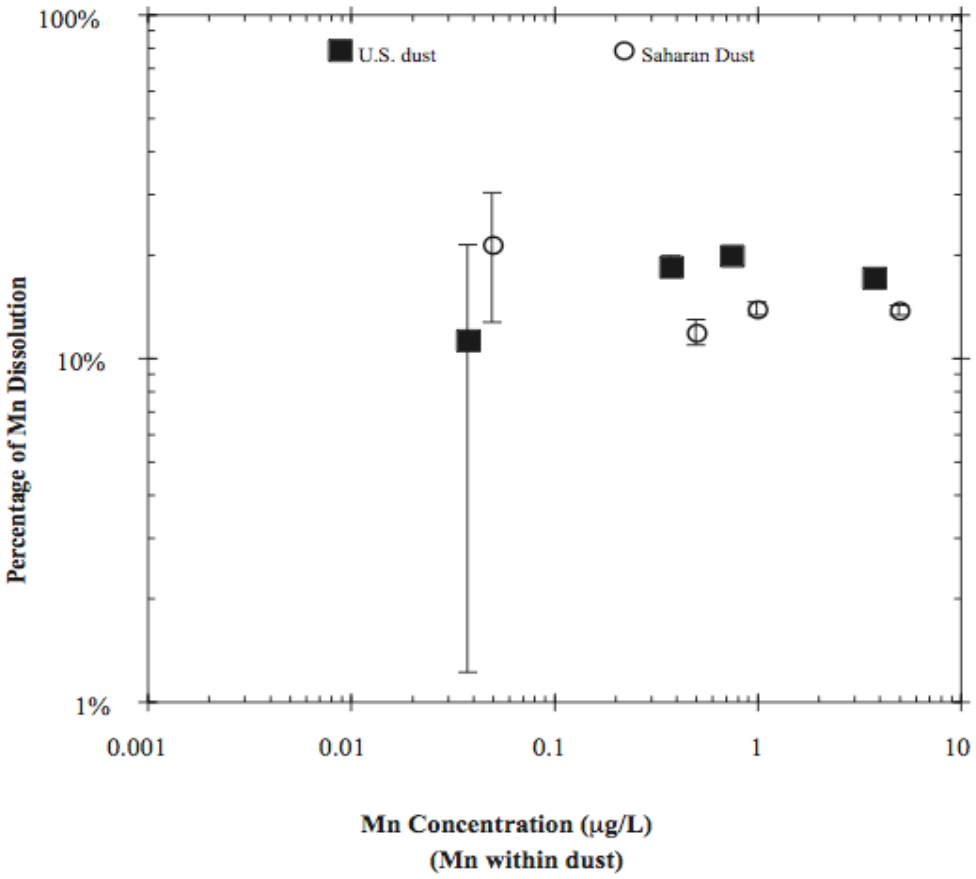

Figure 5: The percentage of Mn dissolved off the dust, taken on day 35 for the 4 highest dust concentrations. The error bars are 2 σ of the standard error of each individual sub-sample propagated through each step of the calculation, and averaged over the two duplicate sub-samples . The samples with low dust concentration have larger errors due to the relative small difference between the Mn increase over time and the initial Mn concentration. The log-log scale has been chosen in order to better compare with the analogous Fe plot, figure 8.

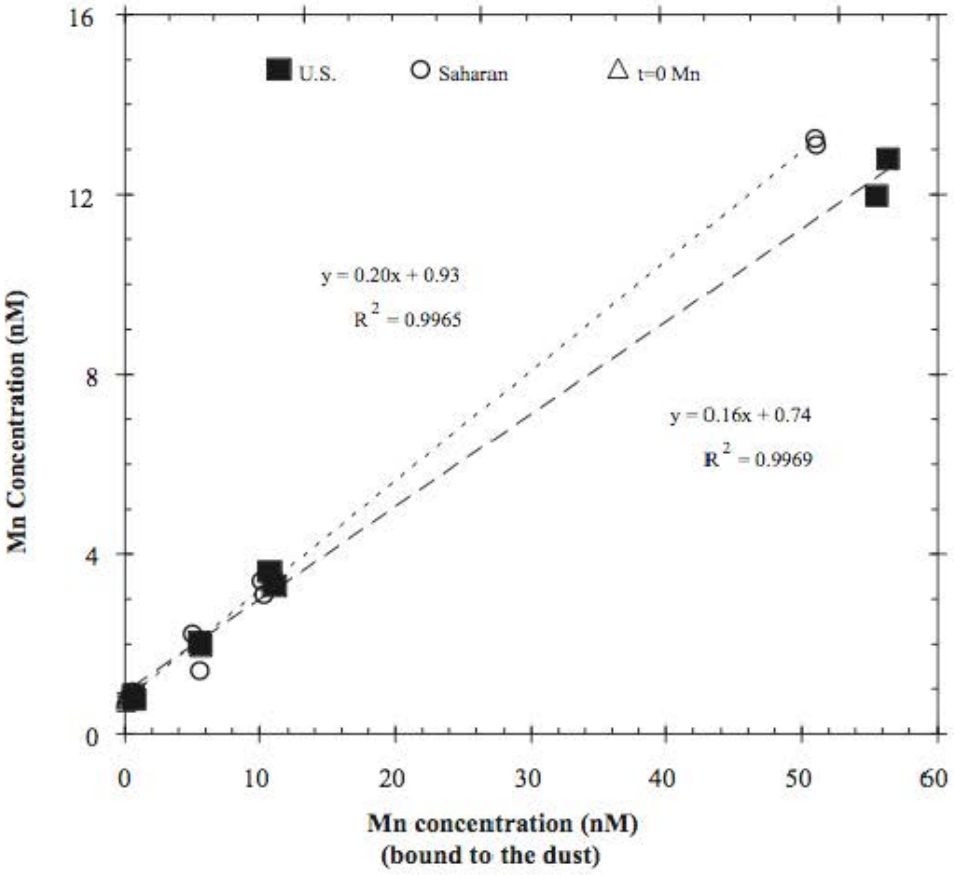

Figure 6: The Mn concentration (day 35) versus the total amount of Mn bound to the dust after dissolution. The Mn bound to the dust was calculated by subtracting the percent dissolved (equation 4) from 100% and multiplying that by the total concentration of Mn in the dust (using the data from table 1). The slope of the data will be the equilibrium constant described in the text.

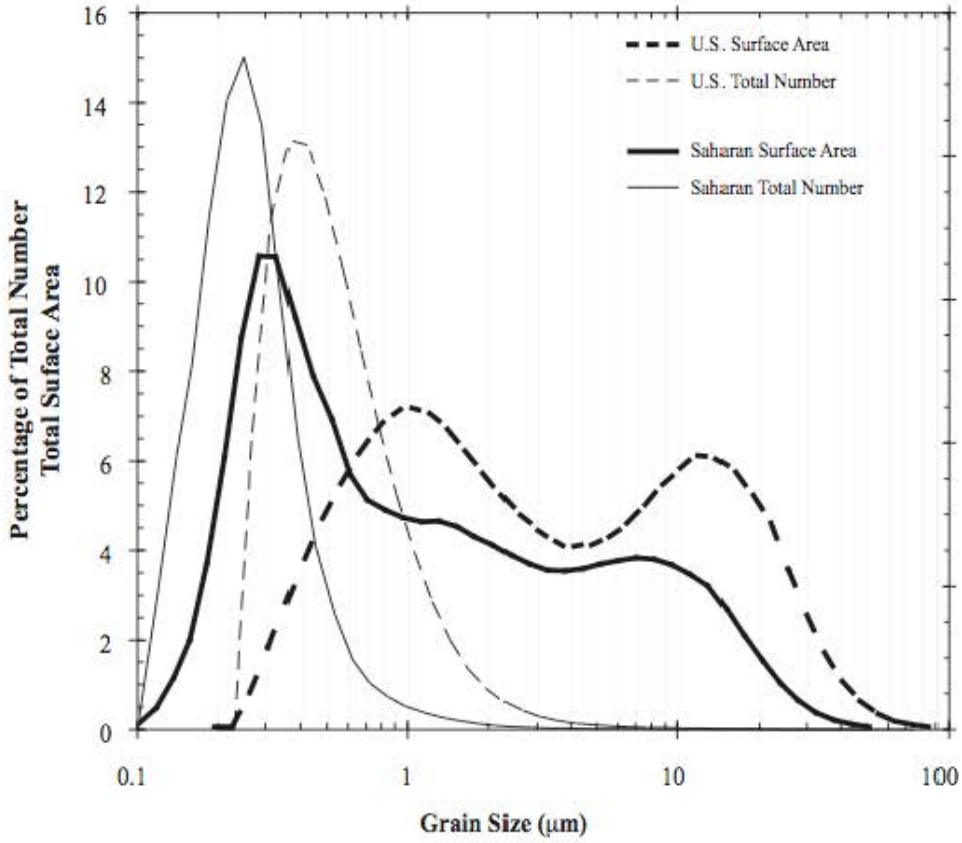

Figure 7: Percentage of surface area (heavy lines) and percentage of total particles number (thin lines) attributed to the size distribution of the dust particles. The Saharan dust (solid lines) has a large percentage of its surface area accounted for within the smaller sized particles, resulting in a larger surface area to volume ratio. The United States dust (dashed lines) has a particulate concentration at higher grain size, with a secondary group above 10 μm.

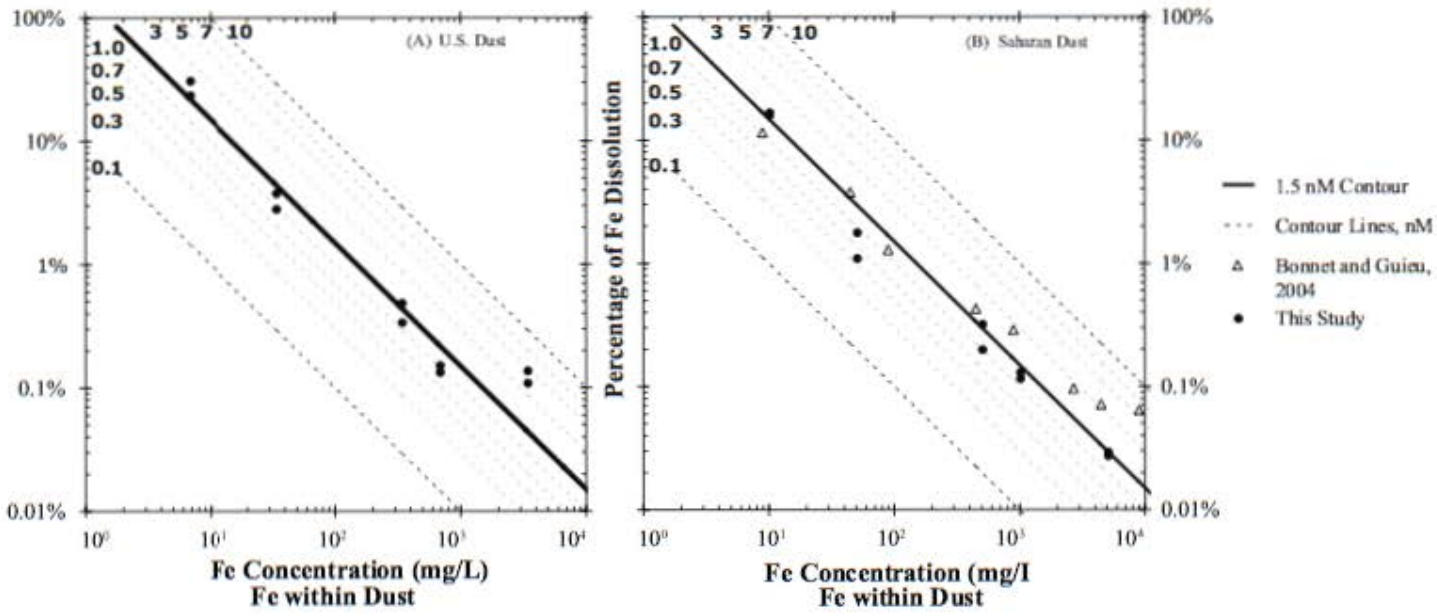

Figure 8: Percentage of Fe dissolved off of the dust after 35 days versus the total concentration of Fe introduced by the dust addition. (A) United States dust data (solid circles). (B) Saharan dust data (this study: solid circles) with data from Bonnet and Guieu, 2004 (open triangles) defined as dissolved Fe concentration in the experimental bottles. Both the Saharan dust and United States dust data are plotted on top of concentration contours from the dust concentration independent model (dashed and solid lines). Each contour represents the percentage of Fe dissolved from dust when the Fe concentration was held constant. Each line is labeled with the assumed constant Fe concentration (nM), both the U.S. and Saharan dust best fit the 1.5 nM line.

BIBLIOGRAPHY

Aumont, O., Maier-Reimer, E., Blain, S. and Monfray, P., 2003. An ecosystem model of the global ocean including Fe, Si, P colimitations. Global Biogeochemical Cycles, 17(2).

Baker, A.R. and Jickells, T.D., 2006. Mineral particle size as a control on aerosol iron solubility. Geophysical Research Letters, 33(L17608): 10.1029/2006GL026557.

Barbeau, K., 2006. Photochemistry of organic iron(III) complexing ligands in oceanic systems. Photochemistry and Photobiology, 82(6): 1505-1516.

Barbeau, K., Rue, E.L., Bruland, K.W. and Butler, A., 2001. Photochemical cycling of iron in the surface ocean mediated by microbial iron(III)-binding ligands. Nature, 413: 409-413.

Bonnet, S. and Guieu, C., 2004. Dissolution of atmospheric iron in seawater. Geophysical Research Letters, 31(3).

Buck, C.S., Landing, W.M., Resing, J.A. and Lebon, G.T., 2006. Aerosol iron and aluminum solubility in the northwest Pacific Ocean: Results from the 2002 IOC cruise. Geochemistry Geophysics Geosystems, 7.

Buck, K.N., M. C. Lohan, C. J. M. Berger, and K. W. Bruland 2007. Dissolved iron speciation in two distinct river plumes and an estuary: Implications for riverine iron supply. Limnology and Oceanography, 52(2).

Chester, R. et al., 1993. Factors Controlling the Solubilities of Trace-Metals from Nonremote Aerosols Deposited to the Sea-Surface by the Dry Deposition Mode. Marine Chemistry, 42(2): 107-126.

Duce, R.A. and Tindale, N.W., 1991. Atmospheric transport of iron and its deposition in the ocean. Limnology and Oceanography, 36(8): 1715-1726.

Gao, Y., Fan, S.M. and Sarmiento, J.L., 2003. Aeolian iron input to the ocean through precipitation scavenging: A modeling perspective and its implication for natural iron fertilization in the ocean. Journal of Geophysical Research-Atmospheres, 108(D7).

Guieu, C., Duce, R. and Arimoto, R., 1994. Dissolved Input of Manganese to the Ocean - Aerosol Source. Journal of Geophysical Research-Atmospheres, 99(D9): 18789-18800.

Guieu, C., Loye-Pilot, M.D., Ridame, C. and Thomas, C., 2002. Chemical characterization of the Saharan dust end-member: Some biogeochemical implications for the western Mediterranean Sea. Journal of Geophysical Research-Atmospheres, 107(D15).

Hand, J.L. et al., 2004. Estimates of atmospheric-processed soluble iron from observations and a global mineral aerosol model: Biogeochemical implications. Journal of Geophysical Research-Atmospheres, 109(D17).

Haygood, M.G., Holt, P.D. and Butler, A., 1993. Aerobactin Production by a Planktonic Marine Vibrio Sp. Limnology and Oceanography, 38(5): 1091-1097.

Heintzenberg, J., 1989. Fine particles in the global troposphere- a review. Tellus, 41B: 149-160.

Horsburgh, M.J., Wharton, S.J., Karavolos, M. and Foster, S.J., 2002. Manganese: elemental defense for a life with oxygen. Trends in Microbiology, 10(11): 496-501.

Jacobson, M.C., Hansson, H.C., Noone, K.J. and Charlson, R.J., 2000. Organic atmospheric aerosols: Review and state of the science. Reviews of Geophysics, 38(2): 267-294.

Kernen, N., Kidd, M.J., Penner-Hahn, J.E. and Pakrasi, H.B., 2002. A light-dependent mechanism for massive accumulation of manganese in the photosynthetic bacterium Synechocytis sp. PCC 6803. Biochemistry, 41(50): 15085-15092.

Kiehl, J.T. and Rodhe, H., 1995. Modeling geographical and seasonal forcing due to aerosols. Aerosol Forcing of Climate. Wiley, New York, 281-296 pp.

Klinkhammer, G.P. and Bender, M.L., 1980. The distribution of manganese in the Pacific Ocean. Earth and Planetary Science Letters, 46: 361-384.

Kraemer, S.M., Butler, A., Borer, P. and Cervini-Silva, J., 2005. Siderophores and the dissolution of iron-bearing minerals in marine systems, Molecular Geomicrobiology. Reviews in Mineralogy & Geochemistry, pp. 53-84.

Küpper, F.C., Carrano, C.J., Kuhn, J.U. and Butler, A., 2006. Photoreactivity of iron(III) - Aerobactin: Photoproduct structure and iron(III) coordination. Inorganic Chemistry, 45(15): 6028-6033.

Martin, J.H. and Fitzwater, S.E., 1988. Iron deficiency limits phytoplankton growth in the north-east Pacific subarctic. Nature, 331: 341-343.

Measures, C.I., Edmond, J.M. and Jickells, T.D., 1986. Aluminum in the Northwest Atlantic. Geochimica Et Cosmochimica Acta, 50(7): 1423-1429.

Moore, J.K., Doney, S.C., Lindsay, K., Mahowald, N. and Michaels, A.F., 2006. Nitrogen fixation amplifies the ocean biogeochemical response to decadal timescale variations in mineral dust deposition. Tellus Series B-Chemical and Physical Meteorology, 58(5): 560-572.

Morel, F.M.M. and Hering, J.G., 1993. Principles and Applications of Aquatic Chemistry. John Wiley & Sons, Inc., New york, 588 pp.

Nozaki, Y., Turekian, K.K. and Von Damm, D., 1980. 210Pb in GEOSECS water profiles from the North Pacific. Earth and Planetary Science Letters, 49: 393-400.

Rose, A.L. and Waite, T.D., 2003. Kinetics of iron complexation by dissolved natural organic matter in coastal waters. marine Chemistry, 84: 85-103.

Rue, E.L. and Bruland, K.W., 1995. Complexation of Iron(III) by Natural Organic-Ligands in the Central North Pacific as Determined by a New Competitive Ligand Equilibration Adsorptive Cathodic Stripping Voltammetric Method. Marine Chemistry, 50(1-4): 117-138.

Siefert, R.L., Johansen, A.M., Hoffmann, M.R. and Pehkonen, S.O., 1998. Measurements of trace metal (Fe, Cu, Mn, Cr) oxidation states in fog and stratus clouds. Journal of the Air & Waste Management Association, 48(2): 128-143.

Statham, P.J. and Chester, R., 1988. Dissolution of Manganese from Marine Atmospheric Particulates into Seawater and Rainwater. Geochimica Et Cosmochimica Acta, 52(10): 2433-2437.

Stumm, W. and Morgan, J.J., 1996. Aquatic Chemistry. Wiley-Interscience, New York, 1022 pp.

Sunda, W.G., Huntsman, S.A. and Harvey, G.R., 1983. Photoreduction of manganese oxides in seawater and its geochemical and biological implications. Nature, 301: 234-236.

Tegen, I. and Fung, I., 1994. Modeling of Mineral Dust in the Atmosphere - Sources, Transport, and Optical-Thickness. Journal of Geophysical Research-Atmospheres, 99(D11): 22897-22914.

van den Berg, C.M.G., 1995. Evidence for Organic Complexation of Iron in Seawater. Marine Chemistry, 50(1-4): 139-157.

Wu, J. and Boyle, E.A., 1997. Low Blank Preconcentration Technique for the Determination of Lead, Copper, and Cadmium in Small-Volume Seawater Samples by Isotope Dilution ICPMS. Analytical Chemistry, 69: 2464-2470.

Wu, J. and Boyle, E.A., 1998. Determination of iron in seawater by high-resolution isotope dilution inductively coupled plasma mass spectrometry after $Mg(OH)_2$ coprecipitation. Analytica Chimica Acta, 367: 183-191.

Zhu, X. et al., 1993. Photoreduction of Iron(Iii) in Marine Mineral Aerosol Solutions. Journal of Geophysical Research-Atmospheres, 98(D5): 9039-9046.

C h a p t e r 3

ATMOSPHERIC INPUT OF MANGANESE AND IRON TO THE OCEAN:

Seawater dissolution experiments with organic ligands

Jeffrey Mendez[a], Kristen Buck[b], Jess Adkins[c]

[a] Department of Environmental Science and Engineering, California Institute of Technology
[b] Scripps Institute of Oceanography, University of California San Diego
[c] Department of Geological and Planetary Sciences, California Institute of Technology

1. Introduction

Iron (Fe) and Manganese (Mn) are essential elements to all biological organisms, including those of the marine environment. These micronutrients are required for enzymatic pathways of respiration, nitrogen and carbon fixation, and electron transfer in photosynthesis (Turner and Hunter, 2001). One of the largest sources of these metals to the oceans is atmospheric deposition (Duce and Tindale, 1991; Guieu *et al.*, 1994; Siefert *et al.*, 1998). Despite the fact that Fe and Mn are key to the ecology of the ocean, there is little mechanistic understanding of their dry aerosol dissolution.

Manganese within a fully oxygenated ocean at natural pH should be Mn(IV) and precipitate out of the water in the form MnO_2. However, the surface ocean contains Mn(II) concentrations as high as 25 nM (Chapter 3). In the open ocean, a portion of this Mn(II) is the result of aerosol deposition (Guieu *et al.*, 1994). Much of the Mn contained within the dust is in the +2 oxidation state. Slow oxidation to the +3 or +4 state allows Mn to stay dissolved on the order of days (Stumm and Morgan, 1996); however, Mn should oxidize over time and precipitate out of the surface ocean. Accumulation of the oxidized Mn is prevented by continual photoreduction of Mn back to the +2 oxidation state by humic materials (Sunda *et al.*, 1983). This photoreduction prevents the Mn from

precipitating out of the surface ocean, and maintains sufficient concentrations of dissolved Mn for biological use.

Fe is the fourth most abundant element in the Earth's crust (Wedepohl, 1995), and yet its thermodynamically stable oxidation state, Fe (III), is relatively insoluble in oxic pH 8 seawater. This limits its inorganic concentration to 0.1 nM (Morel and Hering, 1993). Any inorganic iron above this concentration will either form an Fe oxide solid or quickly adsorb onto nearby surfaces (Rose and Waite, 2002). Despite this limit, oceanic Fe concentrations range from 0.1 – 2 nM (or higher in the coastal ocean, Chapter 3). Fe(II) additions to the surface water from wet or dry deposition can elevate the total dissolved Fe concentration (Erel et al., 1993; Johansen et al., 2000); however, these too will be quickly oxidized to Fe(III). Therefore, Fe must have a non-inorganic method for maintaining dissolved Fe in the seawater. Organic ligands appear to be responsible for this elevation of Fe concentrations. Specific Fe binding ligands called siderophores are produced by bacteria to acquire environmental Fe and strongly bind Fe(III) (Neilands, 1995). Some strong Fe binding ligands in the marine environment appear to resemble siderophores in functional group and molecular size (Macrellis *et al.*, 2001; Witter *et al.*, 2000), although these ligands have not yet been structurally identified (Rue and Bruland, 2001). Additionally, the siderophore aerobactin is produced by marine *Vibrio* bacteria grown under Fe limiting conditions (Haygood *et al.*, 1993). Aerobactin is a di-hydroxamate α-hydroxy-carboxylate siderophore (Fig. 1), and its physical chemistry properties (Harris *et al.*, 1979) and cellular iron transport pathways are well characterized (Braun, 2003). In addition, large undifferentiated molecules, such as humic acids (Voelker *et al.*, 1997) as well as small organic molecules, may specifically facilitate Fe dissolution from dust into the ocean. Oxalate has been shown to dissolve Fe oxides in laboratory settings (Siffert and Sulzberger, 1991), while citrate has been shown to allow Fe concentrations above the inorganic threshold (Waite and Morel, 1984).

Ligand-controlled Fe oxide dissolution proceeds along three steps (Furrer and Stumm, 1986; Zinder *et al.*, 1986):

1. A fast surface complexation by the ligand in a ligand exchange mechanism,
2. A slow, rate-determining detachment of the Fe ion,
3. A fast regeneration of the surface and transport of the metal complex into the bulk solution.

In reductive dissolution, the second step of detachment is preceded by a ligand-to-metal charge transfer from either a thermally- or photolytically-excited ligand. The reduction of Fe polarizes and weakens the Fe-oxygen bonds in the mineral structure, which allows the slow detachment of Fe (Furrer and Stumm, 1986; Siffert and Sulzberger, 1991). This slow rate may lead to a competitive reoxidation of the Fe(II), resulting in even slower Fe dissolution. However, detachment of the Fe(II) from the surface occurs more rapidly in siderophore-promoted dissolution (Borer *et al.*, 2005). Due to its large negative redox potential, the Fe(II)-siderophore complex will quickly reoxidize to the more soluble and stable Fe(III)-siderophore complex once free of the original mineral surface (Boukhalfa and Crumbliss, 2002).

Many siderophores are highly photoreactive. While the hydroxamate moiety (*i.e.* desferrioxamine-B, DFOB) is photochemically inert in both the bound and unbound state (Barbeau *et al.*, 2003), photolysis of the Fe(III)-α-hydroxy carboxylate siderophore (*i.e.* Fe-aerobactin) complex leads to a ligand-to-metal charge transfer and reduction of Fe(III) to Fe(II) (Barbeau *et al.*, 2001; Barbeau *et al.*, 2002). This results in cleavage of small functional groups and decarboxylation of the ligand. In addition, the ligand photo-product can retain strong Fe binding capability from enolate sites formed during decarboxylation (Küpper *et al.*, 2006).

We previously investigated the dissolution of Fe and Mn (Mendez *et al.*, in review) and found that Mn dissolution was proportional to dust concentration. Fe dissolution was found to not only be independent of dust concentration, but the total concentration of Fe within our samples was equivalent over all dust concentrations. We concluded that Fe dissolution is controlled by the Fe binding capacity of the seawater and, thus, ligand concentration and strength. To further investigate Fe dissolution from natural dust, we constructed two new experiments. In the first experiment we varied the ligand field within seawater with amendments of model ligands (oxalate, citrate, and aerobactin), while in the second we investigated the effects of sun light on aerobactin and seawater.

2. Method

2.1 Starting Materials

Two types of open ocean seawater were collected at 30°N, 140°W in November 2004 aboard the *R/V Melville* during the Sampling and Analysis of Iron (SAFe) intercomparison cruise. Surface seawater was collected with the University of California Santa Cruz (UCSC) trace metal clean surface "sipper" sampler (Bruland Lab), and sub-surface seawater was collected with the University of Hawaii's 30 L GO-Flo niskin bottles at a depth of 24-26 m (Measures Lab). There was a 76 m mixed layer during sub-surface sampling; all relevant chemical and physical properties of the sub-surface water used in these experiments should be identical in the 24-26 m depth range. Sub-surface water was in-line filtered at sea through a 0.2 μm cartridge filter and stored in an acid leached 4 L polycarbonate (PC) bottle unacidified and in the dark. Surface water was in-line filtered at sea through a 0.4 mm cartridge filter and stored in a 25 L high-density polyethylene (HDPE) carboy, also unacidified in the dark.

Seawater from two separate coastal locations was collected and treated in two different ways. The first coastal seawater was collected at 10 m depth while at the Santa Monica Bay Observatory Oceanographic Mooring (33° 55.9' N, 118° 42.9' W) aboard the R/V *Seaworld UCLA* in December 2005. Sub-surface sample water was collected using Teflon

coated external spring niskin bottles with Teflon coated messengers (General Oceanics Inc. 1010X-5L) on ¼ inch polyester line. Water was pumped from the niskin bottle through a 0.2 μm cartridge filter (Sartobran cellulose acetate P 150) with a peristaltic pump using C-Flex tubing into a hepa-filtered work space. All sampling and laboratory materials were acid leached using trace metal clean techniques. The second coastal seawater was collected and UV irradiated at UCSC (Bruland Lab) as described in (Donat and Bruland, 1988), but using Biobeads SM-2 and Amberlite XAD-16 resins in lieu of their Sumichelate Q10R resin. Both coastal seawater samples were stored frozen in one or two liter Teflon PFA bottles.

The dust was a composite of 3 superficial deposits collected in natural dust traps in the Nevada desert (South-West of Las Vegas) (courtesy Marith Reheis, USGS). The dust was hand sieved through successive, clean polyethylene meshes of 100 and 20 μm pore diameter. The smallest fraction (<20 μm) was collected and stored in a clean glass bottle. It was then autoclaved to destroy any possible bacteria spores and stored in a dark cabinet. Elemental analyses of the dust show manganese (Mn), iron (Fe), and aluminum (Al) concentrations similar to crustal abundances (Wedepohl, 1995) (Table 1).

2.2 Experiment 1, Seawater Matrix

The first experiment was designed to compare dust dissolution in different seawater matrices, focusing on the effects of model and natural Fe binding ligands. Open ocean surface seawater, Santa Monica Bay coastal seawater, UV irradiated coastal seawater, and UV irradiated seawater with added organic ligands were used in this experiment. Seven separate "seawaters" were prepared.

1. Santa Monica Bay coastal water, "Coastal Water",
2. Open ocean surface seawater, "Open Ocean Water",
3. UV irradiated coastal seawater (Bruland Lab UVSW), "UV Water",

4. UV irradiated coastal seawater with the addition of citric acid (57 nM, Sigma-Aldrich Cat #25,127-5), "Citrate Water",
5. UV irradiated coastal seawater with the addition of oxalic acid dihydrate (69.5 nM, Sigma-Aldrich Cat # 24,753-7), "Oxalate Water",
6. UV irradiated coastal seawater with the addition of a combination of citric acid and oxalic acid dihydrate (57 nM & 69.5 nM, respectively), "Citrate & Oxalate Water",
7. UV irradiated coastal seawater with the addition of aerobactin (EMC Microcollections) at a concentration of 50.1 nM, "Aerobactin Water".

An initial sub-sample was taken from each bottle to measure dissolved metal concentrations (Mn, Fe) and Fe speciation including Fe-binding organic ligand concentrations and binding constants. Each sub-sample was taken by directly filtering, (0.2 μm pore size, 25 mm polycarbonate Whatman) the sample seawater into a sub-sample bottle. Following each filtration, the filter was exchanged and the filter apparatus was rinsed with ~150 mL water (18 MΩ cm) and 5 mL of the next sample. All metal concentration sub-samples were acidified with hydrochloric acid (12 M, SeaStar® HCl), and all Fe speciation sub-samples were sealed and frozen.

After sub-sampling (t=0), the initial seven seawater samples were each split into two 1 L Teflon bottles, for a total of fourteen bottles. One bottle from each water type was sealed as a control, while the other bottle was saved for the dust addition. A mixture of 8.45 mg of dust and 52 mL of seawater was quickly shaken and then proportioned via pipette to each of the seven dust addition sample bottles in order to establish a dust concentration of 1.2 mg/L. This concentration is representative of typical dust deposition over ocean water (Duce and Tindale, 1991). Immediately following the addition of the dust, a sub-sample (t=30 min to 2 hr 40 min) was taken from each bottle to measure the dissolved metal concentrations (Mn, Fe) and Fe speciation.

The sample bottles (including the control bottles) were sealed with parafilm, placed in clear zipper bags, and immersed in a 13°C water bath on the roof of the laboratory under a 50% light screen. The seawater samples were allowed to mature under the diurnal cycle for 28 days. Samples were removed from this bath on days 0.25, 0.5, 1, 2, 4, 7, 14, and 28 for ~2 hours to take sub-samples.

2.3 Experiment 2, Light Exposure

The second experiment was designed to compare the dust dissolution effects of light on seawater, with and without amendments of the siderophore aerobactin, in order to elucidate the mechanism of siderophore-promoted dissolution. Two bottles of open ocean sub-surface seawater (SAFe; see Starting Material) were used in this experiment. One bottle was left unaltered, "Seawater" while aerobactin was added to the second, "Aerobactin Water II."

Aerobactin Water II was prepared by dissolving 1.088 mg of solid aerobactin in 1 mL of seawater. 111 μL of this solution was transferred to the seawater bottle via pipette to establish an aerobactin concentration of 51.1 nM. All work with solid aerobactin was conducted in an Ar filled glove bag in order to reduce any thermal oxidation and decomposition. Sub-samples of Seawater and Aerobactin Water II were then taken to measure initial metal concentrations (Mn, Fe) and dissolved Fe speciation.

A portion of both seawater types was poured into two different types of Teflon bottles. One bottle was translucent Teflon (the "Light" bottle), and the other was an identical bottle wrapped in black electrical tape to prevent light exposure (the "Dark" bottle). These four new samples became the "no dust" controls. A concentrated solution of dust in seawater (0.87 g dust/L) was added via pipette to the remaining Aerobactin Water II and Seawater samples to reach a dust concentration of 1.1 mg/L. Immediately following this addition, a

sub-sample was taken to measure initial Fe speciation. The samples were again partitioned into "Light" and "Dark" bottles, resulting in 8 total samples bottles: Seawater: light-no dust, dark-no dust, light-dust, dark-dust; and Aerobactin: light-no dust, dark-no dust, light-dust, dark-dust.

The Light bottles were sealed with parafilm and placed in a clear zipper bag, while the Dark bottles were sealed and placed in three brown bags to further reduce light exposure. All samples were immersed in a 13°C water bath on the roof of the laboratory under a 50% light screen. The samples were allowed to mature under the diurnal cycle for 18 days. Samples were removed from this bath on days 0.5, 1, 1.5, 2, 2.5, 3, 6, 9, and 18 for ~ 2 hours to take sub-samples.

2.4 Analysis

All sub-samples were analyzed for dissolved Fe and Mn concentrations using a modified magnesium co-precipitation (MagIC) method (Wu and Boyle, 1998). This isotope dilution procedure concentrates the analyte by 20 fold, with isotope ratios measured on the Caltech Element I ICP-MS (Mendez *et al.*, in review). Dissolved Fe speciation, including both ligand concentration and binding strength, was measured using a competitive ligand exchange-adsorptive cathodic stripping voltammetry (CLE-ACSV) with the added ligand salicylaldoxime (Buck *et al.*, 2007).

3. Results

The dissolution of Mn and Fe over time is shown in Figs. 2-5. In general, Mn concentrations increase to 3- 5 nM over the first three days (Figs. 2 & 4), and the pattern of increase was similar to previous experiments (Mendez *et al.*, in review). Mn concentrations in the Coastal Water were significantly higher than all other samples, starting at 4 nM and growing to nearly 7 nM (Fig. 2A). The Mn control samples showed no change over time in dissolved Mn concentration ([Mn] = 0.8 nM, Light experiment, < 0.1 nM all UV Waters, 0.7 nM Open Ocean Water, 4 nM Coastal Water).

Fe concentrations decreased to 0.2 – 0.8 nM over time after dust addition for Open Ocean Water, UV Water, Citrate Water, and Coastal Water (Fig. 3). The Oxalate Water sample had a large scatter in the data, and we could not determine any trends. Control samples showed over 50% loss of dissolved Fe, a majority of which occurred in the first week. The Light and Dark Seawater samples showed a moderate increase (2.0 - 2.5 nM) over the first two days, similar to our previous results (Fig. 5) (Mendez *et al.*, in review). All Aerobactin samples had a large increase in Fe concentration (~6 nM) peaking at 1 – 1.5 days after addition (Fig. 3 & 5). This concentration held constant for about 6 days before there was a noticeable decrease in dissolved Fe.

Error bars in Figs. 2-5 represent the precision of the calculated concentration and are 2σ of the standard error. The isotope ratio of each sub-sample was measured on the ICP-MS. The standard error of this ratio was propagated along the concentration calculation to determine the precision. Accuracy was determined by measurements of archived samples from the Mediterranean, (Fe only, (Bonnet and Guieu, 2004)) and from the Pacific, (SAFe, (Johnson *et al.*, 2007)). While over 20 groups have analyzed the SAFe samples for Fe, only two groups have reported Mn concentrations. Table 2 reports a comparison between our measured concentrations and those of Bonnet (Table 2A), and those of the consensus concentration for the SAFe Fe concentrations and the two reported Mn concentrations (Table 2B).

A laboratory internal seawater standard was processed and analyzed along with these sub-samples to monitor consistency and accuracy over time. Over the course of these experiments, Fe concentrations were measured at 0.060 ± 0.049 nM, n=55, which is well within the error of all other previous analyses of this standard, [Fe] 0.085 ± 0.063 nM, n=145. Mn concentrations were measured at 0.65 ± 0.03 nM, n=65 during this dissolution experiment; this is in agreement with all previous measurements that average 0.66 ± 0.06 nM, n=165.

All samples from day 28 of the seawater matrix showed an increase in Fe concentrations compared to their previous sub-sample (day 14) (Fig. 3). Laboratory internal seawater standards and blanks measured along with these sub-samples showed no signs of contamination, indicating the sub-samples were most likely contaminated with Fe during sample collection.

Ligand concentration and binding constants are reported in Table 3. Open ocean and coastal ocean water are within normal ranges for both concentration and Fe binding constants (Buck *et al.*, 2007; Rue and Bruland, 1995). Coastal Ocean and Aerobactin water were the only samples with multiple ligands types. Most samples had insignificant change or a reduction in ligand concentration over time; however, the dust addition sample for the UV irradiated water had a 56% increase in L_1. The binding constant for the aerobactin sample was Log K_1 = 11.5. A specific measurement of the Log K_{FeL} of aerobactin is 12.9 (Harris *et al.*, 1979), which is comparable our measurements. Because the Citrate & Oxalate Water sample was contaminated for Fe, its ligand binding capacity was not determined. A striking result is that the detectable oxalate ligand concentration was 30 nM before dust addition and 13 nM following dust addition. Open Ocean Water also had a decrease in detectable ligand concentration following dust addition; however, the other sample had such a large change in ligand concentration immediately following the dust addition.

4. Discussion

4.1 Manganese Kinetics

The pattern of Mn dissolution is similar to our previous experiments (Mendez *et al.*, in review) which showed fast initial dissolution followed by a leveling off to an equilibrium value. This earlier work had a Mn dissolution rate of 0.9 nmol Mn/(day·mg dust). Our current results give the same value, (0.88 ± 0.13 nmol Mn/(day·mg dust)) when averaged over a two day time period to match the previous coarse resolution. Further, in the current experiments the time resolution is fine enough to model the results and compute the initial dissolution rate as the first derivative at time zero.

We modeled our data with a two step reaction (Eq. 1): comprised of an irreversible dissolution of Mn from the dust and a reversible exchange reaction. The reversible reaction represents the combination of all the reversible reactions that exchange dissolved Mn with dust particles surfaces, dust particles, the bottle wall, other seawater colloids, and/or solid Mn oxides.

$$Mn_{(dust)} \xrightarrow{k_1} Mn_{(dis)} \underset{k_3}{\overset{k_2}{\rightleftarrows}} Mn_{(ad)} \qquad \text{Eq. 1}$$

A differential equation was constructed and analytically solved for each Mn species. These solutions were used to find the best fit for the three independent variables, Mn_{dust}, k_1, and k_2, to the sample data (the model details and the process used to model the data are described in Appendix 1). Using Mn_{dust}, k_1, and k_2, we computed the first time derivative of Mn_{dis} and calculated the initial dissolution rate of Mn from the dust, by dividing by the dust concentration. The calculated dissolution rates are presented in figure 6.

Oxalate-promoted dissolution was significantly faster than the other seawater matrices (11.23 nmol Mn/day/mg dust, Fig. 6A). This enhancement has been previously described at lower pH and higher concentrations of both oxalate and solid Mn oxides than we use here (Jun and Martin, 2003; Stone and Morgan, 1984; Wang and Stone, 2006; Xyla *et al.*, 1992). We also measured a dramatic reduction in dissolved oxalate concentration after dust addition (Table 3), which we presume is due to the fast binding of oxalate to the mineral surfaces of the dust. This observation is similar to earlier work (Stone, 1987) describing the oxalate-promoted dissolution mechanism where the bidentate oxalate ion binds onto a Mn atom on the mineral surface, displacing two of the hydroxyl groups. This complexation weakens the metal-oxygen bonds which can then be broken upon further protonation, followed finally by dislocation of Mn from the mineral surface, or reduction and dislocation (Stumm and Morgan, 1996). Oxalate binding is known to inhibit proton-promoted dissolution by

blocking dissolution sites, reducing the rate by as much as an order of magnitude; however, this is only for the more soluble Mn(II) in acidic conditions (pH 2 – 5.6) (Banerjee and Nesbitt, 1999). At ocean pH, the proton-promoted dissolution is significantly slower (Stumm and Morgan, 1996). Oxalate-dissolution, on the other hand, is not prohibited at higher pH and is dependent on the concentration of surface adsorbed oxalate (Stone and Morgan, 1984). In addition, oxalate can promote the reductive dissolution of Mn (III) and Mn (IV) (Banerjee and Nesbitt, 1999; Xyla *et al.*, 1992), which may overcome any proton-promoted dissolution inhibited by oxalate. Our data from seawater support the conclusion that oxalate promotes Fe dissolution that has been previously shown in laboratory conditions.

A second clear conclusion is that light promotes Mn dissolution in our experiment (Fig. 6B). We see an increase in Mn dissolution rate in the illuminated samples of both the Seawater and Aerobactin Water. There was no significant difference between the Aerobactin Water and Seawater sample, which is consistent with our previous conclusion that Mn dissolution is only dependent on dust concentration. We previously proposed that Mn dissolution is due to both the release of soluble reduced Mn (II) mineral and the reduction of Mn (III) and Mn (IV) species in the mineral structure of the dust particles (Mendez *et al.*, in review). These new data further support this hypothesis, suggesting that Mn is not only dissolved from the dust particles by dissolution of Mn (II) and the reduction of oxidized Mn, but also photo-reduction of Mn (III) and Mn (IV) that increases the overall dissolution rate above the background solubility of the Mn phases (Fig. 6B).

The Coastal Water sample has a Mn dissolution rate about half that of the majority of the other samples (Fig. 6A), likely due to its large initial Mn concentration (Fig. 2B). Mathematically, our model calculates the increase in dissolved Mn and takes the derivative at time zero as part of the initial dissolution rate. In a system with no initial Mn, the irreversible dissolution proceeds alone and dissolved Mn grows in concentration. As the concentration builds, the exchange reaction develops, reducing the rate of increase until the

system reaches steady state. This model approach works well with low initial Mn concentrations. If the initial Mn concentration is large, the exchange reaction will occur at time zero, competing with the irreversible dissolution. In this case our dissolution rate is more representative of the total rate of change in dissolved Mn and not of Mn dissolution from the dust. Chemically, this means that when dust is added to a system in equilibrium, there is a fast irreversible dissolution releasing Mn and comparably fast exchange reactions re-establishing equilibrium with the new surface area of the dust.

The Mn dissolution rates of the other seawater samples were equivalent, with an average rate of 3.82 ± 0.83 nmol Mn/day/mg dust (excludes the Oxalate Water, Coastal Water, and the two dark samples). While there were slight variations in these rates, they can be attributed to slight differences in initial Mn concentrations, scatter in the data, and slight chemical differences that cannot be distinguished here.

4.2 Manganese Thermodynamics

The dissolution reactions in both the seawater matrix and light experiment appeared to reach equilibrium after one week. The aerobactin samples in the light experiment, on the other hand, had a significant reduction in Mn concentration after day 6 (Fig. 4). Table 4 presents the initial and final Mn concentrations, the change in Mn as a percentage of the total dust Mn for both the data and the model, and the equilibrium constants calculated by the model (defined as $K_{eq} = \frac{Mn_{ads}}{Mn_{dis}}$).

Initial examination of the data from the first experiment reveals that: 1) the K_{eq} values are very similar to each other and 2) with the exception of the Coastal Water, the percentages of Mn dissolution are nearly equivalent. The equilibrium constants are a measure of manganese stability in the dissolved phase compared to the adsorbed phase. Since all the sample K_{eq} values are clustered together (mean = 0.59 ± 0.14) despite their different ligands and below one, we conclude that total Mn dissolution is largely a function of Mn seawater

solubility and not organic complexation, and that Mn prefers the dissolved phase over the adsorbed phase. Furthermore, because the percentages of the total dust Mn dissolution are similar (excluding the Coastal Water sample), we believe that total dissolution is driven more by available or accessible Mn than the presence of organic ligands. As an example, oxalate drove dissolution at a faster rate than the other samples, but its total dissolution was not enhanced. While equilibrium constants are important in systems where steady state is reached, it might not be as important in the surface ocean where transport processes and a rich assortment of organics could alter the equilibrium. Therefore, the redox processes and kinetic enhancement involving ligands are important to Mn cycling.

Two samples had K_{eq} values that were significantly different: the Open Ocean sample and the Citrate Water sample. The Open Ocean sample retained more dissolved Mn than any other sample, thus decreasing the equilibrium constant. This may have resulted from the assemblage of natural organic material present in the water. These natural organics can provide a continual oxidant supply which drives photo-reduction reactions maintaining the soluble Mn(II) concentration (Sunda *et al.*, 1983). The Mn concentration in the Citrate Water sample was consistently below all other samples (Fig. 2A). Citrate may act to hinder Mn release rather than as a reductive promoter of dissolution. Although citrate is known to promote Mn(III) dissolution at high concentration (50 mM, (Klewicki and Morgan, 1999)), our relatively small concentration of citrate (57 nM) may not be enough to promote Mn(III) dissolution to an appreciable amount and may act to reduce total dissolution by occupying surface sites. In addition, within an oxygenated system Mn(II)-citrate complexes can be oxidized to Mn(III) ten times faster than a Mn(II) bicarbonate solution at pH 8 (Klewicki and Morgan, 1998; von Langen *et al.*, 1997). Therefore, total dissolved Mn concentrations may be suppressed due to reoxidation within the Citrate Water sample.

The percentage of the dust Mn that dissolved into the Coastal Water is smaller than that of the other samples. While this may first appear as though less total Mn dissolved from

the dust, we attribute this lower percentage to the relatively high initial Mn concentration adsorbing onto the dust particles and the wall. Table 4 shows the calculated equilibrium constants (K_{eq}) for our two step model. The Coastal Water equilibrium constant is within error of the mean of the other seawater matrix samples. Therefore, Mn has the same preference for the dissolved state within the Coastal Water as the other samples, and it will have the same total Mn dissolution from the dust. As Mn was released from the dust, a portion was adsorbed onto a surface. Because there was a large initial Mn concentration, a large quantity of Mn must adsorb onto a solid surface, resulting in a smaller percentage staying in solution.

Seawater in the light experiment behaved similarly to our seawater matrix experiment, although the Mn concentrations were smaller overall, which resulted in smaller percentages of the total dust Mn and larger K_{eq} values. The similarity in K_{eq} between the Seawater Light and Dark samples indicates that while photoreduction plays a role in the initial release of Mn, there is no process within these samples to keep Mn in solution after the first two days. Aerobactin Water Dark and Light samples were not similar to each other; instead, the Mn concentration in the Dark sample decreased to nearly half that of the Light sample. It is plausible that the lack of light resulted in slow oxidation of Mn into one of its insoluble oxidized forms; however, the Seawater does not behave in this manner. This difference leads us to the conclusion that aerobactin is preventing Mn from interacting with reductive organics present in the seawater, perhaps by temporally stabilizing Mn(III), leading to its greater adsorption to the wall or particles over time. Mn(III) is a high spin trivalent ion with ionic radii equivalent to Fe(III) (Stone, 1987) and may be able to weakly substitute into the siderophore complex similar to chromium (Raymond and Carrano, 1979). Without light to continually reduce the oxidized species back to Mn(II), perhaps this weak interaction leads to overall loss of Mn from solution.

The seawater matrix and the light experiment differ in their final Mn concentrations, resulting in different K_{eq} values. Both experiments used U.S. dust of approximately 1 mg

dust / L, but the seawater matrix experiment yielded a larger final Mn concentration. Our previous experiment (Mendez *et al.*, in review), in which we compared dust concentrations, was more similar to the light experiment and showed smaller final Mn concentrations for the equivalent dust concentration. The most significant difference between these experiments is the time of year during which they were performed. Both the light experiment and the dust concentration experiment were conducted in August, while the seawater matrix experiment was conducted in January and February. It is possible that the greater UV exposure during the winter months lead to the larger Mn concentrations, resulting from an increased rate of photoreduction of re-oxidized Mn. While this seems like a plausible explanation for the difference between the dust concentration and the seawater matrix experiments, it does not explain the similarity between the Seawater Light and Dark samples in the light experiment. If the decrease in UV light during the summer reduced the final Mn concentrations in the dust concentration experiment, then removing UV light from the system should have further decreased this effect, which was not observed.

4.3 Iron Dissolution

The seawater matrix experiment demonstrates the dramatic effect of siderophores on the dissolution and retention of dissolved Fe (Fig. 3 & 5). Aerobactin Water had a large increase in Fe concentration, while the Open Ocean, Coastal, and Citrate Water had small increases in Fe. Fe concentrations declined in UV Water. Although oxalate promoted Mn dissolution, changes in dissolved Fe were not observed given the scatter in this experiment's data.

The ultimate reduction of Fe concentration below initial values in all samples except the aerobactin was initially contradictory to our previous experiment. However, as we will show, the differences in experimental set-up and materials can account for the dramatic differences. The small increases in Fe concentration within the first 12 hours of the experiment are also important to understand. Although the increases are not significant in the long term results of our bottles studies, we will explain that within the surface ocean,

this initial Fe release may play an important role for the biological community. The Aerobactin Water sample has a dramatic increase in Fe concentration, which takes several days to develop. We will lastly discuss the importance of this result to dust deposition as a source of Fe to the surface ocean, and then continue with the discussion of siderophore-promoted dissolution mechanism.

Open Ocean Water (same source as (Mendez *et al.*, in review)) showed Fe release to a maximum concentration of 1.0 -1.25 nM within the first 12 hours, followed by a decrease to 0.25 nM. Mendez *et al.* (in review), on the other hand, found Fe concentrations between 1.5 – 2.0 nM. This difference is most likely due to the change in the natural ligand complexing capacity during 11 months of storage in our lab. Ligand strength measurements made at the time of water collection were:

$[L_1] = 1.67 \pm 0.03$ nM ($\log K_1 = 12$)

$[L_2] = 3.2 \pm 0.1$ nM ($\log K_2 = 11$) (Buck, K.N., unpublished data)

The ligand assemblage in the Open Ocean Water sample at the beginning of the experiment had a larger L_1 concentration than the at sea measurements, but the binding constant was lower and there was no L_2 ligand (Table 3). To quantitatively understand why the results in this experiment were so different, compared to Mendez *et al.*, (in review), we define the iron binding capacity as the maximum quantity of Fe which can be held in solution. To calculate the total Fe binding capacity of this sample, we assume that ligands bind Fe according to the following reaction:

$$Fe + L \underset{\leftarrow}{\overset{K}{\rightarrow}} FeL, \qquad \text{Eq. 2}$$

where the Fe binding capacity is [FeL], [Fe] is the inorganic Fe concentration in seawater (0.1 nM) and L is the unbound ligand. The Fe speciation measurement represents both the

bound and unbound ligand (FeL + L); therefore, to calculate just [FeL] we write the equations:

$$K = \frac{[FeL]}{[Fe][L]} \quad \text{Eq. 3}$$

$$L_T = [FeL] + [L] \quad \text{Eq. 4}$$

where K is the Log of the binding constant (Table 3) and L_T is the Fe speciation measurement. Combining equations 3 and 4, we get the equation for Fe binding capacity:

$$[FeL] = \frac{L_T}{\left(1 + \frac{1}{10^K Fe}\right)} \quad \text{Eq. 5}$$

The FeL binding capacities for the natural seawater matrices are shown in Table 5. Looking at these natural waters we see that the pre-dust open ocean seawater from Mendez *et al.*, (in review) is dramatically under-saturated with respect to the concentration of ligands, yielding a FeL_T / [Fe] ratio of over 18 (Table 5). Therefore, once dust was added, the dust-bound Fe was quickly released, raising the concentration to 1.5 nM. In contrast, the aged and slightly contaminated open ocean seawater had about half the Fe binding capacity and an Fe concentration of over 1 nM. This seawater was not under-saturated in Fe and so there was no dramatic increase in Fe concentration upon dust addition as there was in Mendez *et al.* (in review). In fact, the decrease in Fe is most likely due to the adsorption of initial Fe and ligands onto the container wall or dust particles themselves. The Coastal Water sample yields a very similar result. Coastal Water is not under-saturated in Fe with respect to the Fe binding ligands, and therefore, over time, some of the initial Fe is adsorbed onto the wall of the bottle, reducing the Fe concentration.

The Fe concentration in both the Open Ocean and Coastal Water, as well as the Citrate Water, increased during the first 24 hours; however, the rate of Fe dissolution was

impossible to measure. In each case, this initial increase in Fe concentration was followed by the large decreases described above. These initial increases may be attributed to the dissolution of Fe solubilized by ligands found in the waters (Voelker *et al.*, 1997) or the release of soluble Fe(II) bound to the dust (Pehkonen *et al.*, 1993). Despite the fact that the dust addition did not ultimately increase the Fe concentration, our data show that there is soluble Fe on these dust particles. Leaching experiments by (Buck *et al.*, 2006) showed that there was significant quantities of soluble Fe which could be released from aerosol particles given the right conditions. In these experiments Buck *et al.*, (2006) used ultra-pure water (18 MΩ cm) to remove Fe from the aerosol particles. Although Fe is more soluble in pure water, compared to seawater, they reason that surface microlayer conditions may solubilize Fe to a greater degree. Therefore, pure water is a good substitute for the surface microlayer. However, our data show that unaltered seawater can leach more Fe from the dust particles than is soluble over time. This initial Fe may quickly overwhelm the surrounding ligand field and thus begin the precipitate. However, in the complete system of the surface ocean, the reservoir of available ligands would be less likely to become saturated and that initial Fe would not precipitate. Within the surface ocean this initial Fe release is part of the dust source linked to the Fe cycle and should not be ignored.

The Fe concentration within the Aerobactin Water increased to 5.92 ± 0.13 nM 50 hours after dust addition (Fig. 3). Using the initial linear portion of the curve, we calculate a rate of dissolution of 2.25 ± 0.18 nM Fe/day/mg dust. This is the first experimental evidence of a siderophore facilitating Fe dissolution from a natural dust in natural seawater. Siderophores produced by marine bacteria (*Alteromonas haloplanktis*) have been shown to promote hematite as well as amorphous Fe hydroxide dissolution under acidic conditions and micromolar siderophore concentrations (Yoshida, 2002). In addition, dissolution rates for goethite and poorly crystalline Fe hydroxides at pH 8 were below detection limit (<0.5 μM Fe). Siderophores (DFOB and aerobactin) have been shown to dissolve goethite and lepidocrocite at pH 4 in millimolar siderophore concentrations (Hersman *et al.*, 1995), and

pH 5-6 with 45 - 80 μM siderophore concentration (Borer *et al.*, 2005; Cheah *et al.*, 2003). In each of these studies Fe oxide dissolution is proportional to siderophore concentration, although an extrapolation towards nanomolar concentrations of siderophore was not dissimilar from controls. Our experiments prove that not only can siderophores promote Fe oxide dissolution under optimal laboratory conditions, but that they promote Fe dissolution from natural mineral aerosols in ocean water. This means that siderophore promoted dissolution may be one mechanism for Fe to be released from dust upon dry deposition to the surface ocean. Although scenarios involving micro-environment changes can be useful in facilitating additional Fe dissolution, given the concentrations of Fe binding ligands found in the surface ocean (Buck *et al.*, 2007) they may not be necessary.

4.4 Effects of Light Exposure on Iron Release

There is already substantial knowledge of the mechanism for Fe oxide dissolution in the literature, however the interactions between dust, siderophores, and a natural seawater matrix has not been investigated. Here we discuss the data from our experiment and compare it to several other studies to further understand siderophore-promoted dissolution. We designed the light exposure experiment to elucidate certain mechanistic components of siderophore-promoted dissolution of Fe oxides.

If aerobactin can dissolve Fe oxide minerals through a photolytic mechanism as described in the literature, a dissolution experiment comparing light and dark samples should have two results. The Aerobactin Light sample should proceed faster than a Dark sample and the relative increase in dissolution between light and dark samples should be greater for the Aerobactin sample than for the Seawater sample. Unaltered seawater may have light-promoted Fe dissolution from thermal or photo-reductive pathways of surface Fe(III)-hydroxy groups, excitation of the $O^{2-} \rightarrow Fe^{3+}$ charge transfer band with reduction of the surface Fe(III) (Borer *et al.*, 2005), or photolytic reduction involving natural ligands (Waite and Morel, 1984). If the relative dissolution rate increase due to light exposure is equivalent

between the Aerobactin and Seawater samples, the dissolution increase may be attributed to these processes rather than siderophore photolytic dissolution.

Our light experiment showed that total Fe dissolution was affected by light exposure, and aerobactin reactivity did appear to be enhanced by light more than unaltered seawater. The light experiment results were analyzed using a similar reaction for Fe as was applied to Mn,

$$Fe_{(dust)} \xrightarrow{k_1} Fe_{(dis)} \underset{k_3}{\overset{k_2}{\rightleftarrows}} Fe_{(ad)} \quad , \qquad \text{Eq. 6}$$

to model the kinetics of Fe release and retention in solution. Just as with the Mn system, we constructed three differential equations for each of the species, and solved them analytically. The time derivative of the Fe_{dis} equation at time zero was then used to compute the dissolution rate. For the Fe system here we first used the controls to constrain the ratio of the adsorption and desorption reaction constants and thus solve for one of the independent variables. Using these constraints we then solved the dissolution reactions by fitting the other two independent variables to the data (Appendix 1 has a complete description of the model). Figure 7 shows the rate of initial dissolution for each of the four dissolution reactions.

Fe dissolution in both light exposed samples was faster than their corresponding darks samples. However, the increase in Fe dissolution for the Aerobactin Light sample was 2.1 ± 0.3 times that of the dark sample, where as the Seawater Light sample only increased by 1.1 ± 0.4 times. Because the relative rate increase was larger in the Aerobactin Light sample, we must consider that beyond thermal dissolution there was one or more photolytic dissolution processes at work in the Aerobactin sample or both the Seawater and Aerobactin samples. We can compare our results to those of Borer *et al.*, (2005) to determine the likelihood of light promoted aerobactin dissolution, and to Cheah *et al.*, (2003) to understand the relative rate increase in the aerobactin samples.

(Borer et al., 2005) examined the aerobactin-promoted Fe oxide dissolution mechanism and concluded that aerobactin is not light sensitive. They determined that aerobactin dissolution begins with adsorption of one of the hydroxamate binding groups and follows the mineral dissolution mechanism outlined by Zinder *et al.*, (1986). Borer *et al.*, (2005) reason that because the rate of ligand controlled Fe oxide dissolution is linearly proportional to the ligand binding constant (Duckworth and Martin, 2001) and only one binding group will adsorb onto the mineral surface at a time (Borer et al., 2005; Cocozza et al., 2002), the rates of dissolution may be used as a proxy for ligand-surface binding constants. Examination of the aerobactin Fe oxide dissolution rate can lead to the aerobactin-surface binding constant, which will depend on which one of the binding groups adsorbs to the Fe oxide surface, one of the hydroxamate groups or the α-hydroxycarboxylate. The other binding groups are sterically restricted from involvement and will bond once the Fe is removed from the lattice structure. Fe-hydroxamate binding constants are stronger than similar Fe-α-hydroxycarboxylate, [the Fe stability constant for acetohydroxamic acid (a simple hydroxamic acid) is 8 orders of magnitude larger than for glycolic acid (a simple α-hydroxycarboxylic acid) (Smith *et al.*, 2004)]. In Borer *et al.*, (2005), both aerobactin and DFOB (a tri-hydroxamate siderophore) have a similar dark lepidocrocite dissolution rate, and both have a 4.1 fold increase in dissolution rate upon light exposure. Because DFOB has no light reactivity (Barbeau, 2006), they conclude that the increase in Fe dissolution is caused by the photo-reactivity of the Fe oxide surface and not by a photo-induced reaction of the adsorbed siderophore. This indicates that aerobactin and DFOB have the same binding group, hydroxamate, and that aerobactin does not photoreactively dissolve Fe oxides. There is a 40% difference between the lepidocrocite dissolution rate of DFOB and aerobactin, but because both the light and dark dissolution rates have the 40% difference, it is believed that this is the result of a non-photoreactive property of the siderophores.

The light and dark dissolution rates calculated by Borer *et al.*, (2005) as well as the dissolution rates calculated for both our Light and Dark - Aerobactin and Seawater samples

are presented in Table 6. The two studies used different units to report their dissolution rates; therefore, to properly compare, we converted the units of Borer *et al.*, (2005) using the conversion, 170 m^2/g (P. Borer, per. comm.). In addition, dissolution experiments in Borer *et al.*, (2005) were conducted in pure water and had no background ligand field. Their control had no Fe dissolution. Therefore, all dissolution in their aerobactin experiment is due to the siderophore. Our background seawater had significant Fe dissolution. Therefore, the dissolution rate in our aerobactin sample was a composite of both aerobactin and the natural seawater ligands. To properly compare our results we need to take the absolute difference of our Aerobactin and Seawater samples to remove the effects of the seawater's background ligand field. Finally, since ligand-controlled dissolution is a function of the surface excess of adsorbed ligand (Furrer and Stumm, 1986), we divided our absolute difference rates and the converted rates of Borer *et al.*, (2005) by the total aerobactin concentration.

The calculated dissolution rates from both this study and Borer *et al.*, (2005) are similar despite significant differences in experimental set-up. Borer *et al.*, (2005) used synthesized colloidal Fe oxide (lepidocrocite) in an acidic buffered solution with micromolar concentrations of both siderophore and Fe. We used a natural dust in ocean water at pH 8 with nanomolar Fe and siderophore concentrations. This is an important finding because the similarity in our dissolution rates indicates that initial aerobactin-promoted Fe oxide dissolution is controlled by ligand adsorption to the mineral surface and is not appreciably influenced by proton–promoted dissolution or the dissolution effects of other natural organic ligands.

If aerobactin-promoted Fe oxide dissolution is not specifically photoreactive, and the light enhancement in dissolution was from mineral surface reactions, as was concluded by Borer *et al.*, (2005), then the same mineral surface reactions which occurred in the Aerobactin Light sample should occur in the Seawater Light sample. But as described above, the relative rate increase in the Aerobactin Light sample was larger that the relative rate increase

seen in the Seawater Light sample. Thus, if these surface reactions occurred in the Seawater Light sample they had a diminished effect on Fe dissolution. One explanation of the observation to not use a photoreactive mechanism was outlined by Cheah *et al.*, (2003).

(Cheah et al., 2003) observed that slight additions of a siderophore (*e.g.* DFOB) in combination with another organic ligand (*e.g.* oxalate) will lower the ΔG of the Fe oxide dissolution. They proposed that the undersaturation with respect to the mineral caused by the siderophore's large binding constant and high specificity for Fe will allow other organic ligands to act as a dissolution catalyst. After the ligand removed an Fe atom from the mineral surface, the siderophore would take the Fe away from the smaller ligand and act as a reservoir. Thus, it has been proposed that one function of siderophore production in Fe limited environments is to facilitate other dissolution mechanisms by lowering the solution saturation state (binding free Fe ions and altering the overall thermodynamic equilibrium) (Cocozza *et al.*, 2002; Holmen and Casey, 1996; Kraemer, 2004). However, this was an observation in an acidic environment where, due to protonation, oxalate is more effective at binding to and detaching Fe from Fe oxide surfaces (Cheah *et al.*, 2003). In the oceanic environment (pH ~8), protonation of the oxalate ligand and subsequent detachment of the Fe-oxalate complex from the Fe oxide surface is less likely (Zinder *et al.*, 1986) and, thus, not a likely scenario for oxalate. However, other more effective ligand may be present in natural seawater. The observation by Cheah *et al.*, (2003) may explain the relative rate increase seen in our Aerobactin Light sample. In our experiment, the natural assemblage of organics had a 12% increase of Fe dissolution upon exposure to the light. When aerobactin was added to the water, we saw a 107% increase in Fe dissolution. This effect may be due to the siderophore binding Fe, which otherwise would have been re-oxidized in the natural water system. This suggests that by trapping dissolved Fe as it is removed from the mineral, preventing any re-oxidation and precipitation from solution aerobactin, promotes photodissolution without being photoreactive itself as concluded by Borer *et al.*, (2005).

4.5 Iron Thermodynamics

The long-term decrease in Fe concentration in the aerobactin sample was most likely due to multiple adsorption reactions. From the Aerobactin Water in the seawater matrix experiment we saw a 50% reduction in total dissolved Fe after 28 days. Most of the reduction occurred within the second week of the experiment. We hypothesized that this reduction was due to the destruction of the aerobactin ligand through decomposition or adsorption to a surface (the wall or dust particle). Examination of the aerobactin samples in the light experiment showed similar dissolved Fe loss over time with significant loss between days 6 and 9. There was only a slight difference between the lit and dark aerobactin samples, leading us to conclude that any photodecomposition of the siderophore is minor. (Küpper *et al.*, 2006) found that the aerobactin-Fe complex is photoreactive but stable. They determined that the photo-product has a Fe binding constant which is slightly stronger that the parent aerobactin ligand (Log K = 27.6 ± 0.1, 28.6 ± 0.5 for aerobactin and the aerobactin photo-product respectively).

Direct loss of the Fe-aerobactin complex may occur through adsorption to the bottle wall, or the surface of the dust particles. Adsorption to bottle wall is reduced by "conditioning" sample bottles with sample. Adsorption of the aerobactin-Fe complex to dust or other large particles (filterable at 0.2 mm) is the other explanation for Fe loss over time. The non-Fe binding carboxyl groups can allow aerobactin to re-adsorb to mineral surfaces after Fe complexation (P. Borer, pers. comm.). During Fe dissolution experiments this results in a nonlinearity due to outer sphere adsorption of aerobactin-Fe complexes to the Fe oxide mineral.

5. Conclusions

Dry deposition of dust is a substantial source of both Fe and Mn to the surface ocean (Duce and Tindale, 1991; Guieu *et al.*, 1994). However, the pattern of Fe and Mn dissolution is significantly different. In our experiments, Mn dissolution occurred over the course of several days until the available Mn is depleted and reached a steady state concentration. The rate of Mn dissolution was enhanced by the bidentate ligand oxalate,

but the total quantity of Mn dissolution was not affected. Light also enhanced the Mn dissolution rate, and comparing the final Mn concentrations of both experiments we see that the level of atmospheric radiation lead to differences in the final steady state Mn concentration.

Fe dissolution is highly dependent on the background seawater ligands. Depletion of these ligands lead to the precipitation of Fe oxide from solution, while additions of siderophores enhanced both the total Fe capacity of the seawater and the rate of Fe dissolution from dust. The mechanism of aerobactin-promoted dissolution can be described in terms of bidentate ligand dissolution without a specific photolytic step. Photo-induced dissolution was promoted in both our Seawater and Aerobactin samples. While the relative rate increase was more significant in the Aerobactin sample, this can be explained by siderophore complexation of Fe(III) removed from the mineral surfaces by weaker seawater ligands. Therefore, the reduction of Fe(III) at the mineral surface occurring in amended seawater was transferred to the bulk solution, while Fe(III) in the non-amended seawater reoxidize and remained on the mineral surface. While the Fe-aerobactin complex is photoreactive, there does not appear to be an aerobactin photoreactive dissolution mechanism.

TABLES

	U.S. Dust	Upper Crust, Wedepohl, 1995
Manganese, (Mn)	750 ppm	527 ppm
Iron, (Fe)	3.81 %	3.1 %
Aluminum, (Al)	7.58 %	7.7 %

Table 1: Elemental analysis of the dust samples used in the dissolution experiment. Measurements are total metal mass concentrations.

(A) Mediterranean	[Fe], nM Our Measurement	Bonnet
Sample 1	1.41	1.37
Sample 2	0.87	0.83
Sample 3	1.31	0.89

(B) Pacific	[Fe], nM Our Measurement	Consensus	[Mn], nM Our Measurement	Middag and de Baar, NIOZ	Wu, University of Alaska, Anchorage
SAFe, S1	0.084 ± 0.017	0.097 ± 0.043	0.72 ± 0.06	0.73 ± 0.01	0.90 ± 0.02
SAFe, D2	0.93 ± 0.10	0.91 ± 0.17	0.32 ± 0.03	0.295 ± 0.007	0.45 ± 0.11

Table 2: Comparison in dissolved Fe measurements for three Mediterranean seawater samples provided by Cecile Guieu (Laboratoire d'Océanographie de Villefranche) (A), and dissolved Fe and Mn measurement for the two Pacific SAFe standards for (B). We report our average measurements of Fe and Mn for the SAFe samples along with the consensus values for Fe, and the two other reported measurements of Mn.

	[Fe], (nM)	[L_1], (nM)	K_1	[L_2], (nM)	K_2
UV Water					
Pre-dust	0.72	2.5±0.1	11.3	NA	NA
Control Day 28	0.18	2.4±0.3	11.59±0.05	NA	NA
Post-Dust 30 min	0.79	NA	NA	2.3±0.5	10.89±0.04
Post - Dust 28 days	1.41	NA	NA	3.6±0.4	10.35±0.1
Oxalate Water					
Pre-dust	0.65	NA	NA	30±1	10.11±0.04
Control Day 28	0.85	NA	NA	16.7±1.5	10.76±0.01
Post-Dust 30 min	0.82	NA	NA	12.93±0.1	10.5
Post - Dust 28 days	0.85	NA	NA	5.15±0.1	10.82±0.03
Aerobactin Water					
Pre-dust	3.13	26.0±1.5	11.53±0.1	13±1.0	10±0.2
Control Day 28	2.86	7.8±1	11.4±0.2	NA	NA
Post-Dust 30 min	3.1	30.8±0.1	11.8	18.4±0.8	10
Post - Dust 28 days	2.31	NA	NA	20.5±1	10.6±0.03
Citrate Water					
Pre-dust	0.68	4.05±0.1	11	NA	NA
Control Day 28	0.19	NA	NA	10.1±0.7	10.48±0.05
Post-Dust 30 min	0.84	NA	NA	NA	NA
Post - Dust 28 days	0.67	NA	NA	17±1	10.66±0.01
Open Ocean Water					
Pre-dust	1.04	7.1±1	11.54±0.01	NA	NA
Control Day 28	0.16	3.5±0.8	10.95±0.2	NA	NA
Post-Dust 30 min	0.82	1.9±0.2	11.75±0.05	NA	NA
Post - Dust 28 days	1.2	1.6±0.1	12.18±0.03	NA	NA
Coastal Water					
Pre-dust	2.24	5.4±0.2	11.65±0.06	2.5±0.4	10.85±0.02
Control Day 28	1.69	3.1±0.1	12.47±0.08	2.2±0.1	10.88±0.04
Post-Dust 30 min	2.68	6.5±0.1	11.9	NA	NA
Post - Dust 28 days	1.51	6.4±0.4	11.2±0.1	NA	NA

Table 3: Fe speciation data of the six water samples from the seawater matrix experiment. The Oxalate and Citrate water was not measured due to the large Fe contamination. The distinction between L_1 and L_2 is made by the strength of the binding constant.

Sample	Initial [Mn], nM	Final [Mn], nM	Data: Δ [Mn], % of total Mn_{dust}	Model: Δ [Mn], % of total Mn_{dust}	K_{eq}
Seawater Matrix Experiment					
Open Ocean	0.68	4.60	24.7%	24.2%	0.37 ± 0.06
Coastal Water	4.18	5.64	9.2%	12.1%	0.60 ± 0.08
UV Water	0.00	3.54	22.6%	22.7%	0.54 ± 0.06
Oxalate Water	0.01	3.26	20.5%	22.3%	0.56 ± 0.11
Citrate Water	0.02	3.03	18.9%	19.4%	0.79 ± 0.04
Aerobactin Water	0.34	3.41	19.3%	20.2%	0.68 ± 0.09
Light Experiment					
Aerobactin-Dark	0.75	1.64 (2.53)	6.0% (12.0%)	8.8%	1.96 ± 0.27
Aerobactin-Light	0.75	2.57 (2.71)	12.3% (13.2%)	13.1%	1.25 ± 0.15
Seawater-Dark	0.75	3.37	17.1%	15.8%	0.95 ± 0.03
Seawater-Light	0.75	3.27	16.5%	15.3%	0.99 ± 0.12

Table 4: Final Mn dissolution values for all seven samples. Initial and Final [Mn] are an average of the pre-dust [Mn] (n=3) and the [Mn] from day 28 (Seawater Matrix Experiment) or day 18 (Light Experiment) (n=2). The Δ[Mn] values are the final changes in [Mn] as a percentage of the total dust Mn for both the actual data and the two-step model. Keq is the equilibrium constant defined as the adsorbed Mn over the dissolved Mn. Data in parenthesis are from day 3; [Mn] fell after this point in the Aerobactin samples. Therefore, day 3 represents a maximum in the dissolved Mn concentration and thus should be used to calculate the amount of Mn released from the dust particles.

Sample		FeL_1, nM	FeL_2, nM	FeL_T, nM	[Fe], nM	FeL_T/[Fe]
Mendez *et al.*	Pre-Dust	1.65 ± 0.03	2.91 ± 0.09	4.56 ± 0.1	0.25 ± 0.13	18.25 ± 9.5
	35th day				1.51 ± 0.39	3.04 ± 0.78
Coastal Ocean	Pre-Dust	5.28 ± 0.2	2.19 ± 0.34	7.47 ± 0.39	2.29 ± 0.07	3.26 ± 0.20
	28th day	6.02 ± 0.2	0	6.02 ± 0.84	1.38 ± 0.19	4.36 ± 0.66
Open Ocean	Pre-Dust	6.9 ± 0.001	0	6.9 ± 0.001	1.03 ± 0.02	6.7 ± 0.95
	28th day	1.59 ± 0.07	0	1.59 ± 0.07	0.23 ± 0.02	6.91 ± 0.74

Table 5: Fe binding capacity for the natural seawater samples, as calculated by equation 5. The total Fe binding capacity, FeL_T, is the sum of FeL_1 and FeL_2, and represents the total potential dissolved Fe for the sample. The ratio FeL_T/Fe is a measure of the under-saturation of Fe compared to the total Fe binding capacity. The water used in our previous study had an initial under-saturation of 18 times the initial [Fe]. This under-saturation lead to the Fe dissolution, resulting in much smaller under-saturation after 35 days, calculated by using the initial FeL_T and the final [Fe]. The Open Ocean and Coastal Water samples began with a small under-saturation, and over the coarse of the experiment they both became more under-saturated.

This Study	$\frac{nmol\ Fe}{min \cdot m^2}$	$\frac{nmol\ Fe}{day \cdot g\ Dust}$	$\frac{mol\ Fe}{min \cdot g_{particle} \cdot mol\ aerobactin}$
Aerobactin – Dark		3.31 ± 0.12	
Aerobactin – Light		6.85 ± 1.0	
Seawater – Dark		1.79 ± 0.34	
Seawater – Light		2.00 ± 0.57	
Difference – Dark		1.52 ± 0.21	43 ± 12
Difference – Light		4.84 ± 0.66	137 ± 37
Borer *et al.* 2005			
Aerobactin – Dark	2.8	685	21.9
Aerobactin – Light	11.5	2815	90.1

Table 6: We present the initial Fe dissolution rates from our current study. Listed are the Aerobactin Water samples, the Seawater samples, as well as the "Difference" between Aerobactin and Seawater sample. Also listed are the aerobactin dissolution rates from Borer *et al.*, (2005), in both their original units (nmol Fe min^{-1} m^{-2}) and the units used in this text (170 m^2/g - conversion factor from P. Borer per. comm.) to more effectively compare to our data. Because dissolution rate is a function of adsorbed ligand concentration, we list the dissolution rates divided by the aerobactin concentration used in each experiment: 51 nM in our study and 45 μM for Borer *et al.*, (2005).

FIGURES

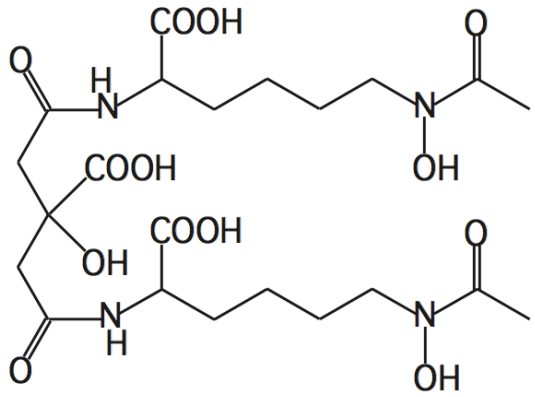

Figure 1: The Fe binding siderophore aerobactin. Aerobactin is a di-hydroxamate α-hydroxy-carboxylate siderophore. Bonding to the Fe atom is done by the end hydroxamate groups and the center citrate moiety (Harris *et al.*, 1979).

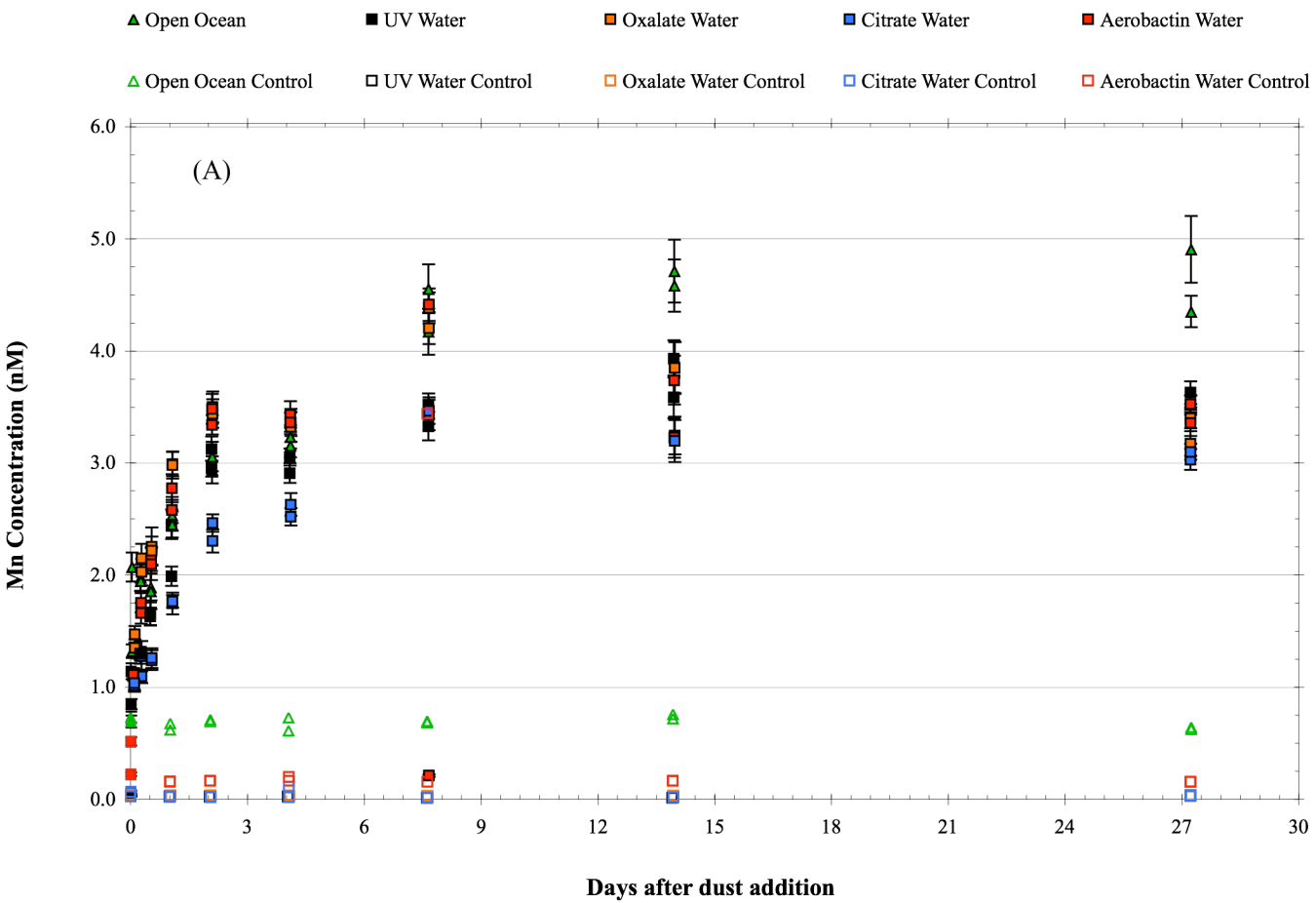

Figure 2: Mn concentrations over time for the seawater matrix samples: Open Ocean Water and all amended water samples A, and Coastal Water B. All samples are presented with their control samples. Error bars are two σ of the standard error of the mean computed from the isotope dilution equation. Error bars were removed from some control samples for clarity, and are smaller that the symbols.

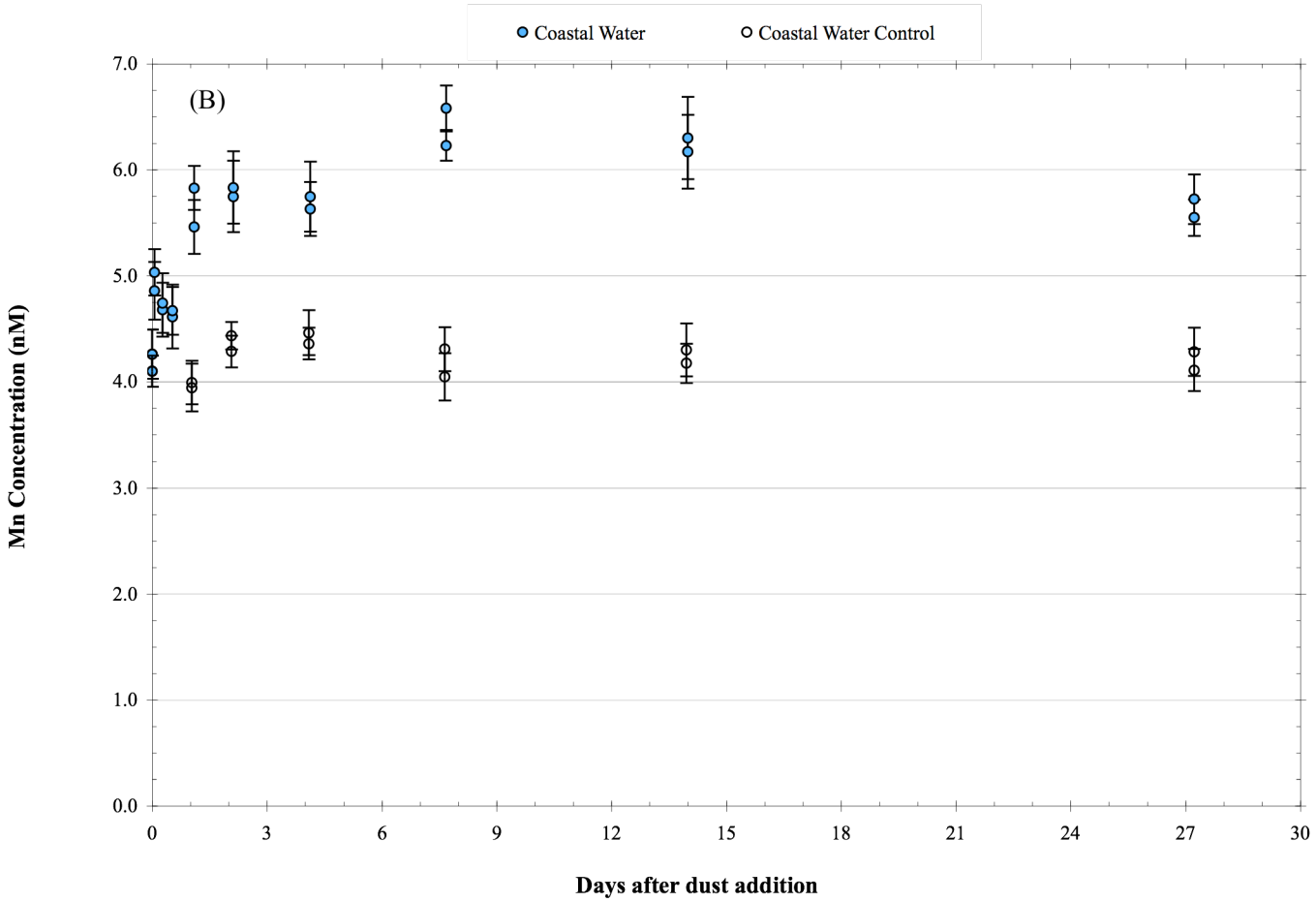

Figure 2: Mn concentrations over time for the seawater matrix samples: Open Ocean Water and all amended water samples A, and Coastal Water B. All samples are presented with their control samples. Error bars are two σ of the standard error of the mean computed from the isotope dilution equation. Error bars were removed from some control samples for clarity, and are smaller that the symbols.

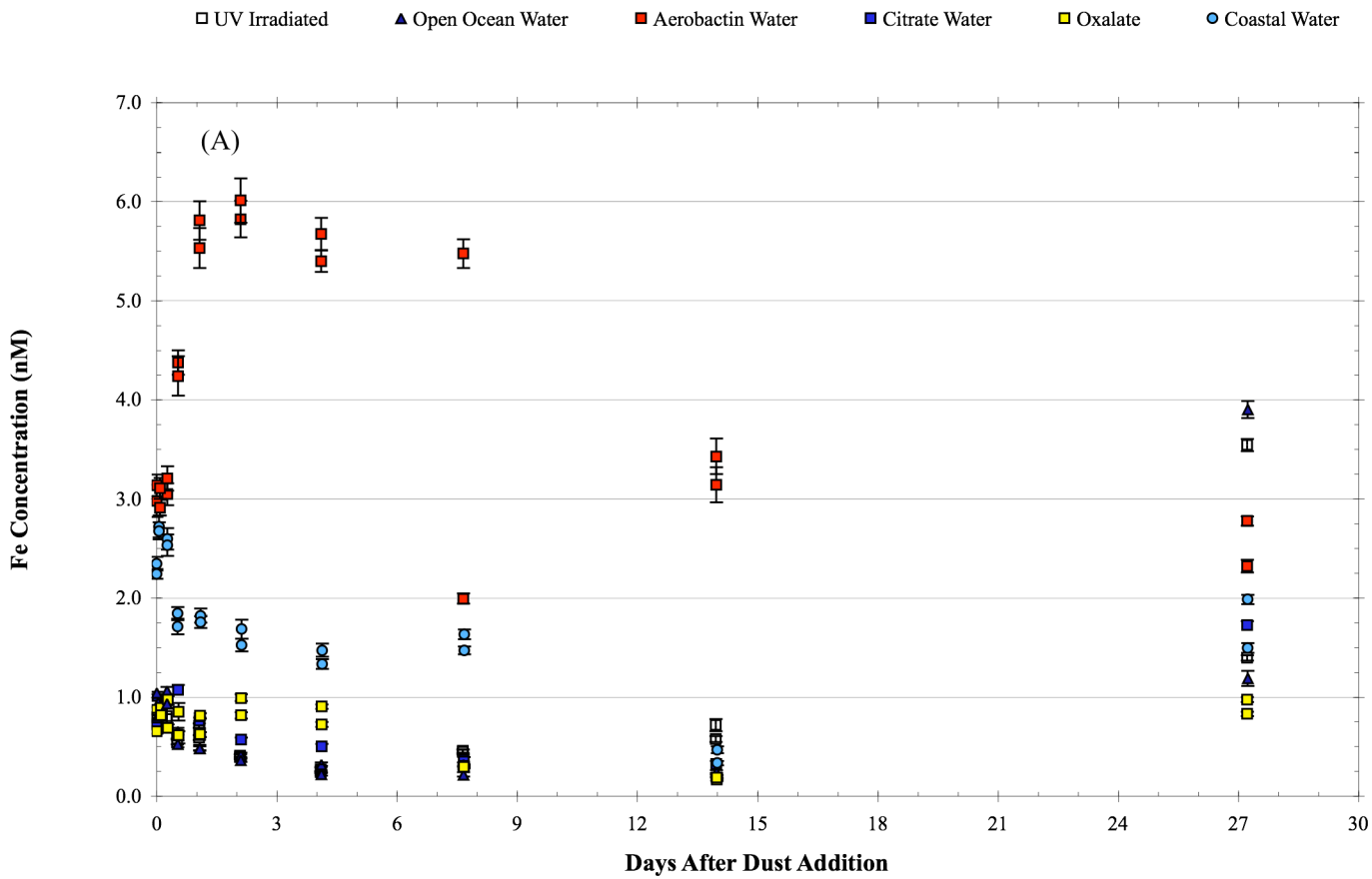

Figure 3: Fe concentrations over time in the seawater matrix experiment. Seawater samples (A) all have reductions in Fe concentration after 28 days, except the Aerobactin Water. Control samples (B) have a slow reduction in Fe concentration as Fe precipitates to the surfaces within the sample. Error bars are two σ of the standard error of the mean computed from the isotope dilution equation. Error bars were removed from some control samples for clarity, and are smaller that the symbols.

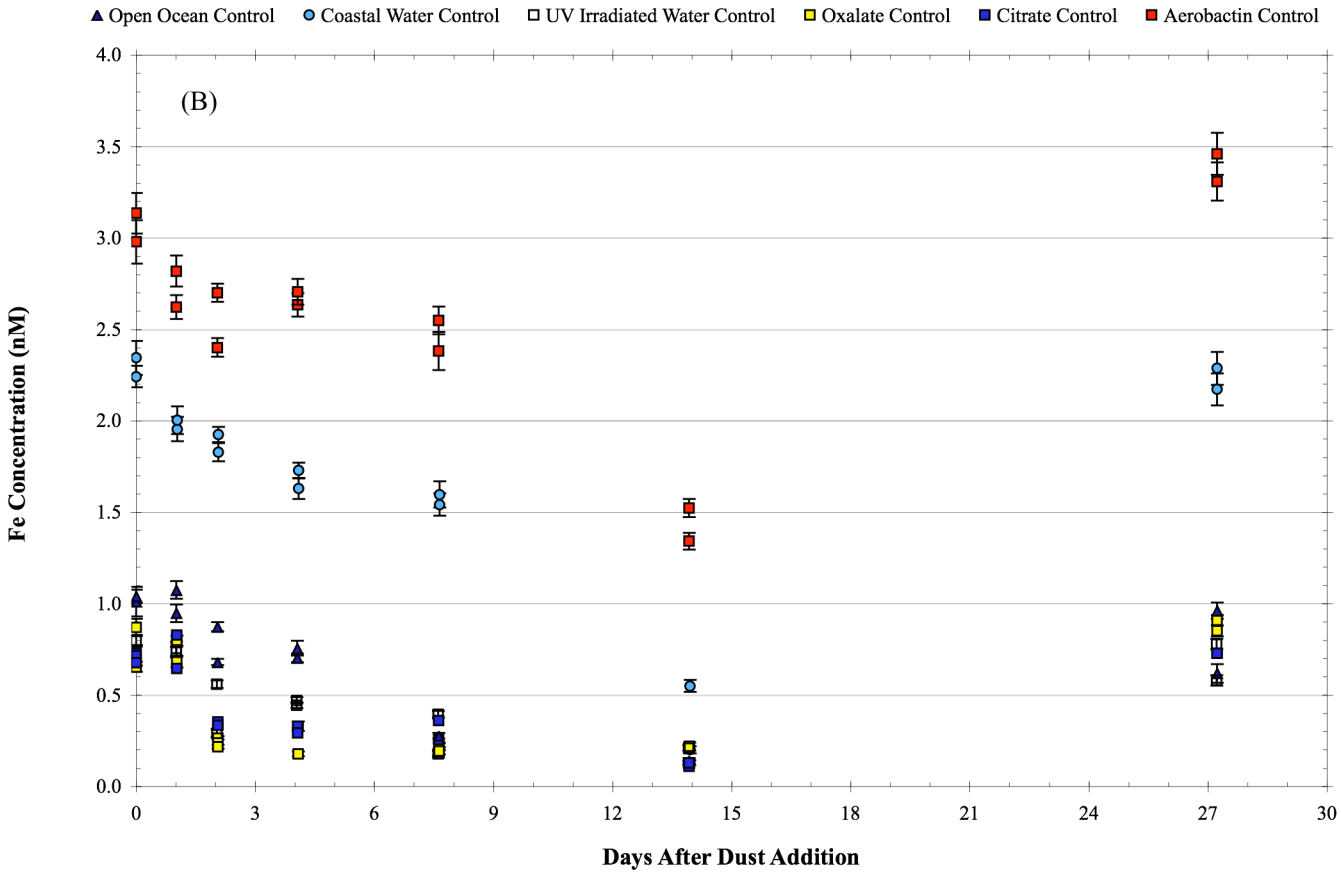

Figure 3: Fe concentrations over time in the seawater matrix experiment. Seawater samples (A) all have reductions in Fe concentration after 28 days, except the Aerobactin Water. Control samples (B) have a slow reduction in Fe concentration as Fe precipitates to the surfaces within the sample. Error bars are two σ of the standard error of the mean computed from the isotope dilution equation. Error bars were removed from some control samples for clarity, and are smaller that the symbols.

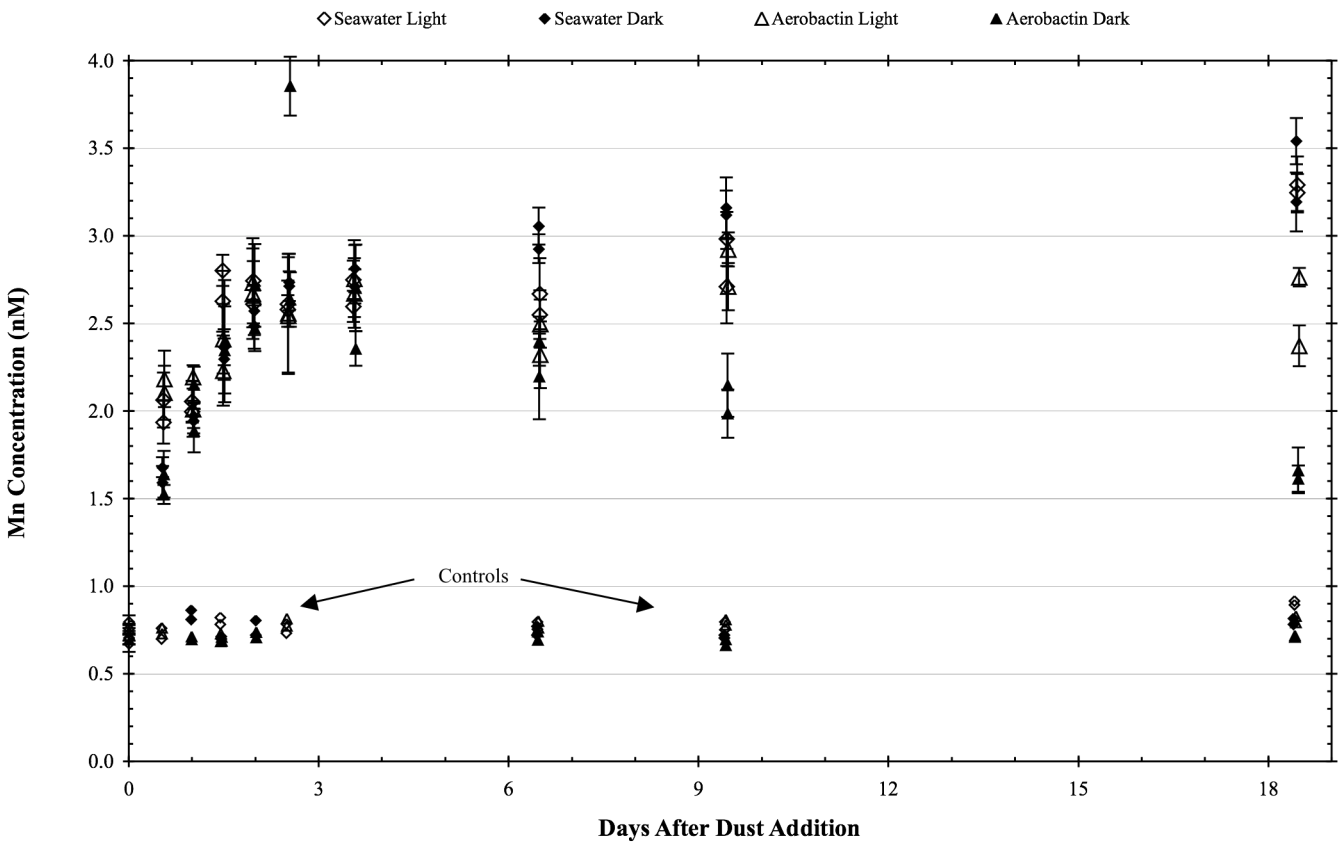

Figure 4: Mn concentrations over time for the light exposure experiment. Seawater samples and controls are shown as diamonds, Aerobactin samples and control are shown as triangles. Light exposure is denoted by the open symbols, while Dark samples are shown as closed symbols. Error bars are two σ of the standard error of the mean computed from the isotope dilution equation. Error bars were removed from some control samples for clarity, and are smaller that the symbols.

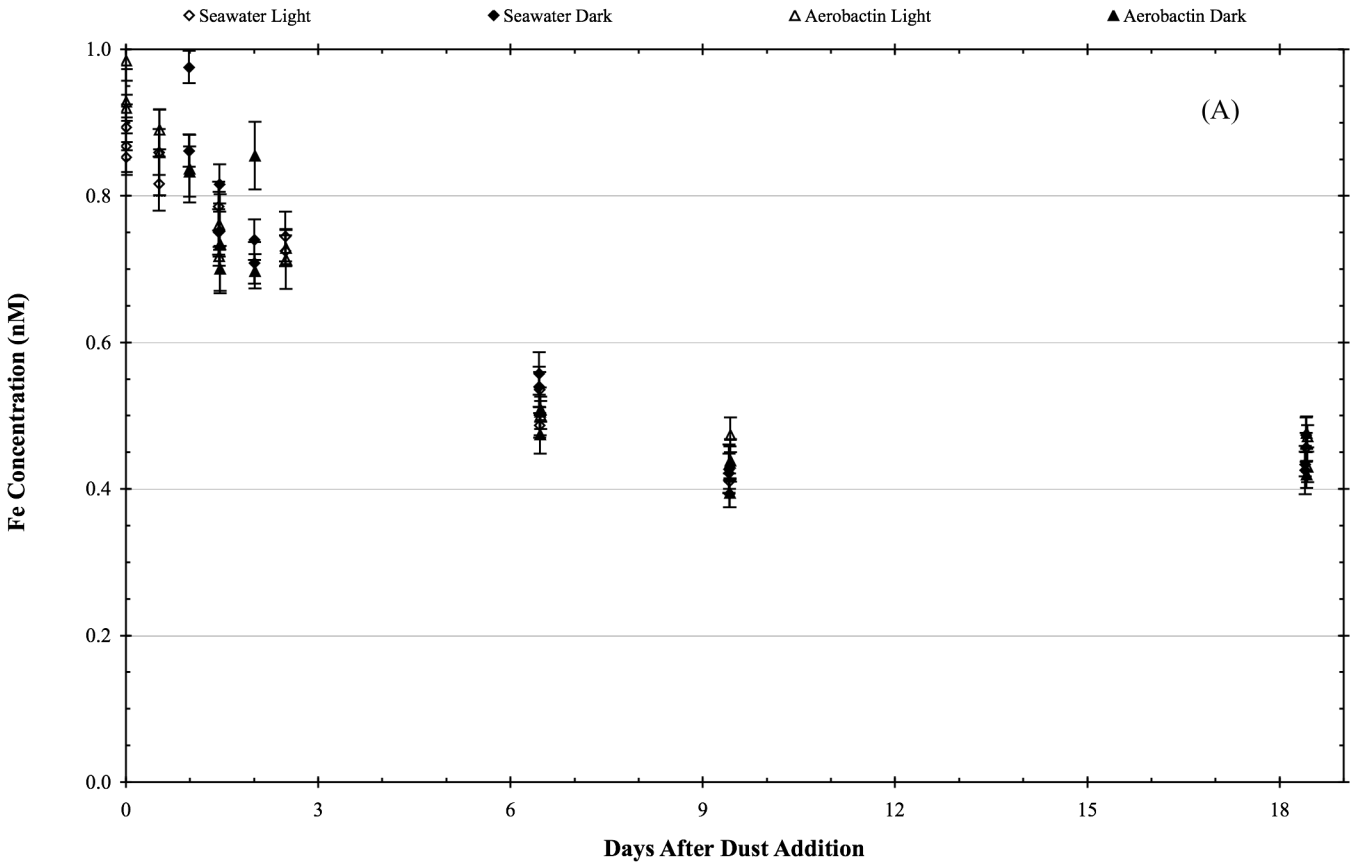

Figure 5: Fe concentration over time for light exposure experiment. Control samples (A) and have a slow reduction in Fe concentration as Fe precipitates to the surfaces within the sample. Aerobactin and Seawater samples (B) have Fe concentration increases above initial values. Error bars are two σ of the standard error of the mean computed from the isotope dilution equation. Error bars were removed from some control samples for clarity, and are smaller that the symbols.

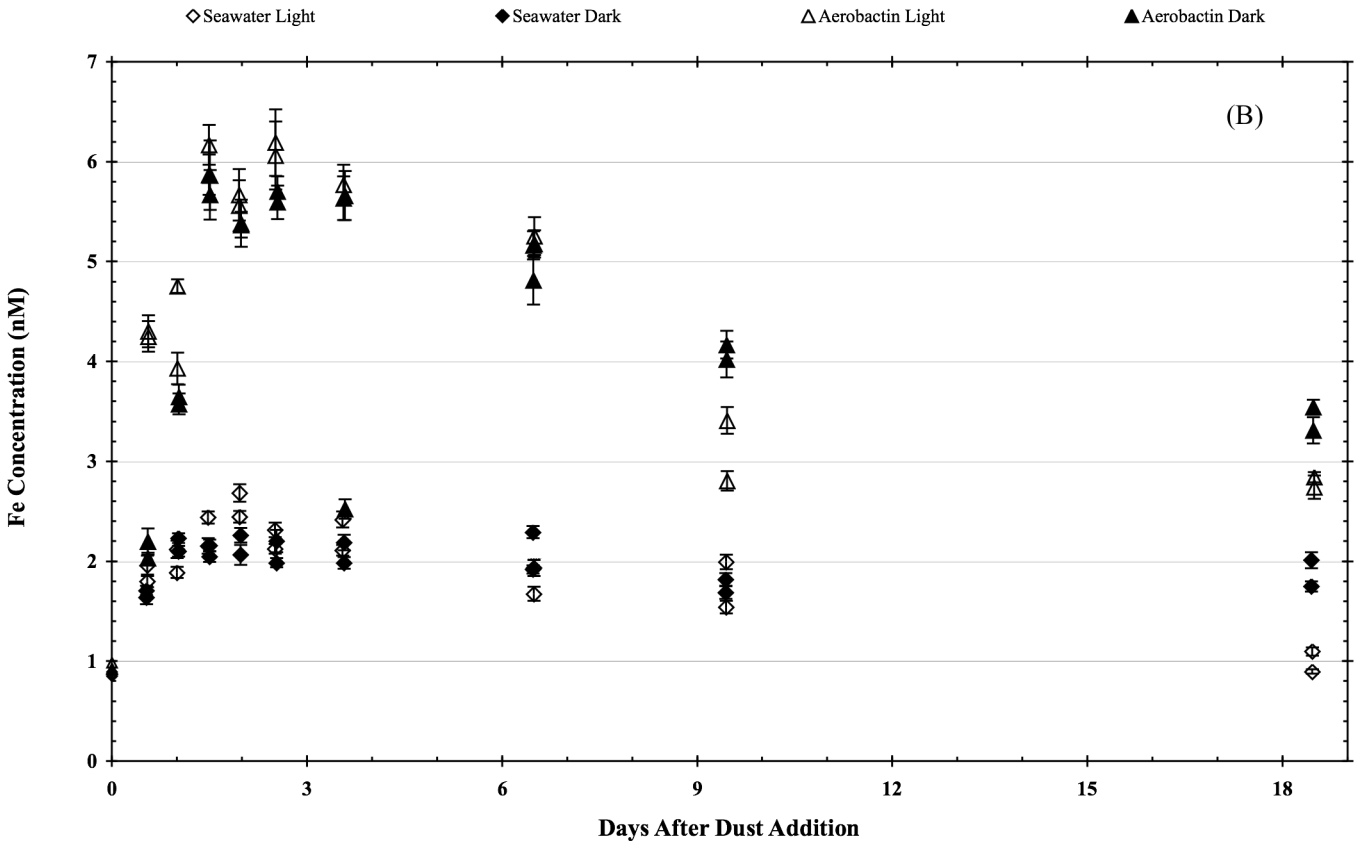

Figure 5: Fe concentration over time for light exposure experiment. Control samples (A) and have a slow reduction in Fe concentration as Fe precipitates to the surfaces within the sample. Aerobactin and Seawater samples (B) have Fe concentration increases above initial values. Error bars are two σ of the standard error of the mean computed from the isotope dilution equation. Error bars were removed from some control samples for clarity, and are smaller that the symbols.

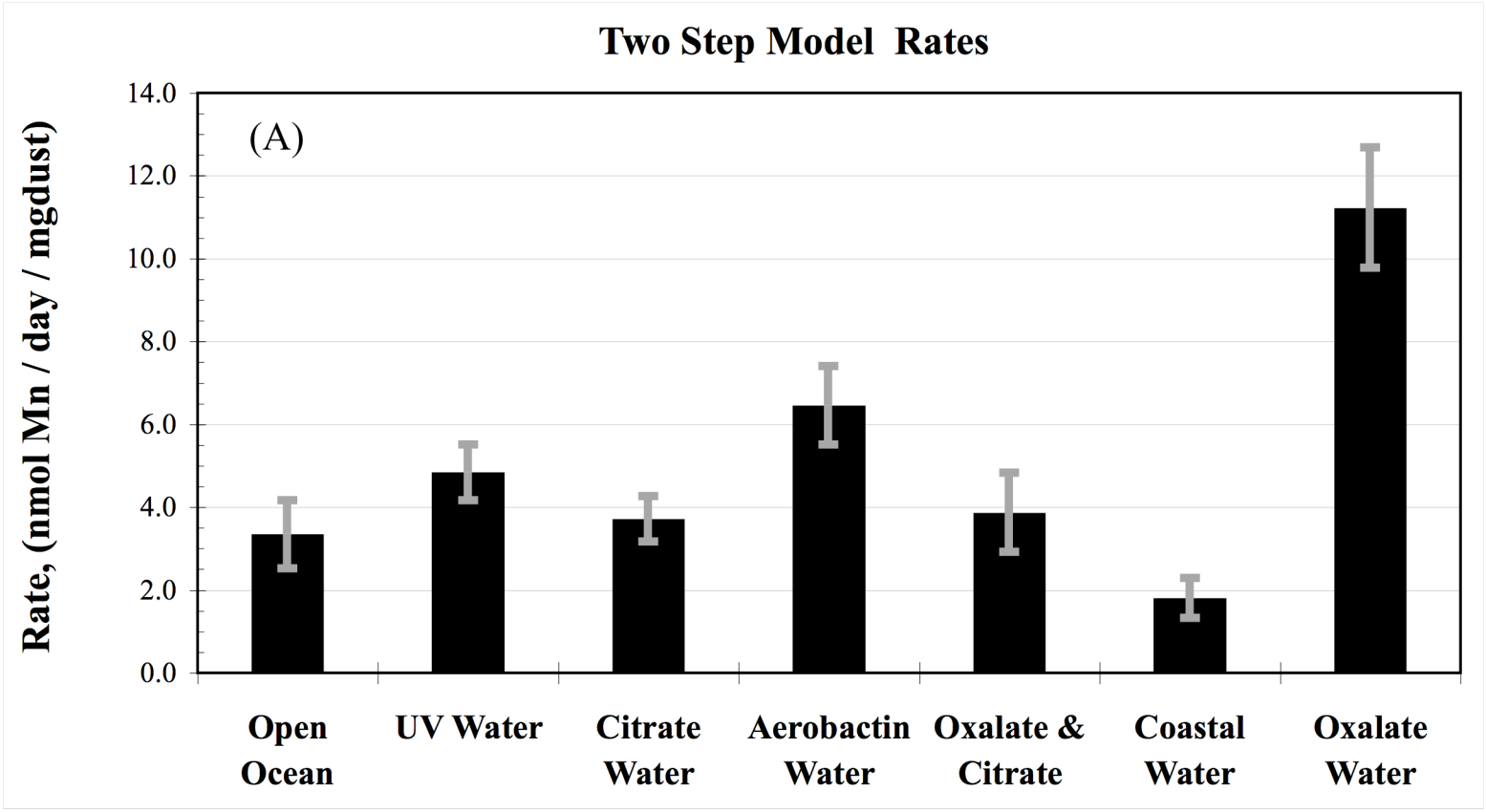

Figure 6: The calculated rates of Mn dissolution for each sample in the seawater matrix experiment (A) and light experiment (B). Oxalate promoted Mn dissolution is significantly faster that all other samples. The Coastal Water is reduced due to its large initial Mn concentration. Both Aerobactin Dark and Seawater Dark samples have diminished Mn dissolution compared to their illuminated counterpart. Error bars are determined to be 12-25% through a series of sensitivity studies on the model which varied the three independent variables.

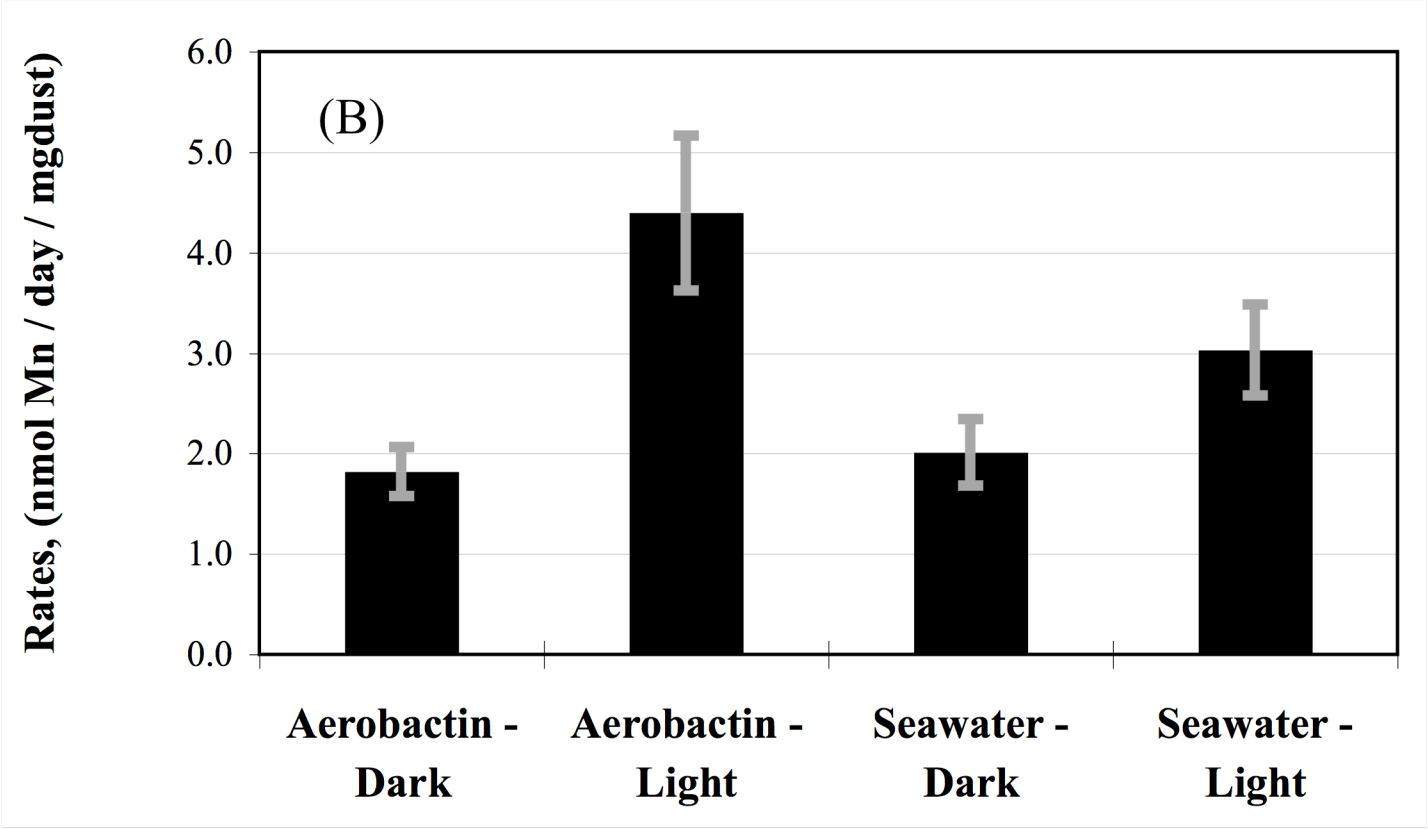

Figure 6: The calculated rates of Mn dissolution for each sample in the seawater matrix experiment (A) and light experiment (B). Oxalate promoted Mn dissolution is significantly faster that all other samples. The Coastal Water is reduced due to its large initial Mn concentration. Both Aerobactin Dark and Seawater Dark samples have diminished Mn dissolution compared to their illuminated counterpart. Error bars are determined to be 12-25% through a series of sensitivity studies on the model which varied the three independent variables.

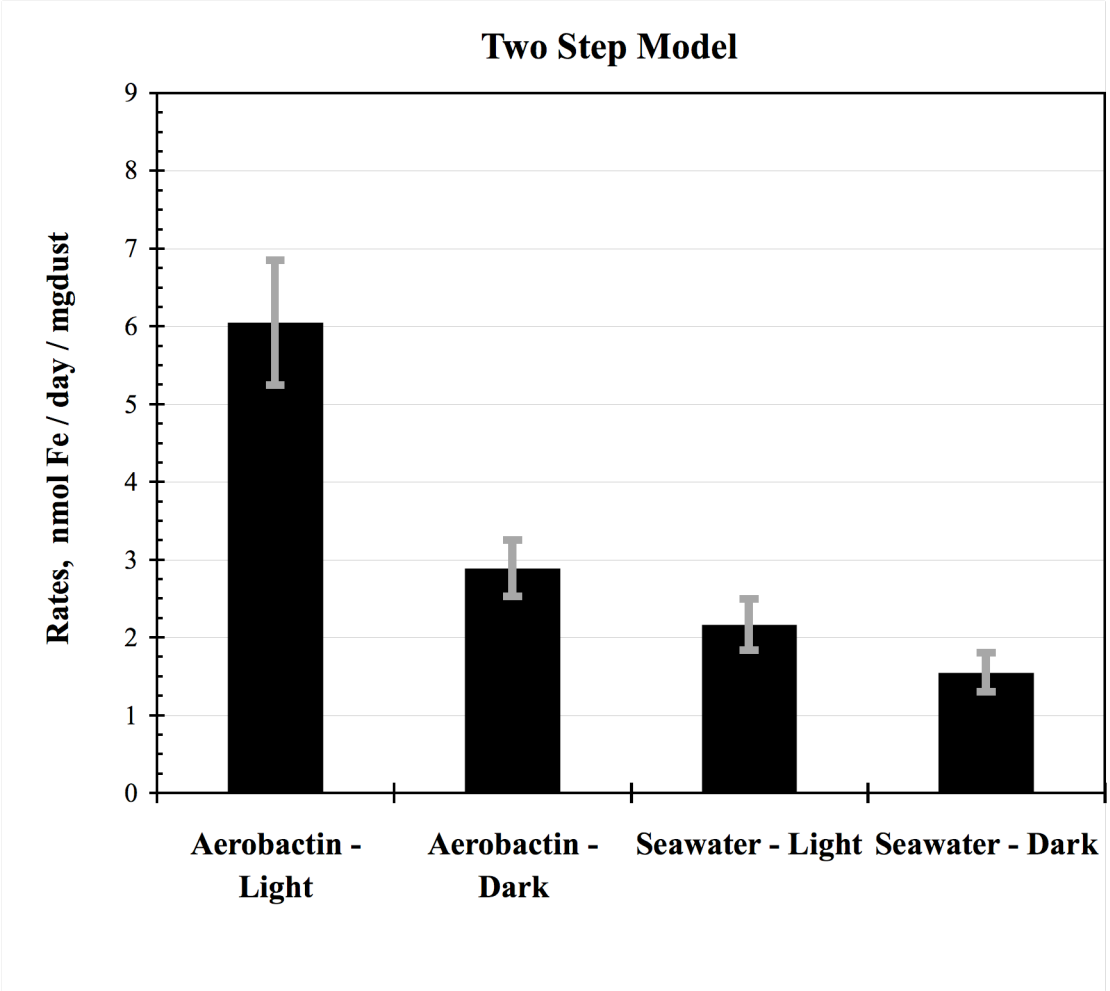

Figure 7: Calculated reaction rates for the initial dissolution of the Fe from dust using a two step reaction. The initial rate is the derivative of the equation at the point of dust addition divided by the dust concentration. Error bars are determined to be 12-25% through a series of sensitivity studies on the model which varied the three independent variables.

APPENDIX I

The dissolution of Mn and Fe in our experiments were modeled using a two step reaction. Our model consists of an irreversible dissolution reaction, followed by an equilibrium reaction between the dissolved and adsorbed metal Eq. 1A (Mn) and 2A (Fe). The irreversible dissolution reaction is meant to model the metal coming off the dust particles, entering into the dissolved phase. Once in the dissolved phase, the metal can stay there, or adsorb onto one of many surfaces found in our experiment.

$$\mathrm{Mn}_{(dust)} \xrightarrow{k_1} \mathrm{Mn}_{(dis)} \underset{k_3}{\overset{k_2}{\rightleftarrows}} \mathrm{Mn}_{(ad)} \qquad \text{Eq. 1A}$$

$$Fe_{(dust)} \xrightarrow{k_1} Fe_{(dis)} \underset{k_3}{\overset{k_2}{\rightleftarrows}} Fe_{(ad)} \qquad \text{Eq. 2A}$$

In order to calculate the dissolution rate of the metal, we need to fit the kinetic solution to the model with our data for each of the experimental samples. To do this we set up three differential equations, one for each of the metal species: metal attached to the original dust, M_{dust}; metal in the dissolved form, M_{dis}; and metal in the adsorbed form, M_{ads}.

$$\frac{\partial}{\partial t}[M_{dust}] = -k_1[M_{dust}] \qquad \text{Eq. 3A}$$

$$\frac{\partial}{\partial t}[M_{dis}] = k_1[M_{dust}] - k_2[M_{dis}] + k_3[M_{ads}] \qquad \text{Eq. 4A}$$

$$\frac{\partial}{\partial t}[M_{ads}] = k_2[M_{dis}] - k_3[M_{ads}] \qquad \text{Eq. 5A}$$

To analytically solve these equations we made the following assumptions:

$M_{dust}^{t=\infty} = 0, \quad M_{dis}^{t=\infty} = M_{dis}^{eq}, \quad M_{ads}^{t=\infty} = M_{ads}^{eq}, \quad M_{ads}^{t=0} = 0$. Where "t" equals time, "eq" represents equilibrium value, and M_{dis}^{eq} is assigned the average value of our data at the final sub-sample.

These assumptions then lead to the assumptions:

$M_{total}^{t=0} = M_{dust}^{t=0} + M_{dis}^{t=0}, \quad M_{total}(t) = M_{dust}(t) + M_{dis}(t) + M_{ads}(t), \quad M_{total}^{t=\infty} = M_{dis}^{t=\infty} + M_{ads}^{t=\infty}$
Where $M_{dis}^{t=0}$ is assigned the value of our data at time equals zero. Combining these assumptions we arrive at equation 6A:

$$M_{ads}(t) = M_{dust}^{t=0} - M_{dust}(t) + M_{dis}^{t=0} - M_{dis}(t) \qquad \text{Eq. 6A}$$

These assumptions were used to find the analytical solution to the three differential equations:

$$M_{dust}^{t} = M_{dust}^{t=0} e^{(-k_1 t)} \qquad \text{Eq. 7A}$$

Eq. 8A

$$M_{dis}^{t} = M_{dust}^{t=0}\frac{(k_1 - k_3)}{(k_2 + k_3 - k_1)}e^{-(k_1 t)} + (M_{dust}^{t=0} + M_{dis}^{t=0})\frac{k_3}{(k_2 + k_3)} - M_{dust}^{t=0}\frac{(k_1 - k_3)}{(k_2 + k_3 - k_1)}e^{-(k_2 + k_3)t} - \left(M_{dust}^{t=0} + M_{dis}^{t=0}\right)\frac{k_3}{(k_2 + k_3)}e^{-(k_2 + k_3)t} + M_{dis}^{t=0}e^{-(k_2 + k_3)t}$$

Eq. 9A

$$M_{ads}^{t} = -M_{dust}^{t=0}\frac{k_2}{(k_2 + k_3 - k_1)}e^{-(k_1 t)} + (M_{dust}^{t=0} + M_{dis}^{t=0})\frac{k_2}{(k_2 + k_3)} + M_{dust}^{t=0}\frac{(k_1 - k_3)}{(k_2 + k_3 - k_1)}e^{-(k_2 + k_3)t} + \left(M_{dust}^{t=0} + M_{dis}^{t=0}\right)\frac{k_3}{(k_2 + k_3)}e^{-(k_2 + k_3)t} - M_{dis}^{t=0}e^{-(k_2 + k_3)t}$$

and the derivative of M_{dis} at t = 0, which we use to calculate the initial dissolution rate.

$$\left.\frac{dM_{dis}}{dt}\right|_{t=0} = -M_{dust}^{t=0}\frac{k_1(k_1 - k_3)}{(k_2 + k_3 - k_1)} + M_{dust}^{t=0}\frac{(k_2 + k_3)(k_1 - k_3)}{(k_2 + k_3 - k_1)} + \left(M_{dust}^{t=0} + M_{dis}^{t=0}\right)k_3 - M_{dis}^{t=0}(k_2 + k_3) \qquad \text{Eq. 10A}$$

These three solutions have five independent variables: $M_{dust}^{t=0}$, $M_{dis}^{t=0}$, k_1, k_2, k_3. To reduce the number of independent variables to three, we define:

$$K_{eq} = \frac{k_2}{k_3} = \frac{M_{ads}^{eq}}{M_{dis}^{eq}} \qquad \text{Eq. 11A}$$

and by substituting in our assumptions we get

$$K_{eq} = \frac{M_{dust}^{t=0} + M_{dis}^{t=0} - M_{dis}^{eq}}{M_{dis}^{eq}} \qquad \text{Eq. 12A}$$

where $M_{dis}^{t=0}$, and M_{dis}^{eq} are calculated from the data. Therefore k_3 is defined by $M_{dust}^{t=0}$ and k_2, and our three independent variables are $M_{dust}^{t=0}$, k_1, and k_2.

To quantify the accuracy of our model fit to the data, we defined

$$\chi^2 = \frac{\left(M_{dis}(t) - M_{data}(t)\right)^2}{\sigma^2_{data}(t)}, \qquad \text{Eq. 13A}$$

where $\boldsymbol{M_{dis}(t)}$ and $\boldsymbol{M_{data}(t)}$ are the concentration of dissolved metal at time t for the model and the data, respectively. We used the Microsoft Excel Solver, which uses a Generalized Reduced Gradient (GRG2) nonlinear optimization algorithm, to fit the three independent variables to best fit the data by minimizing c^2. Multiple combinations of these independent variables are possible solutions; therefore, we optimized one variable at a time. This ensured that the solution was within realistic conditions.

For the Mn model, we began with the assumption that $Mn^{t=0}_{dust}$ is the same for every experiment. We set $M^{t=0}_{dust}$ to 4 nM (the average increase in [Mn] for all experiments) and solved for k_1 and k_2 by minimizing $\sum_t^{t=eq}\chi^2$. We fit k_1 and k_2 for every sample in both experiments then repeated this process for $Mn^{t=0}_{dust}$ = 4.25 – 15 nM. We plot $\sum_t^{t=eq}\chi^2$ for Oxalate Water and total $\sum_t^{t=eq}\chi^2$ for all samples in figure 1A, and show the $Mn^{t=0}_{dust}$ at the minimum $\sum_t^{t=eq}\chi^2$ for each experiment in Table A-1. The $Mn^{t=0}_{dust}$ for all samples has an average of 35% of the total Mn within the added dust. (Guieu *et al.*, 1994) also found 35% dissolution of Mn from aerosol particles in seawater. Therefore, we set $Mn^{t=0}_{dust}$ to 35% of the total Mn of the dust added to each sample. The dust added to each sample was not the same; therefore, $Mn^{t=0}_{dust}$ is different in each sample. With $Mn^{t=0}_{dust}$ set at 35%, we re-solved the model for k_1 and k_2, and calculated $\frac{d}{dt}Mn^{t=0}_{dis}$. The initial rate of Mn dissolutions is $\frac{d}{dt}Mn^{t=0}_{dis}$ divided by the mass of dust for each sample.

Sensitivity of the rate to $Mn_{dust}^{t=0}$, k_1, and k_2 was determined by fixing two of the three independent variables to their "best fit" value, and varying the third ±20%. We tracked the change in $\frac{d}{dt}Mn_{dis}^{t=0}$ with the change in k_1 or k_2, and calculated the mean and standard deviation of $\frac{d}{dt}Mn_{dis}^{t=0}$ over the change. To calculated the sensitivity with respect to $Mn_{dust}^{t=0}$, we "re-fit" the model after each variation to $Mn_{dust}^{t=0}$. The sensitivity of $\frac{d}{dt}Mn_{dis}^{t=0}$ to the variable of interest was defined as the standard deviation of the mean $\frac{d}{dt}Mn_{dis}^{t=0}$ divided by the mean. The sensitivity of dissolution rate to the independent variables is listed in Table A-2. Overall, the samples are most sensitive to k_1, which is the rate constant of the dissolution step, and are insensitive to changes in k_2, because k_2 is important only after significant quantities of dissolved Mn accumulate. Only the Coastal Water sample has any significant quantity of dissolved Mn at time zero, and the Coastal Water is the only sample which is sensitive to changes in k_2. Sensitivity to the quantity of soluble Mn in the dust varies from 0.33% in the Dark Aerobactin sample to 8.3% in the Citrate sample.

For the Fe reaction we used the control samples to constrain k_2, and then fit the other independent variables to the data using the two step reaction model outlined above. In our model for the control samples, Fe_{dis}^{t} was in a reversible reaction with Fe_{ads}^{t}, without the irreversible dissolution step. We only fit the Fe data in the light experiment.

We set up the differential equations

$$\frac{\partial}{\partial t}[Fe_{dis}] = -k_2[Fe_{dis}] + k_3[Fe_{ads}] \quad , \qquad \text{Eq. 14A}$$

$$\frac{\partial}{\partial t}[Fe_{ads}] = k_2[Fe_{dis}] - k_3[Fe_{ads}] \quad , \qquad \text{Eq. 15A}$$

and solved for the dissolved species

$$Fe_{dis}^{t} = \left(Fe_{dis}^{t=0} - Fe_{dis}^{t=eq}\right)e^{-\alpha t} + Fe_{dis}^{t=eq} \quad . \qquad \text{Eq. 16A}$$

We solved for α in each of the four controls, and calculated k_3 for each of the corresponding dust samples using the equation $k_3 = \frac{\alpha}{\left(K_{eq} + 1\right)}$, where $\alpha = k_2 + k_3$. The variable k_2 was constrained by k_3 and the equilibrium constant using Eq. 13A. We then used the Excel solver to solve the best fit for $Fe_{dust}^{t=0}$ and k_1.

The best fit values for $Fe_{dust}^{t=0}$ in the two aerobactin samples (light and dark) and the two natural seawaters (light and dark) were similar to each other. Therefore, we chose to further constrain the Fe dissolution model by forcing both aerobactin samples and both seawater samples to have equivalent $Fe_{dust}^{t=0}$ to each other. Similar to the Mn case, we chose the best $Fe_{dust}^{t=0}$ for each water type by varying $Fe_{dust}^{t=0}$ ±50% while monitoring $\sum_{t}^{t=eq} \chi^2$. The $Fe_{dust}^{t=0}$ value with the minimum $\sum_{Light}^{Dark} \sum_{t}^{t=eq} \chi^2$ was chosen as the $Fe_{dust}^{t=0}$ value for each water type. We then re-solved the model for the best fit in k_1 to the data.

Sensitivity of our model to variations in our three independent variables was measured in an identical manner as the Mn model. We set two independent variables to their best fit values and varied the third. Sensitivity to k_1 or k_2 was determined by changing the constants ±20% and monitoring the change in $\frac{d}{dt} Fe_{dis}^{t=0}$. The sensitivity of the derivative to changes in $Fe_{dust}^{t=0}$ was determined by varying $Fe_{dust}^{t=0}$ ±20% and then re-solving for the best fit for k_1 and k_2. In all cases, the sensitivity of our model to the independent variables was defined as the standard deviation of the mean $\frac{d}{dt} Fe_{dis}^{t=0}$ divided by the mean. The sensitivities are reported in Table A-3. As in the Mn model, the derivative in Fe_{dis} is sensitive to changes in k_1 and insensitive to k_2, with mixed sensitivity to the available Fe in the dust.

APPENDIX TABLES AND FIGURES

Sample	$Mn_{dust}^{t=0}$ at minimum, nM	Percentage of Mn_{total}
Open Ocean	5.25	33.2%
Coastal Water	> 15	-
UV Water	5.50	35.1%
Citrate Water	6.00	37.7%
Aerobactin Water	5.00	31.5%
Oxalate & Citrate Water	4.50	38.9%
Oxalate Water	5.25	33.2%
Aerobactin – Light Water	5.25	35.3%
Aerobactin – Dark Water	>15	-
Seawater – Light Water	5.50	36.0%
Seawater – Dark Water	5.50	36.0%
Average	5.31	35.2%

Table A-1: The quantity of available Mn from the dust according to the Mn two step model. Each value given is the value of Mn_{dust} which resulted in the minimum χ^2 values for the overall fit to the data. The Coastal Water and Aerobactin-Dark samples never reached a minimum.

Sample	Mean $\frac{d}{dt} Mn_{dis}^{t=0}$	Sensitivity to $Mn_{dust}^{t=0}$	Sensitivity to k_1	Sensitivity to k_2
Open Ocean	3.89	4.1%	13.6%	1.6%
Coastal Water	2.11	0.51%	23.9%	11.9%
UV Water	5.56	7.0%	12.0%	0.01%
Citrate Water	4.35	8.3%	12.1%	0.12%
Aerobactin Water	7.53	7.1%	12.8%	0.82%
Oxalate & Citrate Water	3.29	5.9%	13.0%	1.03%
Oxalate Water	13.04	4.7%	12.0%	0.03%
Aerobactin – Light Water	4.79	5.1%	16.2%	4.17%
Aerobactin – Dark Water	1.99	0.33%	13.4%	1.37%
Seawater – Light Water	3.39	2.0%	14.6%	2.59%
Seawater – Dark Water	2.25	3.5%	15.6%	3.61%

Table A-2: Sensitivity study for the Mn two step model. Each independent variable was changed ±20% while monitoring the derivative in Mn_{dis}. The sensitivity of the derivative to the variable was defined as the standard deviation in mean of the derivative divided by the mean.

Sample	Average $\frac{d}{dt}Fe_{dis}^{t=0}$	Sensitivity to $Fe_{dust}^{t=0}$	Sensitivity to k_1	Sensitivity to k_2
Aerobactin – Light Water	6.96	0.66%	12.2%	0.21%
Aerobactin – Dark Water	3.52	5.3%	12.5%	0.51%
Seawater – Light Water	2.63	10.3%	12.6%	0.59%
Seawater – Dark Water	1.94	8.5%	12.4%	0.45%

Table A-3: Sensitivity Study for the Fe two step model. Each independent variable was changed ±20% while monitoring the derivative in Mn_{dis}. The sensitivity of the derivative to the variable was defined as the standard deviation in mean of the derivative divided by the mean.

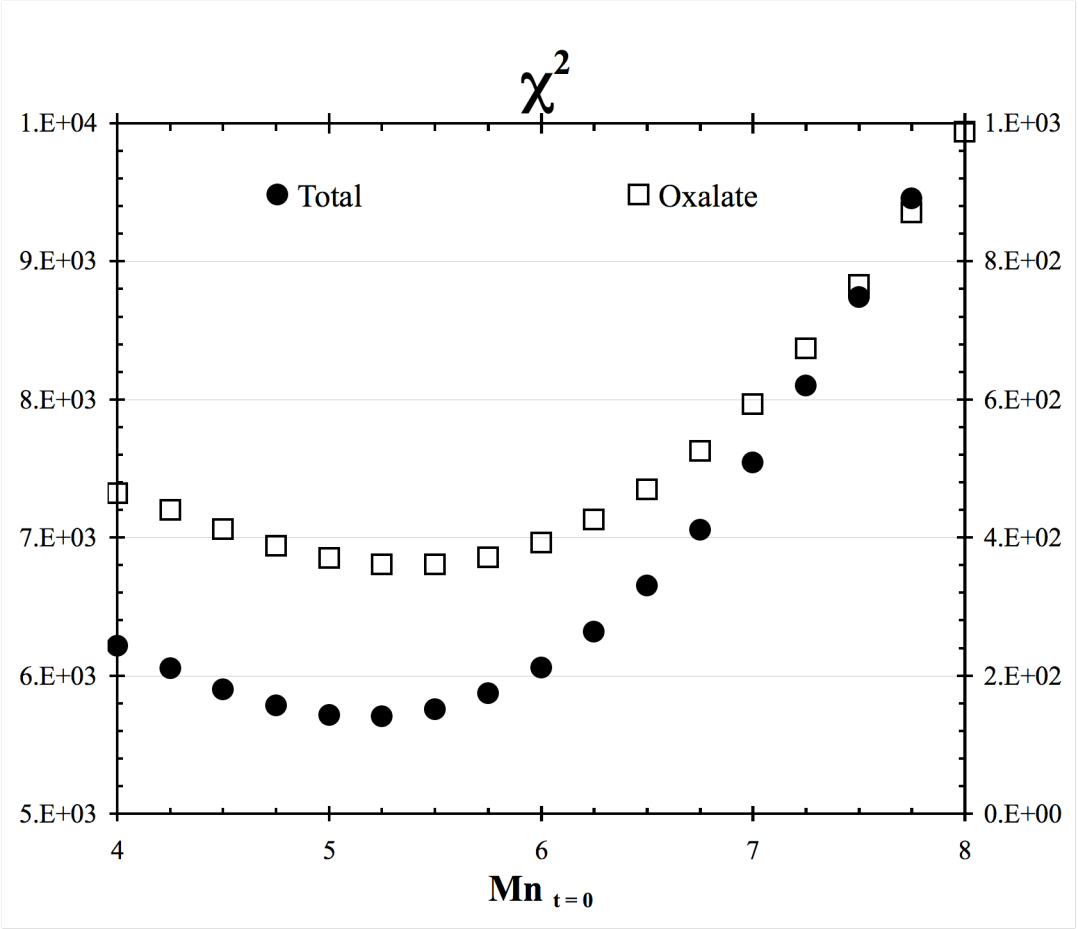

Figure 1A: χ^2 (eq. 13A) is a measure of the accuracy of the model fit to the data. To select the appropriate constants for our model, we minimized χ^2 for each water sample. Here the sum of the χ^2 is plotted against the change in total Mn available from the dust, Mn_{dust}, for both Oxalate Water and the total of all water samples. A value of 5.25 nM was selected as the best fit to the data for this circumstance.

BIBLIOGRAPHY

Banerjee, D. and Nesbitt, H.W., 1999. XPS study of reductive dissolution of birnessite by oxalate: Rates and mechanistic aspects of dissolution and redox processes. Geochimica Et Cosmochimica Acta, 63(19-20): 3025-3038.

Barbeau, K., 2006. Photochemistry of organic iron(III) complexing ligands in oceanic systems. Photochemistry and Photobiology, 82(6): 1505-1516.

Barbeau, K., Rue, E.L., Bruland, K.W. and Butler, A., 2001. Photochemical cycling of iron in the surface ocean mediated by microbial iron(III)-binding ligands. Nature, 413: 409-413.

Barbeau, K., Rue, E.L., Trick, C.G., Bruland, K.T. and Butler, A., 2003. Photochemical reactivity of siderophores produced by marine heterotrophic bacteria and cyanobacteria based on characteristic Fe(III) binding groups. Limnology and Oceanography, 48(3): 1069-1078.

Barbeau, K., Zhang, G.P., Live, D.H. and Butler, A., 2002. Petrobactin, a photoreactive siderophore produced by the oil-degrading marine bacterium Marinobacter hydrocarbonoclasticus. Journal of the American Chemical Society, 124(3): 378-379.

Bonnet, S. and Guieu, C., 2004. Dissolution of atmospheric iron in seawater. Geophysical Research Letters, 31(3).

Borer, P.M., Sulzberger, B., Reichard, P. and Kraemer, S.M., 2005. Effect of siderophores on the light-induced dissolution of colloidal iron(III) (hydr)oxides. Marine Chemistry, 93(2-4): 179-193.

Boukhalfa, H. and Crumbliss, A.L., 2002. Chemical aspects of siderophore mediated iron transport. Biometals, 15(4): 325-339.

Braun, V., 2003. Iron uptake by Escherichia coli. Frontiers in Bioscience, 8: S1409-S1421.

Buck, C.S., Landing, W.M., Resing, J.A. and Lebon, G.T., 2006. Aerosol iron and aluminum solubility in the northwest Pacific Ocean: Results from the 2002 IOC cruise. Geochemistry Geophysics Geosystems, 7.

Buck, K.N., Lohan, M.C., Berger, C.J.M. and Bruland, K.W., 2007. Dissolved iron speciation in two distinct river plumes and an estuary: Implications for riverine iron supply. Limnology and Oceanography, 52(2): 843-855.

Cheah, S.F., Kraemer, S.M., Cervini-Silva, J. and Sposito, G., 2003. Steady-state dissolution kinetics of goethite in the presence of desferrioxamine B and oxalate ligands: implications for the microbial acquisition of iron. Chemical Geology, 198(1-2): 63-75.

Cocozza, C. et al., 2002. Temperature dependence of goethite dissolution promoted by trihydroxamate siderophores. Geochimica Et Cosmochimica Acta, 66(3): 431-438.

Donat, J.R. and Bruland, K.W., 1988. Direct Determination of Dissolved Cobalt and Nickel in Seawater by Differential Pulse Cathodic Stripping Voltammetry Preceded by Adsorptive Collection of Cyclohexane-1,2-Dione Dioxime Complexes. Analytical Chemistry, 60(3): 240-244.

Duce, R.A. and Tindale, N.W., 1991. Atmospheric transport of iron and its deposition in the ocean. Limnology and Oceanography, 36(8): 1715-1726.

Duckworth, O.W. and Martin, S.T., 2001. Surface complexation and dissolution of hematite by C-1-C-6 dicarboxylic acids at pH=5.0. Geochimica Et Cosmochimica Acta, 65(23): 4289-4301.

Erel, Y., Pehkonen, S.O. and Hoffmann, M.R., 1993. Redox Chemistry of Iron in Fog and Stratus Clouds. Journal of Geophysical Research-Atmospheres, 98(D10): 18423-18434.

Furrer, G. and Stumm, W., 1986. The Coordination Chemistry of Weathering .1. Dissolution Kinetics of Delta-Al_2O_3 and BeO_2. Geochimica Et Cosmochimica Acta, 50(9): 1847-1860.

Guieu, C., Duce, R. and Arimoto, R., 1994. Dissolved Input of Manganese to the Ocean - Aerosol Source. Journal of Geophysical Research-Atmospheres, 99(D9): 18789-18800.

Harris, W.R., Carrano, C.J. and Raymond, K.N., 1979. Coordination Chemistry of Microbial Iron Transport Compounds .16. Isolation, Characterization, and Formation-Constants of Ferric Aerobactin. Journal of the American Chemical Society, 101(10): 2722-2727.

Haygood, M.G., Holt, P.D. and Butler, A., 1993. Aerobactin Production by a Planktonic Marine Vibrio Sp. Limnology and Oceanography, 38(5): 1091-1097.

Hersman, L., Lloyd, T. and Sposito, G., 1995. Siderophore-Promoted Dissolution of Hematite. Geochimica Et Cosmochimica Acta, 59(16): 3327-3330.

Holmen, B.A. and Casey, W.H., 1996. Hydroxamate ligands, surface chemistry, and the mechanism of ligand-promoted dissolution of goethite [alpha-FeOOH(s)]. Geochimica Et Cosmochimica Acta, 60(22): 4403-4416.

Johansen, A.M., Siefert, R.L. and Hoffmann, M.R., 2000. Chemical composition of aerosols collected over the tropical North Atlantic Ocean. Journal of Geophysical Research-Atmospheres, 105(D12): 15277-15312.

Johnson, K.S. et al., 2007. Developing Standards for Dissolved Iron in Seawater. EOS, 88(11): 131-132.

Jun, Y.S. and Martin, S.T., 2003. Microscopic observations of reductive manganite dissolution under oxic conditions. Environmental Science & Technology, 37(11): 2363-2370.

Klewicki, J.K. and Morgan, J.J., 1998. Kinetic behavior of Mn(III) complexes of pyrophosphate, EDTA, and citrate. Environmental Science & Technology, 32(19): 2916-2922.

Klewicki, J.K. and Morgan, J.J., 1999. Dissolution of beta-MnOOH particles by ligands: Pyrophosphate, ethylenediaminetetraacetate, and citrate. Geochimica Et Cosmochimica Acta, 63(19-20): 3017-3024.

Kraemer, S.M., 2004. Iron oxide dissolution and solubility in the presence of siderophores. Aquatic Sciences, 66(1): 3-18.

Küpper, F.C., Carrano, C.J., Kuhn, J.U. and Butler, A., 2006. Photoreactivity of iron(III) - Aerobactin: Photoproduct structure and iron(III) coordination. Inorganic Chemistry, 45(15): 6028-6033.

Macrellis, H.M., Trick, C.G., Rue, E.L., Smith, G. and Bruland, K.W., 2001. Collection and detection of natural iron-binding ligands from seawater. Marine Chemistry, 76(3): 175-187.

Mendez, J.M., Guieu, C. and Adkins, J.F., in review. Atmospheric input of Manganese and Iron to the ocean: Sea water dissolution experiments with Saharan and North American dusts. Marine Chemistry: (in review).

Morel, F.M.M. and Hering, J.G., 1993. Principles and Applications of Aquatic Chemistry. John Wiley & Sons, Inc., New york, 588 pp.

Neilands, J.B., 1995. Siderophores - Structure and Function of Microbial Iron Transport Compounds. Journal of Biological Chemistry, 270(45): 26723-26726.

Pehkonen, S.O., Siefert, R., Erel, Y., Webb, S. and Hoffmann, M.R., 1993. Photoreduction of Iron Oxyhydroxides in the Presence of Important Atmospheric Organic-Compounds. Environmental Science & Technology, 27(10): 2056-2062.

Raymond, K.N. and Carrano, C.J., 1979. Coordination Chemistry and Microbial Iron Transport. Accounts of Chemical Research, 12(5): 183-190.

Rose, A.L. and Waite, T.D., 2002. Kinetic model for Fe(II) oxidation in seawater in the absence and presence of natural organic matter. Environmental Science & Technology, 36(3): 433-444.

Rue, E. and Bruland, K., 2001. Domoic acid binds iron and copper: a possible role for the toxin produced by the marine diatom Pseudo-nitzschia. Marine Chemistry, 76(1-2): 127-134.

Rue, E.L. and Bruland, K.W., 1995. Complexation of Iron(III) by Natural Organic-Ligands in the Central North Pacific as Determined by a New Competitive Ligand Equilibration Adsorptive Cathodic Stripping Voltammetric Method. Marine Chemistry, 50(1-4): 117-138.

Siefert, R.L., Johansen, A.M., Hoffmann, M.R. and Pehkonen, S.O., 1998. Measurements of trace metal (Fe, Cu, Mn, Cr) oxidation states in fog and stratus clouds. Journal of the Air & Waste Management Association, 48(2): 128-143.

Siffert, C. and Sulzberger, B., 1991. Light-Induced Dissolution of Hematite in the Presence of Oxalate - a Case-Study. Langmuir, 7(8): 1627-1634.

Smith, R.M., Martell, A.E. and Motekaitis, R.J., 2004. NIST Critically Selected Stability Constants of Metal Complexes Database. National Institute of Standards and Technology.

Stone, A.T., 1987. Microbial Metabolites and the Reductive Dissolution of Manganese Oxides - Oxalate and Pyruvate. Geochimica Et Cosmochimica Acta, 51(4): 919-925.

Stone, A.T. and Morgan, J.J., 1984. Reduction and Dissolution of Manganese(Iii) and Manganese(Iv) Oxides by Organics .2. Survey of the Reactivity of Organics. Environmental Science & Technology, 18(8): 617-624.

Stumm, W. and Morgan, J.J., 1996. Aquatic Chemistry. Wiley-Interscience, New York, 1022 pp.

Sunda, W.G., Huntsman, S.A. and Harvey, G.R., 1983. Photoreduction of manganese oxides in seawater and its geochemical and biological implications. Nature, 301: 234-236.

Turner, D.R. and Hunter, K.A. (Editors), 2001. The biogeochemistry of iron in seawater. IUPAC series on analytical and physical chemistry of environmental systems ; v. 7. J. Wiley, New York.

Voelker, B.M., Morel, F.M.M. and Sulzberger, B., 1997. Iron redox cycling in surface waters: Effects of humic substances and light. Environmental Science & Technology, 31(4): 1004-1011.

von Langen, P.J., Johnson, K.S., Coale, K.H. and Elrod, V.A., 1997. Oxidation kinetics of manganese (II) in seawater at nanomolar concentrations. Geochimica Et Cosmochimica Acta, 61(23): 4945-4954.

Waite, T.D. and Morel, F.M.M., 1984. Photoreductive Dissolution of Colloidal Iron-Oxide - Effect of Citrate. Journal of Colloid and Interface Science, 102(1): 121-137.

Wang, Y. and Stone, A.T., 2006. Reaction of Mn-III,Mn-IV (hydr)oxides with oxalic acid, glyoxylic acid, phosphonoformic acid, and structurally-related organic compounds. Geochimica Et Cosmochimica Acta, 70(17): 4477-4490.

Wedepohl, K.H., 1995. The Composition of the Continental-Crust. Geochimica Et Cosmochimica Acta, 59(7): 1217-1232.

Witter, A.E., Hutchins, D.A., Butler, A. and Luther, G.W., 2000. Determination of conditional stability constants and kinetic constants for strong model Fe-binding ligands in seawater. Marine Chemistry, 69(1-2): 1-17.

Wu, J. and Boyle, E.A., 1998. Determination of iron in seawater by high-resolution isotope dilution inductively coupled plasma mass spectrometry after $Mg(OH)_2$ coprecipitation. Analytica Chimica Acta, 367: 183-191.

Xyla, A.G. et al., 1992. Reductive Dissolution of Manganese(Iii,Iv) (Hydr)Oxides by Oxalate - the Effect of Ph and Light. Langmuir, 8(1): 95-103.

Yoshida, T., 2002. Dissolution of iron hydroxides by marine bacterial siderophore. Chemical geology, 184(1-2): 1-9.

Zinder, B., Furrer, G. and Stumm, W., 1986. The Coordination Chemistry of Weathering .2. Dissolution of Fe(Iii) Oxides. Geochimica Et Cosmochimica Acta, 50(9): 1861-1869.

C h a p t e r 4

SANTA MONICA BAY OCEAN TIME SERIES

Jeffrey Mendez[a], Jess Adkins[b]

[a] Department of Environmental Science and Engineering, California Institute of Technology
[b] Department of Geological and Planetary Sciences, California Institute of Technology

1. Introduction

Trace metals such as iron (Fe) and manganese (Mn) are essential micronutrients required for enzymatic pathways of respiration, nitrogen and carbon fixation, and electron transfer in photosynthesis in marine biology (Turner and Hunter, 2001). As a result, the ocean depth profiles for Mn (Klinkhammer and Bender, 1980) and iron (Fe) (Martin and Fitzwater, 1988) can be affected by phytoplankton in the ocean

Mn is specifically important for photosynthetic and radical scavenging enzymes (Horsburgh *et al.*, 2002; Kernen *et al.*, 2002). Thermodynamically, Mn within a fully oxygenated ocean at natural pH should be Mn(IV) and precipitate out of the water in the form MnO_2. Dissolved Mn ocean profiles reveal that the surface waters contain high levels of soluble Mn(II). A portion of the soluble Mn is from direct dissolution from atmospheric deposition which contains Mn in the +2 oxidation state (Guieu et al., 1994; Siefert et al., 1998). Slow oxidation to the +3 or +4 state allows Mn to stay dissolved on the order of days; however, Mn still should oxidize over time and precipitate out of the surface ocean (Stumm and Morgan, 1996). This oxidation is prevented by photoreduction of Mn to the soluble +2 state in the presence of organic material (Sunda *et al.*, 1983), resulting in a large concentration of Mn in the surface water available for biological use.

Fe is the fourth most abundant element in the Earth's crust (Wedepohl, 1995). However the thermodynamically stable oxidation state, Fe (III), is relatively insoluble in oxic pH 8 seawater, which limits the inorganic concentration to 0.1 nM (Morel and Hering, 1993). Any inorganic iron above this concentration will either form an Fe oxide solid or quickly adsorb onto nearby surfaces (Rose and Waite, 2002). Despite this limit, oceanic Fe concentrations range from 0.1 – 2 nM (or higher in the coastal ocean). Fe(II) additions to the surface water from wet or dry deposition can elevate the total dissolved Fe concentration (Erel et al., 1993; Johansen et al., 2000); however, these too will quickly oxidize. Therefore, Fe must have a non-inorganic method for maintaining dissolved Fe in the seawater. Organic ligands appear to be responsible for this elevation of Fe concentrations (Barbeau et al., 2001; Buck, 2007; Rue and Bruland, 1995; van den Berg, 1995).

Bottle incubations and mesoscale Fe addition experiments have shown Fe to be important to ocean productivity (Martin and Fitzwater, 1988), and in many locations, the limiting or co-limiting nutrient (Maldonado et al., 1999; Martin et al., 1989; Mills et al., 2004). Furthermore, Fe is hypothesized to have a role in the global carbon budget and glacial cycles (Martin, 1990). The importance of Fe to the ocean has lead to its incorporation into computer models (Aumont *et al.*, 2003; Moore *et al.*, 2006) to more accurately describe overall ocean biogeochemical cycles. However, data comparisons to these models can be difficult due to the lack of complete temporal and spatial coverage of the global ocean. An alternative to the global ocean model is a regional ocean model which can be compared to the global ocean. The coastal ocean is important to the global carbon cycle, (Smith and Hollibaugh, 1993; Tsunogai and Noriki, 1991); we therefore propose that the Southern California Bight may be able to be used as a model environment to study global oceans and the carbon cycle. In general, the Southern California Bight is nitrate (NO_3) limited; however, the region is strongly influenced by the Fe depleted California Current. These interactions are caused by mixing of the California Current through the Channel Islands

(Dong and McWilliams, 2007) and may be able to supply the region with Fe depleted water. In addition, Southern California is subject to punctuated wind events, the Santa Ana Winds, which can deposit large masses of particulate Fe onto the ocean surface (200 – 500 μg Fe • m^{-2} • day^{-1}) (Guazzotti et al., 2001; Lu et al., 2003). The changes in Fe concentration caused by these two types of events may cause a change in the biological community or overall production. In both cases, a study of the effects of Fe on the biological production of the coastal ocean is important to the understanding of Fe biogeochemical cycles and the carbon cycle. While the Southern California region has been intensely studied, a continuous high frequency time series (greater than seasonal sampling) of chemically and biologically important species, including trace metals, has not be conducted. This type of time series is needed to capture the events that may lead to changes in the biological production, but more importantly it is required to first understand the basic modes and cycles which characterize the ocean. After these background states have been observed and analyzed, the changes in biological production due to an events can be placed into proper context. We present here the coastal high frequency time series to include Fe and Mn concentrations in conjunction with biological analysis. This time series has been designed to characterize the coastal region. Investigations into biological responses to these events and the eventual effects on the carbon cycle will develop following this analysis.

2. Methods

2.1 Time Series Sample Collection

Time series field work was conducted on the R/V *Seaworld* UCLA at the Santa Monica Bay Observatory Oceanographic Mooring site. The mooring is anchored at 33° 55.9' N, 118° 42.9' W, and drifts about this point depending on the prevailing surface currents, as shown in figure 1. The mooring is located at the mouth of the Santa Monica canyon, a submarine canyon on the continental slope. Seawater was collected using Teflon coated external spring niskin bottles with Teflon coated messengers (General Oceanics Inc. model

1010X-5L) attached to ¼ inch polyester line. Thirteen samples were collected for metal measurements for each profile ranging from the surface (1 m) to the bottom (~400 m). Only twelve samples were taken for all other chemical tracers ranging from the surface to 300 m, no deep water sample was taken. The niskin bottles were rinsed with surface seawater (15 – 40 m) before each day's use and milli-Q (mQ) water after each day of sampling (18.2 MΩ•cm, 2 x 500 mL), and then stored wet.

Water was pumped from each niskin bottle through a 0.2 mm cartridge filter (Sartobran cellulose acetate P 150, 0.45 mm prefilter) with a peristaltic pump using C-Flex tubing (acid leached in 10% v/v reagent HCl) into a trace metal clean work space. The filter and tubing were rinsed with at least one liter of seawater before sampling to remove any residual acid and to condition the walls to reduce sample iron adsorption (Buck *et al.*, 2007). Samples were collected in 60 or 125 mL bottles, rinsing each bottle 3 times with the seawater sample before collection. Final samples were stored acidified with hydrochloric acid (12 M, SeaStar® HCl) at an acid to seawater ratio of 1:1000, ultimately reaching a pH of 2.0 – 2.3. All sampling and laboratory materials were acid leached using standard trace metal clean techniques.

2.2 Analysis

All samples collected in the Santa Monica Bay time series were analyzed for Fe and Mn concentrations. We used a modified MagIC method (Wu and Boyle, 1998) to concentrate the metals by a factor of twenty in order to analyze them by isotope dilution on the Finnegan Element I Inductively Coupled Plasma (ICP) Mass Spectrometer. Analysis of dissolved inorganic carbon (DIC) was done by Anita Leinweber from the University of California, Los Angeles (UCLA). Nutrient concentration measurements were made at the University of California, San Diego, Scripps Institute of Oceanography (Scripps) nutrient analysis lab. Measurements of chlorophyll, biologic silicate, lithogenic silicate, and cell species counts were done at UCLA in the laboratory of Rebecca Shipe. Temperature and

salinity were measured on the Seabird 19plus Conductivity, Temperature, and Depth Sensor (CTD), which was attached to the bottom of the line during each sample collection.

3. Results

3.1 Manganese

The pattern of Mn concentration in the Santa Monica Bay was similar to open ocean Mn depth profiles (Klinkhammer and Bender, 1980), (Fig. 2a). In the Santa Monica Bay, Mn concentration was 2-15 nM in the surface waters (1-20 m) and fell with depth. Surface water concentrations did not have a seasonal signal and were highest from February to October 2005. Sub-surface Mn concentrations were as low as 0.5 nM. Mid-depth Mn peaks did occur below the surface and were correlated to Fe and lithogenic silicate ($L\text{-}SiO_4$) peaks. There was a slight increase in Mn concentration in the bottom water; however, this increase was small, typically increasing 0.5 – 1.0 nM above mid-depth values and never exceeding 3 nM.

3.2 Iron

Fe concentrations in the Santa Monica Bay were highly variable. Concentrations ranged from below 0.1 nM at the surface in late summer to over 25 nM in the deep water (Fig. 3). Overall, the average Fe depth profile was similar to a nutrient profile (Fig. 2b). Average mixed layer concentrations were about 2 nM and grew to over 5 nM at a persistent 75 m depth peak. Below 75 m, the Fe concentration decreased and remained constant between 4 – 5 nM until the bottom. Bottom water concentrations increased rapidly with depth below 300 m, growing to over 8 nM between 350 – 450 m.

The high Fe peak at in the region of 75 m depth was a consistent feature in most of the Fe depth profiles; however, there was variability in the absolute value of the Fe concentration,

the number of peaks, and the depth at which the peaks appeared. A few of the Fe peaks were small, rising above the background Fe concentrations 0.5 nM and spanning as little as 10 m in depth (Fig. 4a); however, most peaks were relatively large. These peaks were several nM higher than the background deep water concentration and span 50 m or more in depth (Fig. 4b). In addition, there were many profiles with two high Fe peaks. Typically the high Fe peaks correlate with lithogenic silicate, although the location of the peaks maxima were not always at the same depth, with the lithogenic silicate usually peaking one sample lower in depth than the Fe peak. (Fig. 4c).

The profile from 10/11/05 (Fig. 4d) shows a good example of three of the four types of high Fe peaks. The top peak was thin and relatively small (1-3 nM) and was seen in the top 50 m. The second peak was composed of a large broad layer of water that had the most dramatic high Fe peak. This peak had an Fe concentration of 5-10 nM and was as much as 50 m thick. The third type of peak was not present in this profile, as it was the most transient peak in the time series. As seen in the profile from 8/16/05 (Fig. 4e), this peak was a broad layer of water ranging from 100 – 150 m in depth with a salinity of about 33.8 – 34.0 PSU. The final peak of Fe seen in the 10/11/05 profile was the deep peak. The deep water occupying 175 – 300 m in depth, was the most salty, and had high Fe concentrations between 5.0 – 8.0 nM.

Bottom water is a thin layer of water just above the sediments, typically enriched in Fe compared to deep water. Due to the layer's location above the sediment and its thickness, true bottom water was not sampled in every profile. For example, the profile collected on 10/11/05 contains a sample from 400 m; the Fe concentration in this deepest sample was 4 nM smaller than the deep layer above (5.4 – 5.6 nM at 200 – 300 m). The next profile, taken on 10/25/05 (Fig. 4f), also contained a sample from 400 m. Unlike the previous profile, this bottom sample had a Fe concentration of 11.5 nM and was likely collected from the bottom water. The inconsistency in sampling from this bottom water layer was partly due to our sampling location (see Section 2.1 Time Series Sampling Sample

Collection). Sample collection was conducted by positioning the boat above the mooring location. During collection of clean samples, the boat's engines were shut off, leaving the boat to drift with the wind and surface currents. With our location near the continental slope, the boat may have drifted into water of a different depth. Thus, the bottom sample may have been 1 – 5 m from the ocean bottom, resulting in our sampling of the bottom water; or the bottom sample may have been 10 – 20 m from the ocean bottom, resulting in our missing the bottom water layer. In addition, we were limited in measuring our sampling depth by "line out," measured by counting 5 m marks on the line. Comparison between our CTD depth at sampling depths and "line out" depths was good for a majority of samples (<1 m error). However, errors in "line out" accumulated with depth and line angle will affect the deepest sample the most, resulting in shallower depths readings.

4. Discussion

4. 1 Manganese

The typical Mn depth profile for the Santa Monica Bay (Fig. 2a) had a high concentration at the surface with reduced values at depth. This profile was similar in shape to the open ocean Mn depth profile (Klinkhammer and Bender, 1980), although, due to the proximity to land, the Mn concentrations in the Santa Monica Bay were much larger. The shape of the Mn profile results from continual production of reduced Mn in the surface ocean (Sunda *et al.*, 1983). The large input of Mn from aerosol deposition and river water adds soluble Mn(II) and insoluble Mn(III) & Mn(IV) to the ocean. At ocean pH and oxygen concentration, all Mn should slowly oxidize to Mn(IV) and precipitate out in the form MnO_2. However, due to the large amount of humic material in the surface ocean, these oxidized Mn species are continually photo-reduced to soluble Mn(II). Mn(II) is oxidized to the stable Mn(IV) form, but this is a slow process (Stumm and Morgan, 1996) which may take days to complete in surface ocean conditions. Together, the photo-reduction of oxidized Mn species and the slow re-oxidation generated the large Mn concentration we found in the surface ocean.

4.1.1 Manganese Input

In the remote open ocean, the two largest sources of Mn are dry deposition of terrestrial aerosols smaller than 20 mm and terrestrial Mn dissolved in rain water (Guieu *et al.*, 1994). The coastal waters have other sources of Mn, including river input, deposition of coarser particles, and both wet and dry deposition of anthropogenic aerosols (Duce and Tindale, 1991; Siefert *et al.*, 1998), leading to larger Mn concentrations. The sources of Mn to the ocean are not continual processes, but rather punctuated events. Therefore, Mn concentrations in our time series grew and dissipated along with the onset and withdraw of these events (Fig. 5). A significant feature in the Mn time series was the large surface concentration beginning in February 2005 and extending into April 2005. This feature represented an elevation in Mn concentrations over 12 nM to depths of 50 m for over 8 weeks. From January 10th to March 28th, 2005 over 25 cm of rain fell on the Santa Monica Bay area (The Weather Underground, 2008). This rain resulted in low surface salinities in each of the profiles measured over this time extending to March 22nd. We therefore conclude that Mn was washed into the Santa Monica Bay by the large influx of rainwater, most of which was transported via Southern California storm drains. The large quantities of organic material found in this water would serve as the reductant needed to keep Mn in solution. Furthermore, while the initial portion of this event was dominated by the salinity and Mn features, beginning on March 1st, we see an increase in lithogenic silicates at, and just below, the surface (Fig. 6). While the influx of lithogenic silicates supports our conclusion that runoff was the ultimate source of this Mn feature, it is unclear why it only appeared at the end of the event. One explanation may be that storm water runoff supplied the initial Mn pulse. Because this water is largely composed of urban runoff, without erosion, this water contained anthropogenic material such as Mn without an equally large lithogenic silicates component. As the event developed, more standard river channels filled with water and began to carry eroded silicates and Mn to the ocean.

After this rain event, surface Mn concentrations fell to 2-6 nM, but increased below the thermocline. This sub-surface Mn concentration increase extended from 50 – 400 m, and in general Mn concentration were 2-3 nM below 100 m (Fig. 5). We believe the source of this deep Mn was the rain event the previous two months. Slow oxidation resulted in a delay in the transport of Mn from the surface ocean to depth.

The next large Mn surface feature in May 2005 was correlated to a smaller rain event. Between April and May 2005, the Southern California area received 2.5 cm of rain spread over three separate days (April 26th, April 28th, and May 9th) (The Weather Underground, 2008). The salinity signature of these rain events were the fresh water peaks between 5 – 15 m (Fig. 7), and were the result of storm water and river flux into the Santa Monica Bay. From February 2006 to May 2006, Mn concentrations at the surface rose and fell with rain events. During this period of time, Southern California received about half as much rain as it did in the previous year (The Weather Underground, 2008). As a result, the intensity of the Mn peaks was substantially lower than in 2005. In addition, this was the other period in our time series during which there was a large pulse of lithogenic silicates into the surface ocean. We therefore feel confident that these smaller Mn peaks were caused by the smaller rain events in 2006.

The last Mn surface feature in September 2005 is not linked to a rain event. While the region did received light rain (0.5 cm) on September 20th (The Weather Underground, 2008), this occurred at the end of the Mn feature. The high Mn surface concentrations were first measured on August 30th and continued for five weeks. Chlorophyll was high during this period of time, lagging Mn by 2 weeks (Fig. 8). Additionally, this chlorophyll bloom was the largest dinoflagellate bloom seen during the time series and was composed of the red tide forming *Lingulodinium polyedra* (R. Shipe pers. comm.). During this period there were no weather events except one day of light rain. In fact, from August 2005 to September 2005, the wind speed, wind direction, daily temperatures, and cloud cover never deviated from an average Southern California summer diurnal pattern (The Weather Underground, 2008).

Ash deposition from nearby fires did not coincide with this event. There were two fires in the greater Los Angeles area during this time. The Blaisdell Fire burned 5,493 acres in North Palm Springs from August 26 to September 29 (California Department of Forestry and Fire Protection, 2008). Satellite images from this period of time did not show smoke over the Santa Monica Bay (MODIS, 2008), and the Palm Springs watershed does not empty into the Santa Monica Bay. The Topanga Fire, near the Santa Monica Bay, was centered in Simi Valley, CA. This fire burned over 24,000 acres (California Department of Forestry and Fire Protection, 2008), although the wind was directed west, leading smoke away from our sampling area. Furthermore, this fire started on September 28, well after the Mn peak developed, and cannot be the cause of the high Mn concentrations. Thus, we do not have a reasonable explanation for the high surface Mn concentrations in September 2005.

4.1.2 Sub-Surface Manganese Peak

The last Mn feature from the Santa Monica Bay is the persistent large deep peak between 50 – 75 m. This peak first developed in mid-February 2005, after the first of the large rain events, and extended to October 11, 2005. After October 2005, there was no similar Mn peak in our time series. This peak correlates to a shallow Fe peak in the time series (discussed in the Fe section); however, the Mn peak only appears at this particular time, while the shallow Fe peak appears at this depth the following year. While the Mn peak only exists during this one period of time, it is possible that the peak represents a particular water mass, which was influenced by the large 2005 rain event. A shallow water mass which moved close to shore could interact with the surface water, incorporating trace material from the surface. As this water mass moved away from shore and sank to 75 m, it would carry the additional surface material. As described above, this rain event deposited a large quantity of Mn in the Santa Monica Bay. Because 2004 and 2006 did not have these large events, it is possible that the same water mass only incorporated a high Mn concentration after the 2005 rain event.

4.2 Iron

Variations in the individual Fe profiles which differ from the typical nutrient profile shape can be divided into three sections. We define these sections as the surface waters (0 – 15 m), the sub-surface and deep waters (15 – 300 m), and the bottom waters (> 400 m). We will discuss each section separately and present hypotheses for their Fe variability.

4.2.1 Surface Ocean Iron

Fe concentrations in the surface waters were highly variable due to direct influence by the atmosphere and weather. The surface was affected by climate events, upwelling events, and biological blooms. During periods of rain, surface Fe was high and correlated to Mn concentrations (Fig. 9b), resembling a scavenging type profile. During warm periods, Fe concentrations dropped below 0.1 nM. In each of the three years we sampled, the lowest Fe concentrations were reached after the mixed layer was at least 10 – 12 m deep for a month, with moderate surface temperatures (Figs. 3 & 10). Fe concentrations dropped to below 0.1 nM in August and early September 2004; to 0.2 – 0.3 nM in late July and early August 2005; and to 0.4 – 0.5 nM in late May early June 2006. In each of these cases, the mixed layer was below 10 m for several weeks before and during the low Fe event, with temperatures about 17 – 19°C (Fig. 3). As summer temperatures rose, the surface ocean further stratified, forming a shallow mixed layer (4 – 6 m). Fe and Mn concentrations increased following these events.

We hypothesize that the Fe concentrations in the Santa Monica Bay and the greater Southern California Bight region can be driven low enough to cause Fe limitation. Given the proper combination of surface water stratification, temperature, and biological blooms, Fe concentrations can drop to between 50 – 200 pM, which have been found to cause Fe limitation (Martin and Gordon, 1988). We believe the mechanism for Fe depletion in this region is the rapid uptake of Fe and other nutrients in combination with a moderately large mixed layer. In the month preceding the low Fe periods we observed an upwelling event (Fig. 10) and correspondingly higher NO_3 concentration (Fig. 11). With an increase of NO_3,

there can be an increase in biological production and removal of other nutrients such as Fe from the water (Wong *et al.*, 2002). With the moderate depth mixed layer, any input of Fe from atmospheric deposition or river flux was more effectively diluted. As the NO_3 concentrations dropped (Fig. 11), biological uptake of Fe slowed. This was followed by rising temperatures and a reduction in mixed layer depth, thus reducing the dilution from the deeper mixed layer. In each of these events, Fe concentrations rose following the increased stratification of the surface ocean, eliminating the brief possibility of Fe limitation (Fig. 3). Our attempts at observing Fe limitation in the Santa Monica Bay in 2006 were not successful (data not shown). These experiments were conducted in July to September 2006, a time frame when low Fe concentrations were observed in 2004 and 2005. However, in 2006, the lowest Fe concentrations were between May and June, and were not at a concentration (0.4 – 0.5 nM) that Fe limitation has been observed. Fe concentrations during our experiments were between 1 – 3 nM, and their profiles were consistent with recent atmospheric input. We therefore observed only NO_3 limitation, as would be expected in those situations.

Other surface processes involving Fe, biological blooms, and carbon uptake are currently being examined by several research groups, including ourselves. These studies will not be discussed here. However, we will continue to work on these processes and present the work elsewhere.

4.2.2 Temperature and Salinity Structure of the Santa Monica Bay

Analysis of Fe concentrations within the sub-surface and deep water requires a discussion of the temperature and salinity (TS) structure of the Santa Monica Bay. Within the time series, the TS structure was composed of seven water bodies, including the surface water (section 4.2.1) and bottom water (section 4.2.4). Figure 12 shows these water bodies and their mixing patterns. Within the sub-surface and deep water, we define the water bodies as:

1. Deep Water: Salinity 34.1 – 34.3 PSU, Temperature 8.5 – 9.8 °C,
2. Shallow Fresh Water: Salinity 33.2 – 33.5 PSU, Temperature 10.2 – 12.9 °C,
3. Shallow Salty Water: Salinity 33.4 – 33.9 PSU, Temperature 9.8 – 11.7 °C,
4. Mixed Layer Fresh Water: Salinity 32.0 – 33.3 PSU, Temperature 11.8 – 16.4 °C,
5. Mixed Layer Salty Water: Salinity 32.4 – 33.5 PSU, Temperature 11.4 – 20.0 °C.

Figure 13 shows four distinct water mass end members which mixed together within the Santa Monica Bay. These were the bottom water, the deep water, the shallow water, and surface water masses. The mixed layer water mass was formed from mixing between the surface water and the shallow water and spans the thermocline. The TS characteristics of the surface water mass and its mixing were largely controlled by seasonal atmospheric temperatures as discussed in section 4.2.1.

In general, each water mass changed depths over the year. During the winters of 2004-2005 and 2005-2006, the Santa Monica Bay had a deep mixed layer, 40 – 50 m (Fig. 10). Within this mixed layer, temperatures were cool, ranging from 14.5 – 16 °C, and due to sporadic rain fall the salinity was low and variable (<32 – 33.3 PSU) (Figs. 7 & 10). The fresh mixed layer water mass occupied the region above and to the base of the thermocline, while the fresh shallow water mass occupied the base region below the thermocline. The temperature change across the thermocline was about 4 °C, while the change in depth was as much as 80 m. Upon the onset of spring (in both 2005 and 2006), the prevailing winds changed, from a weak on-shore/off-shore diurnal pattern to a strongly off shore pattern (The Weather Underground, 2008), which corresponded to a brief upwelling event each year characterized by a shallow cold salty water. Atmospheric temperatures rose, causing a stratification of the water column, isolating the cold water, and forming a shallow mixed layer. Just as in the deep winter mixed layer, the salty mixed layer water mass was within the mixed layer extending to the base of the thermocline, while the salty shallow water mass was below the new thermocline. However, the salty water masses (mixed layer and shallow) were more salty and occupied shallower depths, 5 – 15 m for the mixed layer

water and 25 – 60 m for the shallow water. The mixed layer water still defined the thermocline. Due to the rising summer temperatures and increased stratification, the temperature change over the thermocline was as much as 10 °C (Fig. 13), but now the change in depth was at most 30 m (Fig. 10). The shallow mixed layer persisted until September or October, when atmospheric temperatures fell, lowering the temperature of the surface ocean and deepening the mixed layer back to 50 m in December or January. The bimodal nature of both the mixed layer and shallow water masses did not perfectly correspond to mixed layer depth. The mixed layer depth was controlled by the region's three seasons, with the spring upwelling separating the shallow mixed layer in the summer and the deep mixed layer in the winter. This divided the year into March through October and October through March (Fig. 10). The two modes divided the year in March through August and August through March (Fig. 13). While the mixed layer depth remained shallow in August, the mixed layer water and shallow water masses returned to their fresh mode.

The deep water mass rose and fell with the change in the mixed layer; however, its TS properties were consistent throughout the year (Fig. 13). During the late summer and winter, the deep water mass was between 250 – 300 m and rose to between 150 – 200 m during the spring (Figs. 7 & 10).

4.2.3 Sub-Surface Iron

The Fe concentration profiles (Fig. 2b) showed large peaks within the sub-surface and deep water. We identified these peaks (as described in section 3.2) and overlaid their TS properties onto figure 12 (Fig. 13). We also overlaid the depths of these peaks onto the time series contour plots of temperature and salinity to identify a temporal pattern in peak depth (Figs. 14). Figure 13 shows that the different peaks corresponded to the different water masses, and as these water masses changed, both their TS properties and depth, they remained associated with the high Fe peaks. The top peak (as defined in section 3.2) was within the mixed layer during the winter and extended to the base of the thermocline in the

spring and summer (Fig. 14a). The second large peak occupied the shallow water mass and was located below the thermocline. As the thermocline depth shallowed in the summer, so did the depth of this shallow water Fe peak (Fig. 14a). Both the top and shallow Fe peaks followed the change in depth associated with temperature, rather than salinity (Fig. 15). The third small transient peak lay along the mixing line between shallow and deep water (Fig. 13) and also changed depth with the temperature depth change (Fig. 15). The fourth broad peak is found within the deep water mass and occupied a large depth range from 175-300 m (Fig. 13).

The consistency of each type of Fe peak to occupying a specific water mass indicates that the Fe source for each type of peak was specific to that water mass, rather than random additions of Fe into the system. Therefore, further understanding of the water mass movements may lead to an understanding of the source of the Fe peaks. We also found that lithogenic silicate concentration peaks were consistently within specific water masses and correlated well with Fe peaks (Fig. 4). The correlation between Fe and lithogenic silicate potentially gives us a history of the water mass movements and possible source of Fe.

To investigate this correlation between Fe and lithogenic silicate, we normalized the lithogenic silicate and Fe concentrations with equation 1

$$T_{norm} = \frac{T_i - \overline{T}_{Tot}}{\sigma_{T_{Tot}}} \quad , \qquad \text{Eq. 1}$$

where T is the tracer, i represents individual samples, $\overline{T}_{Tot}$ represents the mean of the tracer in the whole data set, and σ represents standard deviation of the tracer in the whole data set. We plot the histograms of normalized Fe and lithogenic silicate in figure 16. Both populations were skewed from a Guassian, with an extended tail into high values. In addition, Fe appeared to have two large populations centered at -1 and 0. Lithogenic

silicate may have two large populations, but the double peak feature may also be due to under-sampling.

From inspection of the time series, we hypothesized that the large tails in both histograms correspond to the large peaks which are seen in both lithogenic silicate and Fe profiles (Figs. 3 & 6). However, the histograms do not link the lithogenic silicate and the Fe together; the histograms only show that there are similar populations. Therefore, we cannot determine if the peaks within the histograms corresponded to each other. We then plotted the cross histogram of the Fe and lithogenic silicate histograms. This was done by selecting a bin within the Fe histogram (starting with normalized Fe values between -1.5 and -1.3). We identified the lithogenic silicate data points which corresponded to the Fe data points within that bin. A histogram was constructed from these lithogenic silicate data, and the process was repeated for all the Fe histogram bins (-1.5 – 4.2). We plot the normalized Fe and normalized lithogenic silicate cross histogram in figure 17.

Figure 17 demonstrates that while there was correlation between lithogenic silicates and Fe, there were also several modes in both tracers which do not correlate. We identified four regions of this cross plot with possible oceanographic significance.

1. "High LSi": identified by lithogenic silicate > 0.9 and Fe < 0.7,
2. "High Fe": identified by Fe > 0.7 and lithogenic silicate < 0.5,
3. "Fe mode 2": identified as the intersection between the higher of the two Fe modes and the large lithogenic silicate peak,
4. "Correlation section": these data points lie within a region of the cross plot outlined by the two dashed lines of slope 1 (Fig. 11). This section encompasses the lower large Fe mode, "Fe mode 1," and extends out to higher normalized concentrations of both lithogenic silicate and Fe.

It is significant that the region of the cross plot with both high lithogenic silicate and high Fe is empty. This signifies that the two tails of the individual histograms are not correlated, and that the correlation we observe in the individual profiles is predominately within the lower concentration modes. In an attempt to map these population distributions onto the ocean and gain some knowledge about their spatial structure, we divided the Fe and lithogenic silicate histograms into depth regions (Fig. 18 & 19). This allowed us to view the spatial distribution of the normalized concentration populations. From figures 18 and 19, we see that most of the large lithogenic silicate peaks are clustered within the top 10 m of the ocean without a corresponding high Fe population, while about half of the high Fe peaks are found within the bottom water. This spatial disconnect between the two histograms' tails means that there are separate oceanographic processes working each species.

We hypothesize that the "High LSi" region is occupied by points which result from atmospheric deposition. Either wet or dry deposition can add lithogenic silicate to the surface ocean in high concentrations (section 4.1.1), but due to solubility limitations, the Fe concentration may not be significantly increased (Chapters 2 and 3). We can see an example of this lithogenic silicate addition without an addition of Fe in figure 9c. An example of a large lithogenic silicate addition with only a moderate Fe addition is shown in figure 9a. Furthermore, we hypothesize that half of the high Fe population within the tail is the result of the flux of Fe into the bottom water from the sediment (discussed in section 4.2.4). Unfortunately, the bottom water samples do not have lithogenic silicate measurements (see Methods), and we cannot rule out Fe sources such as sediment entrainment, which would increase colloidal Fe and also carry a high lithogenic silicate signature. In addition, these bottom points are not represented in the cross plot because there is no corresponding lithogenic silicate (Fig. 17). Therefore, the "High Fe" region of the cross plot is not explained by the bottom water Fe flux.

To explain the oceanographic relevance of the "High Fe" region, the peaks within the "High LSi" not explained by atmosphere-ocean interactions, and the observed correlation between lithogenic silicate and Fe, we divided the normalized lithogenic silicate and Fe cross plot into depth regions (Figs. 20 & 21). The depths chosen are identical to those in the depth-specific histograms, and roughly correlate to the depths in which we see the different types of high Fe peaks. Scanning through these depth cross plots we see that there is little correlation between lithogenic silicate and Fe in the top 30 m. There are three points within the correlation region that correspond to high Fe points (Fig. 20c), but most of the high peaks in Fe do not directly correlate to the high lithogenic silicate peaks. From 30 – 50 m (Fig. 20c-e), the data is spread through the three regions with only 10 points within the correlated region, also indicating that there is little correlation between lithogenic silicate and Fe. However, looking at figure 14 we see that 39 of the 40 mixed layer high Fe peaks are within the top 50 m, whereas only 14 of the 41 shallow water high Fe peaks (1 mid-depth water) are within the top 50 m. Identifying the location of each of the shallow peaks within the top 50 m reveals that there are 2 high Fe peaks between 20 – 30 m, 5 high Fe peaks between 30 – 40 m, and 8 high Fe peaks between 40 – 50 m (Fig. 14), roughly the same number of points in the correlated region of the depth cross plots (Fig. 20c-e). There is correlation between lithogenic silicate and Fe in the 50 – 75 m and 75 – 100 m depth regions, as seen in the high density of points within the correlated area. Inconsistencies in the correlation at these depths may be due to the differences in depth between the tracer's peak maxima (as described in section 3.2). In the 100 – 175 m depth range, Fe mode 2 begins to develop, but correlation between the two tracer peaks is still present. Between 175 – 300 m, Fe mode 2 dominates the depth region and high lithogenic silicate peaks vanish. This depth-dependent tracer correlation can lead us to a greater understanding of the mechanism behind Fe addition to these water masses.

We conclude that only one type of high Fe peak is correlated to lithogenic silicate. The mixed layer high Fe peaks are not correlated with lithogenic silicate. High lithogenic silicate

in this region is mostly due to atmospheric deposition, and high Fe peaks are from an, as of yet, unknown source. The shallow water high Fe peaks are correlated to high lithogenic silicate. Both high Fe and high lithogenic silicate peaks follow the depth changes of the water mass; therefore, they must be added to this water mass before it enters our observation station, rather than added at a constant depth and moving towards our location. The deep water high Fe peaks showed little correlation with lithogenic silicate, and the mid-depth high Fe peaks which correlated to lithogenic silicate were most likely due to the mixing of high Fe and lithogenic silicate shallow water with the deep water mass. The correlation between Fe and lithogenic silicate in the shallow water was preserved in the new mixture. The irregularity of these high Fe peaks within the mid-depth water mass in time, depth, and concentration may be explained by changes in the mixing pattern of these two water masses.

Fe and lithogenic silicate may be added to the shallow water mass through sediment interaction as the shallow water mass approaches the shore. One possible mechanism for both Fe and lithogenic silicates to be added to a sub-surface layer in 400 m ocean water is for the water mass to have moved close to shore at one point in its history and interacted with the continental slope. Because breaking internal waves can generate turbulence at the sediment-water boundary (Taylor, 1993), the shallow water mass only needs to flow past the continental slope when internal waves break. In addition, our proximity to the continental slope increases the likelihood of wave breaking due to vertical movement of water upslope as wave fronts propagate towards the shore (Lorke *et al.*, 2005). This upslope movement can disturb the stratification within the water column, causing convective mixing at the slope's sediment-water interface. Mixing of the sediments and pore fluid into the water layer will add both Fe and lithogenic silicates. Within the sediments there is Fe(II) production, which can supply the pore fluid enough Fe to generate the observed peaks (see section 4.2.4). In addition, lithogenic silicates will be prevalent in

the coastal sediments due to the proximity to land. Therefore, any suspension of these sediments will incorporate both lithogenic silicate and Fe into a nearby water mass.

Despite the likelihood of sediments to become entrained in a water mass interacting with the continental slope, our data cannot specifically determine if this is the cause of the high Fe and lithogenic silicate peaks. However, Changming Dong from the University of California Los Angeles (UCLA) was able to run a physical oceanography model of the Santa Monica Bay and surrounding region to answer that question. Based on wind data from May and June 2002, he ran the ocean model and tracked the water masses which reached the observation site. He then compiled that data and produced a movie which followed the top 80 m of the water column from our station back through time (Mov. 1). The movie shows that one day before entering our location, the water mass at 30 – 70 m flows past the Palos Verdes peninsula. Because the mixed layer is shallow in late May and June, the shallow high Fe peaks will occupy the 30 – 70 m depth range. Although this brief movie does not show direct contact with the sediment, it is encouraging that the shallow water mass stays near the shore and towards the Palos Verdes peninsula rather that away from the shore and the sediment. Thus, the mechanism of sediment entrainment from the continental slope remains a possibility.

We have considered other mechanisms for Fe addition. Sub-surface ground water discharge into the ocean has been characterized in the Mediterranean (Swarzenski *et al.*, 2006) and can carry dissolved metals. However, it is also characterized by decreases in salinity, as large as 20 PSU, depending on the flow of ground water and the depth of the coastal ocean (Swarzenski *et al.*, 2006). We did not see a consistent association of the high Fe peaks with decreases in salinity; however, we did observe a seasonal salinity decrease which corresponded to the period of time when the mixed layer high Fe peaks were predominately above the thermocline (Fig. 14a). Due to their seasonality, the peaks occurring between October 2004 and April 2005 may more likely be explained by river plumes rather than ground water (Buck *et al.*, 2007).

To truly identify the sources of the Fe peaks, and the nature the Fe cycles in the coastal water, we must have a better understanding of the water masses themselves. We have begun to identify the TS structure of these water masses, as well as the seasonal changes in depth and salinity. However, we do not have a good understanding of the flow patterns and sources of these water masses outside the California Bight. Despite this lack of knowledge, we have been able to determine that there is structure in the subsurface Fe data despite the many processes occurring.

4.2.4 Bottom Water Iron

There was a large increase in Fe concentration with the bottom water depth (Fig. 2b). This increase in concentration can be explained by the interaction between the sediment pore fluids and the bottom water. Within the sediments, organic carbon oxidation depletes oxygen concentrations several cm below the sediment water interface. Under the suboxic region, organic carbon is oxidized by a series of other species, including Fe, each with decreasing oxidative power (Froelich *et al.*, 1979). Fe(II), resulting from Fe oxidation of organic carbon, enriches the pore fluids which diffuse into the bottom water (Hammond *et al.*, 1990). Fe(II) fluxes from the Central California coast (Monterey Bay) are 1.3 – 11 $\mu mol \cdot m^{-2} \cdot day^{-1}$ (Berelson *et al.*, 2003). Although the measurements of oxygen concentration we have for the entire time series are in sensor voltage from November 2005 – September 2006 (Fig. 22), they show reduced values at depth, and we know from others that the bottom of the Santa Monica Bay is suboxic (5 – 35 μmol/Kg) (Berelson, 1991). In addition, we have O_2 concentration measurements for the San Pedro Basin on 11/07/04 and the Santa Monica Bay from November 2005 (Fig. 23). The San Pedro Basin is a suboxic basin adjacent directly up-current of our observation station, with bottom water O_2 concentration of 5.5 μmol / Kg (Fig. 24). We believe that the source of bottom water in the Santa Monica Bay can be identified in the San Pedro Basin water column.

We compared the TS structures of the San Pedro Basin on 11/07/04 and the Santa Monica Bay on 11/02/04 and 11/16/04. The San Pedro Basin TS structure mapped well onto both

Santa Monica Bay profiles (Fig. 25). The deep water, as defined in section 4.2.2, was particularly similar between the San Pedro Basin and the later Santa Monica Bay profile, although there is fresh deep water intrusion in the Santa Monica Bay profile from 11/02/04. The deep water mass in both locations was found at the same depth (210 – 250 m), and the mixing line between it and bottom water followed the same pattern in all three profiles. Bottom water from these two days in the Santa Monica Bay had a temperature of 7.3 – 7.6 °C and salinity of 34.25 – 34.26 PSU. Water with this TS characteristic in the San Pedro Basin corresponded to a depth range of 385 – 430 m, the same depth of our bottom water. We conclude that the bottom water found at our observation station in the Santa Monica Bay was a mixture of the region's deep water mass and the bottom water mass found in the San Pedro Basin. Therefore, the oxygen concentration found in the San Pedro Basin at 400 m, 28 μmol/Kg, should be found in the bottom water of the Santa Monica Bay. This is at the high end of suboxic conditions (Johnson *et al.*, 1996), and the Fe(II) half life in this water is 4 times smaller than in San Pedro Basin bottom water (30 minutes. compared to 2 hours) (Murray and Gill, 1978; Rose and Waite, 2002; Sung and Morgan, 1980). This is slow enough to maintain approximately 2.5 % of the average bottom water Fe concentration as Fe(II) (Rose and Waite, 2002). This is within range of (Ussher *et al.*, 2007), who found suboxic bottom waters from the English Channel and North Sea to contain 8% Fe(II). The remaining total iron concentration was composed of ligand complexed Fe(III) >50% and colloidal Fe(III) in the form FeOOH.

The Fe concentration in the bottom water had several seasonal components. We plot the difference in Fe concentration between the bottom two samples (400 - 300 m) against the bottom temperature (Fig. 26). There are two distinct water masses which arise from this plot. The first water mass had a mixing pattern with a slope of -0.14 °C/ nM and extended from the cloud of data centered at a temperature of 7.7 °C to the coldest temperatures. The other water mass had a mixing pattern with a shallower slope and extended to the largest Δ[Fe]. We labeled each point with the corresponding date in figure 26 to show the seasonal

pattern of these two water masses. The colder water mass (mixing along a line with slope -0.14 °C/ nM) occurs in the spring, from March to early May in both 2005 and 2006. The high Fe water mass (mixing along a line with slope -0.02 °C/ nM) is composed of profiles from both the winter and summer and does not appear to have any further seasonal pattern. This seasonal appearance of the cold water mass was seen in the Fe time series (Fig. 3), as the low Fe masses which occurred during the spring. In addition, there is a decrease in bottom water temperatures (Fig. 10) corresponding to the upwelling events in both 2005 and 2006. Thus, upwelling in the Santa Monica Bay affected the entire water column, and pulled cold Fe poor water in from another source.

Isolation of this spring event from the other Fe profiles allowed us to discern another seasonal pattern. We divided the remaining profiles into winter and summer profiles. The winter was defined as the period of time after mixed layer deepening until the spring event, while the summer was defined as the onset of mixed layer warming following the spring event until the deepening of the mixed layer. Typically, the summer was from mid-May to late November or early December, while the winter was from late November or early December to March or April. Averaging the Fe profiles for the summer and winter seasons showed the second seasonal pattern (Fig. 27). Both the summer and winter bottom water masses had Fe concentrations of 8 – 9 nM. However, while the winter bottom water mass appeared to have a linear and conservative mixing with the deep water mass at 300 m, the summer bottom water mass appeared to lose Fe at a greater rate than was explained by deep water mixing. There are two possible explanations for this non-conservative mixing. The first is that oxygen concentrations in the deep water mass were lower in the winter, allowing Fe(II) to mix into the deep water without additional oxidation and subsequent precipitation from solution. We do not believe that this is a likely scenario. The oxygen concentrations (in voltage, Fig. 22) from November 2005 to February 2006 in the bottom and deep water were equivalent or slightly higher than in the summer of 2006; therefore, the opposite Fe mixing pattern would be expected to result. In addition, Fe (II) is a small

component (< 10%) of the total Fe concentration; thus, a change in O_2 concentration would only effect a small percentage of the total Fe. The second hypothesis is that Fe(III) is scavenged from the water column at a greater rate during the summer as compared to the winter due to a greater particle flux to the sediment. Berelson *et al.*, (2003) observed a seasonal cycle of organic carbon oxidation correlated to primary production in the Monterey Bay. They concluded that because primary production varied over the year, peaking in early summer following the seasonal upwelling events, the rain of organic carbon out of the surface ocean to the sediments varied, supplying the sediment with a seasonal flux of fresh organic material to be oxidized. Seasonal fluxes of particles have also been observed in the Southern California Bight (Rathburn *et al.*, 2001; Shipe and Brzezinski, 2001). In each case, biogenic silicates were observed in the bottom water particle fluxes following diatom blooms in the late spring and summer. Our data show that there was a seasonal increase in biogenic silicates corresponding to the spring blooms (Fig. 28) and that this increase was not limited to the surface waters but extended into the deep water (Fig. 28 53). Furthermore, deep ocean biogenic silicates were more concentrated in the summer than the winter (Fig. 29). Because Fe is a particle reactive element (Stumm and Morgan, 1996), both ligand bound Fe (defined in Chapter 2) and colloidal Fe can readily adsorb onto particles. An increase in particles in the deep ocean would lead to increased Fe adsorption and removal from the dissolved phase. We conclude that the seasonal removal of Fe from deep water was caused by the seasonal flux of particles, with biogenic silicates being a likely source of these particles.

5. Conclusions

We have observed the Santa Monica Bay Observatory Oceanographic Mooring site for two and a half years. Over that time we have determined that the coastal ocean has three distinct seasons, a long summer, a winter, and a brief spring associated with a yearly upwelling event. Mn concentrations are elevated to as much as 25 nM in the surface ocean. Rain events appear to increase the surface concentration of Mn as well as lithogenic silicate.

Furthermore, the large influx of Mn to the Santa Monica Bay during the winter of 2004-2005 caused an increase in Mn concentrations below the thermocline.

We have observed the several seasonal changes within the water column, from the surface to the bottom water. Summer mixed layer depths are between 5 – 15 m, while winter mixed layer depths are 20 – 50 m. The water masses associated with the surface mixed layer and the shallow water mass below the thermocline have a change in both their salinity and temperature in response to the season change. The sub-surface iron peaks are associated with these specific water masses, and remain with those masses throughout the seasons. In addition, we concluded that lithogenic silicate and Fe in these high tracer peaks have a specific terrigenous source, which we hypothesize is the entrainment of sediment and pore fluids following sub-surface wave breaking against the continental slope. We also observed a season change in bottom water Fe concentrations and the mixing patterns with the deep water mass. Seasonal changes in biological productivity changed the flux of particles to the deep, changing the reactive surface concentration in the water. During the summer these particles are in high concentration and scavenge Fe from the water column. During the less productive winter, the particle concentration is lower, and thus bottom water Fe concentrations mix with the deep water without scavenging.

FIGURE CAPTIONS

Figure 1: The Santa Monica Bay Observatory Oceanographic Mooring site is anchored at 33° 55.9' N, 118°42.9' W. Due to surface and sub-surface currents the mooring rotates on its chain about this point. Time series samples were collected as close to this mooring site as possible.

Figure 2: Depth profile of dissolved Mn (A) and Dissolved Fe (B). Both profiles are an average of all profiles in the time series. Mn concentrations were high (7 – 10 nM) in the surface ocean, and rapidly decrease in concentrations. Fe concentrations were lowest in the surface ocean (2 nM), and increased to over 12 nM in the deep. The peak in Fe concentration at about 75 m was a persistent feature throughout the time series.

Figure 3: Contour plot of dissolved Fe concentration over time within the Santa Monica Bay. Our time series ran from July 20, 2004 to September 19, 2006. Individual samples are plotted as black dots. Fe concentrations are contoured every 1 nM from 0 – 12 nM, and are lowest in the period following the spring upwelling events when mixed layer depths are 10 – 15 m (Fig. 10). Overlaid in the shallow water panel is the mixed layer depth (black line). Moderately deep summer mixed layer depths (15 m) were observed in July –August 2004 and 2005, and May – June 2006. In each of the timeframes Fe concentrations were at their lowest for the year. After each of these periods, the mixed layer depth shallowed and Fe concentrations increased.

Figure 4: Profiles of Fe (blue), Mn (green), and lithogenic silicate (red) from the Santa Monica Bay from February 15, 2005 (A), May 9, 2005 (B), November 16, 2004 (C), October 11, 2005 (D), August 16, 2005 (E), and October 25, 2005 (F). The high Fe peaks seen in these profiles can be divided into four categories based on their depth and shape: a mixed layer peaks seen in D, and shallow water peaks seen in B and C, a mid-depth peak seen in A and F, and a deep water peak seen in E. The shallow water peaks have a strong correlation to lithogenic silicate.

Figure 5: Contour plot of dissolved Mn concentration over time within the Santa Monica Bay. Individual samples are plotted as black dots. Mn concentrations are contoured every 1 nM from 0 – 12 nM. High Mn concentrations at the surface are driven by reduction by organics and large rain fall events. Overlaid in the shallow water panel is the mixed layer depth (black line).

Figure 6: Contour plot of dissolved lithogenic silicate concentration over time within the Santa Monica Bay. Individual samples are plotted as black dots. Samples were only collected from the surface to 300 m. Lithogenic silicate was measured in the Rebecca Shipe's lab at UCLA, and are contoured every 0.1 μM from 0 – 1.0 μM. High lithogenic silicate concentrations at the surface are caused by wet and dry atmospheric deposition as well as storm water runoff. Sub-surface lithogenic silicate peaks were correlated with dissolved Fe peaks.

Figure 7: Contour plot of salinity over time within the Santa Monica Bay. Data was taken from the CTD sensors, which had a 1 m depth resolution. The location of the samples taken along with the CTD cast are plotted as black dots. Overlaid in the shallow water panel is the mixed layer depth (black line). Salinity is contoured every 0.1 PSU from 32.5 – 34.3 PSU. Fresh water additions during the rain events of 2005 were observed between January and April

2005. The relative high surface water salinity in the winter of 2005-2006 was the result of reduced rain fall.

Figure 8: Contour plot of chlorophyll-a over time within the Santa Monica Bay. Individual samples are plotted as black dots. Samples were only collected from the surface to 300 m. Chlorophyll-a measurements were made in the Rebecca Shipe's lab at UCLA, and are contoured every 0.3 μg/L from 0 – 3.0 μg/L. Chlorophyll-a was higher in concentration during the two spring upwelling events, the result of diatom blooms. In addition, the period of time between September 2005 and October 2005 had the largest recorded chlorophyll-a concentrations within the time series, and resulted from the red-tide causing dinoflagellate - *Lingulodinium polyedra*.

Figure 9: Profiles of Fe (blue), Mn (green), and lithogenic silicate (red) on September 21, 2004 (A), May 1, 2005 (B), and September 27, 2005 (C). In A, The surface water increases in Fe, Mn, and lithogenic silicate correlate to the shallowing of the mixed layer and atmospheric deposition. In B, the surface water increases in Fe, Mn, and lithogenic silicate correlate to heavy rains during the winter of 2005. In C, the surface water increases in Mn and lithogenic silicate are due to atmospheric deposition.

Figure 10: Contour plot of temperature over time within the Santa Monica Bay. Data was taken from the CTD sensors, which had a 1 m depth resolution. The location of the samples taken along with the CTD cast are plotted as black dots. Upwelling events were observed in April 2005 and March 2006. These are characterized by cold waters (< 11 °C) rising to the surface and bottom water temperatures falling to 6 – 7 °C. Overlaid in the shallow water panel is the mixed layer depth (black line) which changed depth over the seasons, deep in the winter (40 – 50 m) and shallow in the summer (5 – 20 m). This change in mixed layer depth divided the year into three seasons: summer, winter, and spring when the season upwelling event occurs.

Figure 11: Contour plot of NO_3 concentrations within the Santa Monica Bay. Individual samples are plotted as black dots. Samples were only collected from the surface to 300 m. Surface values of NO_3 were typical low (< 0.01 μmol/Kg), however the spring upwelling events brought NO3 concentrations of ~ 5 μmol/Kg to the surface.

Figure 12: Temperature (T) versus salinity (S) plot. The block dots represent the TS properties of the individual samples. There are 6 distinct water masses, which are characterized as the vertices of the curved regions of the TS plot.

Figure 13: TS plot with labeled water masses, and overlaid with of the high Fe peaks as defined in section 3.2. The block dots represent the TS properties of all the individual samples, the high Fe peaks are labeled with red circles (mixed layer peaks), blue squares (shallow water peaks), green diamonds (mid-depth water peaks), purple triangles (deep water peaks), and orange crosses (bottom water peaks). There are 6 distinct water masses, circled and labeled as bottom water, deep water, shallow water (fresh and salty), and surface water (fresh and salty).

Figure 14: Contour plot of shallow water temperature (A) and salinity (B) within the Santa Monica Bay. Data was taken from the CTD sensors, which had a 1 m depth resolution. The location and type of high Fe peaks are indicated by the symbols, mixed layer peaks (circles), shallow water peaks (squares), mid-depth peaks (diamonds). Overlaid is the mixed layer depth

(black line). Each type of peak stays within a range of temperatures and moved up and down in the water column with the depth of the mixed layer and temperature contours.

Figure 15: Contour plot of temperature within the Santa Monica Bay. Data was taken from the CTD sensors, which had a 1 m depth resolution. The location and type of high Fe peaks are indicated by the symbols, mixed layer peaks (circles), shallow water peaks (squares), mid-depth peaks (diamonds), and deep water (triangle). Each type of peak stays within a range of temperatures and moved up and down in the water column with seasons.

Figure 16: Histogram of normalized Fe concentrations (A), and normalized lithogenic silicate concentrations (B). The population of each concentration was multi-modal and skewed towards larger concentrations. The conversion line between the normalized number and the concentration are seen in the inset.

Figure 17: The cross plot of the normalized Fe and lithogenic silicate histograms. The separation of the normalized histograms in the cross plot allows for analysis of correlation between lithogenic silicate and Fe. There are four regions of interest: High LSi (Fe < 0.7, lith. SiO_4 > 0.9), High Fe (Fe > 0.7, Lith. SiO_4 < 0.5), Fe mode 2 (Fe ≈ 0.3), and the region of correlation between lithogenic silicate and Fe (occupied the region between the dashed gray lines).

Figure 18: Depth specific normalized Fe histogram. The normalized Fe histogram (Fig. 27) is divided in depth regions associated with high Fe peaks. Low concentration modes are seen in the upper 40 m, where the higher concentration mode develops. The tail associated with the Fe histogram is split between the bottom water and depth range of 50 – 75 m.

Figure 19: Depth specific normalized lithogenic silicate histogram. The normalized lithogenic silicate histogram (Fig. 28) is divided in depth regions associated with high Fe peaks. There is no data below 350 m for lithogenic silicate. High lithogenic silicate is seen in the 0 – 20 m depth range.

Figure 20 – 21: Depth stack of the cross plot of the normalized Fe and lithogenic silicate histogram. Depth regions are equivalent to those used in the depth specific histograms. From 0 – 30 m there is little correlation between Fe and lithogenic silicate. There is correlation between the shallow water high Fe peaks and lithogenic silicates. Bottom water high Fe peaks are not seen in these cross plots because there is not corresponding lithogenic silicate points.

Figure 22: Contour plot of oxygen (reported in sensor voltage) within the Santa Monica Bay. Data was taken from the CTD sensors, which had a 1 m depth resolution. The conversion to chemically relevant units could not be done on all profiles due to sensor failures, therefore contour data profiles are reported in voltage.

Figure 23: Oxygen profile from November 11, 2005. Sensor conversions were working properly for this profile, and units are in μmol O_2/Kg. Bottom water O_2 concentrations were 25 μmol O_2/Kg.

Figure 24: CTD profile of the San Pedro Basin on November 11, 2004. The San Pedro Basin is a 880 m deep suboxic basin to the south of the Santa Monica Bay. Oxygen concentrations fall to 5.5 μmol O_2/Kg at 880 m, and 28 μmol O_2/Kg at 400 m.

Figure 25: TS plot of two profiles from the Santa Monica Bay, 11/2/04 (blue line) and 11/16/04 (red line), and the profile from November 11, 2004 in the San Pedro Basin (black line). TS characteristics of all three water masses are similar. Water located between 385 – 430 m in both the San Pedro Basin and the Santa Monica Bay have the identical TS properties. High Fe peaks are shown with circles, filled blue from the Santa Monica Bay and open for the San Pedro Basin.

Figure 26: Temperature versus Δ Fe for the bottom water. Δ Fe was calculated by subtracting the bottom sample (~400 m) from the deep sample (~300 m). The data fit fall along two trends. The first is the Cold Water Mass which extends below 6 °C and has a slope of -0.14 °C/nM, and the High Fe Water Mass which extends to ΔFe values above 6 nM and has a slope of -0.02 °C/nM. Each data point is labeled with the date it was collected. The Cold Water Mass trend is composed of points which correspond to March, April, and early May 2005 and 2006 (blue text), while the High Fe Water Mass has no correlation to time of year (red text). There is a period of four profiles (6 – 8 weeks) in which the deep water mass warmed; these profiles are represented by the four data point in black forming a vertical line at ΔFe = 8 nM. The remaining data is labeled in green text.

Figure 27: The three season average Fe profiles over the entire time series. We divided the Santa Monica Bay into three seasons, defined as: summer (red), the period after upwelling to the mixed layer deepening (> 20 m); winter (blue), the period from the mixed layer deepening to the upwelling event; spring (green), the time of the upwelling event.

Figure 28: Contour plot of biogenic silicate over time within the Santa Monica Bay. Individual samples are plotted as black dots. Measurements of biogenic silicate were made in the Rebecca Shipe's lab at UCLA and are contours every 0.3 μM from 0 – 3 μM. Surface biogenic silicate is composed of diatoms and is highest following the spring upwelling events into the summer. Winter concentrations are lower than spring and summer concentration.

Figure 29: Integrated deep biogenic silicate (75 – 315 m). Integration of each profile is drawn in black, while the seasonal average is draw as red bars. The two spring upwelling events have the largest deep biogenic silicate concentration. The summer integrated biogenic silicate concentration is about twice that of the winter integrated biogenic silicate concentration.

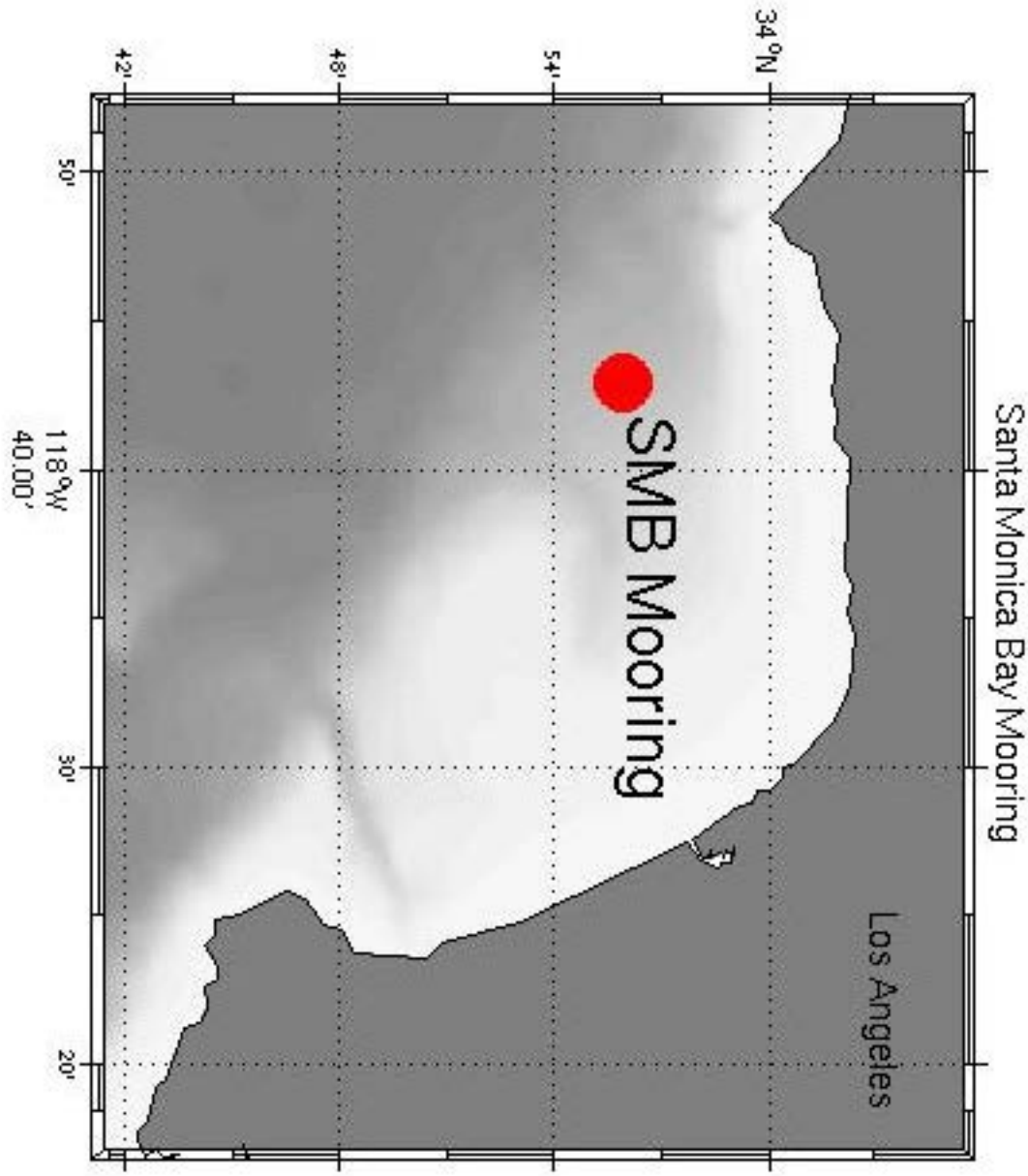
Santa Monica Bay Mooring
Los Angeles
SMB Mooring
34°N
54'
48'
42'
50'
30'
20'
118°W
40.00'

Depth (m)
0
50
100
150
200
250
300
350
400
450
0
2
4
6
8
10
12
Manganese, nM
(A)
Iron, (nM)
(B)
Depth (m)

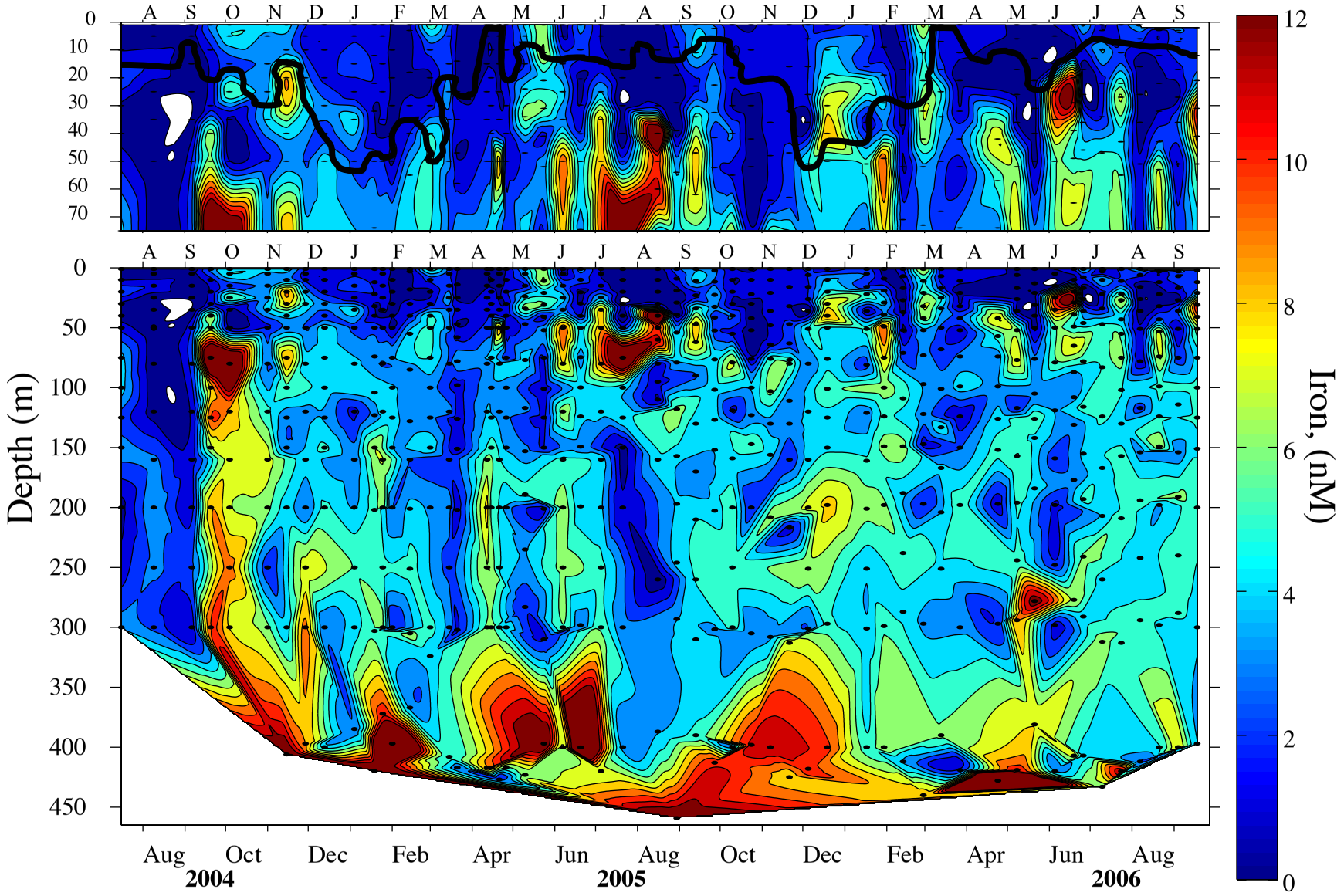
A S O N D J F M A M J J A S O N D J F M A M J J A S
0
10
20
30
40
50
60
70
0
50
100
150
200
250
300
350
400
450
Depth (m)
Aug Oct Dec Feb Apr Jun Aug Oct Dec Feb Apr Jun Aug
2004
2005
2006
12
10
8
6
4
2
0
Iron, (nM)

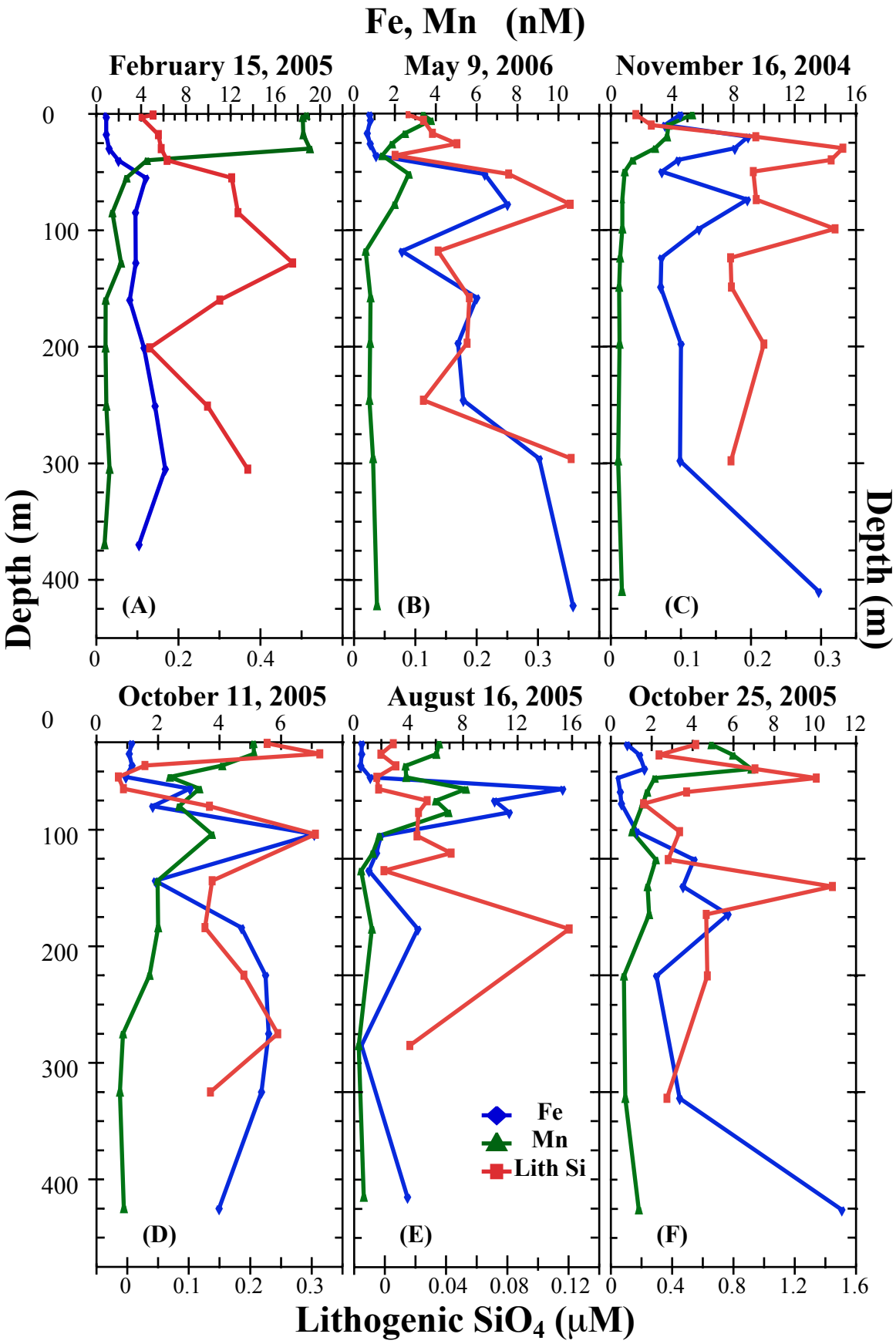
Fe, Mn (nM)
February 15, 2005
May 9, 2006
November 16, 2004
October 11, 2005
August 16, 2005
October 25, 2005
Depth (m)
Depth (m)
(A)
(B)
(C)
(D)
(E)
(F)
Fe
Mn
Lith Si
Lithogenic SiO4 (μM)

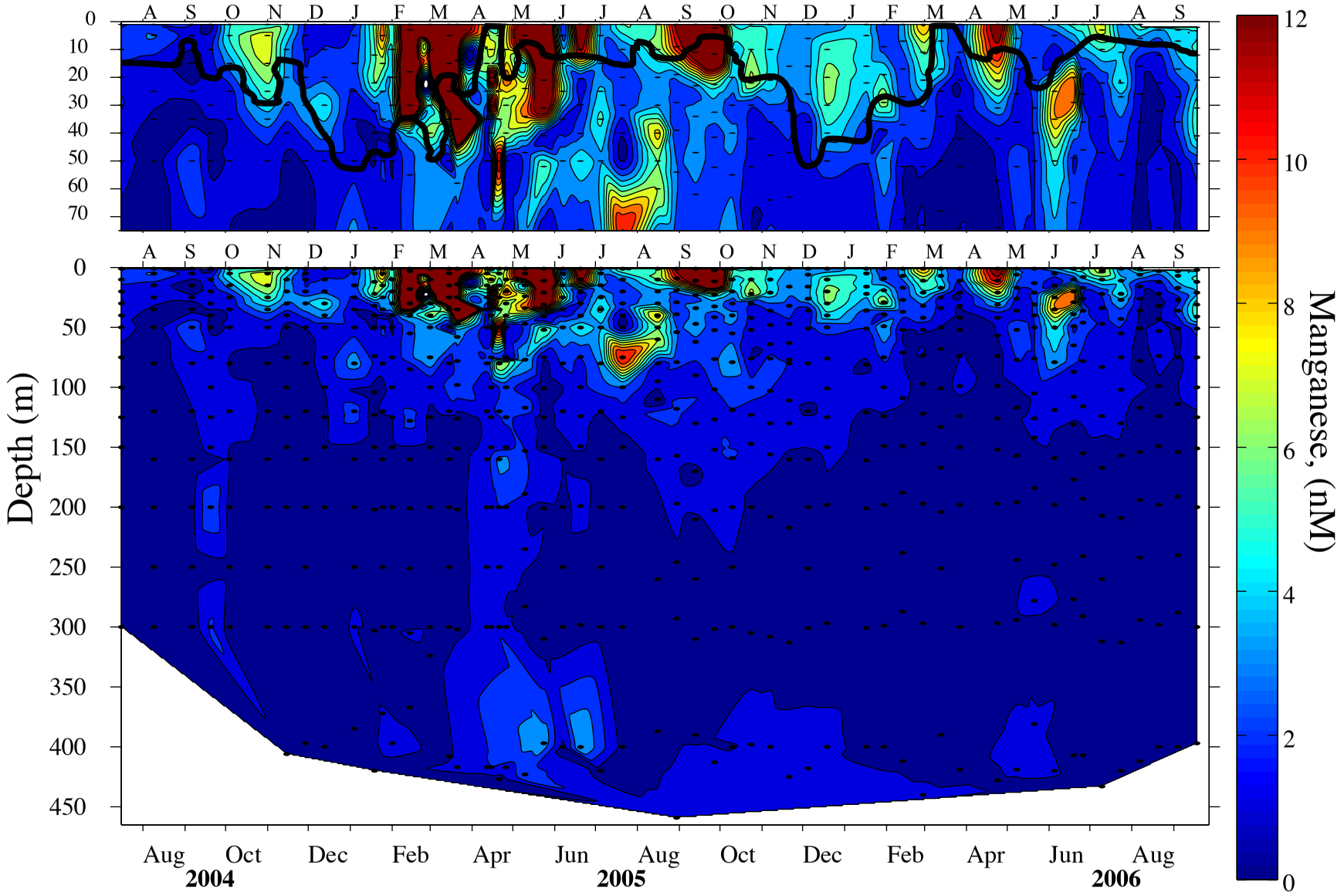
A S O N D J F M A M J J A S O N D J F M A M J J A S
0
10
20
30
40
50
60
70
0
50
100
150
200
250
300
350
400
450
Depth (m)
Aug
Oct
Dec
Feb
Apr
Jun
Aug
Oct
Dec
Feb
Apr
Jun
Aug
2004
2005
2006
12
10
8
6
4
2
0
Manganese, (nM)

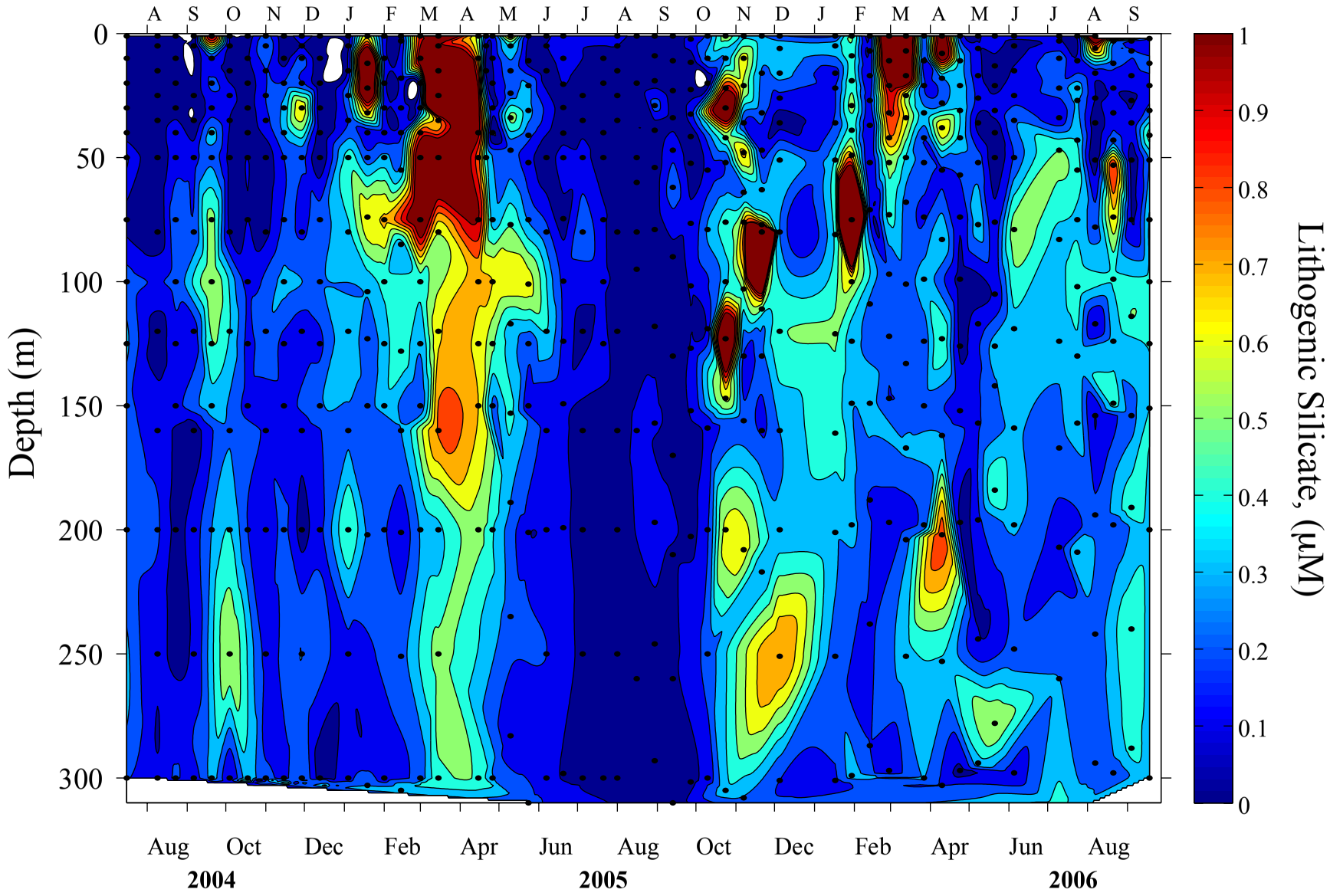
A S O N D J F M A M J J A S O N D J F M A M J J A S
0
50
100
150
200
250
300
Depth (m)
Aug Oct Dec Feb Apr Jun Aug Oct Dec Feb Apr Jun Aug
2004
2005
2006
1
0.9
0.8
0.7
0.6
0.5
0.4
0.3
0.2
0.1
0
Lithogenic Silicate, (µM)

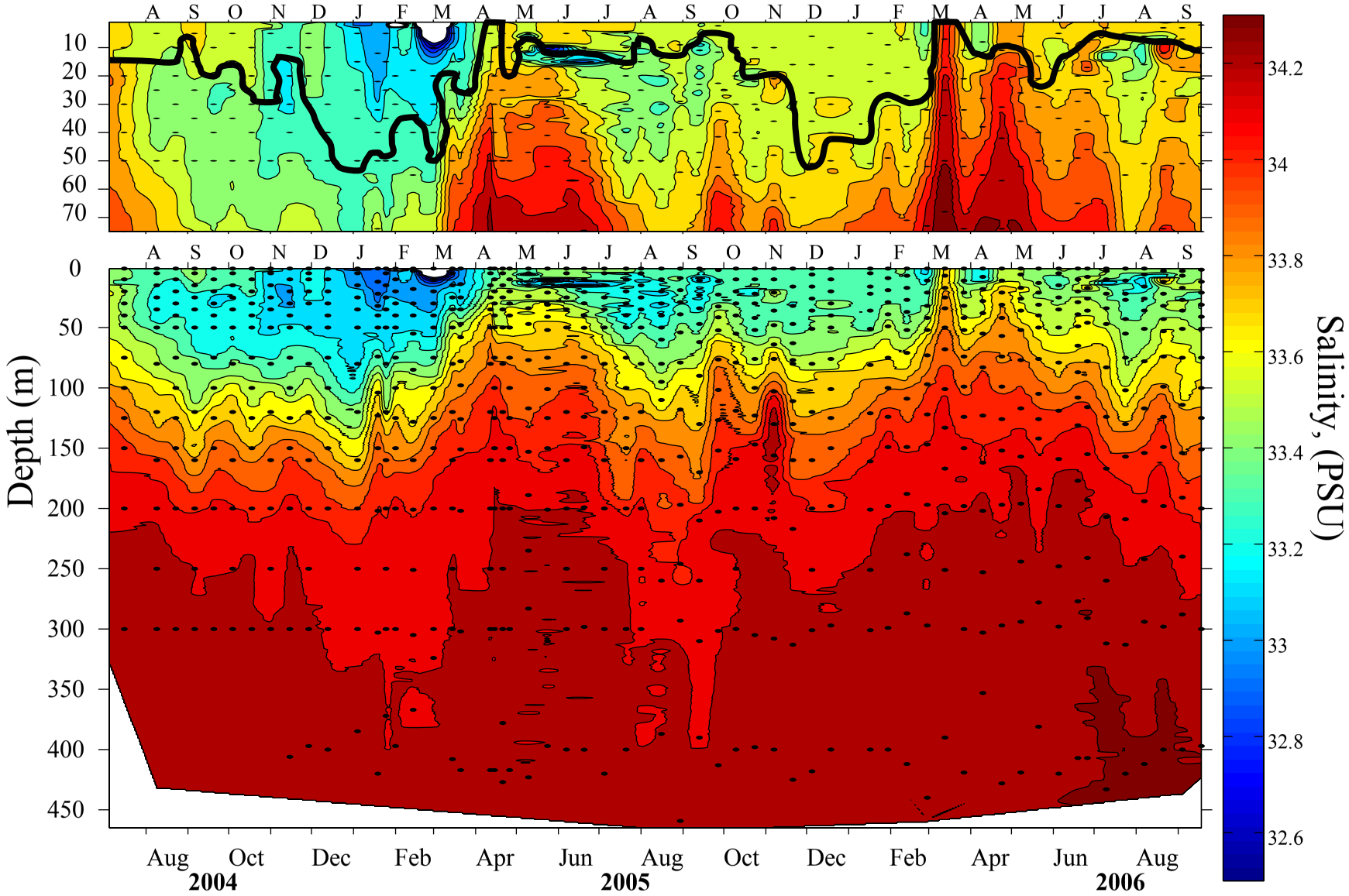
A S O N D J F M A M J J A S O N D J F M A M J J A S
10
20
30
40
50
60
70
0
50
100
150
200
250
300
350
400
450
Depth (m)
Aug
Oct
Dec
Feb
Apr
Jun
Aug
Oct
Dec
Feb
Apr
Jun
Aug
2004
2005
2006
34.2
34
33.8
33.6
33.4
33.2
33
32.8
32.6
Salinity, (PSU)

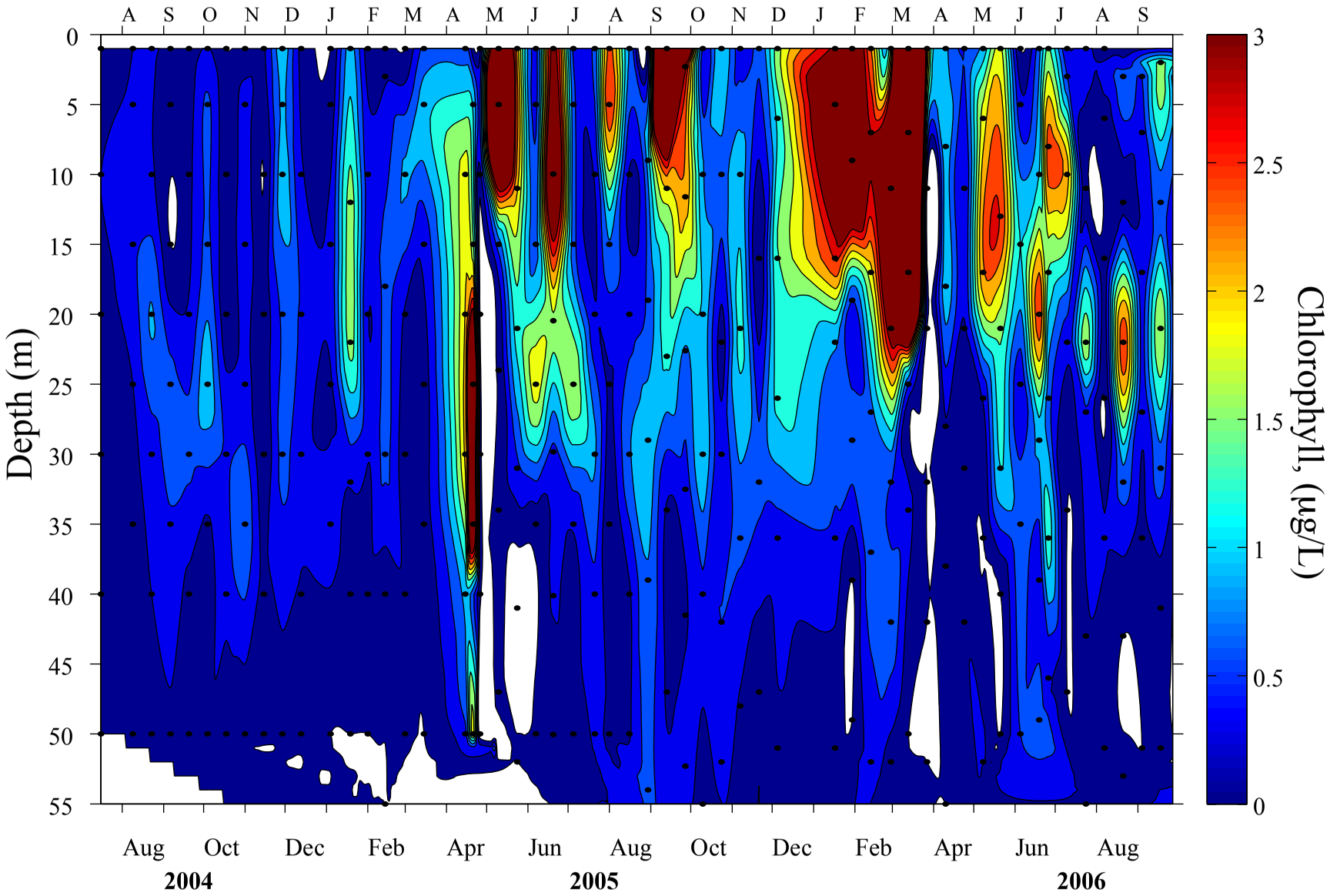
A S O N D J F M A M J J A S O N D J F M A M J J A S
0
5
10
15
20
25
30
35
40
45
50
55
Depth (m)
Aug Oct Dec Feb Apr Jun Aug Oct Dec Feb Apr Jun Aug
2004
2005
2006
3
2.5
2
1.5
1
0.5
0
Chlorophyll, (ug/L)

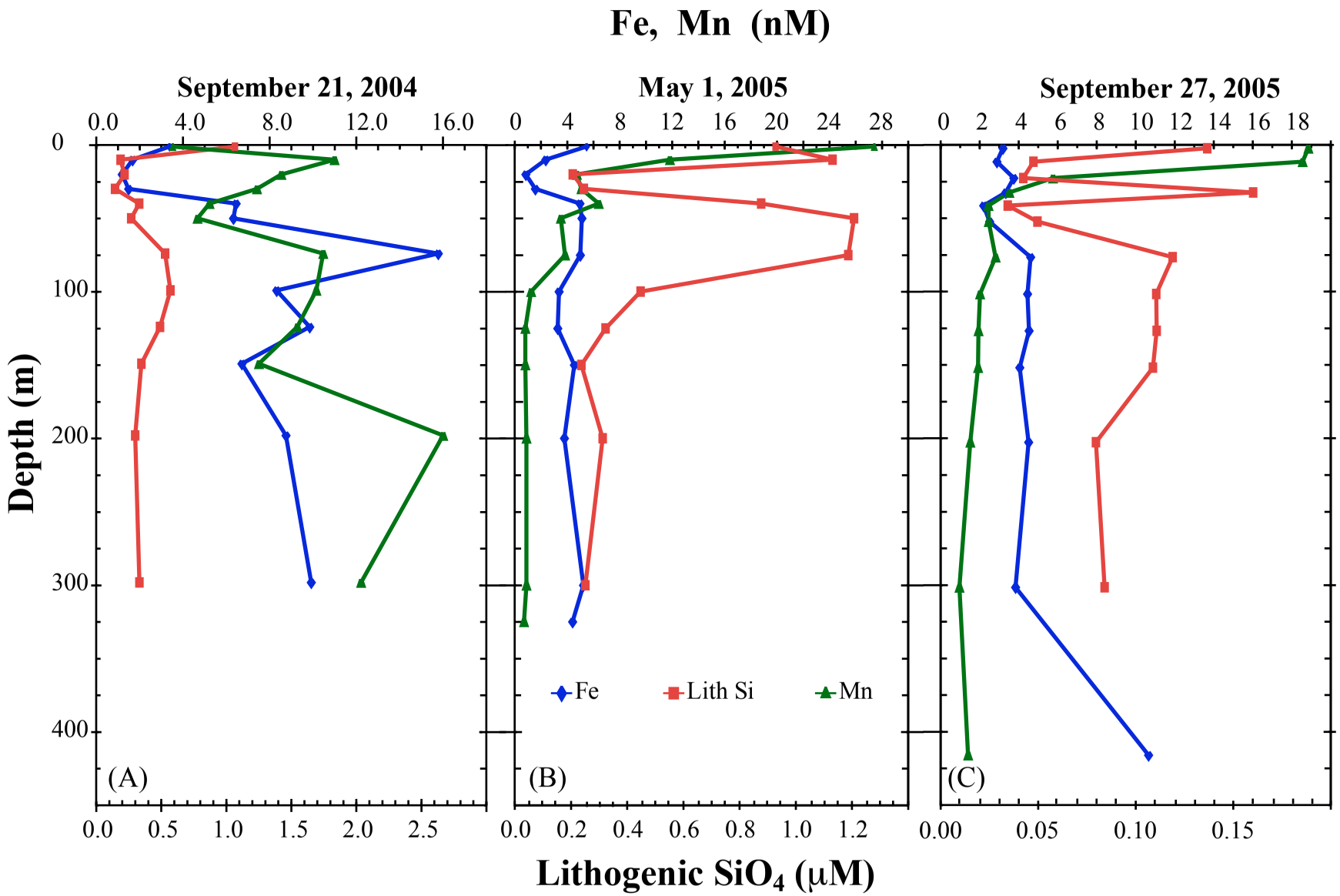
Fe, Mn (nM)
September 21, 2004
May 1, 2005
September 27, 2005
Depth (m)
Fe
Lith Si
Mn
(A)
(B)
(C)
Lithogenic SiO4 (μM)

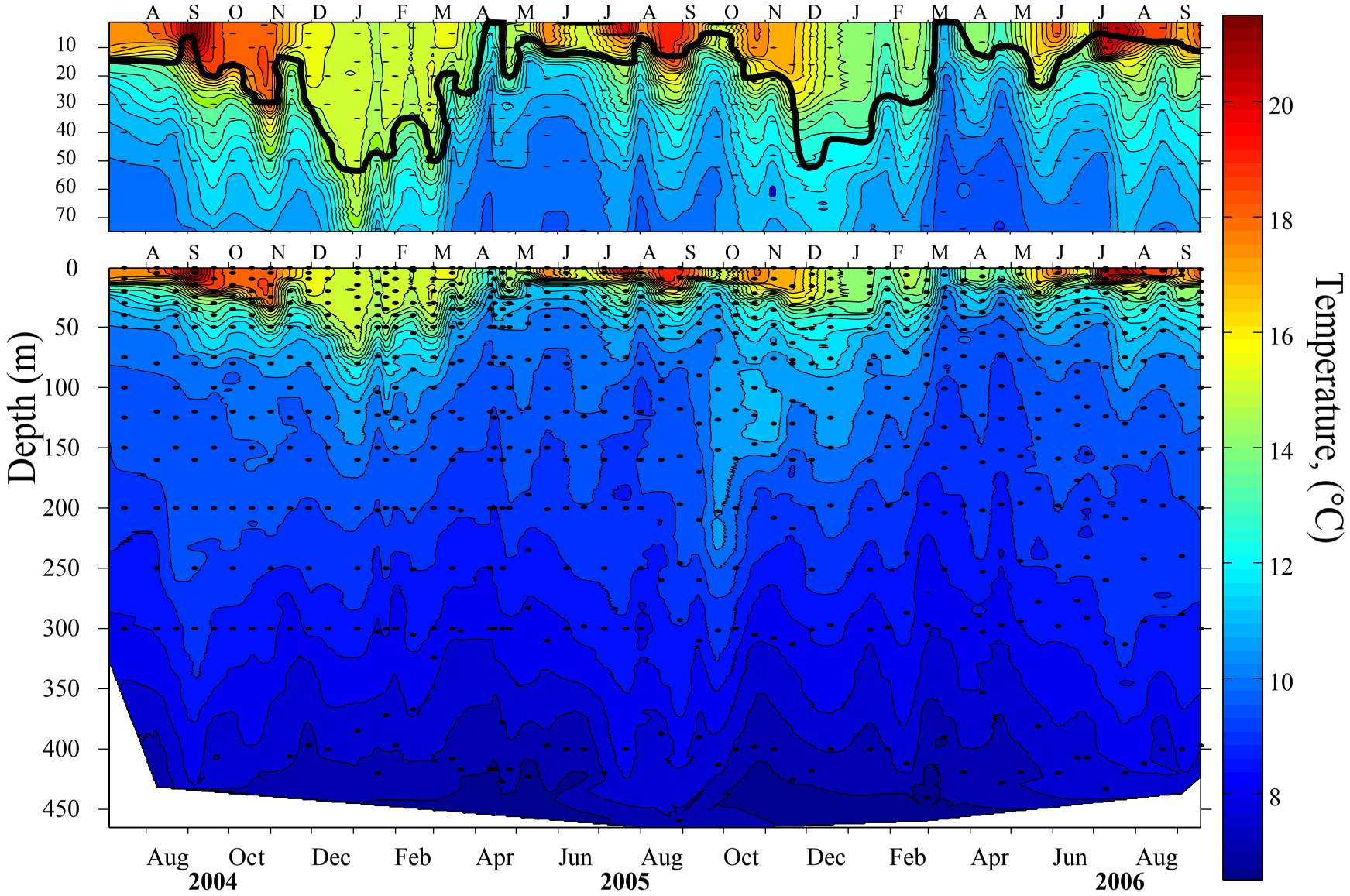
A S O N D J F M A M J J A S O N D J F M A M J J A S
10
20
30
40
50
60
70
0
50
100
150
200
250
300
350
400
450
Depth (m)
Aug
Oct
Dec
Feb
Apr
Jun
Aug
Oct
Dec
Feb
Apr
Jun
Aug
2004
2005
2006
20
18
16
14
12
10
8
Temperature, (°C)

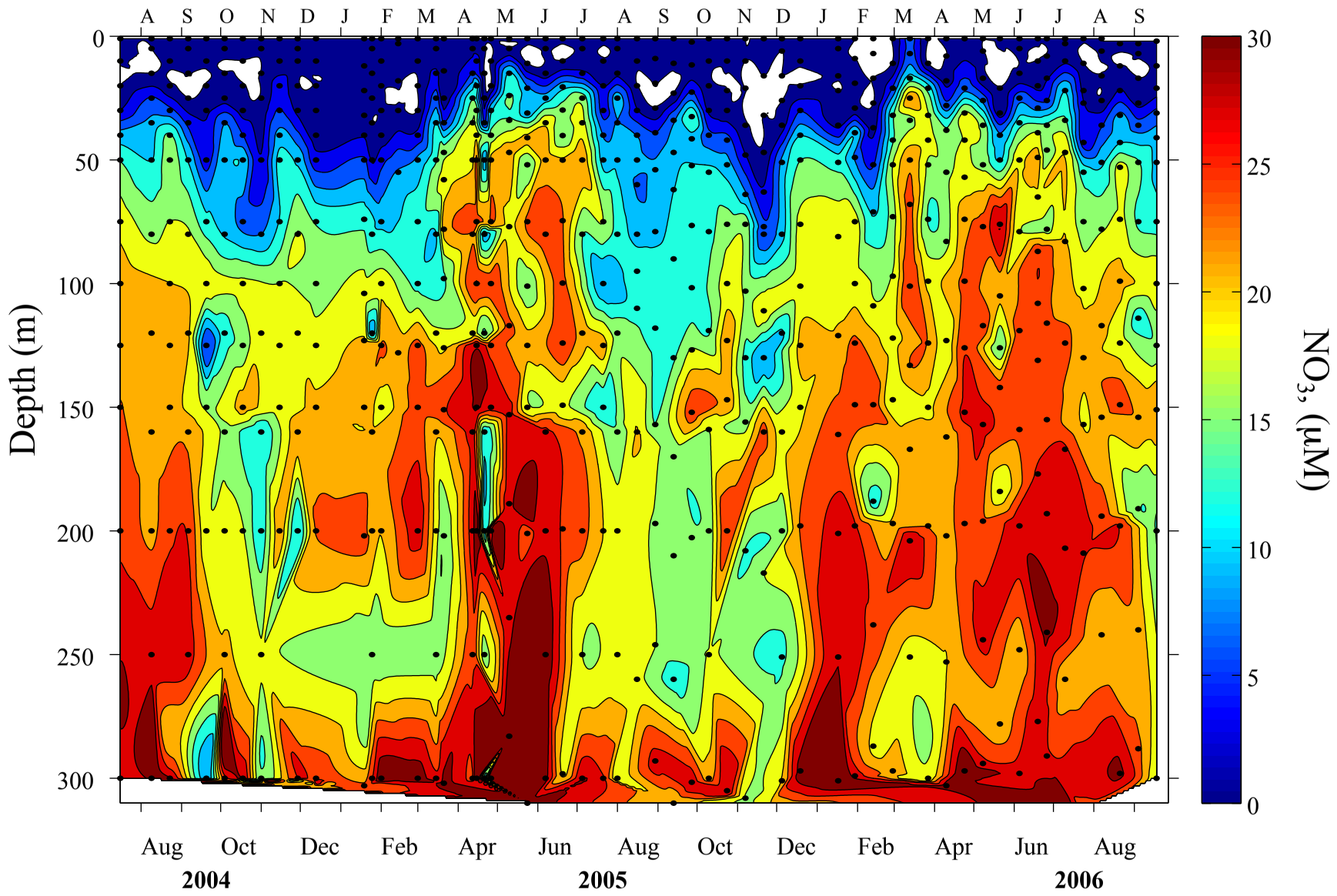
A S O N D J F M A M J J A S O N D J F M A M J J A S
0
50
100
150
200
250
300
Depth (m)
Aug Oct Dec Feb Apr Jun Aug Oct Dec Feb Apr Jun Aug
2004
2005
2006
30
25
20
15
10
5
0
NO3, (µM)

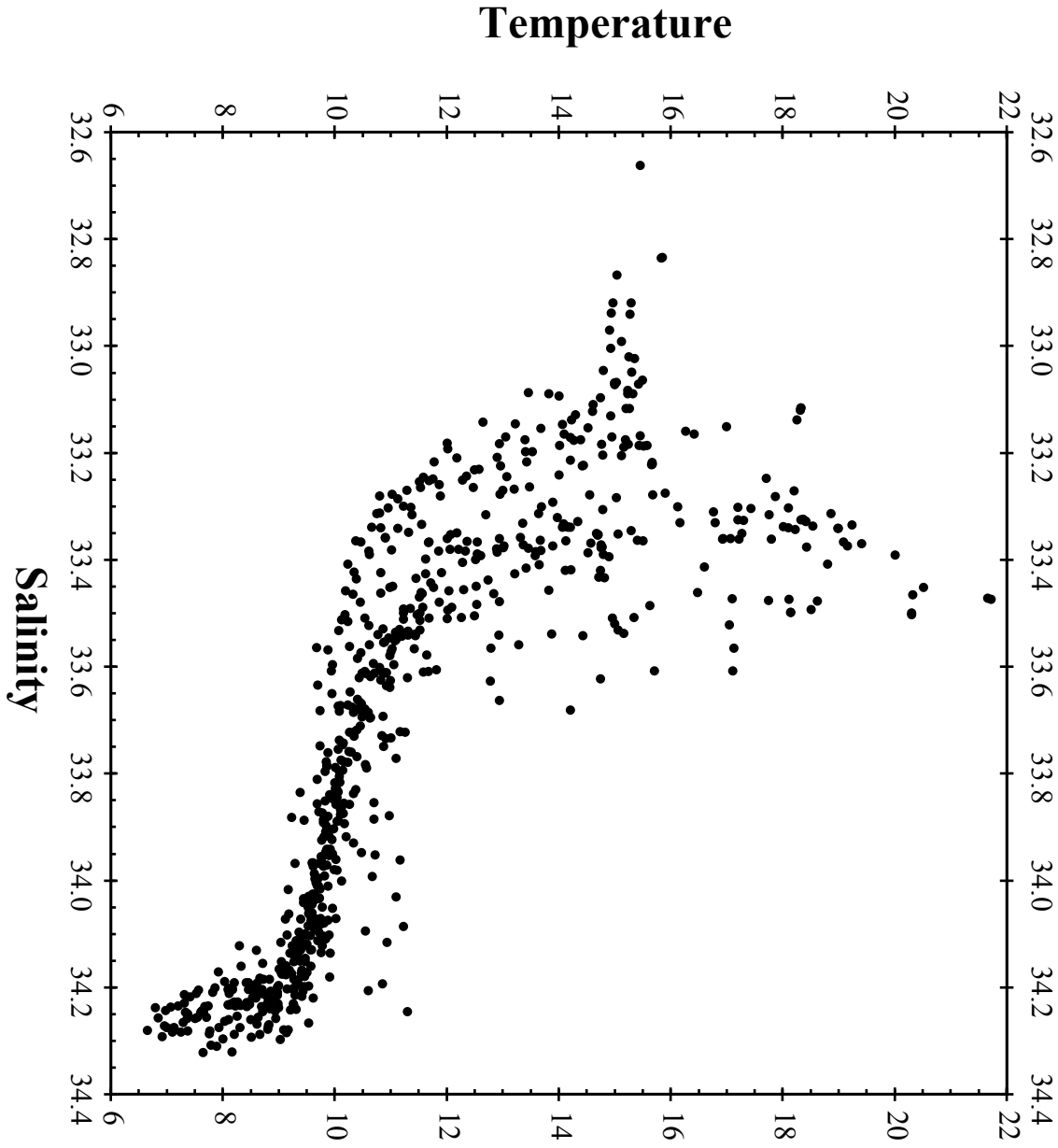
Temperature
Salinity
22
20
18
16
14
12
10
8
6
32.6
32.8
33.0
33.2
33.4
33.6
33.8
34.0
34.2
34.4

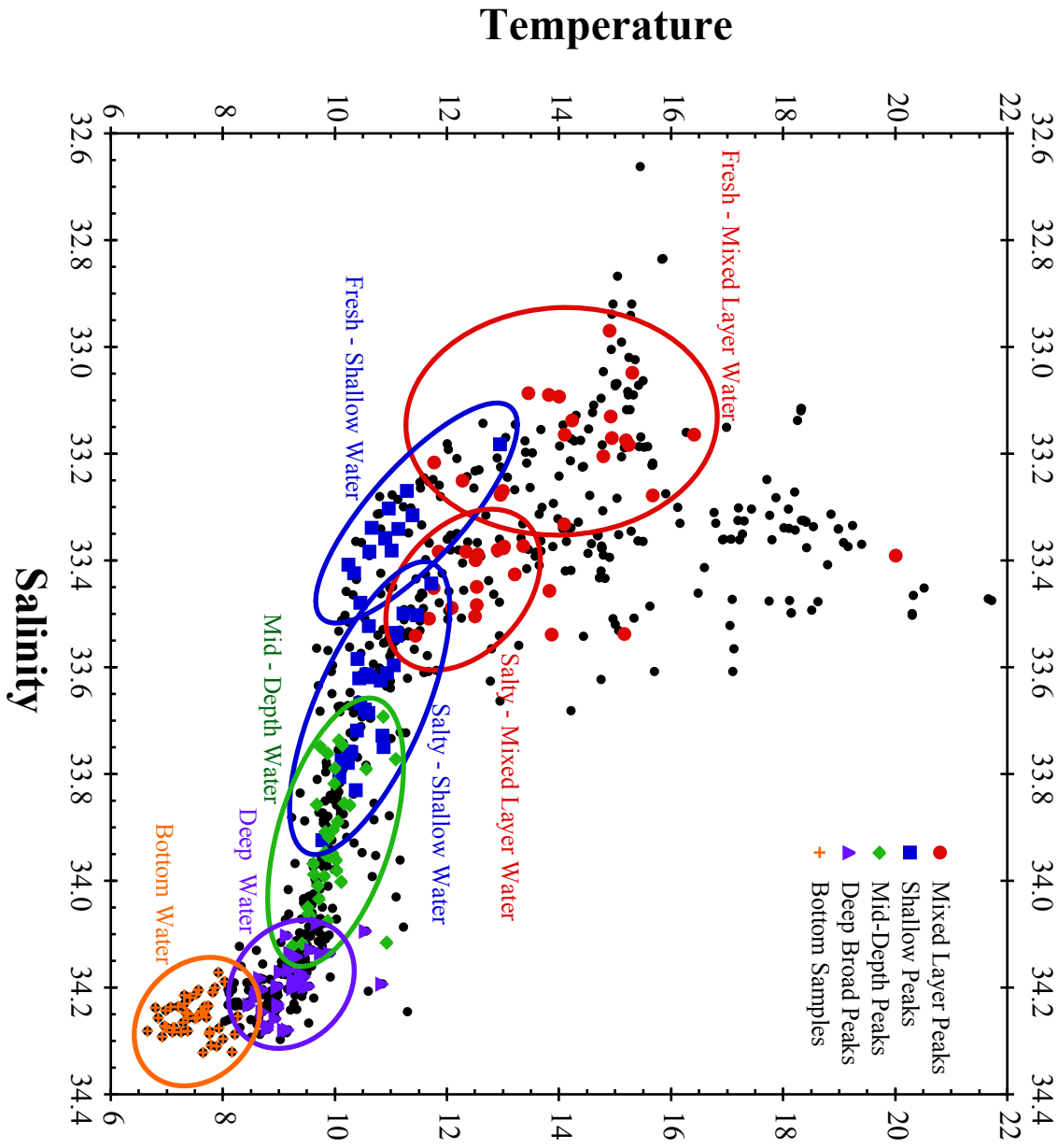
Temperature
Salinity
Mixed Layer Peaks
Shallow Peaks
Mid-Depth Peaks
Deep Broad Peaks
Bottom Samples
Fresh - Mixed Layer Water
Salty - Mixed Layer Water
Fresh - Shallow Water
Salty - Shallow Water
Mid - Depth Water
Deep Water
Bottom Water
22
20
18
16
14
12
10
8
6
32.6
32.8
33.0
33.2
33.4
33.6
33.8
34.0
34.2
34.4

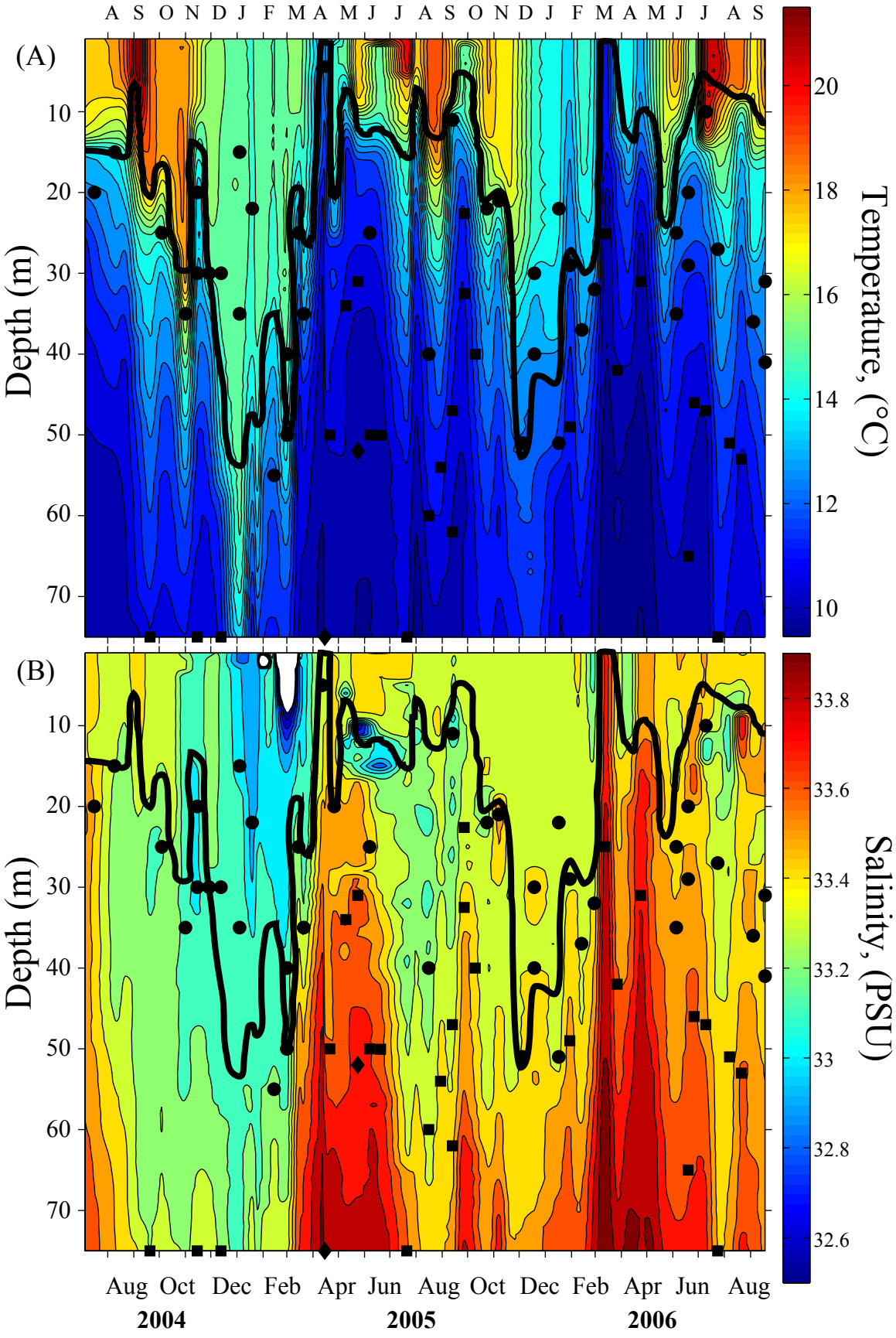
A S O N D J F M A M J J A S O N D J F M A M J J A S
(A)
Depth (m)
10
20
30
40
50
60
70
Temperature, (°C)
20
18
16
14
12
10
(B)
Depth (m)
10
20
30
40
50
60
70
Salinity, (PSU)
33.8
33.6
33.4
33.2
33
32.8
32.6
Aug Oct Dec Feb Apr Jun Aug Oct Dec Feb Apr Jun Aug
2004
2005
2006

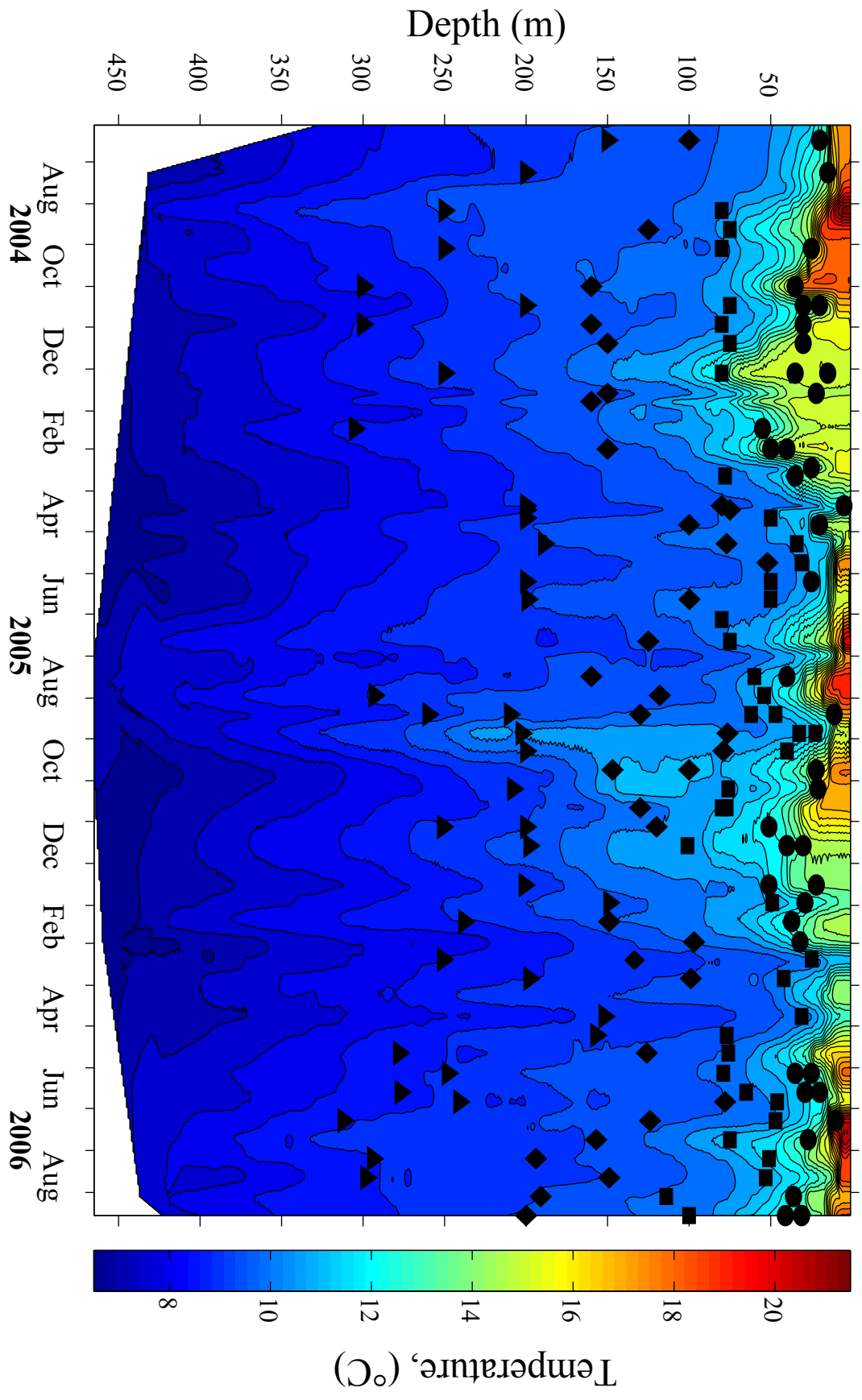
Depth (m)
50
100
150
200
250
300
350
400
450
A S O N D J F M A M J J A S O N D J F M A M J J A S
Aug Oct Dec Feb Apr Jun Aug Oct Dec Feb Apr Jun Aug
2004
2005
2006
Temperature, (°C)
8
10
12
14
16
18
20

Histograms of Iron and Lithogenic Silicate Distributions

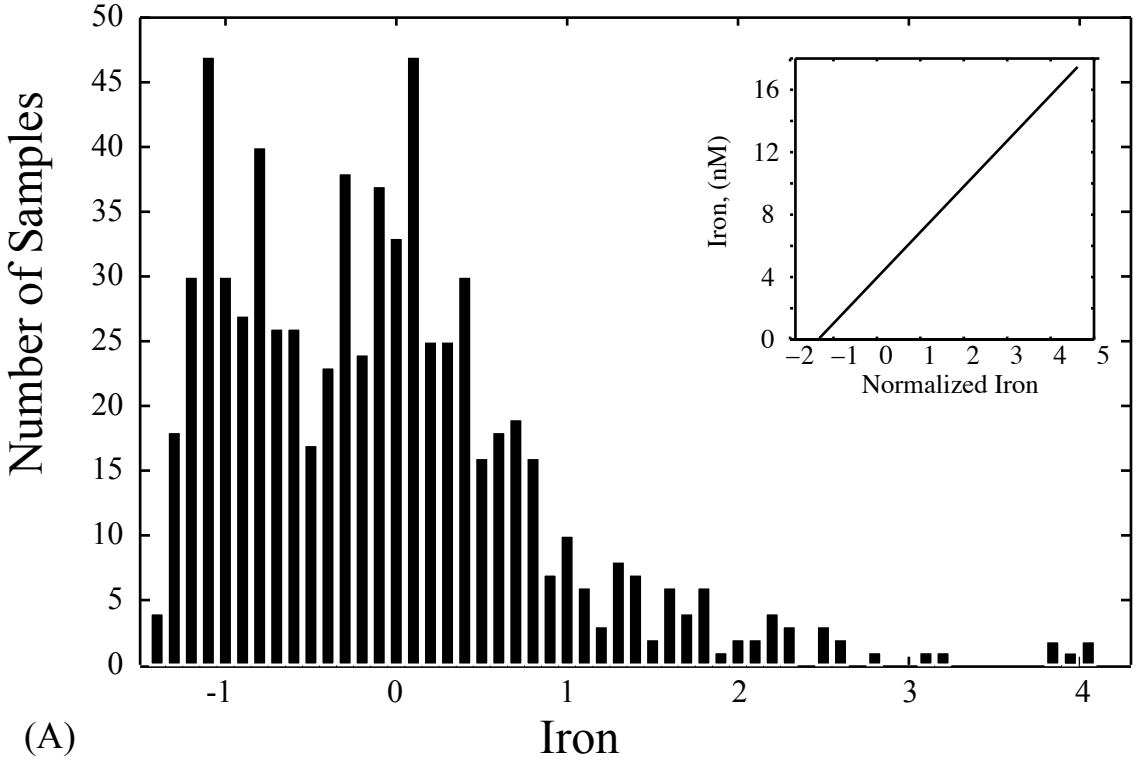

(A)

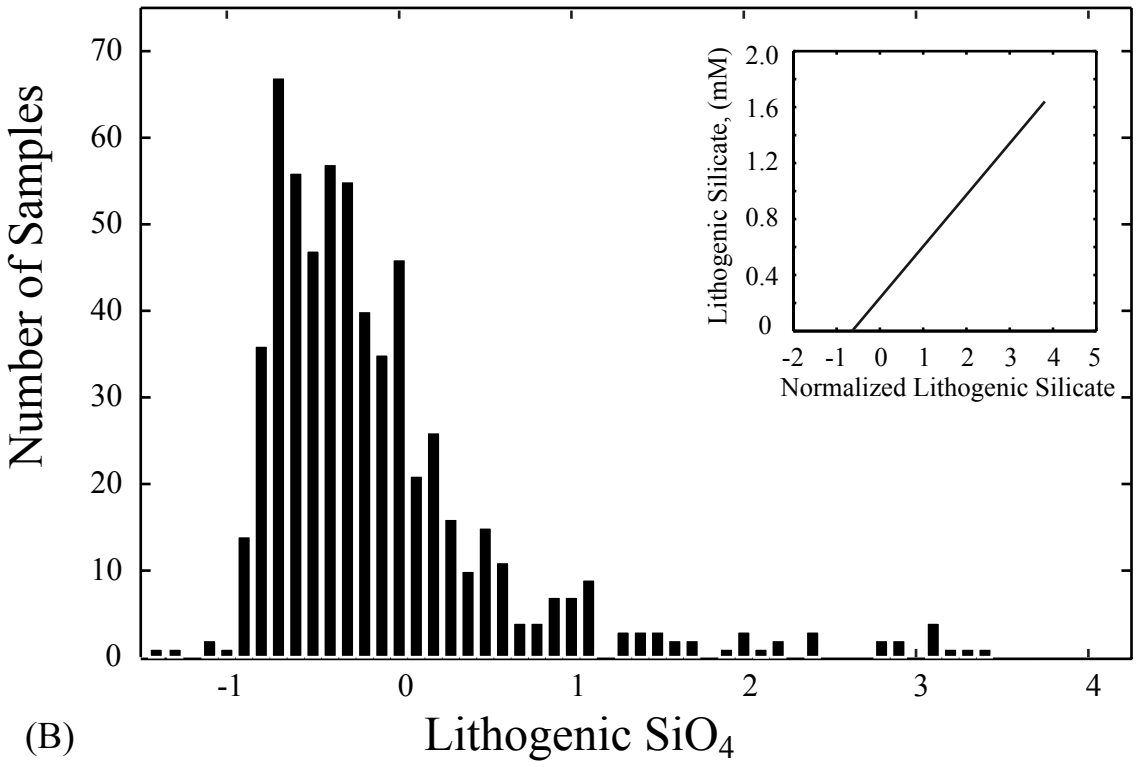

(B)

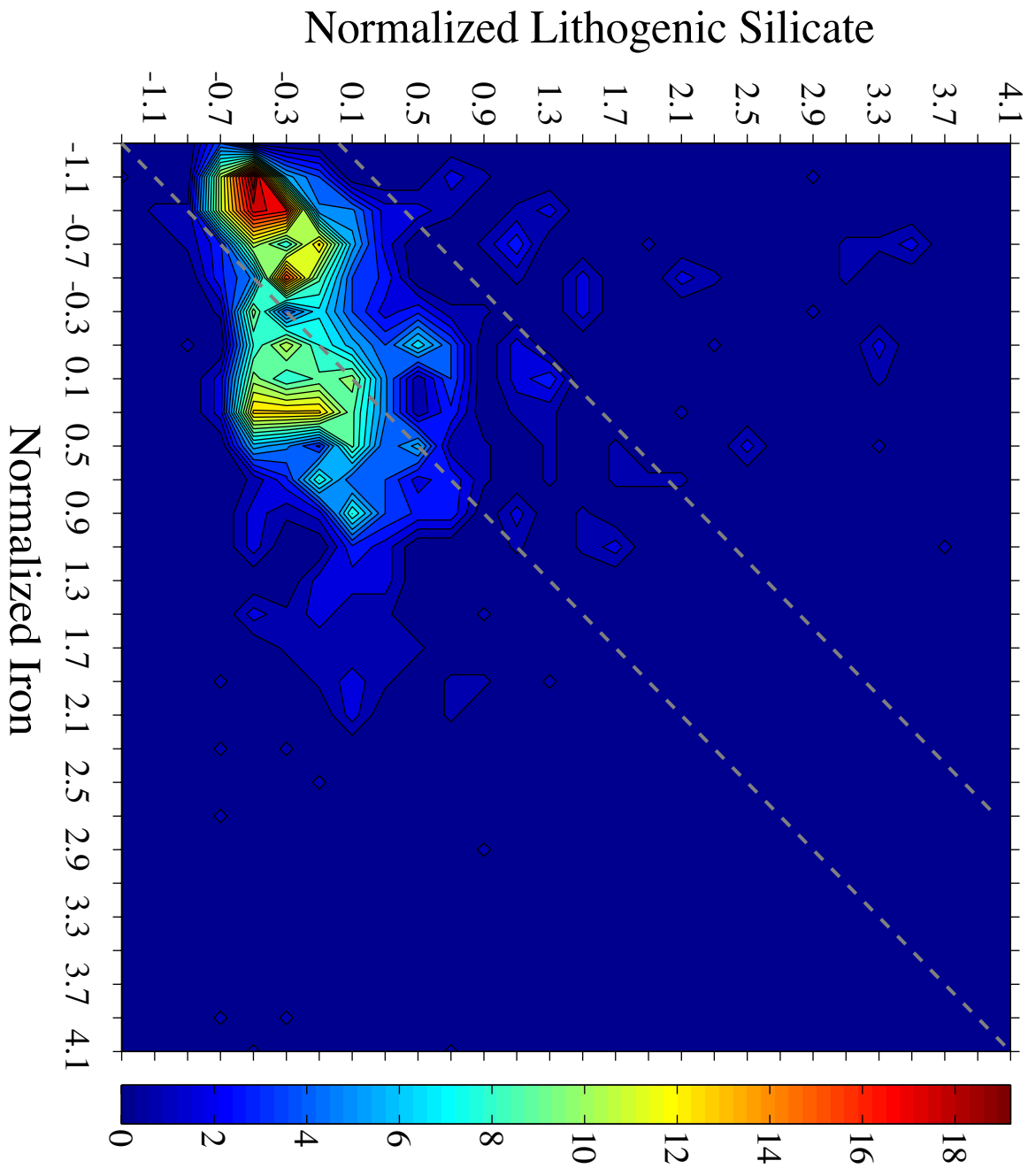
Normalized Lithogenic Silicate
4.1
3.7
3.3
2.9
2.5
2.1
1.7
1.3
0.9
0.5
0.1
-0.3
-0.7
-1.1
Normalized Iron
-1.1 -0.7 -0.3 0.1 0.5 0.9 1.3 1.7 2.1 2.5 2.9 3.3 3.7 4.1
0
2
4
6
8
10
12
14
16
18

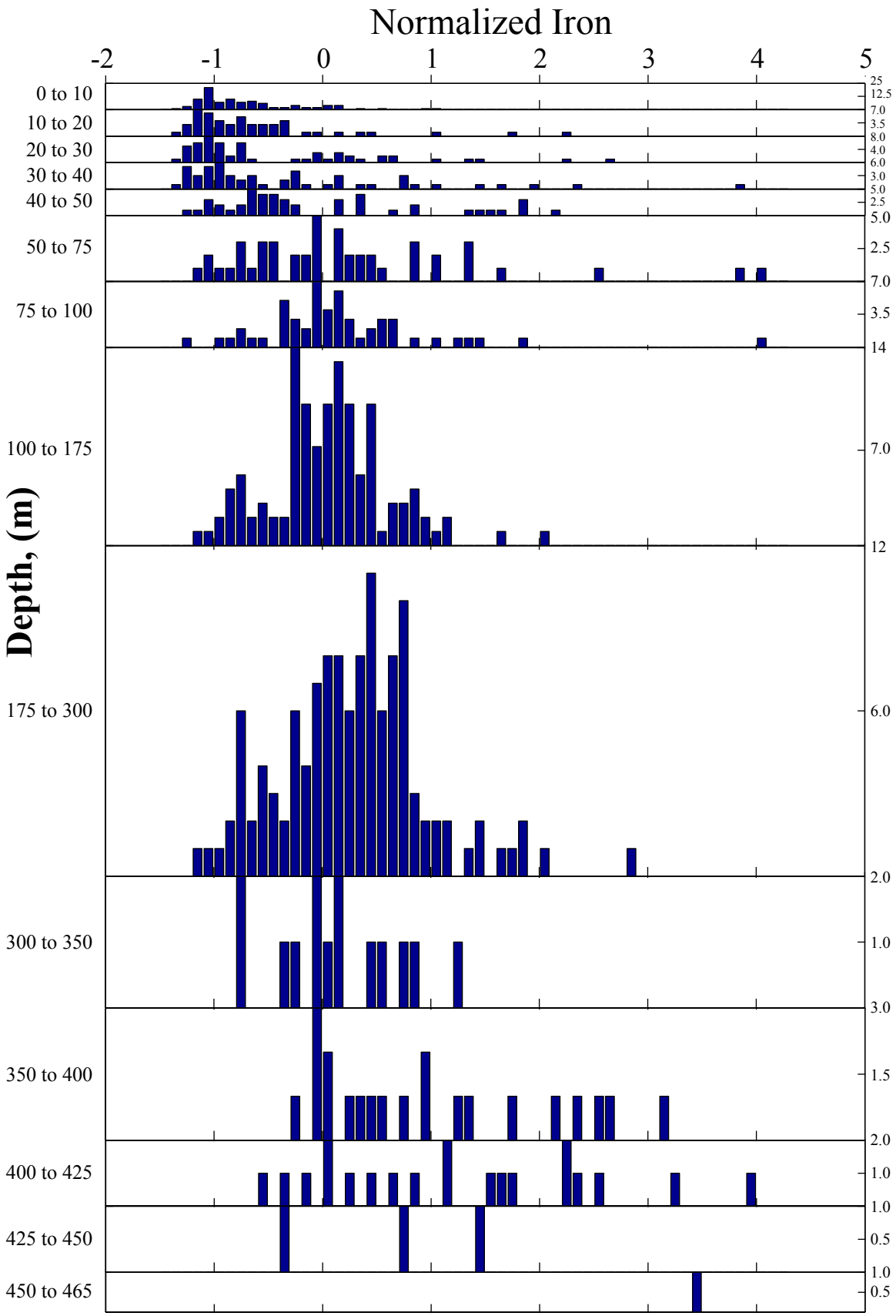
Normalized Iron
-2
-1
0
1
2
3
4
5
Depth, (m)
0 to 10
10 to 20
20 to 30
30 to 40
40 to 50
50 to 75
75 to 100
100 to 175
175 to 300
300 to 350
350 to 400
400 to 425
425 to 450
450 to 465
25
12.5
7.0
3.5
8.0
4.0
6.0
3.0
5.0
2.5
5.0
2.5
7.0
3.5
14
7.0
12
6.0
2.0
1.0
3.0
1.5
2.0
1.0
1.0
0.5
1.0
0.5

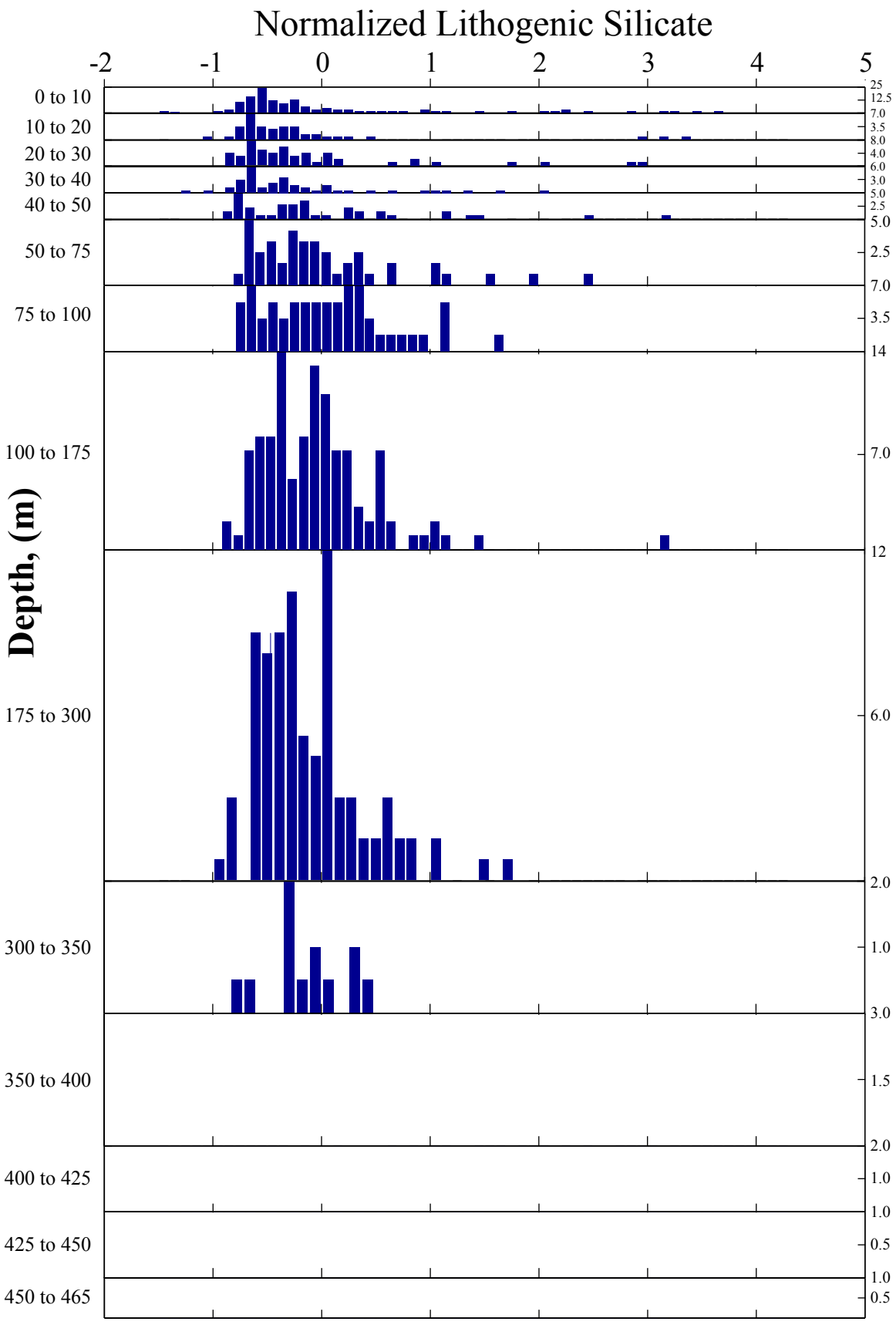
Normalized Lithogenic Silicate
-2
-1
0
1
2
3
4
5
Depth, (m)
0 to 10
10 to 20
20 to 30
30 to 40
40 to 50
50 to 75
75 to 100
100 to 175
175 to 300
300 to 350
350 to 400
400 to 425
425 to 450
450 to 465
25
12.5
7.0
3.5
8.0
4.0
6.0
3.0
5.0
2.5
5.0
2.5
7.0
3.5
14
7.0
12
6.0
2.0
1.0
3.0
1.5
2.0
1.0
1.0
0.5
1.0
0.5

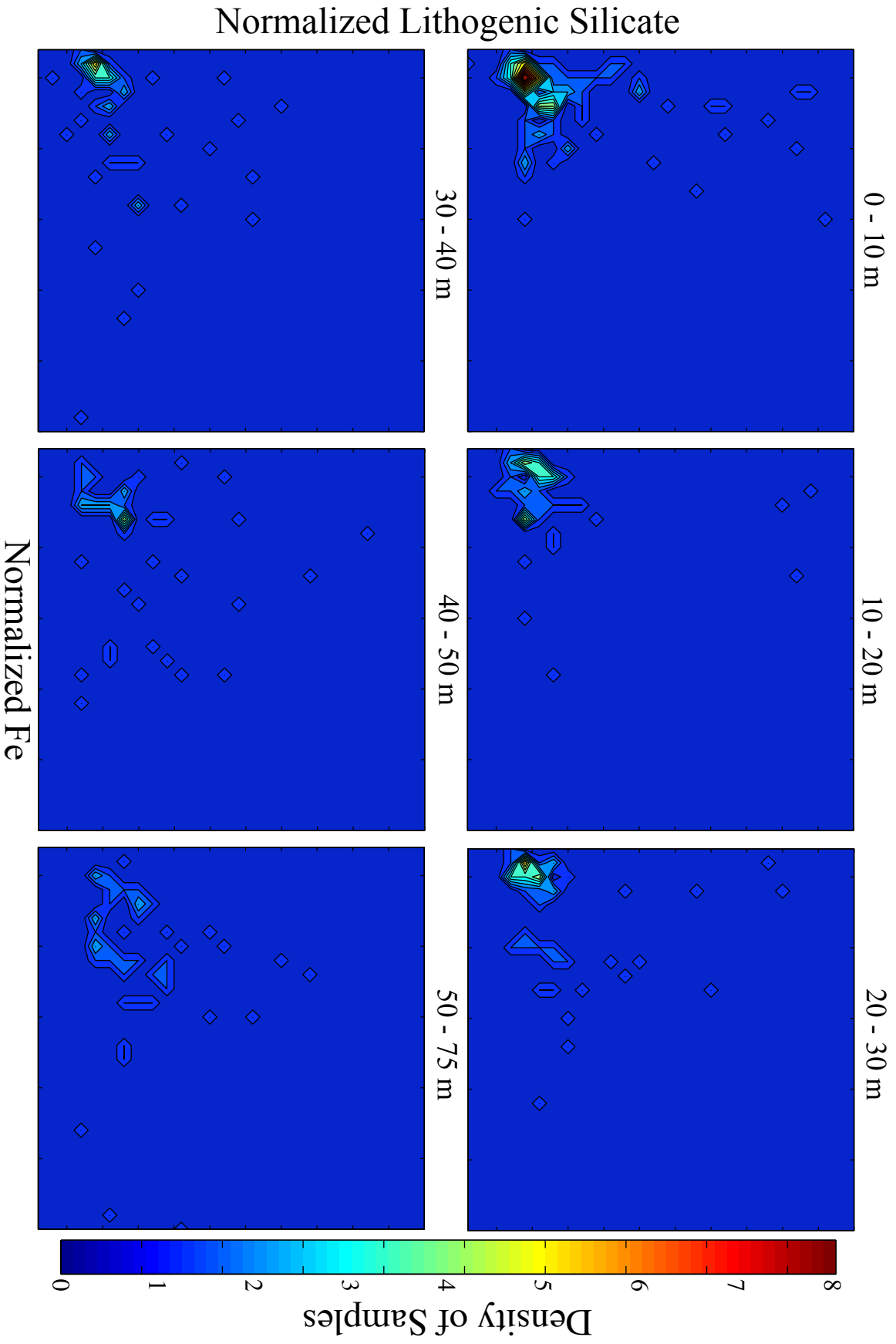
Normalized Lithogenic Silicate
Normalized Fe
0 - 10 m
10 - 20 m
20 - 30 m
30 - 40 m
40 - 50 m
50 - 75 m
Density of Samples
0
1
2
3
4
5
6
7
8

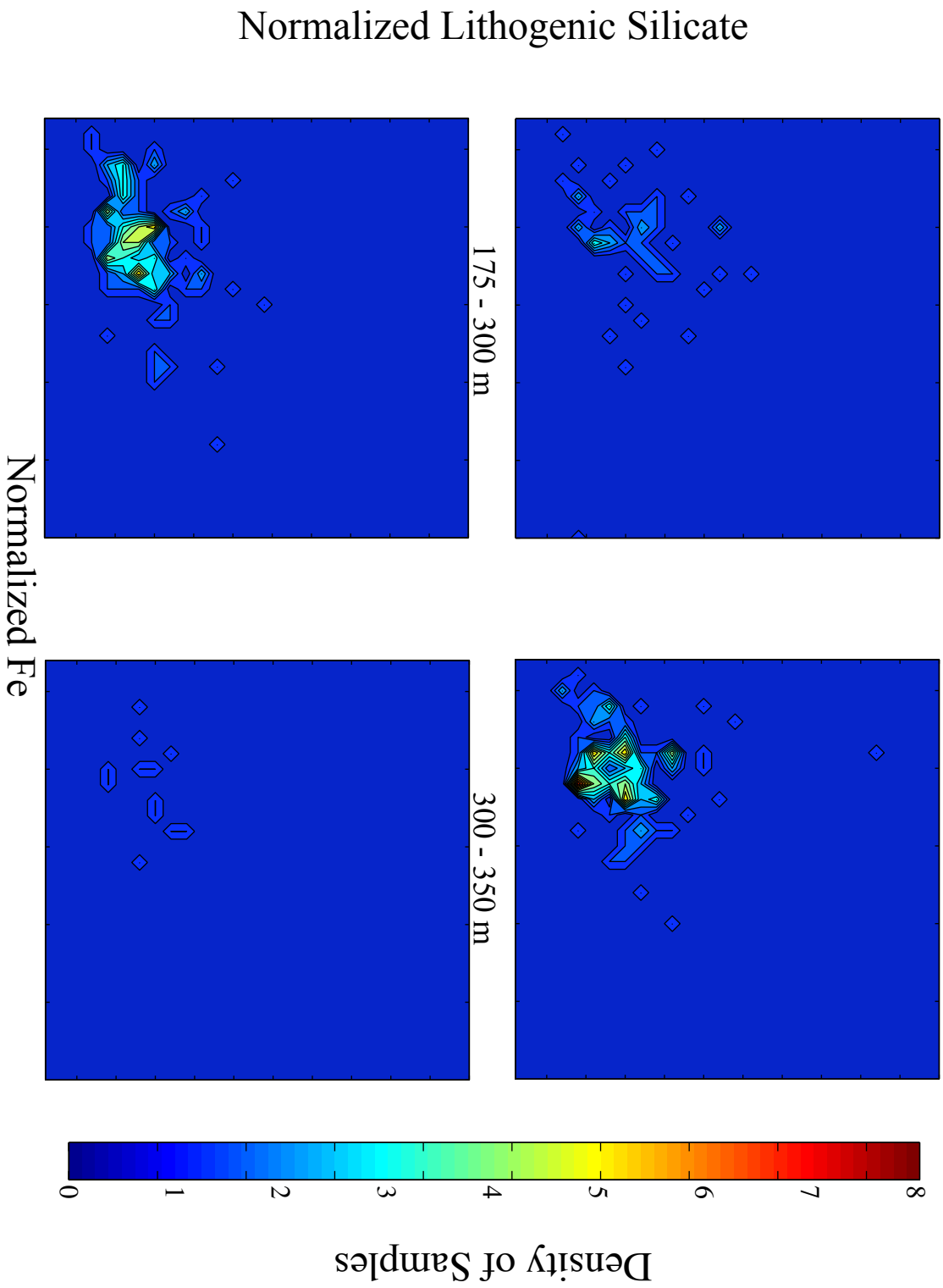
Normalized Lithogenic Silicate
75 - 100 m
175 - 300 m
100 - 175 m
300 - 350 m
Normalized Fe
Density of Samples
0
1
2
3
4
5
6
7
8

Depth (m)
50
100
150
200
250
300
350
400
450
A S O N D J F M A M J J A S O N D J F M A M J J A S
Aug Oct Dec Feb Apr Jun Aug Oct Dec Feb Apr Jun Aug
2004
2005
2006
Oxygen, (V)
1
1.5
2
2.5
3
3.5

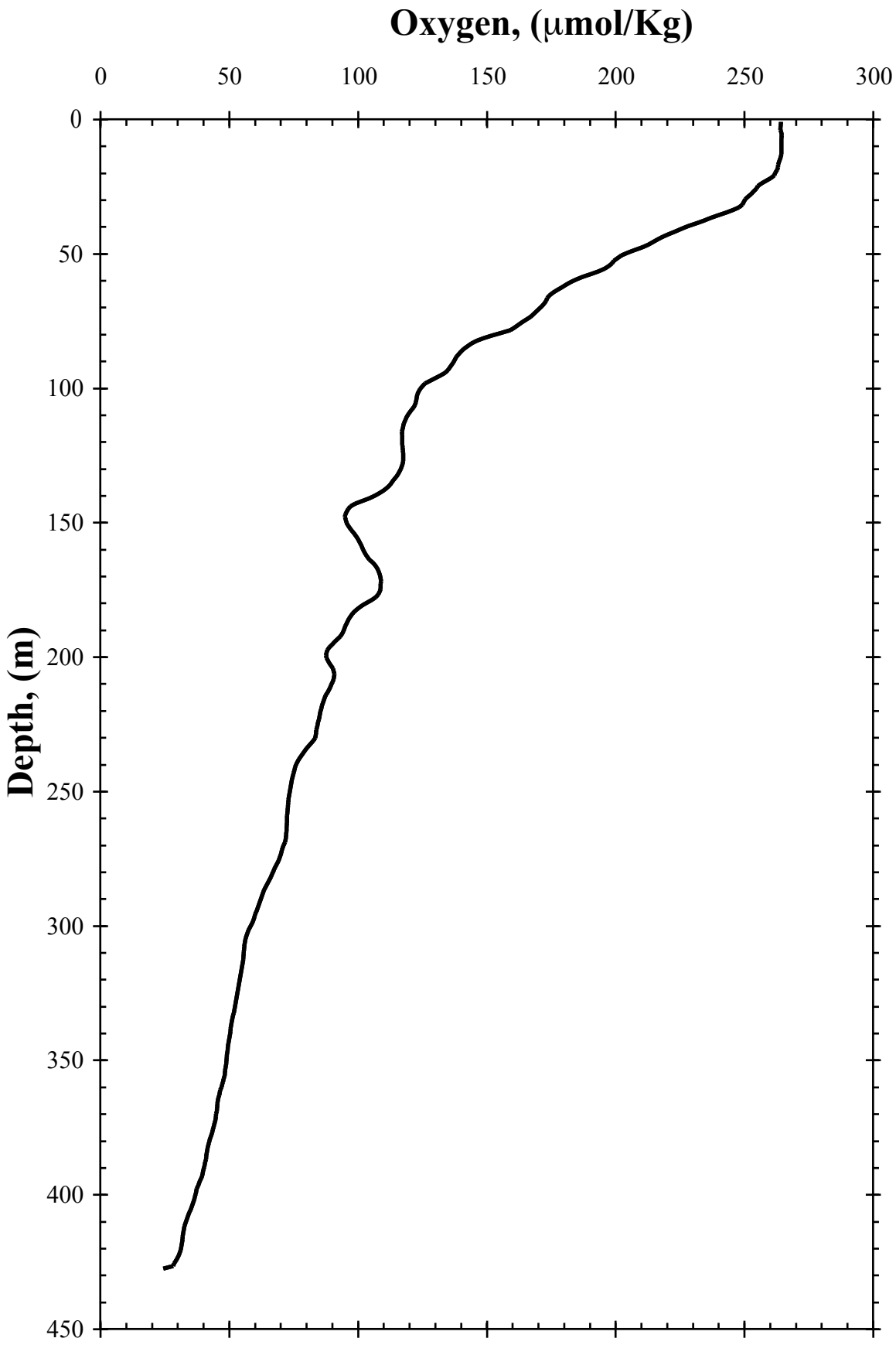
Oxygen, (μmol/Kg)
0
50
100
150
200
250
300
Depth, (m)
0
50
100
150
200
250
300
350
400
450

San Pedro Basin CTD Profile, 11/07/2004

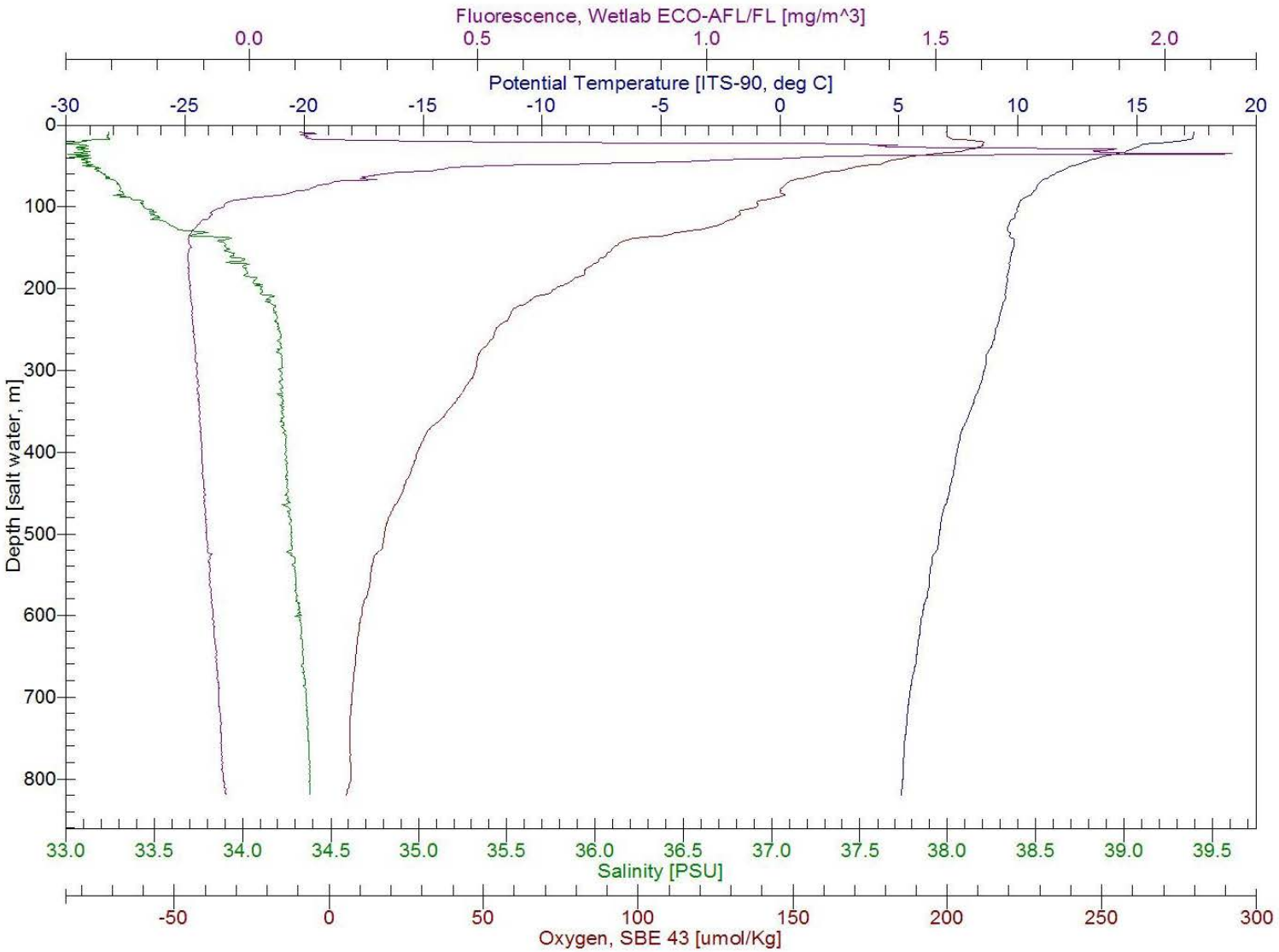

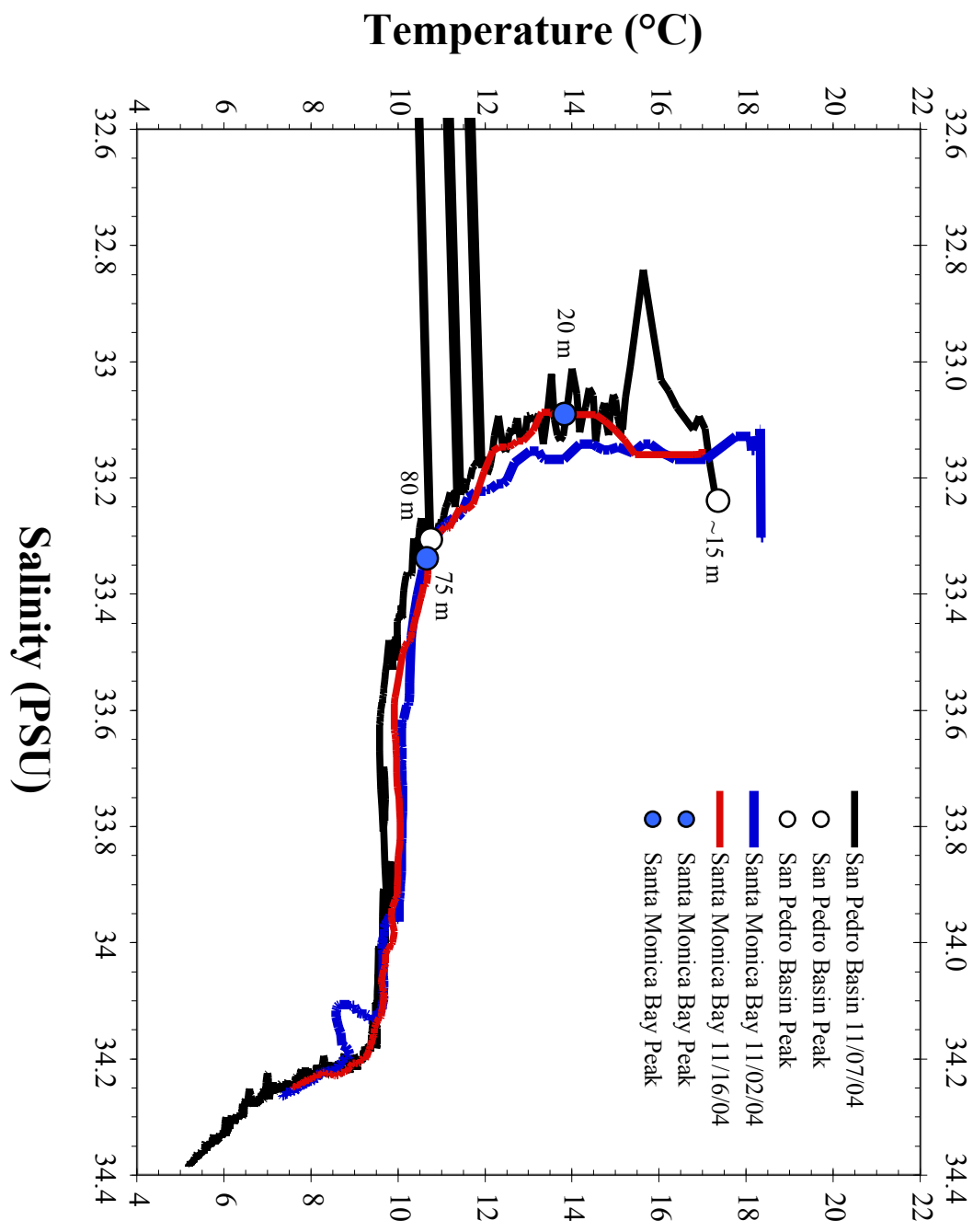
San Pedro Basin vs. Santa Monica Bay
Temperature (°C)
Salinity (PSU)
San Pedro Basin 11/07/04
San Pedro Basin Peak
San Pedro Basin Peak
Santa Monica Bay 11/02/04
Santa Monica Bay 11/16/04
Santa Monica Bay Peak
Santa Monica Bay Peak
~15 m
20 m
80 m
75 m
22
20
18
16
14
12
10
8
6
4
32.6
32.8
33.0
33.2
33.4
33.6
33.8
34.0
34.2
34.4

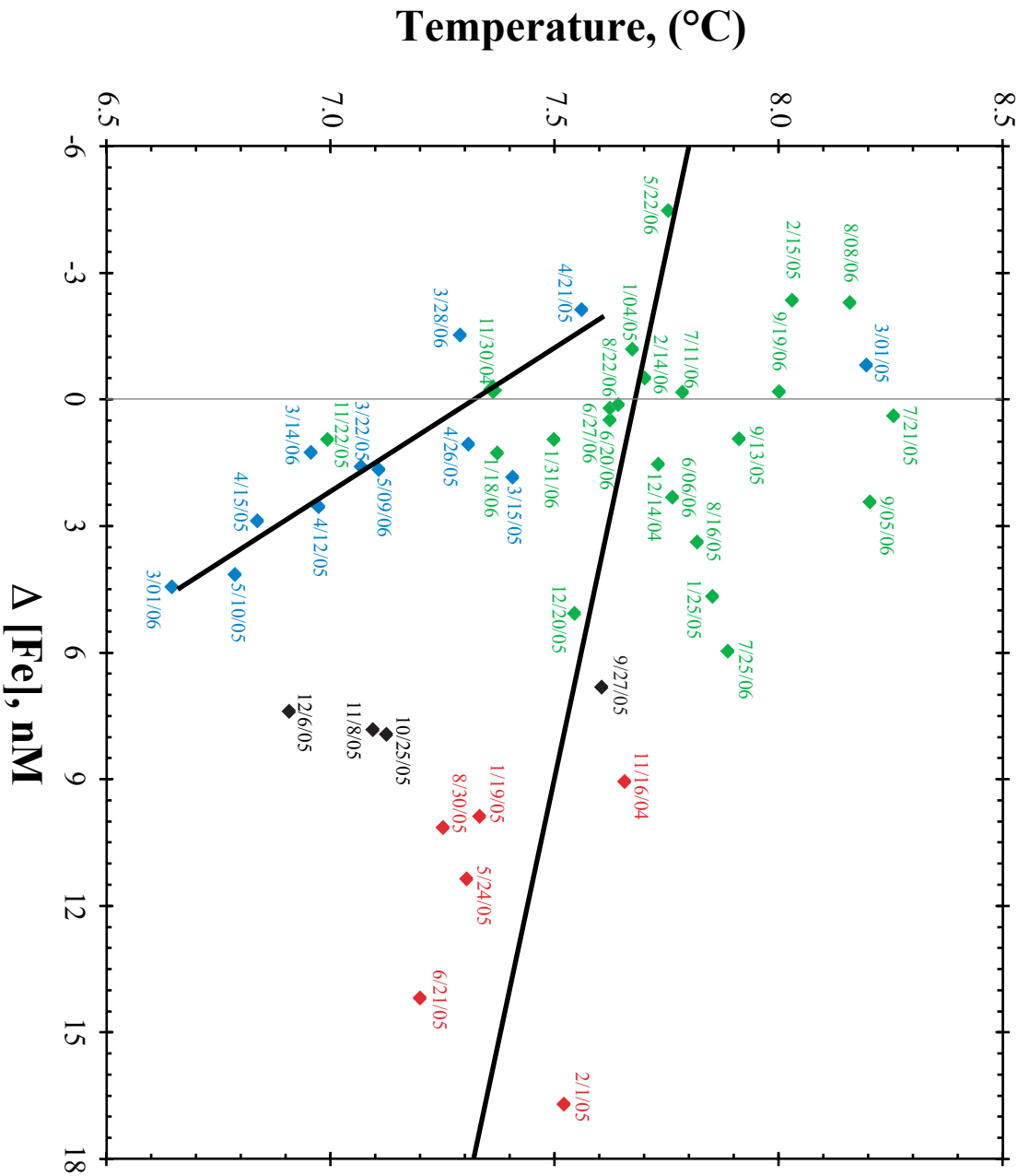
Bottom Water
Temperature, (°C)
Δ [Fe], nM
8.5
8.0
7.5
7.0
6.5
-6
-3
0
3
6
9
12
15
18
5/22/06
8/08/06
2/15/05
3/01/05
9/19/06
7/21/05
4/21/05
1/04/05
8/22/06
2/14/06
9/05/06
3/28/06
7/11/06
9/13/05
11/30/04
6/27/06
6/20/06
6/06/06
12/14/04
1/31/06
8/16/05
1/25/05
3/15/05
4/26/05
1/18/06
12/20/05
7/25/06
3/14/06
11/22/05
3/22/05
5/09/06
9/27/05
11/16/04
4/15/05
4/12/05
12/6/05
11/8/05
10/25/05
3/01/06
5/10/05
1/19/05
8/30/05
5/24/05
6/21/05
2/1/05

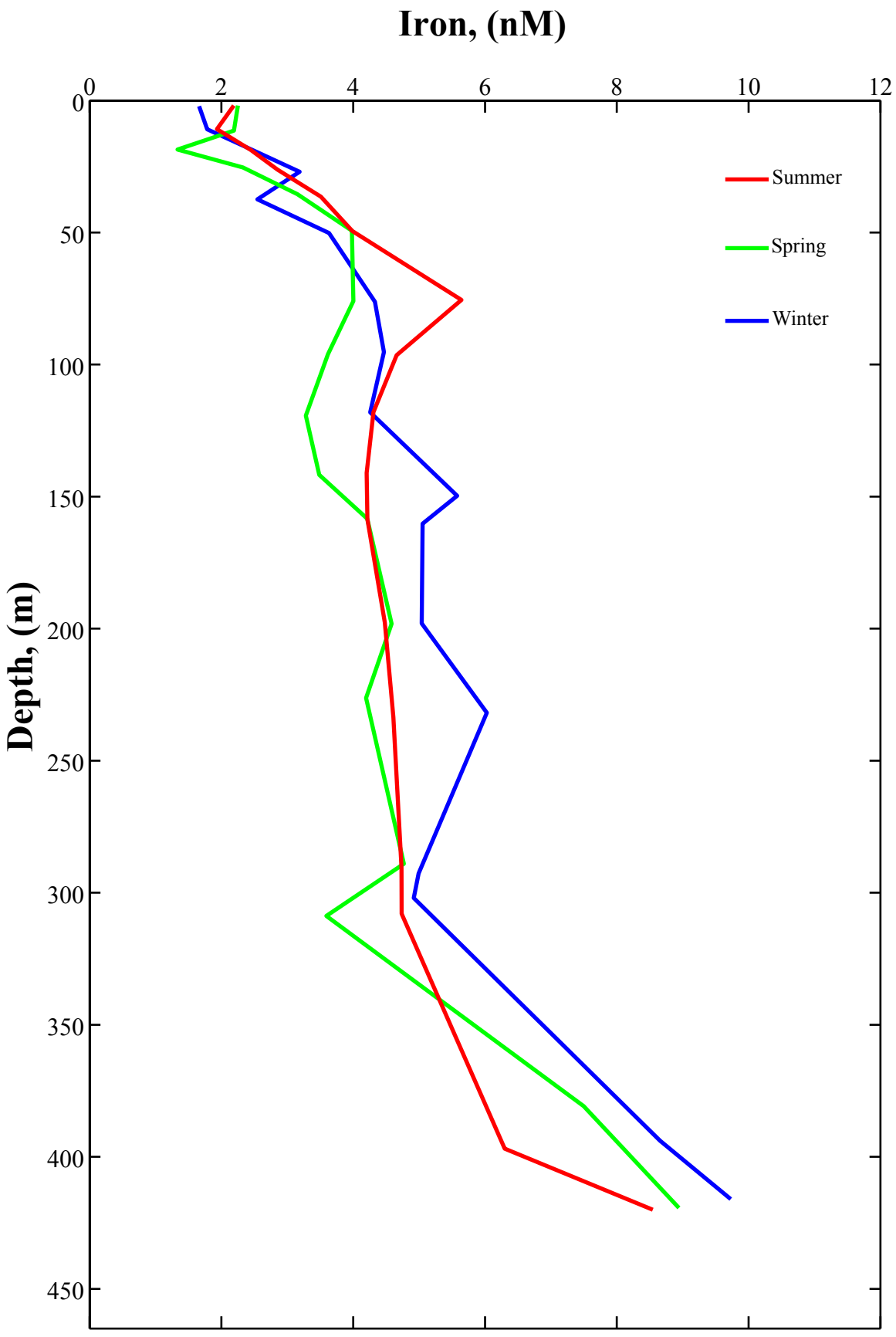
Iron, (nM)
0
2
4
6
8
10
12
Depth, (m)
0
50
100
150
200
250
300
350
400
450
Summer
Spring
Winter

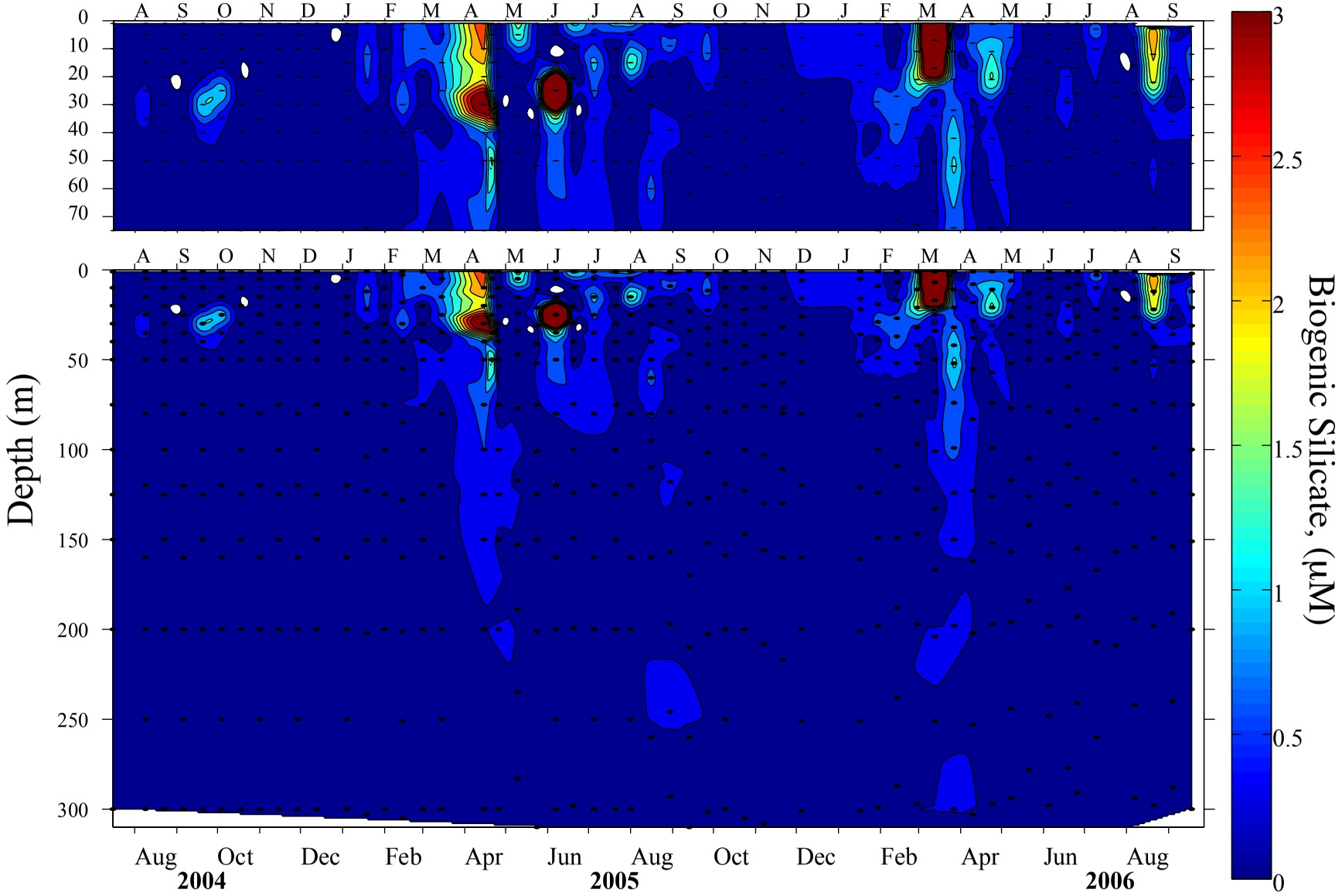
A S O N D J F M A M J J A S O N D J F M A M J J A S
0 10 20 30 40 50 60 70
0 50 100 150 200 250 300
Depth (m)
Aug Oct Dec Feb Apr Jun Aug Oct Dec Feb Apr Jun Aug
2004
2005
2006
Biogenic Silicate, (µM)
3 2.5 2 1.5 1 0.5 0

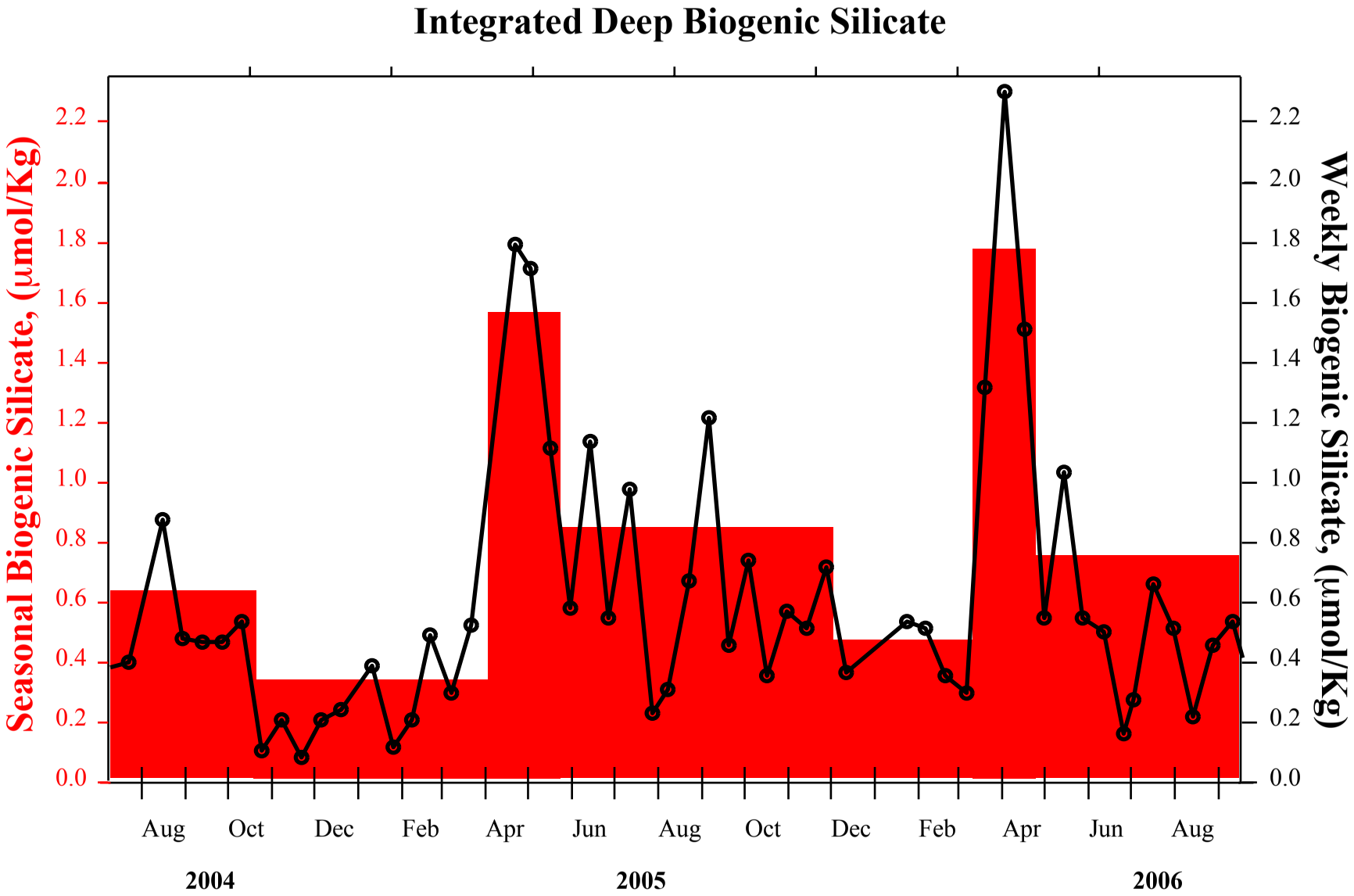
Integrated Deep Biogenic Silicate
Seasonal Biogenic Silicate, (µmol/Kg)
Weekly Biogenic Silicate, (µmol/Kg)
0.0
0.2
0.4
0.6
0.8
1.0
1.2
1.4
1.6
1.8
2.0
2.2
Aug
Oct
Dec
Feb
Apr
Jun
Aug
Oct
Dec
Feb
Apr
Jun
Aug
2004
2005
2006

BIBLIOGRAPHY

Aumont, O., Maier-Reimer, E., Blain, S. and Monfray, P., 2003. An ecosystem model of the global ocean including Fe, Si, P colimitations. Global Biogeochemical Cycles, 17(2).

Barbeau, K., Rue, E.L., Bruland, K.W. and Butler, A., 2001. Photochemical cycling of iron in the surface ocean mediated by microbial iron(III)-binding ligands. Nature, 413: 409-413.

Berelson, W. et al., 2003. A time series of benthic flux measurements from Monterey Bay, CA. Continental Shelf Research, 23(5): 457-481.

Berelson, W.M., 1991. The Flushing of 2 Deep-Sea Basins, Southern California Borderland. Limnology and Oceanography, 36(6): 1150-1166.

Buck, K.N., Lohan, M.C., Berger, C.J.M. and Bruland, K.W., 2007. Dissolved iron speciation in two distinct river plumes and an estuary: Implications for riverine iron supply. Limnology and Oceanography, 52(2): 843-855.

Buck, K.N., M. C. Lohan, C. J. M. Berger, and K. W. Bruland 2007. Dissolved iron speciation in two distinct river plumes and an estuary: Implications for riverine iron supply. Limnology and Oceanography, 52(2).

Dong, C.M. and McWilliams, J.C., 2007. A numerical study of island wakes in the Southern California Bight. Continental Shelf Research, 27(9): 1233-1248.

Duce, R.A. and Tindale, N.W., 1991. Atmospheric transport of iron and its deposition in the ocean. Limnology and Oceanography, 36(8): 1715-1726.

Erel, Y., Pehkonen, S.O. and Hoffmann, M.R., 1993. Redox Chemistry of Iron in Fog and Stratus Clouds. Journal of Geophysical Research-Atmospheres, 98(D10): 18423-18434.

Froelich, P.N. et al., 1979. Early Oxidation of Organic-Matter in Pelagic Sediments of the Eastern Equatorial Atlantic - Suboxic Diagenesis. Geochimica Et Cosmochimica Acta, 43(7): 1075-1090.

Guazzotti, S.A., Whiteaker, J.R., Suess, D., Coffee, K.R. and Prather, K.A., 2001. Real-time measurements of the chemical composition of size-resolved particles during a Santa Ana wind episode, California USA. Atmospheric Environment, 35: 3229-3240.

Guieu, C., Duce, R. and Arimoto, R., 1994. Dissolved Input of Manganese to the Ocean - Aerosol Source. Journal of Geophysical Research-Atmospheres, 99(D9): 18789-18800.

Hammond, D.E., Marton, R.A., Berelson, W.M. and Ku, T.L., 1990. Ra-228 Distribution and Mixing in San-Nicolas and San-Pedro Basins, Southern California Borderland. Journal of Geophysical Research-Oceans, 95(C3): 3321-3335.

Horsburgh, M.J., Wharton, S.J., Karavolos, M. and Foster, S.J., 2002. Manganese: elemental defense for a life with oxygen. Trends in Microbiology, 10(11): 496-501.

Johansen, A.M., Siefert, R.L. and Hoffmann, M.R., 2000. Chemical composition of aerosols collected over the tropical North Atlantic Ocean. Journal of Geophysical Research-Atmospheres, 105(D12): 15277-15312.

Johnson, K.S., Coale, K.H., Berelson, W.M. and Gordon, R.M., 1996. On the formation of the manganese maximum in the oxygen minimum. Geochimica Et Cosmochimica Acta, 60(8): 1291-1299.

Kernen, N., Kidd, M.J., Penner-Hahn, J.E. and Pakrasi, H.B., 2002. A light-dependent mechanism for massive accumulation of manganese in the photosynthetic bacterium Synechocytis sp. PCC 6803. Biochemistry, 41(50): 15085-15092.

Klinkhammer, G.P. and Bender, M.L., 1980. The Distribution of Manganese in the Pacific-Ocean. Earth and Planetary Science Letters, 46(3): 361-384.

Lorke, A., Peeters, F. and Wuest, A., 2005. Shear-induced convective mixing in bottom boundary layers on slopes. Limnology and Oceanography, 50(5): 1612-1619.

Lu, R. et al., 2003. Dry deposition of airborne trace metals on the Los Angeles Basin and adjacent coastal waters. Journal of Geophysical Research-Atmospheres, 108(D2).

Maldonado, M.T., Boyd, P.W., Harrison, P.J. and Price, N.M., 1999. Co-limitation of phytoplankton growth by light and Fe during winter in the NE subarctic Pacific Ocean. Deep-Sea Research Part Ii-Topical Studies in Oceanography, 46(11-12): 2475-2485.

Martin, J.H., 1990. Glacial-interglacial CO_2 change: The Iron Hyphothesis. Paleoceanography, 5(1): 1-13.

Martin, J.H. and Fitzwater, S.E., 1988. Iron deficiency limits phytoplankton growth in the north-east Pacific subarctic. Nature, 331: 341-343.

Martin, J.H. and Gordon, M., 1988. Northest Pacific iron distributions in relation to phytoplankton productivity. Deep-Sea Research, 35(2): 177-196.

Martin, J.H., Gordon, R.M., Fitzwater, S. and Broenkow, W.W., 1989. VERTEX: phytoplankton/iron studies in the Gulf of Alaska. Deep-Sea Research, 36(5): 649-680.

Mills, M.M., Ridame, C., Davey, M., La Roche, J. and Geider, R.J., 2004. Iron and phosphorus co-limit nitrogen fixation in the eastern tropical North Atlantic. Nature, 429(6989): 292-294.

MODIS, 2008. MODIS Rapid Response System. NASA/GSFC, http://modis.gsfc.nasa.gov/.

Moore, J.K., Doney, S.C., Lindsay, K., Mahowald, N. and Michaels, A.F., 2006. Nitrogen fixation amplifies the ocean biogeochemical response to decadal timescale variations in mineral dust deposition. Tellus Series B-Chemical and Physical Meteorology, 58(5): 560-572.

Morel, F.M.M. and Hering, J.G., 1993. Principles and Applications of Aquatic Chemistry. John Wiley & Sons, Inc., New york, 588 pp.

Murray, J.W. and Gill, G., 1978. Geochemistry of Iron in Puget Sound. Geochimica Et Cosmochimica Acta, 42(1): 9-19.

California Department of Forestry and Fire Protection, 2008. Fire Incident Webpage. California Department of Forestry and Fire Protection, http://www.fire.ca.gov/.

Rathburn, A.E., Perez, M.E. and Lange, C.B., 2001. Benthic-pelagic coupling in the Southern California Bight: Relationships between sinking organic material, diatoms and benthic foraminifera. Marine Micropaleontology, 43(3-4): 261-271.

Rose, A.L. and Waite, T.D., 2002. Kinetic model for Fe(II) oxidation in seawater in the absence and presence of natural organic matter. Environmental Science & Technology, 36(3): 433-444.

Rue, E.L. and Bruland, K.W., 1995. Complexation of Iron(III) by Natural Organic-Ligands in the Central North Pacific as Determined by a New Competitive Ligand Equilibration Adsorptive Cathodic Stripping Voltammetric Method. Marine Chemistry, 50(1-4): 117-138.

Shipe, R.F. and Brzezinski, M.A., 2001. A time series study of silica production and flux in an eastern boundary region: Santa Barbara Basin, California. Global Biogeochemical Cycles, 15(2): 517-531.

Siefert, R.L., Johansen, A.M., Hoffmann, M.R. and Pehkonen, S.O., 1998. Measurements of trace metal (Fe, Cu, Mn, Cr) oxidation states in fog and stratus clouds. Journal of the Air & Waste Management Association, 48(2): 128-143.

Smith, S.V. and Hollibaugh, J.T., 1993. Coastal Metabolism and the Oceanic Organic-Carbon Balance. Reviews of Geophysics, 31(1): 75-89.

Stumm, W. and Morgan, J.J., 1996. Aquatic Chemistry. Wiley-Interscience, New York, 1022 pp.

Sunda, W.G., Huntsman, S.A. and Harvey, G.R., 1983. Photoreduction of manganese oxides in seawater and its geochemical and biological implications. Nature, 301: 234-236.

Sung, W. and Morgan, J.J., 1980. Kinetics and Product of Ferrous Iron Oxygenation in Aqueous Systems. Environmental Science & Technology, 14(5): 561-568.

Swarzenski, P.W. et al., 2006. Combined time-series resistivity and geochemical tracer techniques to examine submarine groundwater discharge at Dor Beach, Israel. Geophysical Research Letters, 33(24).

Taylor, J.R., 1993. Turbulence and Mixing in the Boundary-Layer Generated by Shoaling Internal Waves. Dynamics of Atmospheres and Oceans, 19(1-4): 233-258.

Tsunogai, S. and Noriki, S., 1991. Particulate Fluxes of Carbonate and Organic-Carbon in the Ocean - Is the Marine Biological-Activity Working as a Sink of the Atmospheric Carbon. Tellus Series B-Chemical and Physical Meteorology, 43(2): 256-266.

Turner, D.R. and Hunter, K.A. (Editors), 2001. The biogeochemistry of iron in seawater. IUPAC series on analytical and physical chemistry of environmental systems ; v. 7. J. Wiley, New York.

The Weather Underground, 2008. The Weather Underground, Inc, http://www.wunderground.com/.

Ussher, S.J. et al., 2007. Distribution and redox speciation of dissolved iron on the European continental margin. Limnology and Oceanography, 52(6): 2530-2539.

van den Berg, C.M.G., 1995. Evidence for Organic Complexation of Iron in Seawater. Marine Chemistry, 50(1-4): 139-157.

Wedepohl, K.H., 1995. The Composition of the Continental-Crust. Geochimica Et Cosmochimica Acta, 59(7): 1217-1232.

Wong, C.S. et al., 2002. Seasonal cycles of nutrients and dissolved inorganic carbon at high and mid latitudes in the North Pacific Ocean during the Skaugran cruises: determination of new production and nutrient uptake ratios. Deep-Sea Research Part Ii-Topical Studies in Oceanography, 49(24-25): 5317-5338.

Wu, J. and Boyle, E.A., 1998. Determination of iron in seawater by high-resolution isotope dilution inductively coupled plasma mass spectrometry after $Mg(OH)_2$ coprecipitation. Analytica Chimica Acta, 367: 183-191.